Hydrodynamics of Shocked Interfaces

by

Michael J. Wadas

A dissertation submitted in partial fulfillment
of the requirements for the degree of
Doctor of Philosophy
(Mechanical Engineering)
in the University of Michigan
2023

Doctoral Committee:

Associate Professor Eric Johnsen, Chair
Professor David R. Dowling
Associate Professor Carolyn C. Kuranz
Doctor Marius A. Millot, Lawrence Livermore National Laboratory
Assistant Professor Aaron Towne

Michael J. Wadas
mwadas@umich.edu
ORCID iD: 0000-0002-7853-4964

To my ciu-ziu, both living and in memory.

ACKNOWLEDGEMENTS

I am deeply grateful for my advisor, Prof. Eric Johnsen, whose technical and professional mentorship has enabled me to grow as a researcher, engineer, and scientist. My gratitude extends to my committee, Dr. Marius Millot, Prof. Carolyn Kurnaz, Prof. Aaron Towne, and Prof. David Dowling for their guidance and feedback on my research.

I'd also like to thank friends and colleagues in the Scientific Computing and Flow Physics Laboratory, the Mechanical Engineering Department, and the greater University of Michigan communities, among them, Brian and Brandon, for early support and encouragement, Shahab, for late nights in the Auto Lab, Mauro, for rousing discussions of Beleriand and the First Age, Siddhesh, for highly efficient cat-identifying neural nets, Phil, for help running code, Kazuya, for pickup basketball, Lauren, for captivating tales of med school, Loc, for sharing whiskey tasting notes, Heath, for kitchen-inspired laser experiments, Sallee, for mushroom talk and the steadiest of hands, Sam, for constant mentoring and help with vortex sheets, Suyash, for clean presentations and logos, Minki, for introducing me to Yoon's, Mani, for advice on stability theory with a side of panipuri, Eunhye, for championing XSEDE, Griffin, for orchestrating Ronan's demise, Kevin, for runs and culinary expertise, Sonya, for inspiration to climb a 14er, Erin, for Swiftie hysteria, Codie, for tasty vegan treats, Baudouin, for delicious plantains, Ziyang, for reminiscing about Purdue and knowledge on all things methods, and William, for pickleball and an unmatched fervor for implementing new code features.

Throughout my graduate studies, I've been showered with love and support by friends and family, including my parents, John and Carrie, my siblings, John, Kathryn, and Elizabeth, grandparents, aunts, uncles, cousins, nieces, nephews, in-laws, my D&D group, PackDev, and Ann Arbor friends, but by none so much as my wife Ally.

This work is supported by the Lawrence Livermore National Laboratory (LLNL) under subcontract B632749 and was performed under the auspices of the U. S. Department of Energy (DOE) by the LLNL under Contract No. DE-AC52-07NA27344 with partial support provided by LDRD 19-ERD-031 and the U.S. DOE NNSA Center of Excellence under cooperative agreement number DE-NA0003869. Additionally, VISAR and SOP data were analyzed with LLNL AnalyzeVISAR code. Computational resources were provided by the Extreme Science and Engineering Discovery Environment (XSEDE) Comet GPU and Stampede2 systems under grant TG-CTS130005 and the

Oak Ridge Leadership Computing Facility, a DOE Office of Science User Facility supported under Contract DE-AC05-00OR22725. Finally, this work is supported by the U. S. DOE as part of the Stewardship Science Graduate Fellowship (SSGF) Program under grants DE-NA0003864 and DE-NA0003960.

TABLE OF CONTENTS

CHAPTER

LIST OF FIGURES

FIGURE

LIST OF TABLES

TABLE

LIST OF ACRONYMS

CHI Iodine-Doped Hydrocarbon

CI Crow Instability

CRF Carbonized Resorcinol Formaldehyde

DAC Diamond Anvil Cell

DCS Dynamic Compression Sector

DFT Density Functional Theory

DOE Department of Energy

EOS Equation of State

ER Equatorial Ring

FPEOS First Principles Equation of State

HED High Energy Density

ICF Inertial Confinement Fusion

LLNL Lawrence Livermore National Laboratory

MD Molecular Dynamics

MEC Matter in Extreme Conditions instrument

MOC Method of Characteristics

NC Number of Characteristics

NIF National Ignition Facility

PAI Polyamide-Imide

PIMC Path Integral Monte-Carlo

RMI Richtmyer-Meshkov Instability

REOS Rostock Equation of State

SN1987A Supernova 1987A

SOP Streaked Optical Pyrometry

SSGF Stewardship Science Graduate Fellowship

VISAR Velocity Interferometry for Any Reflector

XSEDE Extreme Science and Engineering Discovery Environment

ABSTRACT

Shock waves emerge following the rapid release of energy in a flow. The interaction of shocks with interfaces separating dissimilar fluids generates complex systems of waves and stimulates mixing between those fluids. Shock waves are utilized in engineering applications for their ability to rapidly compress materials. In dynamic compression experiments, such shock waves are utilized to access extreme pressure states that can be measured in the laboratory, uncovering the behavior of materials at conditions consistent with and improving models for the interiors of gas giant planets or the atmospheres of white dwarf stars. In inertial confinement fusion, shock waves compress a spherical capsule of fusion fuel to the point where nuclear fusion may take place, releasing an enormous amount of energy that may one day be harvested to generate electricity. However, the shock-induced mixing between different layers of the fuel capsule inhibits the confinement of the fuel required for a self-sustaining reaction. The same type of mixing occurs during the cataclysmic collapse and rebound of stars during type-II supernovae and stimulates the transport of stellar core elements throughout the universe. Furthermore, shocks generated from supernovae and other astrophysical phenomena can interact with interstellar gas, stimulating the hydrodynamic motion that is responsible for the structure of molecular clouds, nebulae, and debris rings. The objective of this thesis is to advance the current understanding of shocked interfacial hydrodynamics for the development of improved dynamic compression experiments, the mitigation of mixing in inertial confinement fusion, and an enhanced understanding of how shock-induced mixing affects supernovae and other astrophysical flows.

To this end, an approach for strengthening shocks in compression experiments is developed. The method replaces sharp interfaces with an intermediate region bridging the impedance mismatch between two materials. By appropriately designing this region, up to twenty-five percent greater shock pressures can be achieved for a finite duration of time, with an exponential discretization of the intermediate region impedance being the most effective distribution for strengthening strong shocks.

Next, data are obtained from dynamic compression experiments examining helium in excess of 3.5 Mbar. The data show significant reflectivity and an increase in compressibility, likely caused by the onset of continuous ionization. The novel data serve as important benchmarks for density functional theory and models for Jovian interiors and white dwarf atmospheres.

In two spatial dimensions, the interaction of two adjacent bubbles of different sizes in a shock-induced mixing region is investigated numerically. A significant departure from existing bubble-merging models is observed, resulting in the ejection of vortex dipoles that escape the confines of the mixing region, which is well predicted from a vorticity-based criterion. Theory is subsequently developed to describe the formation and scaling of vortex rings, the azimuthally symmetric analog to vortex dipoles, emerging from shocked interfacial mixing regions.

Finally, the three-dimensional stability of vortex cores, including those generated from shock-interface interactions, is investigated, and the behavior of linear perturbations undergoing the cylindrical Crow instability is uncovered. The analysis is applied to Supernova 1987A, a system with an equatorial ring surrounding the location of the progenitor star along which there are 28 mass clumps. The dominant unstable wavenumber is consistent with the number of observed clumps, suggesting that the Crow instability initiates clumping in Supernova 1987A and other star systems with equatorial rings.

CHAPTER 1

Introduction

The rapid release of energy in a fluid flow can lead to the generation of shock waves, flow discontinuities across which the pressure and density increase, often dramatically [50]. Shocks occur in a wide variety of natural contexts including volcanic eruptions [260], cavitation bubble collapse [288], and supernovae [1], and engineering applications such as supersonic flight [6] and inertial confinement fusion (ICF) [17]. In many scenarios, the shock passes through an interface separating materials of different densities, as in laser-driven shock compression experiments designed to study the behavior of materials in extreme pressure environments like those in planetary interiors [29, 36, 75, 176]. In addition to the compression of the material into which a shock propagates, a shock wave passing through an interface can give rise to fluid mixing through the Richtmyer-Meshkov instability (RMI) [162, 220]. This mixing occurs during supernovae, affecting the development of any ensuing nebulae [110], as well as in ICF, where it is detrimental to the confinement of fusion fuel [286]. Finally, the dynamics of vortex cores, potentially generated from interfacial vorticity deposited by a shock, may stimulate the formation of isolated vortex structures and clumping in astrophysical debris clouds [8, 53].

The objective of this thesis is to advance the current understanding of hydrodynamic phenomena that emerge as a consequence of a shock wave passing through a fluid interface, with applications to dynamic compression research, RMI mixing in ICF and supernovae, and vortex-core dynamics in both astrophysical and Earth-bound flows. This introduction provides an overview of the physical system of interest relevant to the applications along with necessary background required to interpret the technical chapters that follow.

1.1 Physical System and Governing Equations

A fluid is a substance that continuously deforms under the application of shear. Fluids include liquids, which conform to the shape of but do not expand to fill their container, and gases, which both conform to and fill the volume of any bounding container. Plasma, being ionized gas, is also a fluid, though one where additional physics may emerge as a result of the presence of charged particles. At any given time, the fluid is characterized by a number of thermodynamic state variables (e.g., pressure, density, internal energy, etc.) that may vary in space. The flow, or time evolution of the state, of a fluid is governed by statements expressing conservation of mass, momentum, and energy. Simply put, the rate at which these quantities increase or decrease in an arbitrary volume must equal the sum of the rate at which that quantity enters or leaves through the boundary of that volume and the rate at which that quantity is generated or dissipated within that volume. This statement holds for fluids, which are made up of a collection of molecules, when the relevant lengths, scaling as the cubic root of the relevant volume, in the flow are large compared to intermolecular distances, the basic assumption of continuum mechanics.

Given that continuum mechanics holds, the governing equations emerging from the principles of mass, momentum, and energy conservation can be closed with a relationship, known as an equation of state (EOS), that describes how any state variable changes as a function of any two other independent state variables. In flows with shock waves, the fluid's inertia is often large such that the effects of viscosity, an intrinsic property of a fluid to resist flowing, are rendered negligible. Furthermore, the time dynamics on which shocked flows develop often exceed those of body forces, like gravity, motivating their exclusion. Under these constraints, the physical system of interest is governed by the Euler equations,

$$\frac{D\rho}{Dt} + \rho\nabla\cdot\mathbf{u} = 0 \tag{1.1}$$

$$\frac{D\mathbf{u}}{Dt} + \frac{1}{\rho}\nabla p = 0 \tag{1.2}$$

$$\frac{De}{Dt} + \frac{p}{\rho}\nabla\cdot\mathbf{u} = 0, \tag{1.3}$$

where ρ, p, $\mathbf{u}$, and e are the fluid density, pressure, velocity, and internal energy, respectively, and $\frac{D}{Dt} = \frac{\partial}{\partial t} + \mathbf{u}\cdot\nabla$. Unless otherwise stated, a calorically perfect gas is assumed such that $e = c_v T$, where the constant c_v is the specific heat at constant volume and T is temperature. The governing system of equations is then closed by the ideal gas EOS, $p = \rho R T$, where $R = c_p - c_v$ is the specific gas constant and the constant c_p is the specific heat at constant pressure.

1.2 One-Dimensional Flows

While the Euler equations are a complex system of nonlinear partial differential equations, analytical solutions exist when certain approximations hold. The intuition gained from examining a simplified

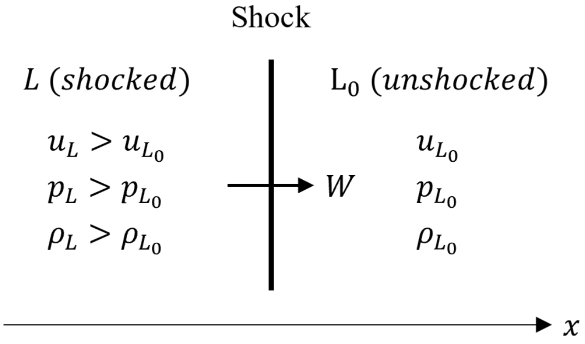

Figure 1.1: Schematic showing the propagation of a steady shock wave.

set of equations can often aid in the interpretation of complex physics that emerge when such approximations are relaxed. The intuition required to understand the technical chapters of this thesis is therefore built by systematically adding dimensions, in both space and time, starting from the simplest nontrivial shocked flow, the steady shock in one spatial dimension.

1.2.1 Steady Shocks

Consider a disturbance propagating in one dimension x at some constant velocity W that separates two uniform flow regions of constant aerothermodynamic states (i.e., thermodynamic state with velocity additionally specified, herein referred to only as "state") $L = [u_L, p_L, \rho_L]$ and $L_0 = [u_{L_0}, p_{L_0}, \rho_{L_0}]$, as shown in Figure 1.1. If the steady, i.e., time-independent, disturbance propagating into state L_0 is a shock wave, then $u_L > u_{L_0}$, $p_L > p_{L_0}$, and $\rho_L > \rho_{L_0}$. The strength of the shock can be defined in terms of its propagation speed with respect to the sound speed $a = \sqrt{\gamma p/\rho}$, where $\gamma = c_p/c_v$, of the fluid into which it propagates, a quantity known as the Mach number $M = (W - u_{L_0})/a_{L_0}$. The relationship between states L, the shocked state, and L_0, the unshocked state, can be determined as functions of M [6].

1.2.2 Unsteady Shocks

The flow becomes more complex with the introduction of any unsteadiness, e.g., if the shock suddenly changes velocity from passing into a different material with state R such that $p_R = p_{L_0}$, $u_R = u_{L_0}$, and $\rho_R \neq \rho_{L_0}$, as shown in Figure 1.2, where a new axis is added to represent time t. When the shock meets such an interface, it is transmitted into the new material, a wave is reflected back into the shocked material, and the velocity of the interface increases in the direction of shock propagation. Two new states L^* and R^* emerge between the interface and the reflected wave and transmitted shock, respectively [267]. If the impedance, the product of density and sound speed, of

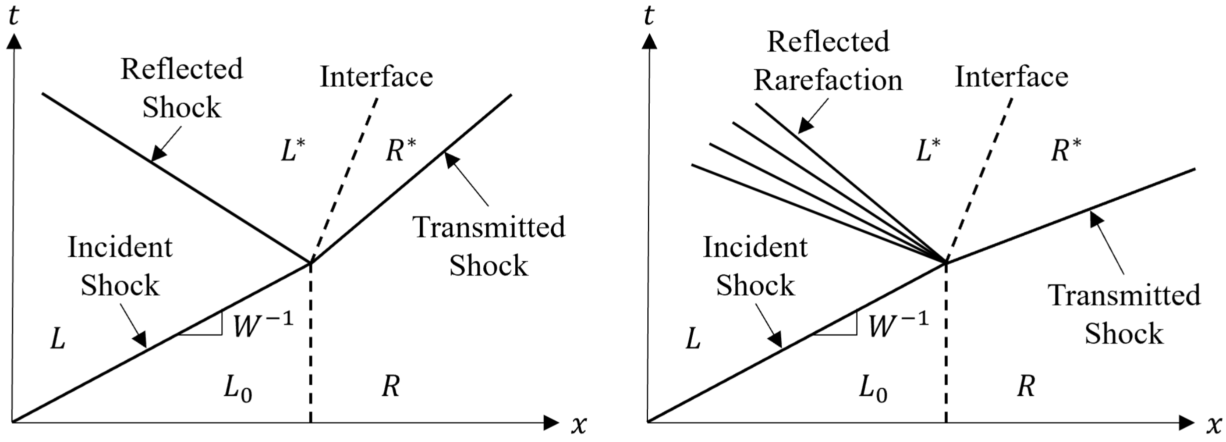

Figure 1.2: Diagram showing the states and propagation of waves when a shock meets an interface across which the impedance increases (left) or decreases (right).

state R exceeds that of state L_0, the transmitted shock travels slower, i.e., has a steeper slope in x-t space, while propagating through state R, and the reflected wave is a shock. If the impedance of state R is less than that of state L_0, the shock travels faster through state R and the reflected wave is a rarefaction, or decompression, wave. Unlike a shock, the rarefaction spreads out in time, with continuously varying state variables.

States L^* and R^* and the strengths of the transmitted and reflected waves can be determined by solving the Riemann problem, which determines the system of waves that emerge between any two adjacent states. However, the Riemann problem is more general than the present case, where L is a fixed function of L_0 and M, and R is defined previously. Specifically, the Riemann problem can be solved to determine the states resulting from the interaction of any two waves, including shocks, interfaces, and rarefactions. When these interactions occur instantaneously, as is the case for a shock intersecting an interface or another shock, the Riemann problem fully prescribes the time dynamics. Because interactions involving rarefactions occur over a finite amount of time, an additional technique, called the method of characteristics (MOC), is required to resolve the time dynamics.

The MOC is a method for solving systems of hyperbolic partial differential equations, including the Euler equations, by reducing them to ordinary differential equations along specific trajectories of their independent variables, i.e., space and time, called characteristics. As Figure 1.3 shows, the MOC can be used to solve the interaction between colliding rarefactions. A boundary condition on shocks and interfaces from the solution to the Riemann problem enables their incorporation in flows with rarefactions. As a result, the MOC and the solution to the Riemann problem can be used to construct semianalytical solutions to the unsteady Euler equations in one spatial dimension [243, 267].

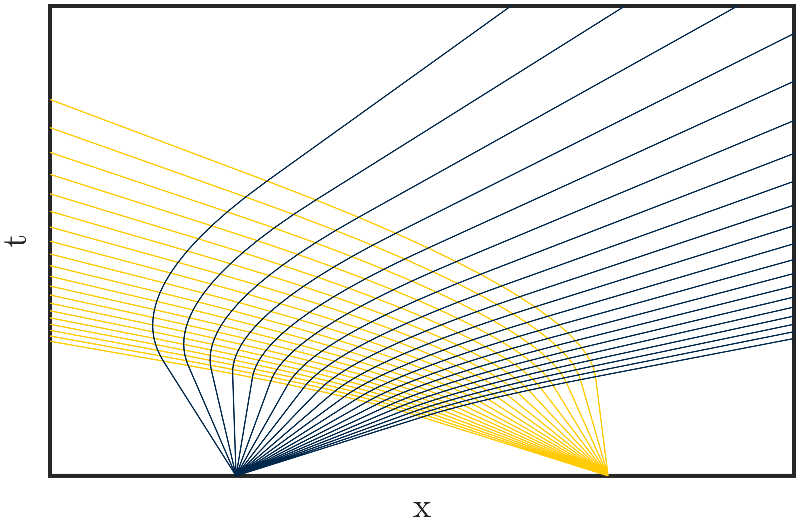

Figure 1.3: The paths of characteristics during the interaction of two rarefactions.

1.3 Advective Mixing in Multiple Spatial Dimensions

In the absence of diffusive mechanisms, fluid mixing cannot occur in one spatial dimension. However, unsteady flows in two or three spatial dimensions governed by Equation 1.1 are further complicated by the possibility that a region of some fluid will move around or penetrate another fluid, i.e., that two fluids will mix by advection. In particular, a surface separating two fluids can stretch under the action of hydrodynamic forces, leading to the rapid lengthening of the interface and the development of large structures comprised of one fluid that may engulf parcels of the other fluid [70]. In shocked interfacial flows, this mixing can result from the RMI. On its own, or coupled with other instability mechanisms, the RMI may cause the flow to evolve to a state of chaotic turbulence characterized by the presence of a wide spectrum of fluid scales, the transition to which is currently not well understood.

1.3.1 Baroclinic Vorticity and the Richtmyer-Meshkov Instability

The RMI is the process by which a shocked interface separating two dissimilar fluids causes those fluids to mix and can be understood as a consequence of vorticity generation during the interaction of the shock with the interface [231]. In two spatial dimensions, the curl of the momentum equation, Equation 1.2, yields the vorticity equation,

$$\frac{\partial \omega}{\partial t} = -\left(\mathbf{u} \cdot \nabla\right) \omega - \omega \left(\nabla \cdot \mathbf{u}\right) + \frac{\nabla \rho \times \nabla p}{\rho^2}, \tag{1.4}$$

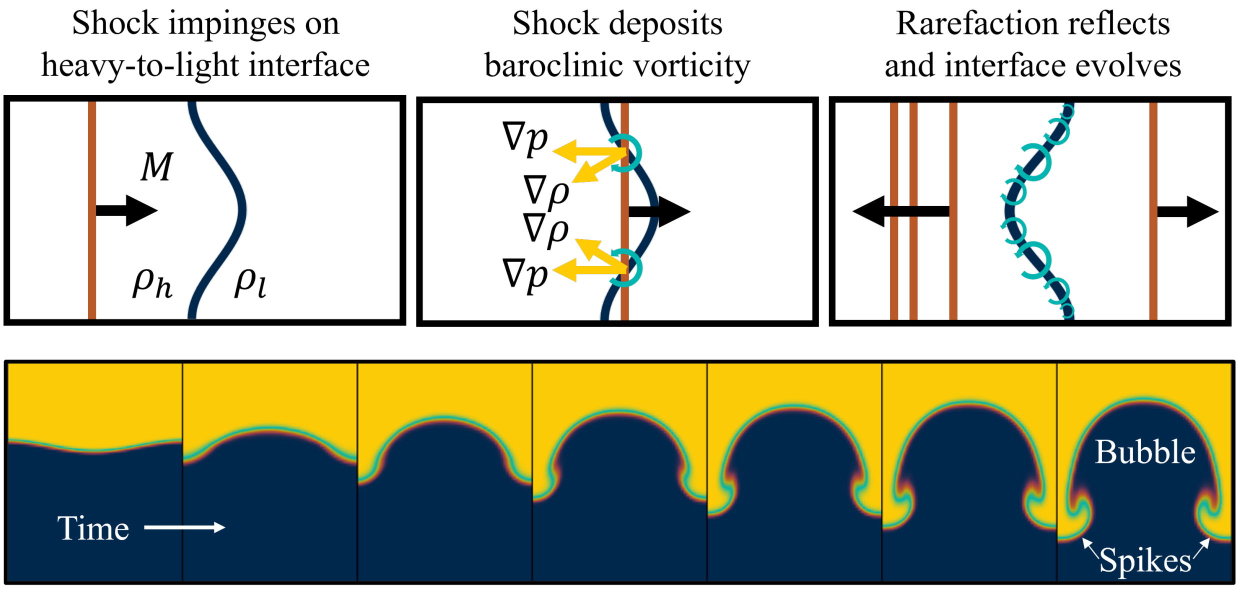

Figure 1.4: A schematic showing the deposition of baroclinic vorticity onto an interface from a shock (top) and a simulation of shocked perturbed interface growth (bottom) where the yellow fluid, in which the shock (not shown) is initialized has a greater density than the blue fluid.

where $\omega = \nabla \times \mathbf{u}$ is the out-of-plane component of vorticity. When a shock wave passes through a perturbed interface separating two fluids with different densities, the misalignment of the density gradient, a portion of which points normal to the interface, and the pressure gradient, which points normal to the shock front, causes the deposition of baroclinic vorticity, as indicated by the last term in Equation 1.4 and shown schematically in Figure 1.4 for a shock wave passing from a heavy fluid with density ρ_h to a light fluid with density ρ_l. After the wave interaction, the flow in the vicinity of the interface is often reasonably approximated as incompressible, $\nabla \cdot \mathbf{u} = 0$, and having negligible baroclinicity, $\nabla \rho \times \nabla p = 0$. As a result, the interface evolves under the influence of the vorticity deposited during shock passage.

The bottom portion of Figure 1.4 demonstrates the vorticity-induced evolution of the RMI with a simulation of a shocked perturbed interface. Because the shock wave passes from the heavy fluid to the light fluid, the sign of the baroclinic vorticity deposited causes the initial perturbation to invert its phase, which can be seen by comparing the first two panels. After inversion, the perturbation begins to increase in size. The continued growth of the interface results in narrow spikes of heavy fluid penetrating into the light fluid between which wide bubbles of light fluid rise in the heavy fluid. Over time, the region of flow where the two fluids mix grows and becomes increasingly complex as nonlinear effects start to dominate.

The RMI has been extensively studied since its discovery [162, 220]. Ongoing research aims to determine the size and intensity of the region where the two fluids interpenetrate and mix. The

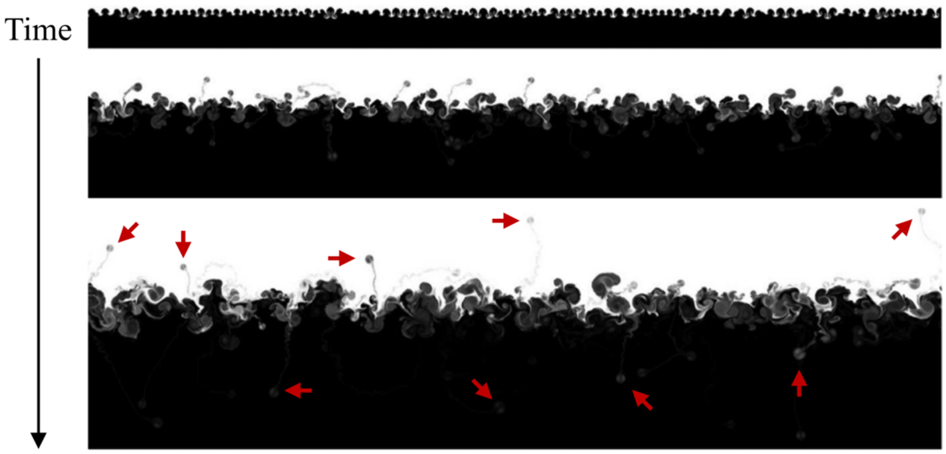

Figure 1.5: Simulations from [265] showing the increasing complexity of the RMI at late times. Red arrows indicate isolated vortex dipoles.

first linear analysis revealed that perturbations initially grow linearly with time [162, 220], after which nonlinear effects cause perturbation modes to couple [222, 228], leading to increasingly complex, possibly turbulent mixing, as shown in Figure 1.5. Numerous attempts have been made to characterize this nonlinear behavior. Theoretical models based on potential flow aim to calculate the buoyancy and drag forces experienced by bubbles and spikes to quantify the width of the mixing region [5, 95, 228]. In parallel, experimental collaborations focus on quantifying the exponent of an assumed power-law dependence of the mixing width on time [241, 263]. While such efforts have yielded some success describing the late-time growth of the RMI, they cannot describe the observed ejection of high-vorticity structures from the confines of the mixing region, which can also be seen in Figure 1.5. In addition to these ejected structures affecting the growth of the mixing region from which they depart, they can disturb other regions of the flow, including other interfaces. Furthermore, the energy they transport out of the mixing region, which cannot be captured by existing models, is expected to affect the subsequent transition of the flow to a turbulent state. Recent improvements in the resolution of experiments [71, 77, 148, 221] and numerical simulations [91, 264, 265] indicate that such structures share many characteristics with classical vortex rings and dipoles, which are discussed next.

1.3.2 Vortex Ring Formation

A vortex can generally be considered to be a region of flow where rotation dominates straining motion [99]. Common examples are vortex rings, which include smoke rings blown by cigar aficionados and bubble rings generated by dolphins, and vortex dipoles, the planar analog to vortex rings. Vortex rings can be generated by ejecting a column of fluid into a surrounding quiescent

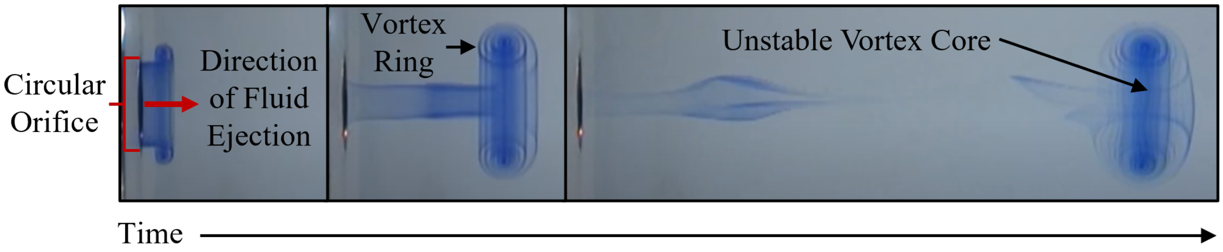

Figure 1.6: Experiments showing vortex ring formation in water at three subsequent times [3].

flow with a piston-cylinder device, as shown in Figure 1.6 [3]. As the fluid exits the circular orifice, it "rolls up" into a ring with vorticity that causes it to translate at a nearly constant velocity once the ring is fully formed [199, 200]. Because vortex rings are coherent, isolated structures that form the building blocks of more complicated flows, and because of their direct relevance to applications in propulsion systems [54, 195] and cardiac hemodynamics [180], they have been the focus of many prior research works [55, 150, 183, 225]. Driven by these applications, the study of classical vortex rings has been primarily focused on single-fluid, incompressible flows. The vortex rings and dipoles that emerge from the confines of shock-induced mixing regions, however, involve multi-fluid, compressible flows [193, 264, 265].

The formation of a vortex ring is driven by the circulation (a spatially integrated measure of vorticity), impulse (a change in momentum from the application of a force), and energy injected into the flow by a vortex ring generator, e.g., a piston-cylinder device. The vortex ring essentially acts as a reservoir for these quantities that satisfies a variational principle first proposed by Kelvin [262]. However, there is a limit to the amount of these quantities, each of which is related to the piston-cylinder stroke length, that a vortex ring can sustain [84, 182]. Therefore, there is a critical piston-cylinder aspect ratio (cylinder length divided by diameter) that generates a vortex ring fully saturated with circulation, impulse, and energy. In theory, a similar argument could be made for vortex rings generated from shock-accelerated interfaces, if an appropriate system can be defined that enables the quantification the circulation, impulse, and energy of the vortex-ring-generating interface. Once a vortex ring or dipole is formed, like those affecting the development of the RMI, it is subject to three-dimensional vortex-core instabilities, which are the subject of the next section.

1.3.3 Vortex-Core Instabilities

Interacting vortex cores, including the interaction of a single vortex ring with itself, are potentially unstable [292]. For example, careful inspection of the final time frame of Figure 1.6 reveals that the vortex core has a wavy appearance caused by the growth of azimuthal perturbations [3]. Such perturbations grow under the influence of the vorticity and strain fields imposed by the vortices

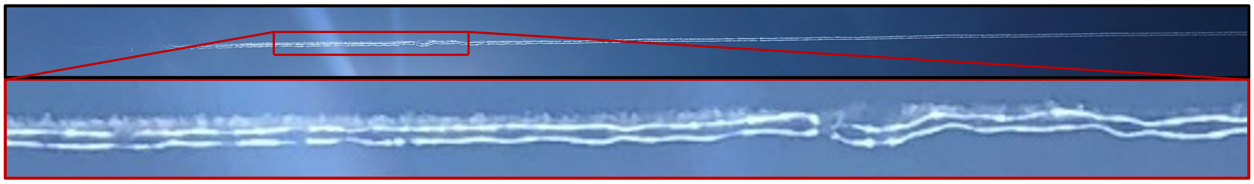

Figure 1.7: The growth of the Crow instability along jet contrails.

present in the flow [135]. These instabilities are frequently compounded by the presence of other cores, stimulating vortex stretching that quickly increases the complexity of the flow.

A significant body of research on vortex-core instabilities addresses the dissipation of aircraft vortices, violent and highly coherent structures that pose a safety hazard to other craft, via the Crow instability (CI) [53, 251]. Although vortex cores are typically subject to a number of different unstable mechanisms [135], the large-scale motion stimulated by the CI often serves as the background flow on which other instabilities develop. The CI can frequently be visualized along jet condensation trails, as shown in Figure 1.7. These wavy perturbations along the adjacent cores grow until they touch, triggering a complex vortex reconnection process that results in rapid dissipation [39, 46, 272]. The CI can also be visualized during the collision of vortex rings [141], a system that has recently received considerable attention as a way to isolate the vortex-core interactions fundamental to transitioning and turbulent flow [157, 158], like those that occur along vortex cores resulting from the baroclinic vorticity deposited on an interface by a shock. Furthermore, evidence of the CI can be seen along vortex dipoles formed from laterally shocked gaseous cylinders [202]. The conditions for the formation of such dipoles may exist along circumstellar gas clouds accelerated by shock waves and/or stellar wind. Regularly spaced clumps along such gas clouds is observed in many astrophysical systems [7, 151]. The mechanism that stimulates the clumping is currently unknown but may be related to the CI.

1.4 Application to High-Energy-Density Physics

Shocked interface hydrodynamics are ubiquitous in high-energy-density (HED) physics. The HED regime is characterized by pressures in excess of 1 Mbar, which is on the order of the binding energy density, dimensionally equivalent to pressure, of a hydrogen atom [73]. While such large pressures often cause the emergence of additional physics, including those related to ionization, the backbone of many HED systems is the fluid flow represented by the Euler equations. HED physics includes engineering applications in ICF research [17] as well as natural astrophysical applications including supernovae [227], gas-giant interiors [172, 237, 255], and white dwarf atmospheres [236].

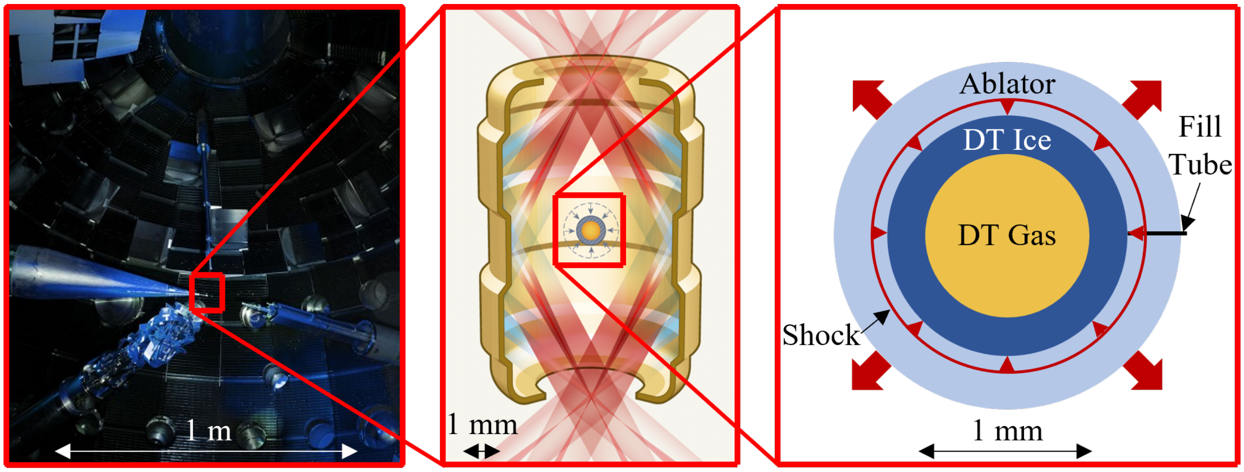

Figure 1.8: The target chamber at the National Ignition Facility (left), a schematic of a hohlraum (center) [125], and a schematic of an ICF fuel capsule (right).

1.4.1 Inertial Confinement Fusion

Nuclear fusion is the process by which light elements combine to form heavier elements. When fusion reactants have an atomic number less than 56, this process can be accompanied by a substantial release of energy, particularly for the fusion of two hydrogen atoms into helium. For fusion to occur, two nuclei must be brought in close enough contact, or confined, in such a way that the attractive strong nuclear force overcomes the repulsive Coulomb force. In stars, confinement results from massive gravitational forces, and the energy released, including the tiny fraction of the Sun's energy that reaches Earth, powers the cosmos. Harnessing fusion as a power source has an enormous potential to satisfy global energy needs. Just one gallon of seawater contains enough deuterium, an isotope of hydrogen, to replace three-hundred gallons of gasoline. Accessing this energy on Earth, however, which is nowhere near massive enough for gravitational confinement, is a challenge that has defined decades of scientific research [17].

ICF is the process by which laser-generated shock waves accelerate a spherical capsule of fusion fuel radially inward, confining and compressing the fuel via its own inertia to the extreme conditions at which self-sustaining nuclear fusion may occur, illustrated in Figure 1.8 [17]. In indirect-drive ICF, the scheme utilized at the National Ignition Facility (NIF), lasers irradiate the inside of a gold container called a hohlraum. The resulting x-rays deposit energy on the outer layer, called the ablator, of the fuel capsule. The outward explosion of the ablator drives a radially convergent shock wave that compresses and confines the deuterium-tritium fuel. Indirect-drive ICF at the NIF is capable of fusion-energy breakthroughs, as recently demonstrated by the achievement of thermonuclear ignition and a release of fusion energy that exceeded the energy contained in the laser drive [2]. However, significant challenges, including the hydrodynamic stability of fuel-capsule

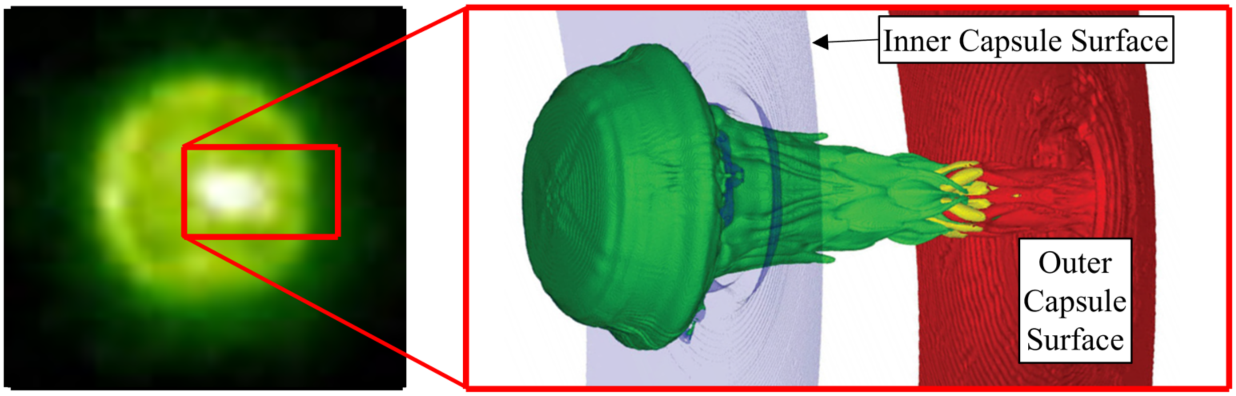

Figure 1.9: An experiment [10] (left) and simulation [91] (right) showing mix induced by the ICF capsule fill tube.

interfaces to shock waves, remain before fusion can satisfy global energy needs [219].

When the shock is converging toward and after it rebounds off of the capsule center, it passes through a series of interfaces between capsule layers. These shock-interface interactions are subject to the RMI, which causes mixing between outer capsule layers and the highly compressed material in the center, ultimately leading to decreased compression and a severe penalty to fusion performance [93, 286]. The challenge of mitigating this mixing is a primary motivation for the extensive research on the RMI discussed in Section 1.3.1. Outstanding questions surround the transition of the shocked interfaces in an ICF capsule to a state of turbulent mixing [284, 285, 307, 308], which is of critical importance for the ability of simulation tools to describe the implosion process [69]. Transport mechanisms in the late nonlinear regime of the RMI must play a significant role in any turbulent transition and therefore must be considered in the development of hydrocodes aiding the development of ICF technology. Such mechanisms include energy transported by vortex rings and dipoles ejected from the mixing region, which currently lack description by existing models [5, 95, 228].

Finally, a particularly detrimental form of mixing in ICF capsules is stimulated by the passage of the shock wave through small defects on the capsule surface and the gas fill tube, causing jets of cool, fusion-quenching material to pollute the central burn region [14, 102]. Improved experimental diagnostics and simulation tools have enabled unprecedented visualizations of this jetting process, as shown in Figure 1.9 [10, 91], from which many parallels can be drawn to single-fluid, incompressible starting jets, including the formation of a vortex ring at the leading edge [84]. The generalization of the classical theory to interfacial, shock-induced jets would enable an unprecedented understanding of such jets in ICF implosions.

1.4.2 Astrophysics

At length scales more than twenty orders of magnitude greater than an ICF capsule, shock waves are generated from the enormous and rapid release of energy during type-II supernovae [8, 227]. While shock waves are used in ICF to inertially confine fusion reactants, stars are so massive that their own gravity provides sufficient confinement for fusion to occur. While hydrogen-fusion is the primary source of energy in the Sun and other low-mass main-sequence stars, stars with between 8 and 50 times the mass of the Sun are large enough to induce fusion that generates iron, nickel, and other heavy elements [86]. However, the energy output of heavy-element-generating fusion reactions is significantly less than that of hydrogen fusion. A catastrophic implosion occurs after the star runs out of adequate fusion reactants, when energy released from fusion in a star's core is no longer able to support the weight of the star [139]. The collapse of the heavy-element core is followed by the collapse of the now unsupported outer layers. The pressure at the center of the collapsing star eventually becomes so great that the implosion rebounds, generating an outward propagating shock that causes the star to explode during the ensuing supernova. As the shock wave passes through different stellar layers, which get progressively less dense further from the center, it induces hydrodynamic mixing via the RMI [110]. This process initiates the transport of heavy elements like nickel and iron [127, 128] from the location of their synthesis, the centers of stars, throughout the universe, where they eventually comprise dense objects like asteroids and planets, including Earth.

The importance of the RMI in supernova dynamics, with far-reaching implications for galaxy composition, motivates studies of shocked-induced interfacial mixing. In particular, unresolved questions remain about the precise mechanism that propels heavy core elements to large distances from the center of the blast. Thought to be related to the RMI, torus-shaped "bullets" of heavy elements are frequently seen in simulations of supernova dynamics, like the one shown in Figure 1.10 [232], which result in simulated x-ray spectra consistent with observations. As with the fill-tube jet in ICF implosions and high-vorticity structures escaping RMI mixing regions, the mechanisms driving heavy supernova ejecta may be related to classical fluid starting jets.

After emerging from the surface of the star, shock waves then expand into the interstellar medium, where they interact with and heat any preexisting gas clouds, stimulating hydrodynamic motion. In addition to supernovae, astrophysical shocks can be generated by interacting solar winds, merging stars, and molecular cloud collisions [19, 45, 190, 191]. A famous example of a shock interacting with interstellar dust is the blast from Supernova 1987A illuminating a preexisting clumpy debris ring surrounding the progenitor star [81, 208]. Although the clumps predate the supernova, similar vorticity-dominated interfacial hydrodynamics, possibly driven by weaker shocks resulting from a binary star merger and/or the interaction of stellar winds, may be responsible for the formation of the clumps and similar structures throughout the universe.

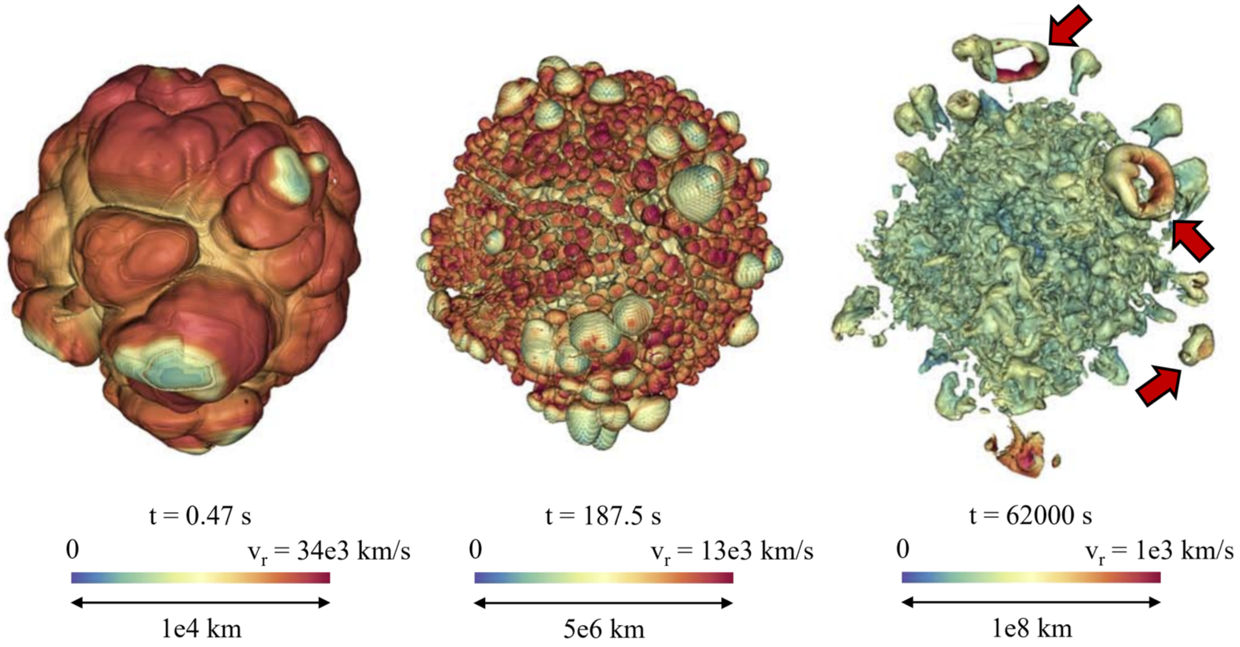

Figure 1.10: Simulations showing isocontours of nickel concentration at three different times during a supernova [232]. Red arrows indicate possible vortex rings.

In addition to stars, shock waves play an important role in our understanding of other high-pressure environments in astrophysics. Apart from earthquakes, asteroid collisions, and other rare or intermittent events, shock waves do not directly affect the dynamics of planetary interiors. However, shocks can be utilized to experimentally probe the behavior of materials at the extreme pressures found inside planets and other high-pressure systems [75, 105]. Analysis of the shock physics in such compression experiments enables characterization of a material's equation of state [30]. Such measurements are essential for constraining models for the interiors of gas giant planets and the atmospheres of white dwarf stars [36, 236, 249]. The abundance of high-pressure astrophysical systems motivates the persistent need to experimentally probe evermore extreme states, which require stronger shock waves. Techniques for strengthening shocks, particularly those that are inexpensive and do not require modification to existing experimental facilities, therefore have the potential to enhance our understanding of high-pressure environments in the universe.

1.5 Thesis Overview

This PhD thesis advances what is currently understood about hydrodynamic phenomena occurring at shocked interfaces. Much like this Introduction, the overall thesis is organized as a journey through the physics and applications that emerge with increasing dimensionality. Chapters 2 and 3 focus on the application of one-dimensional shock theory to dynamic compression experiments for EOS characterization. Chapters 4 and 5 explore the emergence of high-vorticity ejecta from multi-dimensional mixing regions. Chapters 6 and 7 uncover the behavior of a three-dimensional vortex-core instability. Finally Chapter 8 summarizes the thesis and suggests opportunities for future work. Each technical chapter presents novel research contributions, including

1. a technique for strengthening shock waves in dynamic compression experiments to access extreme pressure conditions for EOS measurements (M. J. Wadas, G. Cearley, J. Eggert, E. Johnsen, and M. Millot, A theoretical approach for transient shock strengthening in high-energy-density laser compression experiments, *Physics of Plasmas*, 28(8):082708, 2021),

2. the density, temperature, and conductivity of shock-compressed helium at record pressures exceeding 3.5 Mbar (M. J. Wadas et al., Shock compression of helium to 3.5 Mbar, *In preparation for Physical Review Letters*),

3. a criterion for the ejection of vortex dipoles from two-dimensional shock-induced mixing regions (M. J. Wadas and E. Johnsen, Interactions of two bubbles along a gaseous interface undergoing the Richtmyer-Meshkov instability in two dimensions, *Physica D: Nonlinear Phenomena*, 409:132489, 2020),

4. the formation and scaling of vortex rings ejected from shocked interfaces (M. J. Wadas, L. H. Khieu, G. S. Cearley, H. J. LeFevre, C. C. Kuranz, and E. Johnsen, Saturation of vortex rings ejected from shock-accelerated interfaces, *Physical Review Letters*, 130:194001, 2023),

5. the linear stability analysis of the cylindrical Crow instability (M. J. Wadas, S. Balakrishna, H. J. LeFevre, C. C. Kuranz, A. Towne, and E. Johnsen, On the stability of a pair of vortex rings, *Under Review in Journal of Fluid Mechanics*),

6. the mechanism that stimulates clumping along stellar debris rings including that of Supernova 1987A (M. J. Wadas, W. White, H. J. LeFevre, C. C. Kuranz, A. Towne, and E. Johnsen, A hydrodynamic mechanism initiating clumping along the equatorial rings of SN1987A and other stars, *In Preparation for Physical Review Letters*).

CHAPTER 2

A Theoretical Approach for Transient Shock Strengthening in High-Energy-Density Laser Compression Experiments

This chapter is adapted from M. J. Wadas, G. Cearley, J. Eggert, E. Johnsen, and M. Millot, A theoretical approach for transient shock strengthening in high-energy-density laser compression experiments, *Physics of Plasmas*, 28(8):082708, 2021 [279].

2.1 Abstract

In high-energy-density shock compression experiments, the desired state of compression is typically achieved by passing shock waves through a sequence of different materials. In this study, a theoretical approach for transiently strengthening such shocks passing through interfaces of experimentally relevant impedance ratios is examined. A semi-analytical method based on characteristics analysis is used to solve the problem of a shock passing from one material to another through an intermediate region of non-uniform impedance; by appropriately designing this region, a greater shock strength can be achieved in the second material for a finite duration than in the absence of this region. When a shock passes into a material of higher impedance, the shock strengthening increases to a maximum before decreasing to an asymptotic value as the strength of the incident shock is increased. For shocks passing into materials of decreasing impedance, the shock strengthening increases monotonically as the strength of the incident shock is increased when the impedance ratio is above a critical threshold. Incorporating multiple intermediate materials can further increase the strength of the transmitted shock, with an exponential discretization of intermediate material impedances being the most effective distribution for strengthening strong shocks. The results suggest that up to 25% and 9% increases in pressure behind the leading shock can be achieved for materials of increasing and decreasing impedance, respectively. The technique is applied to the

design of laser-driven dynamic compression experiments, and the results of the analysis are verified via comparison to simulations performed with the HYADES hydrodynamics code.

2.2 Introduction

Advances in laser-driven compression experimental platforms [105] have enabled access to unprecedented pressure and temperature regimes in high-energy-density (HED) physics, setting the stage for discoveries in inertial confinement fusion (ICF) research [209] and planetary science, such as the equation of state of materials at conditions representative of planetary interiors [30, 49, 245, 246] and superionic water ice [174, 176]. In these experiments, laser energy is deposited onto an ablator, generating a compression wave [259]. This wave then passes through the layers of the experimental apparatus designed to achieve the desired state of compression in the sample, as in a diamond anvil cell (DAC) or similar platforms [30, 49, 105, 174, 176, 245, 246]. Because of the finite laser pulses at facilities like the OMEGA laser, the rarefaction launched when the laser pulse terminates can significantly weaken the wave by the time the latter reaches the sample. Strengthening the shock just before interacting with the sample would extend experimental access to even more extreme states.

As a shock wave propagates through a DAC or similar experimental apparatus, it encounters a number of material interfaces, including the interface with the sample, where reflected waves divert energy from the compression of the sample. This problem of a shock passing through regions of non-uniform impedance (whether continuous or sharp impedance variations) has been explored previously. Analytical approaches exist for weak shocks in gases [50, 243] and were extended to shocks of moderate strength by using the Rankine-Hugoniot conditions to link the state immediately downstream of a shock wave of known strength to the differential equations governing the flow characteristics in the shocked medium [42, 43, 289]. More complete solutions later focused on similarity solutions for specific density profiles [87, 201, 298] and considered additional phenomena such as the "re-reflection" of waves that eventually overtake the transmitted shock front [34, 44, 297]. Prior to the completion of the re-reflection process, however, the shock transmitted after passing through a region of non-uniform impedance spanning the impedances of two outer materials is, for a finite time duration, stronger than the shock that would emerge if the non-uniform impedance region consisted of a discontinuity [18]. Exploiting and optimizing this phenomenon is the focus of the present work.

In addition to the DAC and other apparatus, the strengthening of shock waves considered in this work is highly relevant to a recently developed platform that uses a "ring-up" target with a high-impedance anvil to access extreme states using sub-kilojoule laser HED experimental platforms [155]. Both the ablator-anvil and anvil-sample interfaces present opportunities for shock strengthening, providing access to even higher pressures. The strengthening of shock waves passing through material interfaces is also relevant to ICF, where the traditional design involves shocks passing from an ablator to deuterium-tritium ice and subsequently to deuterium-tritium gas [17]. More exploratory designs such as the double shell [161, 185] and revolver [184, 239] concepts rely on high-Z pushers surrounding the fusion fuel, thus incorporating even more layers, further enhancing the potential for the shock strengthening explored in the present work.

Our objective is to develop a theoretical technique for predicting transient shock strengthening through an experimental apparatus such as the DAC and into a sample in HED laser-driven compression experiments. Inspired by classical gas dynamics theory, the technique leverages the fact that a steady shock transmitted into a material from another material of different impedance is stronger before the arrival of any re-reflected waves if it first passes through a discrete, intermediate material of impedance between the impedances of the two outer materials. The incorporation of such an intermediate material is relatively straightforward on existing laser-driven compression platforms given that the materials comprising the target are frequently in a solid state prior to the experiment. In addition to enabling even higher achievable pressures at high-energy laser facilities like the National Ignition Facility and the OMEGA laser facility, a technique for shock strengthening can also enable less-energetic lasers like the Dynamic Compression Sector (DCS)[27] and the Matter in Extreme Conditions instrument (MEC) of the Linac Coherent Light Source (LCLS)[194] to achieve more extreme pressure and temperature regimes. The chapter is organized as follows. Section 2.3 describes the problem setup and method of analysis. Section 2.4 presents the results in the context of the experimental applications. Results are summarized and conclusions drawn in Section 2.5, and supplemental material is included in Section 2.6.

2.3 Models and Methods

Following a description of the setup for studying shock strengthening, our approach is presented, which combines the method of characteristics (MOC) with the exact solution to the Riemann problem [267]. Finally, a description of the radiation hydrodynamics code (HYADES) used for comparison to the theoretical results is included.

2.3.1 Problem Setup

The canonical problem underlying the wave dynamics in an experimental apparatus like the DAC is a shock passing from material L to material R through a series of intermediate materials, as illustrated in Figure 2.1. We use this setup for investigating the strengthening of the shock that emerges in material R. The geometry is one-dimensional, consisting of a semi-infinite material L of

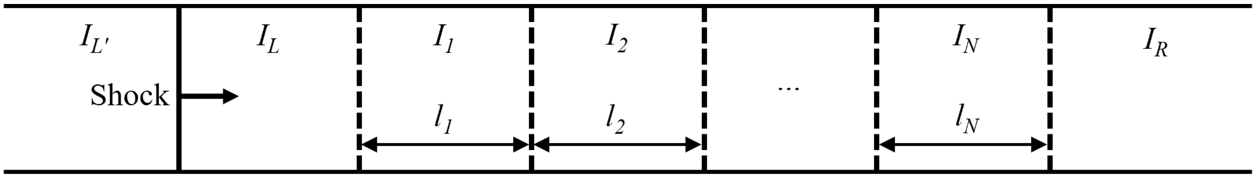

Figure 2.1: Problem setup for a shock passing through a series of discrete intermediate materials of varying impedance.

impedance I_L separated from another semi-infinite material R of impedance I_R by an intermediate material made up of N elements at states $j \in (1, N)$ of size l_j and impedance I_j. The limit $N = 0$ corresponds to the reference problem of material R being in direct contact with material L. Initially, the pressure and velocity are constant throughout the domain, i.e., $p_L = p_j = p_R$ and $u_L = u_j = u_R$ for all j. For cases that explore regions of increasing impedance, corresponding to experiments exploring relatively high-impedance substances, the left material has the lowest impedance and the right material has the greatest impedance. Conversely, for cases that explore regions of decreasing impedance, corresponding to experiments exploring relatively low-impedance substances, the left material has the greatest impedance and the right material has the lowest impedance. We consider $N = 1$ to $N = 5$.

A steady shock, such as a shock in a laser compression experiment prior to the termination of the laser pulse, propagates in material L toward material R. Upon interaction with an interface, a wave (shock or rarefaction, depending on the impedance of the two materials) is reflected back into the original material, a shock is transmitted into the second material, and the interface is set into motion. States and state quantities within each material after the passage of n waves are referenced with n “prime” superscripts (e.g., L' and $I_{L'}$ refer to the state and impedance, respectively, in the left material after the passage of the incident shock wave). The strength of the shock in the left material is prescribed by the density jump across it, $\rho_{L'}/\rho_L$. The pressure behind the shock that initially emerges in material R, $p_{R'}$, is compared to the pressure behind the shock that would emerge in material R if there was no intermediate impedance region, $p_{R'_0}$, i.e., if $N = 0$. This ratio, $p_{R'}/p_{R'_0}$, is herein referred to as the shock strengthening when it exceeds unity.

2.3.2 Method of Characteristics

We solve the one-dimensional unsteady Euler equations, which govern compressible flow of a continuum, including the evolution and interaction of waves and contact surfaces, using the MOC. Boundary conditions at entropy discontinuities (i.e., shocks, contact discontinuities, material interfaces, and material contacts) are provided by exactly solving the corresponding Riemann problem. The flow is assumed to remain isentropic except across entropy discontinuities. In such regions, the equations of motion describing the propagation of finite-amplitude (rarefaction and compression) waves can be expressed as

$$\left[\frac{\partial u}{\partial t} + (u \pm a)\frac{\partial u}{\partial x}\right] \pm \frac{1}{\rho a}\left[\frac{\partial p}{\partial t} + (u \pm a)\frac{\partial p}{\partial x}\right] = 0 \tag{2.1}$$

where u is the fluid velocity, a is the local sound speed, ρ is the density, p is the pressure, and x and t are the space and time coordinates, respectively. If the solution is examined along characteristic paths satisfying

$$\frac{dx}{dt} = u \pm a, \tag{2.2}$$

Equation 2.1 simplifies to

$$du \pm \frac{dp}{\rho a} = 0. \tag{2.3}$$

Specializing to an ideal gas with constant specific heats, Equation 2.3 can be integrated along the path specified by Equation 2.2 to yield the Riemann invariants,

$$J_{\pm} = u \pm \frac{2a}{\gamma - 1}, \tag{2.4}$$

where γ is the ratio of specific heats. Without loss of generality, a constant ratio of specific heats of $\gamma = 5/3$ is used throughout the present work to demonstrate the theory. Equation 2.4 is then used to solve the isentropic wave interactions in space and time according to the standard isentropic MOC procedure [6]. All quantities are non-dimensionalized by the the density, ρ_L, and sound speed, a_L, of the left material and the size of the first intermediate material, l_1.

Entropy discontinuities are handled by applying a boundary condition derived from the exact solution to the Riemann problem [160]. We distinguish between discontinuities across which the velocity and pressure are discontinuous, i.e., shocks (for which density and temperature are discontinuous as well), and those across which velocity and pressure are continuous, i.e., contact discontinuities (discontinuous density and temperature), material interfaces (discontinuous composition and density), and material contacts (discontinuous composition, density, and temperature). The procedure for handling the latter three is the same, so without loss of generality we herein refer to them collectively as contact surfaces. Further, we consider constant specific heat ratios, in which case the impedance $I = \rho a$ depends on a single thermodynamic quantity since the flow is isentropic everywhere but across shocks and contact surfaces. Six cases require this boundary condition: the interaction of a shock and a contact surface, the interaction between a rarefaction and a contact surface, a rarefaction overtaking a shock of the same wave family, a shock overtaking a rarefaction of the same wave family, a collision of a shock and a rarefaction of different wave families, and a compression wave steepening into a shock. We consider these cases individually in Section 2.6.

2.3.3 HYADES Code

Direct simulations of the one-dimensional Euler equations are conducted using the HYADES Lagrangian radiation-hydrodynamics code [129]. In this work, HYADES is used to both verify the method of analysis (see Section 2.6) and the shock-strengthening results with both tabular and ideal gas equations of state. The geometry for the simulations parallels the setup outlined in Figure 2.1 where the steady shock is generated via a square laser pulse that is turned on at the start of the simulation and terminated within the last nanosecond. Additional laser drive details and the specific substances used are presented with the results that follow.

2.4 Results

We apply our theory to elucidate the role of an impedance variation between two different materials on the strength of a shock passing through this system. First, we examine the case of a single intermediate material of a given impedance between two outer materials. Next, a generalization of these findings is presented for multiple intermediate materials, followed by a discussion of the application and practicality of using such impedance profiles on existing HED shock compression platforms.

2.4.1 Shock Strengthening with a Single Intermediate Material

We first determine the dependence of shock strengthening on a single intermediate material with a given impedance. The system consists of a composite geometry made up of material L of impedance I_L, material 1 of impedance I_1 and length l_1, and material R of impedance I_R. Here, I_R could be larger or smaller than I_L. A shock of initial strength $\rho_{L'}/\rho_L$ is initialized in material L and propagates through the system. Wave diagrams showing the paths of the shocks and rarefactions in Lagrangian space and time and pressure-particle velocity diagrams for the cases of increasing ($I_L < I_1 < I_R$) and decreasing ($I_L > I_1 > I_R$) impedance are shown in Figures 2.2 and 2.3, respectively.

To determine the shock strengthening caused by introducing a single intermediate material between the left and right materials, we first examine the dynamics in the absence of any intermediate material. When a shock intersects a contact surface separating two materials L and R, where $I_L < I_R$, a shock is transmitted into material R, and a shock is reflected back into material L due to the higher impedance of material R, as shown in Figure 2.2a. The shocked state R_0' is constrained by

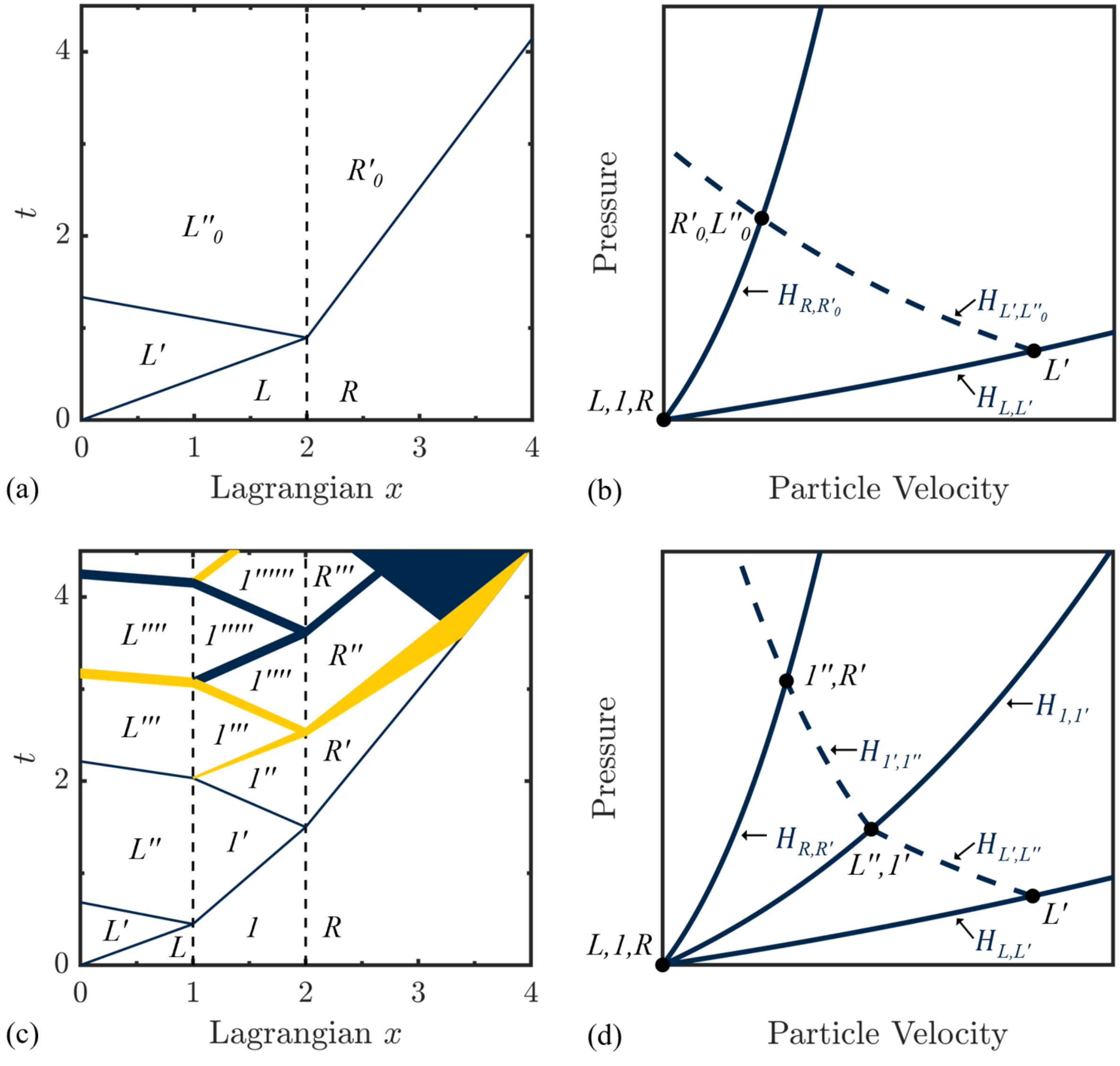

Figure 2.2: Wave diagrams (a,c) and pressure-particle velocity diagrams (b,d) showing the relationship between the states for an incident $\rho_{L'}/\rho_L = 2$ shock passing through materials of increasing impedance ($I_1/I_L = 3$, $I_R/I_L = 5$) without (a,b) and with (c,d) a single intermediate material. In the wave diagrams, solid blue lines represent shocks and compression waves, solid yellow lines represent rarefactions, and dashed black lines represent contact surfaces. In the pressure-particle velocity diagrams, solid blue lines represent right-running shocks and dashed blue lines represent left-running shocks. Hugoniot curves are labeled as H, where the subscript indicates the states across the shock.

the Hugoniot corresponding to the right-running shock passing through the right material, H_{R,R'_0}, where the subscripts indicate the states across the shock. As shown in Figure 2.2b, the state is fixed by the intersection of H_{R,R'_0} and the Hugoniot corresponding to the left-running shock reflected at the contact surface, H_{L',L''_0}, the origin of which is the state downstream of the incident shock in the left material, L', which lies along the Hugoniot corresponding to the incident shock, $H_{L,L'}$, and is a function only of the strength of the incident shock. In the presence of an intermediate material 1, where $I_L < I_1 < I_R$, a transmitted shock and a reflected shock result from the interaction of the incident shock with the first contact surface due to the higher impedance of material 1, as in Figure 2.2c. The same process occurs at the second contact surface for the transmitted shock, which produces a shock in material R. With the presence of the intermediate material, the state R' is now fixed by the intersection of $H_{R,R'}$ (equivalent to H_{R,R'_0}) and the Hugoniot corresponding to the left-running shock reflected back into the intermediate material at the second contact surface, $H_{1',1''}$, the origin of which is the state downstream of the shock initially transmitted into the intermediate material, $1'$. The state $1'$ is fixed by the intersection of the Hugoniot corresponding to the right-running shock initially transmitted into the intermediate material, $H_{1,1'}$, and $H_{L',L''}$ (equivalent to H_{L',L''_0}). The pressure $p_{R'}$ exceeds $p_{R'_0}$ because the pressure and density of state $1'$, the origin of $H_{1',1''}$, are higher than those of state L', the origin of H_{L',L''_0}, such that $H_{1',1''}$ is steeper than H_{L',L''_0}. Therefore, $p_{R'}/p_{R'_0}$ exceeds unity and shock strengthening is achieved.

The intermediate material therefore enables a shock of strength greater than in the absence of the intermediate material to initially break out into the right material, though the stronger shock only exists for a finite duration. When the shock reflected from the second contact surface reaches the first contact surface, a shock is transmitted into the left material, and a rarefaction is reflected back into the intermediate material due to the lower impedance of state L''. This rarefaction is transmitted through the second contact surface, ultimately overtaking and weakening the shock initially transmitted into the right material. Waves continue to reflect off of the contact surfaces resulting in alternating shocks and rarefactions passing into the left and right materials, though they progressively become weaker. Due to the nonlinearity of the waves, rarefactions spread out and compression waves steepen in time, causing the thickening and thinning, respectively, of the lines used to represent those waves in Figure 2.2, while shocks remain sharp. Following these interactions, the strength of the leading reflected wave in material L and that of the transmitted wave in material R eventually tend to the strengths of the waves corresponding to those of the reflected and transmitted waves in the case of no intermediate material. Because the incident shock is steady and the left and right materials are semi-infinite, the paths of all of the waves scale with the thickness of the intermediate material, while their strengths depend only on the initial shock strength and the impedances of the three materials, I_L, I_1, and I_R.

For the case of a shock passing through a contact surface of decreasing impedance ($I_L > I_R$), as

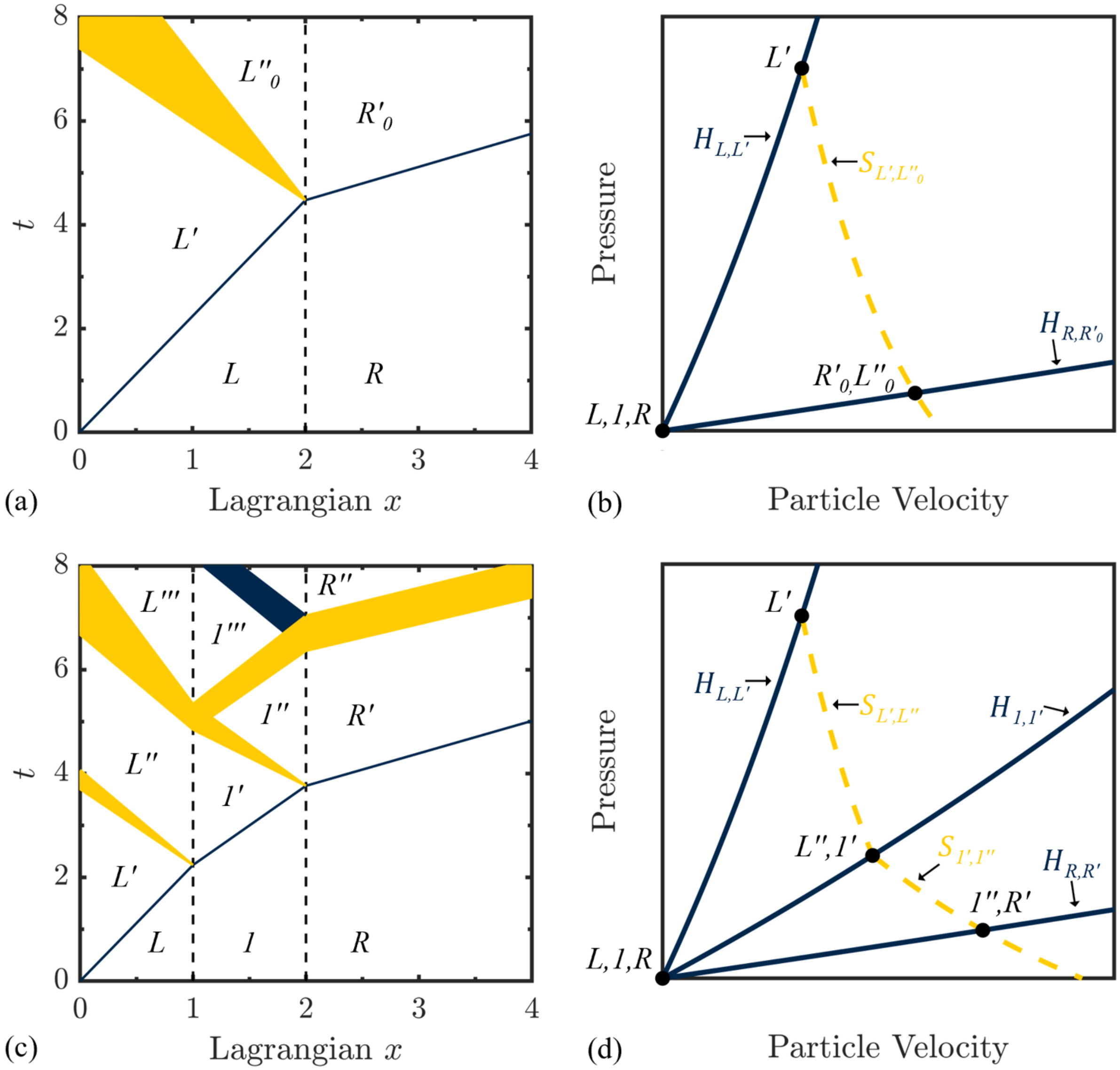

Figure 2.3: Wave diagrams (a,c) and pressure-particle velocity diagrams (b,d) showing the relationship between the states for an incident $\rho_{L'}/\rho_L = 2$ shock passing through materials of decreasing impedance ($I_L/I_R = 5$, $I_1/I_R = 3$) without (a,b) and with (c,d) a single intermediate material. In the wave diagrams, solid blue lines represent shocks and compression waves, solid yellow lines represent rarefactions, and dashed black lines represent contact surfaces. In the pressure-particle velocity diagrams, solid blue lines represent right-running shocks and dashed yellow lines represent left-running rarefactions. Hugoniot (isentrope) curves are labeled as H (S), where the subscript indicates the states across the wave.

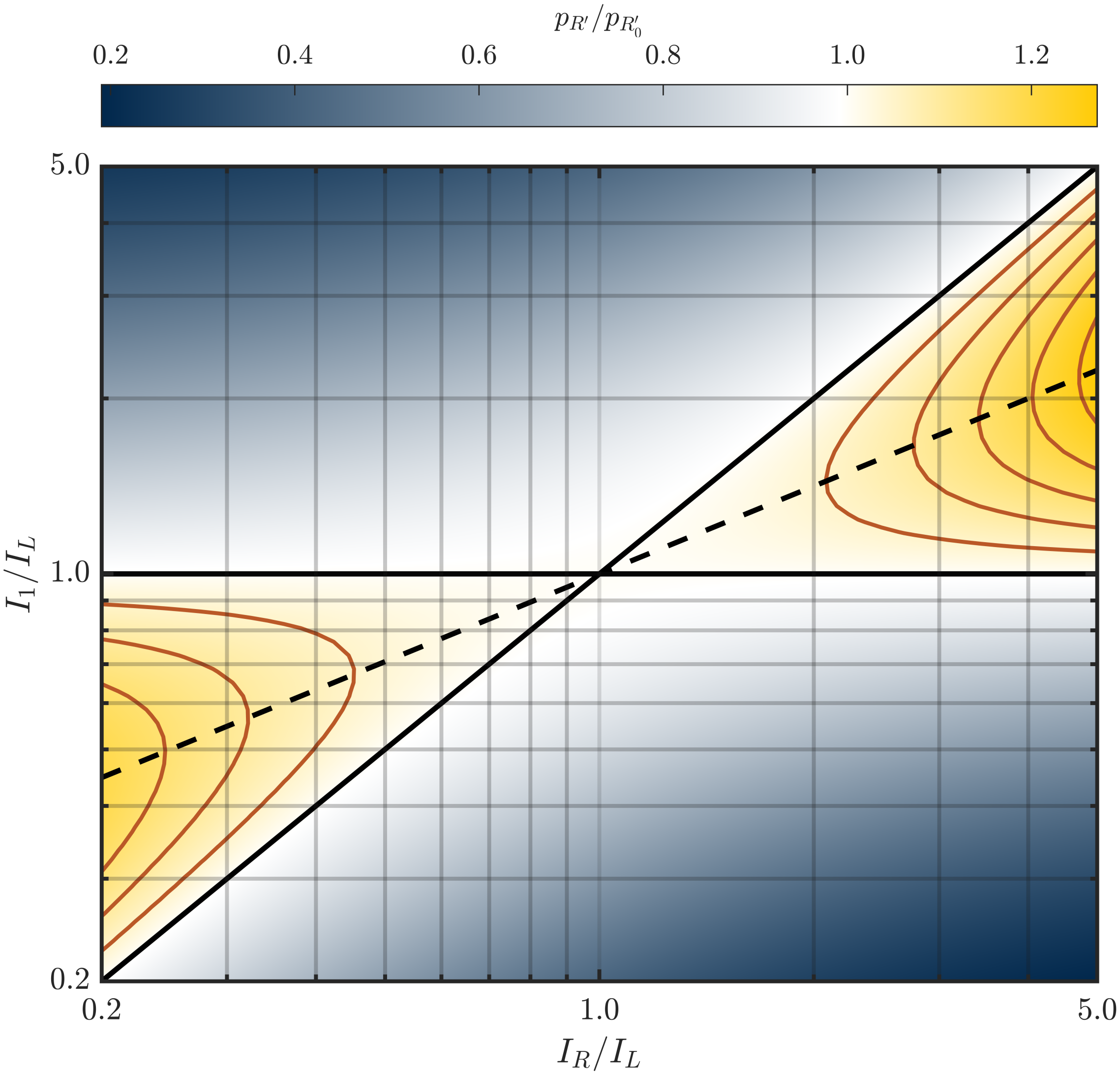

Figure 2.4: The pressure behind the shock that initially emerges in the right material of impedance I_R after passing through a material of impedance I_1 for an incident $\rho_{L'}/\rho_L = 4$ shock initialized in the left material of impedance I_L, normalized by the pressure behind the shock in the right material if there was no intermediate material. The solid black lines indicate where $I_1 = I_L$ and $I_1 = I_R$, between which (I_1 between I_L and I_R) shock strengthening occurs, and the dashed black line indicates where $I_1 = \sqrt{I_L I_R}$. Shock strengthening contours (orange lines) span $p_{R'}/p_{R'_0} \in (1.05, 1.25)$ in increments of 0.05 increasing from $(I_R/I_L, I_1/I_L) = (1.0, 1.0)$ moving outward along the dashed black line.

shown in Figure 2.3a, a shock is transmitted into material R, but now a rarefaction is reflected back into material L due to the lower impedance of material R. As shown in Figure 2.3b, the shocked state R'_0 is fixed by the intersection of H_{R,R'_0} and the isentrope corresponding to the left-running rarefaction reflected at the contact surface, S_{L',L''_0}, as shown in Figure 2.3b. In the presence of an intermediate material 1, where $I_L > I_1 > I_R$, a transmitted shock and a reflected rarefaction result from the interaction of the incident shock with the first contact surface due to the lower impedance of material 1, as shown in Figure 2.3c. The same process occurs at the second contact surface for the transmitted shock, which produces a shock in material R. With the presence of the intermediate material, the state R' is now fixed by the intersection of $H_{R,R'}$ and the isentrope corresponding to the left-running rarefaction reflected back into the intermediate material at the second contact surface, $S_{1',1''}$, the origin of which is the state downstream of the shock initially transmitted into the intermediate material, $1'$. The state $1'$ is fixed by the intersection of the Hugoniot corresponding to the right-running shock initially transmitted into the intermediate material, $H_{1,1'}$, and $S_{L',L''}$ (equivalent to S_{L',L''_0}). The pressure $p_{R'}$ exceeds $p_{R'_0}$ because the pressure and density of state $1'$, the origin of $S_{1',1''}$, are lower than those of state L', the origin of S_{L',L''_0}, such that $S_{1',1''}$ is less steep than S_{L',L''_0}. Therefore, $p_{R'}/p_{R'_0}$ exceeds unity and shock strengthening is achieved.

As in the increasing density case, the intermediate material enables a shock of strength greater than in the absence of the intermediate material to exist in the right material for a finite duration. When the rarefaction reflected from the second contact surface reaches the first contact surface, a rarefaction is both transmitted into the left material and reflected back into the intermediate material due to the higher impedance of state L''. This reflected rarefaction is transmitted through the second contact surface, where it overtakes and weakens the shock initially transmitted into the right material. Waves continue to reflect off of the contact surfaces resulting in alternating rarefactions and shocks passing into the left and right materials, though they progressively become weaker. Following these interactions, the strength of the leading reflected wave in material L and that of the transmitted wave in material R eventually tend to the strengths of the waves corresponding to those of the reflected and transmitted waves in the case of no intermediate material. The paths of the waves scale with the thickness of the intermediate material, while their strengths depend only on the initial shock strength and the impedances of the three materials.

Figures 2.2 and 2.3 therefore demonstrate that, for a given left and right material and incident shock strength, the strength of the shock that initially emerges in the right material depends on the Hugoniot and, in the case of decreasing impedance, isentrope of the intermediate material and can thus be calculated for an intermediate material of any impedance. To quantify the shock strengthening, Figure 2.4 shows the ratio $p_{R'}/p_{R'_0}$ as a function of the impedance of the intermediate material and the ratio of impedances of the left and right materials for an incident shock strength of $\rho_{L'}/\rho_L = 4$. The right half of the phase space corresponds to cases where $I_L < I_R$ (increasing impedance) and the left half to $I_L > I_R$ (decreasing impedance), while the top half of the phase space corresponds to cases where $I_L < I_1$ and the bottom half to $I_L > I_1$. The solid lines indicate where $I_L = I_1$ (horizontal) or $I_1 = I_R$ (slope equal to 1), in which case there is effectively no intermediate material and $p_{R'}/p_{R'_0} = 1$. In the triangular regions between these two solid lines, the impedance of the intermediate material is between that of the left and right material, and the shock is strengthened ($p_{R'}/p_{R'_0} > 1$). Outside of this region, the shock is weakened ($p_{R'}/p_{R'_0} < 1$). Thus, shock strengthening occurs only if I_1 is between I_L and I_R. In fact, for a given ratio of impedances of the left and right materials, the shock strengthening is greatest if I_1 is the geometric mean of the left and right impedances, i.e., $I_1 = \sqrt{I_L I_R}$ (dashed line in Figure 2.4) in both the weak and strong incident shock limits ($\rho_{L'}/\rho_L \to 1$ and $\rho_{L'}/\rho_L \to 4$, respectively, for $\gamma = 5/3$). This relationship can be determined analytically (see Section 2.6) by seeking the shock Hugoniot of the intermediate material that maximizes the pressure downstream of the shock emerging in the right material. For shocks of moderate strength, the intermediate material impedance that maximizes the shock strengthening is slightly less than the geometric mean of the impedances of the left and right materials, deviating by as much as 1.2% depending on the strength of the incident shock. However, an intermediate material impedance equal to the geometric mean of the impedances of the left and right materials results in shock strengthening that is within 99.99% of the true maximum over the range of overall impedance ratios explored in the present work for an incident shock of any strength.

The maximum achievable shock strengthening also depends on the strength of the incoming shock in the left material. Figure 2.5 shows the shock strengthening for an intermediate material of impedance equal to the geometric mean of the impedances of the left and right materials as a function of the overall impedance ratio, as well as the incident shock strength, for an experimentally relevant range of impedance ratios. In the present framework, a shock of strength $\rho_{L'}/\rho_L = 4$ generates maximum compression and corresponds to the strong shock limit. For the case of increasing impedance ($I_L < I_R$), the shock strengthening increases to a maximum before decreasing to an asymptotic value as the strength of the incident shock is increased. For the case of decreasing impedance ($I_L > I_R$) above a critical impedance ratio, which in the present system is calculated to be $I_L/I_R = 2.29$, the shock strengthening increases monotonically as the incident shock strength is increased; otherwise, it increases to a maximum before decreasing as the strong shock limit is approached. For both increasing and decreasing impedance, the shock strengthening increases as the impedance ratio is increased.

Simulations with different intermediate materials are performed with the HYADES code to verify our theory. For the case of increasing impedance, a steady shock is generated in parylene ($\rho_{CH} = 1.420$ g/cm^3) using an 8 TW/cm^2 laser pulse, passes through an intermediate material composed of a substance shown in Table 2.1, and ultimately is transmitted into gold ($\rho_{Au} = 19.300$ g/cm^3). The shock strength in gold is the quantity of interest. Parylene and gold are chosen as

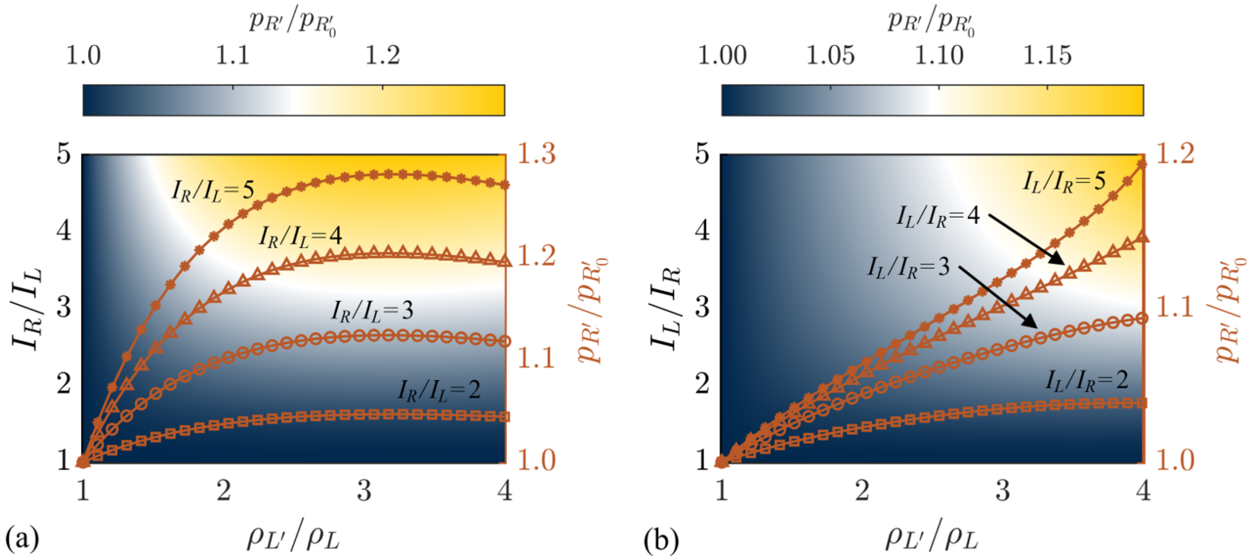

Figure 2.5: Shock strengthening for a single intermediate material with impedance $I_1 = \sqrt{I_L I_R}$ as a function of the incident shock strength and overall impedance ratio for contact surfaces with (a) increasing and (b) decreasing impedance. Lineouts with respect to the right axis show the shock strengthening for specific values of constant overall impedance ratios of $I_L/I_R \in [2, 3, 4, 5]$ (squares, circles, triangles, stars, respectively).

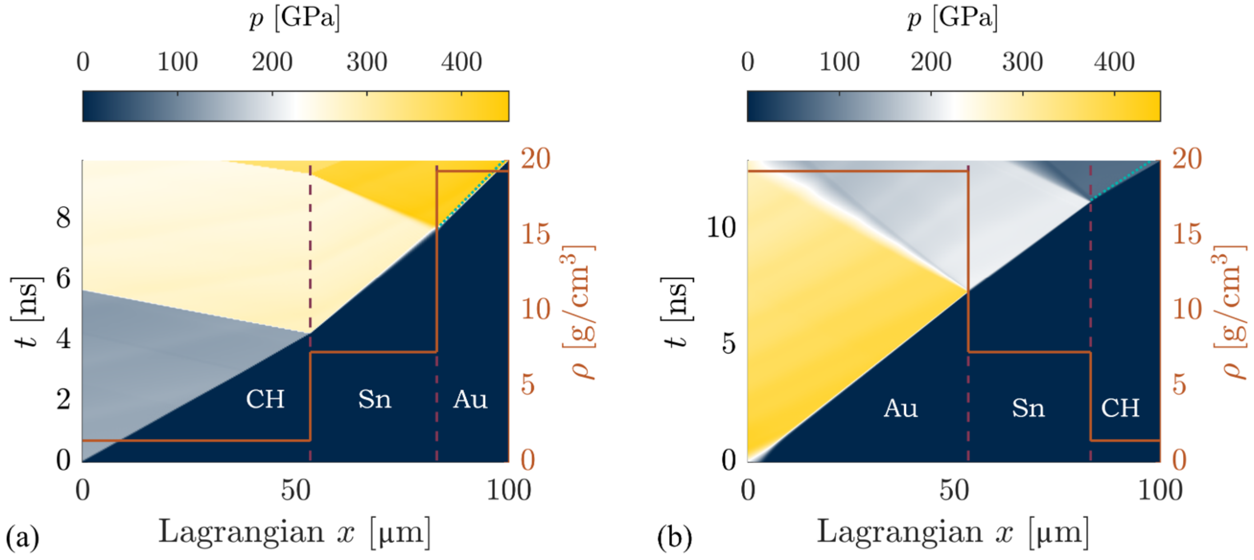

Figure 2.6: Wave diagrams showing the pressure and initial density profiles (solid orange lines) from HYADES simulations for a shock passing from (a) parylene to gold and (b) gold to parylene with a tin intermediate material (dashed purple lines delineate contact surfaces). The paths of the shocks breaking out into the right material from simulations without the intermediate material (dotted teal lines) are also shown.

Table 2.1: Densities, impedances (for ideal gas calculations), and equation of state tables (Los Alamos National Laboratory SESAME table number) of the substances used in the HYADES simulations.

Substance	ρ_1 $[g/cm^3]$	I_1 $[g/cm^2/s]$	SESAME #
Parylene (CH)	1.420	1417	7770
Beryllium (Be)	1.845	1615	2020
Fused Silica (FSi)	2.204	1765	7381
Aluminum (Al)	2.700	1954	3718
Beryllium Oxide (BeO)	3.008	2062	7611
Gallium (Ga)	5.918	2893	2370
Zirconium (Zr)	6.506	3033	3180
Tin (Sn)	7.290	3211	2160
Iron (Fe)	7.850	3332	2140
Copper (Cu)	8.930	3554	3330
Molybdenum (Mo)	10.200	3798	2980
Silver (Ag)	10.500	3853	2720
Tungsten Carbide (WC)	14.970	4601	3560
Tantalum (Ta)	16.654	4853	3520
Gold (Au)	19.300	5224	2700

substances to demonstrate the theory because of their large impedance ratio and prevalence in laser compression experiments at both large and sub-kilojoule laser facilities [26]. The laser irradiance is chosen to be relevant to both long-pulse laser drives at the OMEGA EP facility and those at less energetic facilities like the DCS and MEC. Because a steady incident shock is desired to illustrate our theory, we use a square laser pulse that is turned on at the start of the simulation and terminated within the last nanosecond. This pulse prevents the rarefaction generated when the laser terminates from interacting with the leading steady shock as it passes through the different materials. Finally, we ensure that the parylene ablator is sufficiently long to ensure there are no waves re-reflected off of the ablation layer. For the case of decreasing impedance, the same laser pulse is used with a parylene ablator to generate a steady shock in gold, which passes through an intermediate material, and ultimately into a final layer of parylene. The strength of the shock in the second parylene layer (as opposed to the parylene ablator) is the quantity of interest.

Figure 2.6 shows the wave diagrams with pressure contours from HYADES simulations for a shock passing through layers of increasing and decreasing impedance with an intermediate tin material, where the origin is the position and time that the shock passes from the parylene ablator into the left material. The pre-shock density profiles, the Lagrangian locations of the contact surfaces, and the paths of the shocks breaking out into the right material without the intermediate material are also shown. For increasing impedance (Figure 2.6a), the wave diagram clearly shows

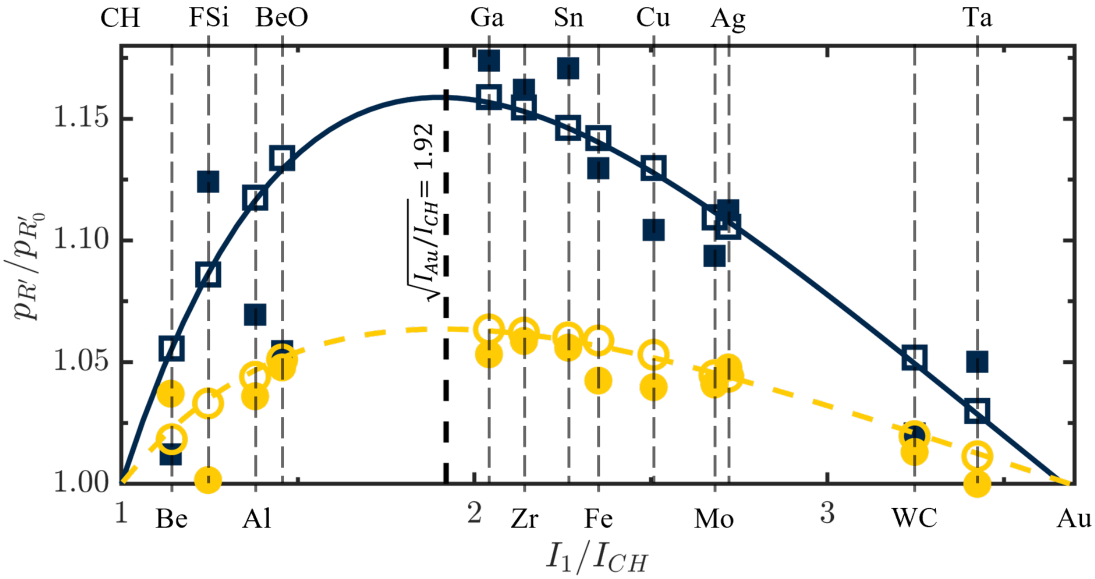

Figure 2.7: Shock strengthening from a single intermediate material vs. the impedance of the intermediate material (see Table 2.1) for a parylene-to-gold (theory: solid blue line; simulations with tabular equation of state: filled blue squares; simulations with ideal gas equation of state: open blue squares) and a gold-to-parylene (theory: dashed yellow line; simulations with tabular equation of state: filled yellow circles; simulations with ideal gas equation of state: open yellow circles) contact surface. Maximum shock strengthening is indicated at $I_1/I_{CH} = \sqrt{I_{Au}/I_{CH}}$. For the case of increasing (decreasing) impedance, $p_{R'_0} = 381.4\,\text{GPa}$ (73.3 GPa).

the anticipated decrease in shock speed as the shock passes into layers of greater impedance. Similarly, for decreasing impedance (Figure 2.6b), the wave diagram clearly shows the anticipated increase in shock speed as the shock passes into layers of lower impedance. Consistent with our theory, the shock that initially emerges in the right material is stronger than the shock that would emerge without the inclusion of the intermediate material, i.e., $p_{R'}/p_{R'_0} > 1$. The enhanced strength of the shock is additionally highlighted by its greater speed in the right material compared to that without the intermediate material, as seen by comparing the slopes of the shock paths in the right material. Eventually, reflections from within the intermediate material generate waves with an overall rarefying effect that overtake and weaken the transmitted shock, such that the strength of the transmitted shock eventually approaches the strength that would be achieved if there were no intermediate material [18].

Figure 2.7 shows the shock strengthening from our theory and from simulations as a function of the impedance of the intermediate material for both increasing and decreasing impedance; for this purpose, the different materials listed in Table 2.1 are used, and simulations utilizing both ideal gas and tabular equations of state are performed. For the ideal gas simulations, the initial impedances are calculated as $I_1 = \rho_1 a_1 = \rho_1\sqrt{\frac{\gamma p_1}{\rho_1}}$ with a reference ambient pressure of $p_1 = 101\,\text{kPa}$ (shown in the third column of Table 2.1). The results from the simulations utilizing tabular equations of state are displayed at the same location along the abscissa as the corresponding ideal gas simulations. Our theory accurately predicts both the trends and magnitude of the shock strengthening. Minor discrepancies are observed in the ideal gas simulations due to minor numerical fluctuations. More significant, yet still small, discrepancies are observed in the results with tabular equations of state, which is expected due to departures from ideal gas conditions. For the laser pulse utilized, up to a 16% (6%) increase in the pressure behind the shock transmitted into the right material is obtained from the inclusion of a single intermediate material for the contact surface of increasing (decreasing) impedance.

Finally, an important constraint related to experimental diagnostics is the duration over which the strengthened shock is supported in the sample before the waves reflected from within the intermediate material begin to overtake and weaken the strengthened shock. Figure 2.8 shows this duration, in time per unit intermediate material thickness, as a function of the incident shock strength and overall impedance ratio for a shock strengthened by a single intermediate material of impedance $I_1 = \sqrt{I_L I_R}$. The duration over which the steady shock propagates decreases as the incident shock strength increases. While this trend implies that diagnosing the state behind the strengthened shock may be challenging for experiments involving very strong incident shocks, which are commonly desired for probing new regimes of substances, the fast dynamics of the system are a consequence of the strength of the incident shock and not made worse by our proposed method of intermediate materials. For the case of decreasing impedance ($I_L > I_R$), the duration decreases as the overall impedance ratio increases. However, for the case of increasing impedance ($I_L < I_R$), the duration does not vary monotonically with the overall impedance ratio over the range of impedance ratios considered. There is a kink in the contours of duration at $I_R/I_L = 1$ caused by the change from decreasing to increasing impedance.

As an example experiment, a HYADES simulation is performed with tabular equations of state for a shock passing from a parylene ablator, through a shock-strengthening intermediate beryllium oxide layer, and into tin. These materials are chosen to approximate the impedance condition for maximum shock strengthening ($I_{BeO} \approx \sqrt{I_{CH} I_{Sn}}$). The laser pulse is identical to that used for the simulations in Figure 2.7. The time per unit intermediate material thickness between the moment the shock emerges in the tin and the moment the rarefaction reflected off the beryllium oxide layer first overtakes it is 0.345 ns μm^{-1}, which agrees well with the prediction of 0.338 ns μm^{-1} from our theory. This experiment is represented in Figure 2.8 by the symbol, colored by the steady shock duration (and outlined by the dashed black line for clarity, as the symbol is almost indistinguishable from the color map due to the excellent agreement between our method and the simulation), located at $\rho_{L'}/\rho_L = 2.94$ and $I_R/I_L = 2.27$. For such an experiment, both our theory and the HYADES simulation results suggest that a 20 μm intermediate beryllium oxide layer leads to a strengthened

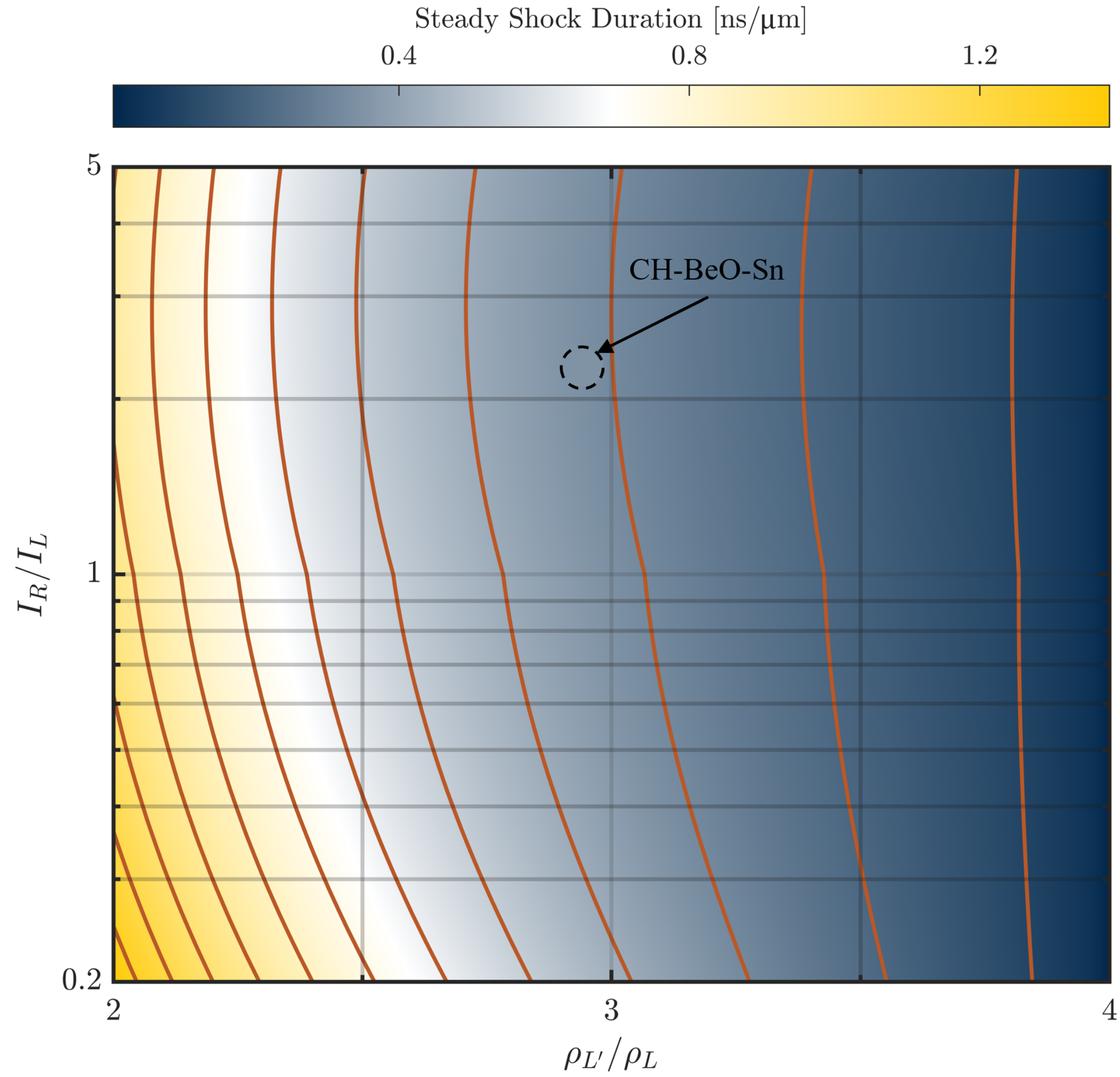

Figure 2.8: The duration, in time per unit intermediate material thickness, over which a steady, strengthened shock will propagate in the right material before being overtaken by the rarefaction generated within a single intermediate material of impedance $I_1 = \sqrt{I_L I_R}$ as a function of the incident shock strength and the overall impedance ratio. Contours (orange lines) span durations of $(0.1, 1.3)\,\mathrm{ns}\,\mu\mathrm{m}^{-1}$ in increments of $0.1\,\mathrm{ns}\,\mu\mathrm{m}^{-1}$ from right to left. Also shown is the steady shock duration from a simulation with tabular equations of state for a shock passing from parylene to beryllium oxide to tin (circle, colored by the present colormap, outlined by the dashed black line).

shock in tin for an approximately 7 ns diagnostic window. Additionally, the anticipated shock strengthening calculated using our method is $p_{R'}/p_{R'_0} = 1.061$, which is slightly greater than that achieved in the simulation, which predicts $p_{R'}/p_{R'_0} = 1.043$. This discrepancy, however, is expected due to the impedance of the beryllium oxide being slightly less than the ideal intermediate material impedance for shock strengthening.

2.4.2 Shock Strengthening with Multiple Intermediate Materials

The findings from the previous section suggest that a strategy to enhance shock strengthening is to incorporate multiple intermediate materials, i.e., by making the intermediate region piecewise constant. Because maximum shock strengthening (or at worst, shock strengthening within 99.99% of the true maximum) for a single intermediate material is achieved when the impedance of the intermediate material is the geometric mean of the impedances of the adjacent materials (see Figure 2.4), it follows by induction that an exponential distribution ($\frac{I_j}{I_L} = (\frac{I_R}{I_L})^{j/(N+1)}$) in intermediate material impedance gives rise to the greatest shock strengthening for a finite number N of intermediate materials, since the exponential distribution satisfies the condition that the impedance of each intermediate material is the geometric mean of its adjacent materials. We consider a maximum of $N = 5$ intermediate materials. Although additional shock strengthening can theoretically be achieved with more intermediate materials, albeit with diminishing returns for each additional material, mounting more than five intermediate materials on current experimental platforms poses additional challenges for target fabrication.

Simulations are performed with the HYADES code to verify our theory for shock strengthening with multiple intermediate materials. The simulation parameters are identical to those of the simulations exploring a single intermediate material, except now there is a series of discrete, exponentially spaced intermediate materials composed of substances listed in Table 2.1. Figure 2.9 shows wave diagrams superposed onto pressure contours for the cases of increasing and decreasing impedance with three intermediate materials approximating an exponential distribution (an exact exponential distribution cannot be achieved due to the constraint of the choice of substances in Table 2.1), where the origin is the position and time that the shock passes from the parylene ablator into the left material. The pre-shock density profiles, the Lagrangian locations of the contact surfaces, and the paths of the shocks breaking out into the right material without any intermediate materials are also shown. For increasing impedance (Figure 2.9a), the wave diagram clearly shows the anticipated decrease in shock speed as the shock passes into layers of greater impedance. Similarly, for decreasing impedance (Figure 2.9b), the wave diagram clearly shows the anticipated increase in shock speed as the shock passes into layers of lower impedance. The strength of the shock that initially emerges in the right material is greater than that of the shock that would emerge without the

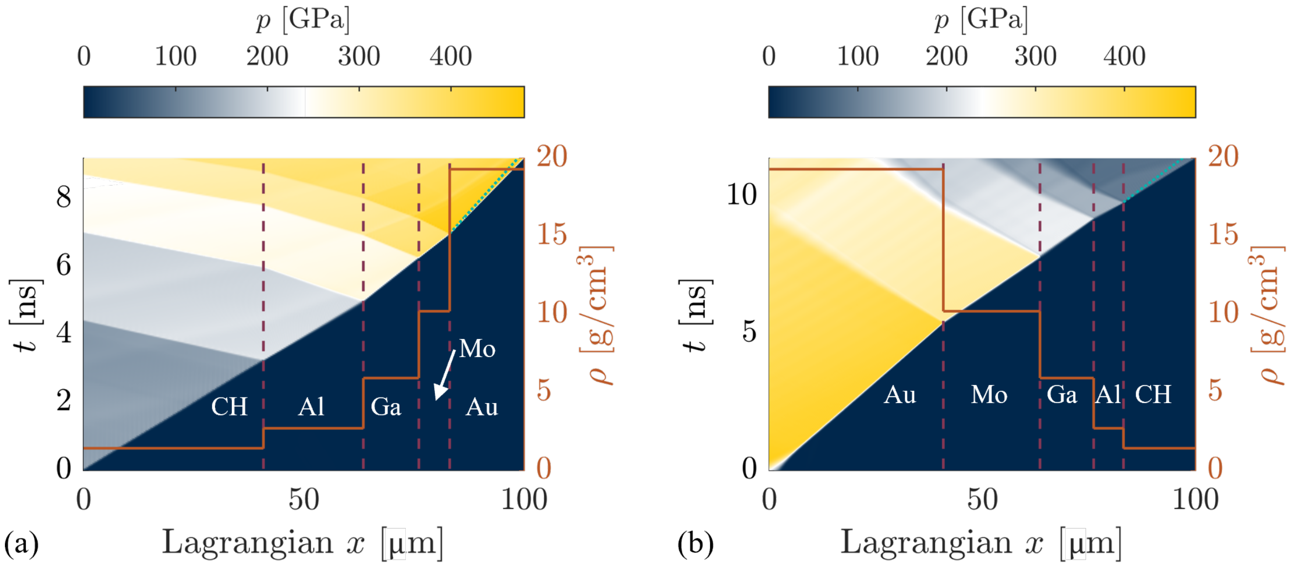

Figure 2.9: Wave diagrams and initial density profiles (solid orange lines) from HYADES simulations with pressure contours for a shock passing from (a) parylene-to-gold and (b) gold-to-parylene with three intermediate materials (dashed purple lines delineate contact surfaces). Intermediate material substances from Table 2.1 are chosen to approximate an exponential impedance distribution. The paths of the shocks breaking out into the right material from simulations without the intermediate materials (dotted teal lines) are also shown.

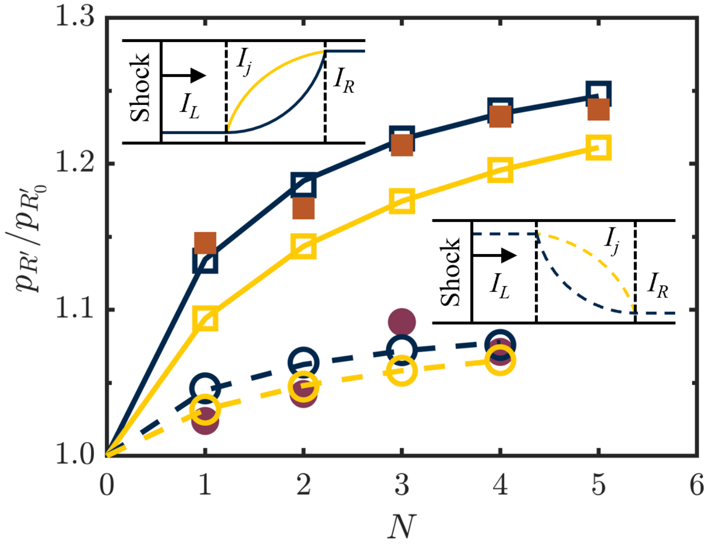

Figure 2.10: Shock strengthening from multiple intermediate impedance materials vs. the number of intermediate materials for exponential (blue lines) and square-root (yellow lines) impedance distributions for a parylene-to-gold (theory: solid lines, simulations with tabular equation of state: filled orange squares, simulations with ideal gas equation of state: open squares) and a gold-to-parylene (theory: dashed lines, simulations with tabular equation of state: filled purple circles, simulations with ideal gas equation of state: open circles) contact surface.

inclusion of any intermediate materials, and increases with the number of intermediate materials. The enhanced strength of the shock is additionally highlighted by the greater shock speed in the right material compared to that without any intermediate materials. A comparison of Figures 2.6 and 2.9 also demonstrates that the shock speed and strength in the right material are greater with multiple intermediate materials compared to a single intermediate material. Each material width is adjusted to ensure that there are no re-reflected wave interactions with the transmitted shock prior to the breakout of the shock into the right material. As in the case of a single intermediate material, reflections from within the intermediate materials generate waves with an overall rarefying effect that eventually overtake and weaken the transmitted shock. Eventually, the strength of the transmitted shock approaches that without the inclusion of the intermediate materials [18]. To transmit a steady shock into the final material, the intermediate materials must be of discrete, decreasing thicknesses. If the impedance profile in the intermediate region between the left and right materials is continuous, the wave interactions weakening the leading shock would occur prior to the breakout of this shock into the final material. Although this effect is undesirable for the generation of a steady shock, it has been used among other techniques to generate a quasi-isentropic compression wave from a shock [142, 247].

Figure 2.10 shows the shock strengthening from both our theory and simulations with tabular and ideal gas equations of state for exponentially spaced intermediate materials as a function of the number of intermediate materials for contact surfaces of both increasing and decreasing impedance. For comparison to the exponential distribution, the shock strengthening for a square-root distribution of intermediate materials ($\frac{I_j}{I_L} = \sqrt{1 + \frac{j}{N+1}\left(\frac{I_R^2 - I_L^2}{I_L^2}\right)}$), corresponding to a linear spacing in density, is both calculated using our theory and simulated with an ideal gas equation of state. As expected, the square-root impedance distribution is less effective than an exponential distribution for shock strengthening. For the case of increasing impedance ($I_L < I_R$), our theory agrees well with both the trend and magnitude of the shock strengthening determined from simulations in which tabular material equations of state are used, as the data lie between the theoretical prediction for exponentially and square-root spaced intermediate materials. Because the intermediate materials can only approximate an exponential distribution due to the choice of substances in Table 2.1, it is expected that the data fall slightly below the theoretical prediction for a truly exponential impedance distribution. For the case of decreasing impedance ($I_L > I_R$), the simulation data show more scatter, but are still generally well predicted by our theory. As expected, the shock strengthening determined from simulations using an ideal gas equation of state matches our theory closely, with minor differences likely attributable to numerical fluctuations. The results show that for the laser pulse utilized, up to a 25% (9%) increase in the pressure behind the shock transmitted into the right material is obtained with the inclusion of up to 5 intermediate materials for the contact surfaces of increasing (decreasing) impedance.

Shock strengthening for multiple intermediate materials varies with the incident shock strength and the overall impedance ratio in a manner qualitatively similar to that for a single intermediate material (see Figure 2.5), with the additional materials magnifying the shock strengthening, as Figure 2.10 demonstrates.

2.4.3 Application to HED Shock Compression Platforms

While our theory indicates that intermediate materials following an exponential distribution in impedance between the left and right materials can strengthen shocks, there are several practical limitations. First, experiments are limited by the choice of real substances, which may make it difficult to achieve the desired impedance profile because of the availability of a substance with a desired impedance. Second, to prevent the re-reflected waves from the intermediate contact surfaces from weakening the leading shock, the size of each successive intermediate material must be significantly decreased. Targets must therefore incorporate a thick first intermediate material to achieve the successive-material aspect ratio required to prevent the unwanted effects of the re-reflected waves. Such longer targets may be prohibitive for applications involving relatively brief laser pulses, as the strengthening achieved with the technique may be negated if the rarefaction launched when the laser terminates significantly weakens the shock front as it passes through the intermediate materials. Third, because the shock strengthening is achieved primarily in the vicinity of the intermediate materials due to the eventual weakening caused by the re-reflected waves (see Figure 2.8), this technique may not be suitable for strengthening shocks passing through contact surfaces of large impedance mismatches if these contact surfaces are not near the sample under study. For example, in many experiments utilizing a DAC, a thin layer of gold is used far upstream of the sample for shielding purposes. While this high-impedance gold layer presents a significant opportunity for shock strengthening, by the time the shock reaches the sample under study, it will likely have been weakened by the action of re-reflected waves to its strength in the absence of any intermediate materials near the gold shielding layer. This constraint then requires that the intermediate materials be placed immediately upstream of the sample. The contact surface under consideration in the context of a DAC would therefore be that between the diamond and the sample. Furthermore, because the shock strengthening becomes significant with large impedance ratios, shocks in samples with an impedance similar to diamond have little to gain from this technique, while shocks in gaseous and other low-density samples may benefit greatly. Finally, although our theory was developed under the assumption of a steady incident shock, significant shock strengthening can still be achieved for unsteady shocks, provided that the magnitude of the decay of the unsteady shock as it travels through the region of intermediate materials does not exceed that of the shock strengthening caused by the intermediate materials. However, for a decaying shock, the shock strengthening realized using our proposed method of intermediate materials will be less than the magnitudes reported for a steady shock in the present work. Because the decay rate of an unsteady, laser-driven shock is a complex function of many experimental variables including the laser drive and target geometry, we advise caution when deciding if the method of intermediate materials is appropriate for strengthening shocks in experiments involving rapidly decaying incident shocks.

2.5 Conclusions

A technique for strengthening shocks passing through a contact surface in high-energy-density laser-driven compression experiments is presented. A semi-analytical method based on characteristics analysis is used to solve the problem of a shock passing through a region of non-uniform impedance that increases the strength of the shock initially transmitted into the sample. By taking advantage of transient wave dynamics, the strength of a shock transmitted from one material of a given impedance to another material of another impedance can be increased for a finite time duration if it first passes through yet another material of an intermediate impedance. As an example, for a shock capable of being generated on one beam of the OMEGA EP laser facility passing between parylene and gold, an increase of up to 25% in the pressure behind the shock can be achieved.

For experimentally relevant contact surfaces of increasing impedance, the shock strengthening increases to a maximum before decreasing as the strength of the incident shock is increased. For those of decreasing impedance above a critical value, the shock strengthening increases monotonically as the strength of the incident shock is increased. For contact surfaces of both increasing and decreasing impedance, the shock strengthening for a given incident shock strength increases with increasing impedance ratio. Our theory is verified for cases involving both single and multiple intermediate materials via simulations using the HYADES code. The most effective shock strengthening for a single intermediate material is achieved with an intermediate material impedance that is the geometric mean of the impedances of the outer two materials for strong incident shocks. It follows that, when using multiple intermediate materials, an exponential distribution of intermediate material impedances maximizes the shock strengthening. Though only planar geometries are presently considered, the shock strengthening technique could have important implications for systems exploiting convergent geometries like ICF capsules including double shell and revolver designs. Practical limitations for the technique include the availability of real substances to achieve a desired impedance profile, the requirement that the intermediate materials not be so large that the shock is significantly weakened by the rarefaction launched when the laser pulse terminates, and the requirement that the intermediate materials be adjacent to the sample.

This work is supported by the Lawrence Livermore National Laboratory (LLNL) under subcontract B632749 and was performed under the auspices of the U. S. Department of Energy (DOE) by the LLNL under Contract No. DE-AC52-07NA27344 with partial support provided by LDRD 19-ERD-031. Furthermore, this work is supported by the U. S. DOE as part of the Stewardship Science Graduate Fellowship (SSGF) Program under grant DE-NA0003960.

2.6 Supplemental Material

This supplemental material provides additional detail on the treatment of entropy discontinuities with the MOC and an analytical proof showing that an exponential distribution of intermediate step impedance maximizes shock strengthening.

2.6.1 Treatment of Entropy Discontinuities

Six interactions (the interaction of a shock and a contact surface, the interaction between a rarefaction and a contact surface, a rarefaction overtaking a shock of the same wave family, a shock overtaking a rarefaction of the same wave family, a collision of a shock and a rarefaction of different wave families, and a compression wave steepening into a shock) between shocks, rarefactions, compression waves, and contact surfaces requiring the boundary condition derived from the exact solution to the Riemann problem in our method of characteristics are herein detailed, followed by their verification using the HYADES code.

2.6.1.1 Shock-Contact Surface Interaction

When a shock intersects a contact surface, the resulting system of waves is given by the exact solution to the Riemann problem where one of the initial states is the post-shock state and the other is the undisturbed state on the other side of the contact surface. This interaction results in a transmitted and reflected shock if the shock travels into a medium of greater impedance. Conversely, the interaction results in a transmitted shock and a reflected rarefaction if the shock travels into a medium of lower impedance. The resulting solution is exact.

2.6.1.2 Rarefaction-Contact Surface Interaction

The case of a rarefaction wave interacting with a contact surface is solved by discretizing the rarefaction into K characteristics and exactly solving the resulting Riemann problem for each characteristic-contact surface interaction, as well as each subsequent interaction between incoming characteristics and reflected characteristics. The exact solution to the Riemann problem consistent with the interaction of the first incoming characteristic of the rarefaction with the contact surface yields the contact surface velocity, the state along the characteristic transmitted through the contact surface, and the state along the reflected characteristic. The contact surface velocity is used to update its position, and the effect of the reflected characteristic on the incident rarefaction is treated by the MOC. The Riemann problem is again solved where now one of the initial states is given by the state along the transmitted characteristic, and the other is given by the state along the subsequent characteristic of the incident rarefaction after modification by the reflected characteristic. This procedure is repeated for each characteristic used to represent the incident rarefaction. Figure 2.11 provides a wave diagram of this interaction and a flowchart that details the steps of the calculation. This interaction results in a transmitted and reflected rarefaction if the incident rarefaction travels into a medium of greater impedance. Conversely, this interaction results in a transmitted rarefaction and a reflected compression wave if the incident rarefaction travels into a medium of lower impedance. Figure 2.12 demonstrates the convergence of the method for wave interactions involving incident rarefactions. For the test problem, a rarefaction with a pressure ratio of 0.50 impinges on a light-to-heavy contact surface with a density ratio of 41.05, similar to the density ratio between diamond and cryogenic liquid hydrogen. These values are chosen to challenge the method such that the range of densities after the wave interaction span two orders of magnitude. The reference solution is a high-resolution ($K = 10^4$) simulation. The relative error

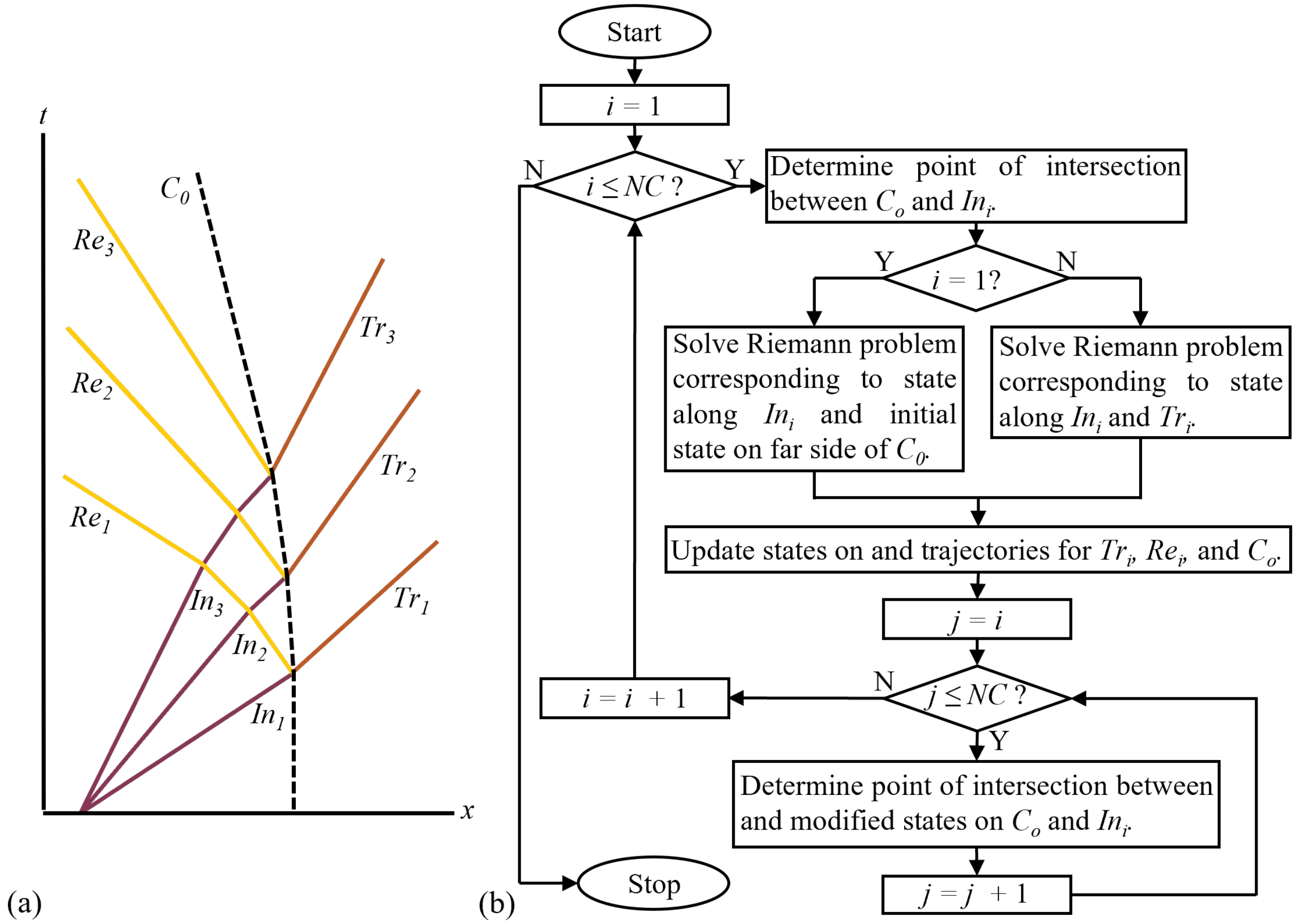

Figure 2.11: A wave diagram (a) and flowchart (b) detailing the treatment of the rarefaction-contact surface interaction with $NC = 3$ characteristics used for the incident rarefaction. The incident characteristics (solid purple, labeled In_i) generate both reflected (solid yellow, labeled Re_i) and transmitted (solid orange, labeled Tr_i) characteristics and accelerate the contact surface (dashed black, labeled C_0).

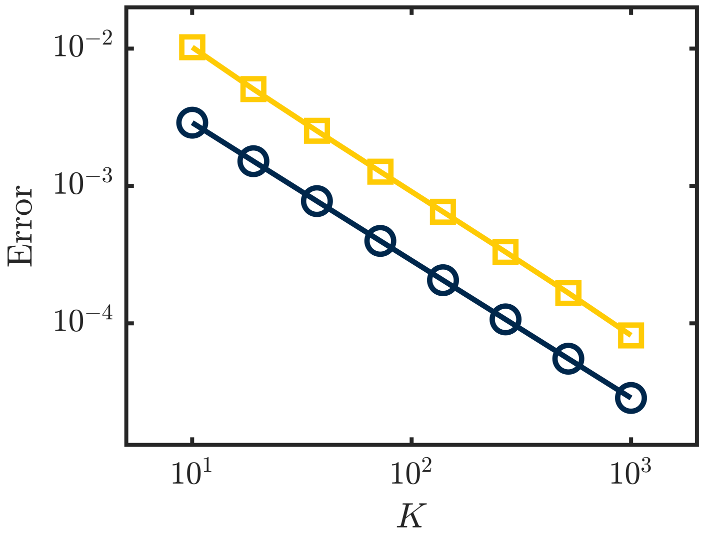

Figure 2.12: Error in pressure (blue circles) and contact surface location (yellow squares) vs. number of characteristics used to represent the incident wave.

of the pressure between the reflected and transmitted waves and the contact surface location at the end of the interaction are shown in Figure 2.12. The convergence rate is first order.

2.6.1.3 Rarefaction Overtaking a Shock

When a rarefaction overtakes a shock, the Riemann problem is solved where one of the initial states is given by the state along the first incoming characteristic (constant for a simple wave) of the rarefaction and the other is the unshocked state. The exact solution to the Riemann problem then gives the state along the reflected characteristic and the updated shock speed, which is used to update its position, and the effect of the reflected characteristic on the incident rarefaction is treated by the MOC. The Riemann problem is again solved where now one of the initial states is given by that along the subsequent characteristic of the incident rarefaction after modification by the reflected characteristic and the other remains the unshocked state. This procedure is repeated for each characteristic used to represent the incident rarefaction. A flowchart detailing this calculation would be similar to that of Figure 2.11b, only the Riemann problem is always solved between the state along the incident characteristics and the unshocked state; there is no wave transmitted ahead of the shock.

In addition to the shock and reflected wave, the exact solution to this Riemann problem also yields a contact surface that emerges every time a characteristic from the incident rarefaction intersects the shock. Solving for the interaction of this contact surface, and every other contact surface emerging from the interaction of every other characteristic of the incident rarefaction with the shock, with both families of characteristics downstream of the shock quickly leads to an intractable problem due to the ever-increasing number of characteristics (from two prior to each interaction to three thereafter, and so on) [243]. Additionally, we are primarily interested in solving for the shock and reflected wave that emerge from the interaction because they can interact with contact surfaces, whereas contact surfaces, by definition, cannot intersect. For these reasons, we account for a single contact surface from the intersection of the final characteristic of the incident rarefaction and the shock front; all other contact surfaces are ignored. To justify this assumption, Figure 2.13 demonstrates the relationship between the interaction of a rarefaction overtaking a shock and the exact solution to the Riemann problem corresponding to initial conditions given by the states upstream of the shock and downstream of the rarefaction prior to their interaction, hereby referred to as the "outer Riemann" problem. Although the contact surfaces produced throughout the shock-rarefaction interaction affect the paths of the characteristics during the interaction, the strengths of the reflected wave, contact surface, and shock after the interaction are accurately calculated because the states separating these waves (states 3 and 4 in Figure 2.13a) are independent of the solution details through the contact region that would emerge if each individual contact surface was considered. This result is a consequence of the fact that there is a unique, entropy-obeying thermodynamic path after the wave interaction connecting the state upstream of the shock to that downstream of the incident rarefaction (states 2 and 0 in Figure 2.13a) [160]. This path is exactly given by the solution to the outer Riemann problem corresponding to these states, shown in Figure 2.13b, where states L and R are equivalent to states 0 and 2, respectively, in Figure 2.13a. The state downstream of the reflected wave (state 3 in Figure 2.13a) must therefore be equal to the state downstream of the right-running wave of the outer Riemann problem (state L^* in Figure 2.13b). The solution to the Riemann problem solved when the final characteristic of the incident rarefaction intersects the shock front, corresponding to states 2 and 3 in Figure 2.13a and equivalent to states R and L^*, respectively, in Figure 2.13b, therefore yields only two waves: a shock and a contact surface between which the state (state 4 in Figure 2.13a) is equivalent to state R^* in Figure 2.13b.

The assumption that the contact surface emerges as a discontinuity from the intersection of the final characteristic of the incident rarefaction and the shock therefore typically yields three waves: a weakened shock, a contact surface, and a non-centered reflected wave. The strengths, and therefore the speeds, of these waves are equal to those calculated if each individual contact surface was considered, though the location where they emerge from the interaction is approximate due to the ignored influence of each individual contact surface on characteristic trajectories during the interaction. While this approximation may have a small effect on the timing of some wave interactions, it is not expected to significantly alter the solution. If the shock weakens to the point where there is no change in thermodynamic quantities across it (i.e., zero strength) while being overtaken by the rarefaction, the interaction persists indefinitely.

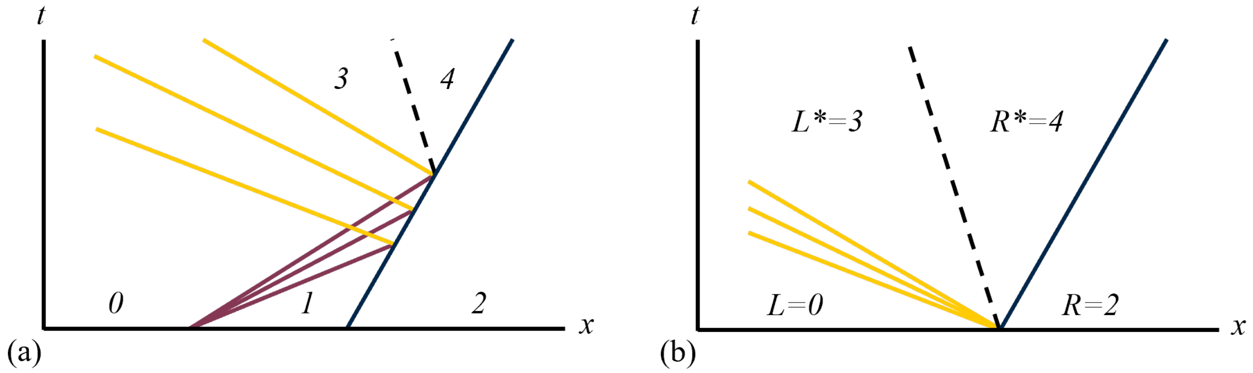

Figure 2.13: Wave diagrams (purple solid: right-running rarefaction, yellow solid: left-running rarefactions, blue solid: shocks, black dashed: contact surfaces) with Eulerian position, x, for (a) a rarefaction overtaking a shock and (b) the corresponding outer Riemann problem. All waves are represented schematically as straight lines. Constant states are labeled.

2.6.1.4 Shock Overtaking a Rarefaction

When a shock overtakes a rarefaction, the Riemann problem is solved where one of the initial states is given by the shocked state and the other is given by the state along the first characteristic (constant for a simple wave) of the rarefaction to intersect the shock. The exact solution to the Riemann problem then yields the state along the characteristic transmitted into the shocked state and the updated shock speed, which is used to update its position. The Riemann problem is again solved where now one of the initial states is given by that along the characteristic transmitted into the shocked state and the other is given by that along the next characteristic of the rarefaction to intersect the shock. This procedure is repeated for each characteristic used to represent the incident rarefaction.

Contact surfaces are generated at every interaction between a characteristic and the shock. These contact surfaces are treated in the same manner as in the case of a rarefaction overtaking a shock (Section 2.6.1.3): a single contact surface is assumed to emerge from the intersection of the final characteristic of the rarefaction and the shock. The strength of this contact surface and the final strengths of the shock and transmitted wave are equal to the strengths calculated if each contact surface was considered. If the shock weakens to the point where there is no change in thermodynamic quantities across it (i.e., zero strength), the interaction persists indefinitely.

2.6.1.5 Head-On Shock-Rarefaction Collision

The treatment of a head-on collision of a shock and a rarefaction of different wave families is identical to the case of a shock overtaking a rarefaction, though the interaction always results in a shock and a rarefaction of the same families as the incident waves. Furthermore, this interaction is always of finite duration.

2.6.1.6 Steepening Compression Wave

Prior to any shock steepening, the treatment of a compression wave interacting with an entropy discontinuity is procedurally identical to a rarefaction interacting with an entropy discontinuity. Shock formation is handled by solving the Riemann problem at the intersection of the first two characteristics of the compression wave where each state is given by that along the characteristics (constant for a simple wave). The exact solution to the Riemann problem then gives the velocity of the shock formed and the state along the reflected characteristic. The Riemann problem is again solved at the intersection of the shock with the subsequent characteristic of the incident compression wave after the latter has been modified by the reflected characteristic. The procedure is repeated for each characteristic of the incident compression wave. As in the cases involving the interaction of a shock and a rarefaction, a single contact surface is assumed to emerge from the intersection of the shock and the final characteristic of the initial compression wave. The strength of the contact surface, the reflected wave, and the steady shock that emerge from this interaction are equal to the strengths calculated if each contact surface was considered.

2.6.1.7 Verification with the HYADES Code

The accuracy of our approach is verified by comparison to HYADES simulations assuming ideal gas behavior. Space-time contours of density obtained from the HYADES simulations for the elementary wave interactions described in the previous sections are shown in Figure 2.14. The strengths of the shocks, contact surfaces, and rarefactions are chosen to challenge the method by spanning two orders of magnitude in density except for the case of a rarefaction overtaking a shock, where the maximum and minimum densities are limited by the density jump that can be achieved across the shock wave. The sound speed utilized for non-dimensionalization is that for an ideal gas at a reference ambient pressure of 101 kPa. In addition to the states after the wave interactions, Figure 2.14 verifies that the paths of the waves are correctly calculated for each wave interaction. Though difficult to distinguish, careful inspection of Figure 2.14d reveals the contact surface that emerges as the rarefaction overtakes the shock. This contact surface is the primary cause for the change in density between the state downstream of the incident rarefaction and the state downstream of the shock after the interaction. The near-parallel characteristics of the wave reflected off of the shock front indicate that it is very weak. Though spurious oscillations in the simulations are in the most part avoided by appropriate mesh feathering, some oscillations are visible, particularly where the shock is initialized at $(x, t) = (0.65, 0.00)$ in Figure 2.14d. These oscillations, however, do not

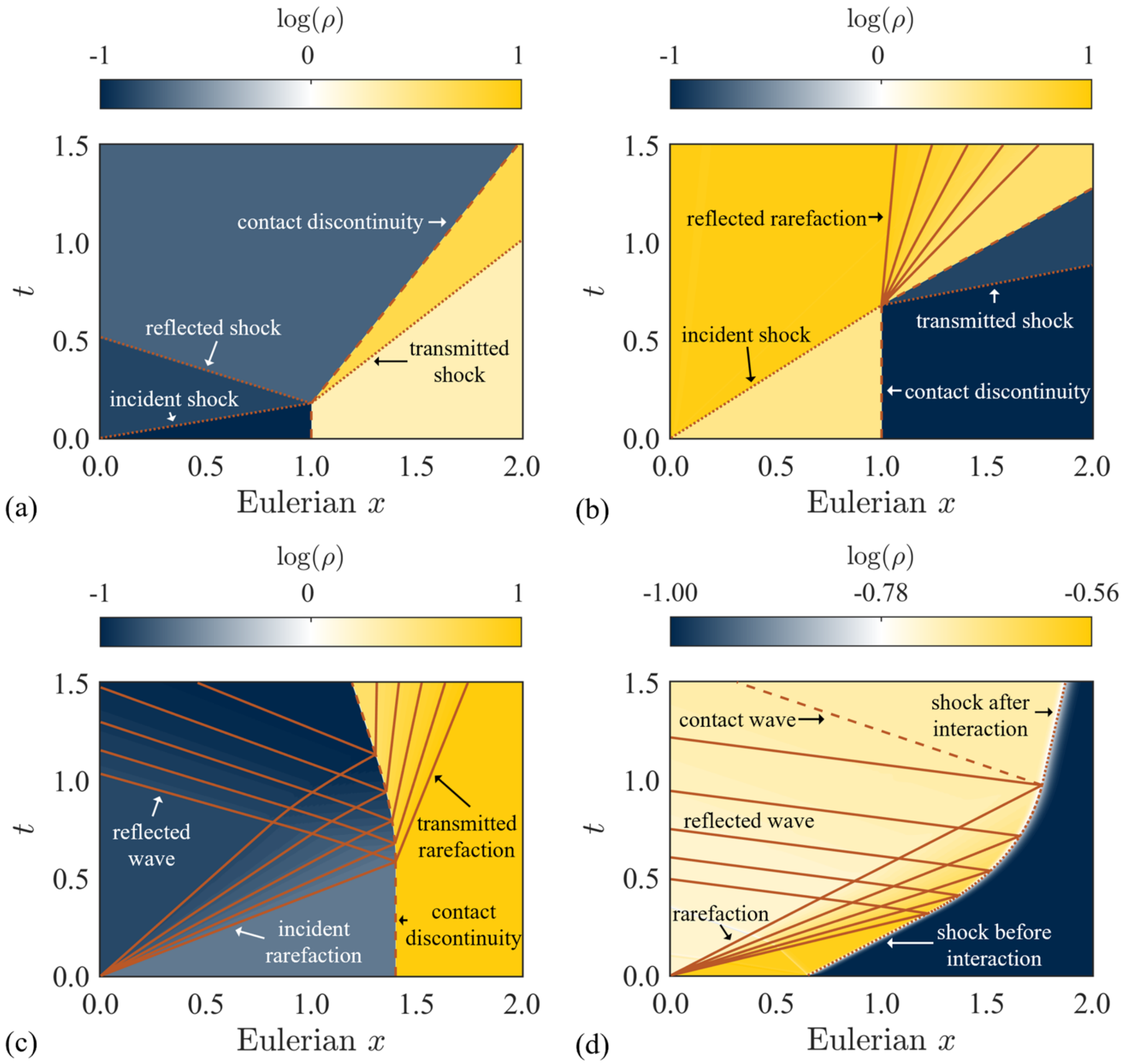

Figure 2.14: Density contours from HYADES simulations overlaid with the characteristic paths (solid orange lines), contact surfaces (dashed orange lines), and shocks (dotted orange lines) obtained using our theory for (a) a shock interacting with a light-to-heavy contact surface, (b) a shock interacting with a heavy-to-light contact surface, (c) a rarefaction interacting with a contact surface, and (d) a rarefaction overtaking a shock. A logarithmic color scheme is utilized to enhance the density contrast across the waves.

appear to affect the results.

2.6.2 Intermediate Material Impedance for Maximum Shock Strengthening

For a shock of strength $\rho_{L'}/\rho_L$ traveling into a region of uniform pressure ($p_L = p_1 = p_R$) and velocity ($u_L = u_1 = u_R = 0$) and increasing impedance ($I_L < I_1 < I_R$), see Figure 2.6, the pressure $p_{L'',1'}$ can be determined by finding the root of the equation,

$$(p_{L'',1'} - p_{L'})\left[\frac{\frac{2}{(\gamma+1)\rho_{L'}}}{p_{L'',1'} + \frac{\gamma-1}{\gamma+1}p_{L'}}\right]^{\frac{1}{2}} + (p_{L'',1'} - p_1)\left[\frac{\frac{2}{(\gamma+1)\rho_1}}{p_{L'',1'} + \frac{\gamma-1}{\gamma+1}p_1}\right]^{\frac{1}{2}} - u_{L'} = 0, \tag{2.5}$$

where

$$p_{L'} = p_L\left(\frac{1 - \frac{\gamma+1}{\gamma-1}\frac{\rho_{L'}}{\rho_L}}{\frac{\rho_{L'}}{\rho_L} - \frac{\gamma+1}{\gamma-1}}\right), \tag{2.6}$$

and

$$u_{L'} = \left(\frac{p_L}{\gamma\rho_L}\right)^{\frac{1}{2}}\left(\frac{p_{L'}}{p_L} - 1\right)\left(\frac{\frac{2\gamma}{\gamma+1}}{\frac{p_{L'}}{p_L} + \frac{\gamma-1}{\gamma+1}}\right)^{\frac{1}{2}}. \tag{2.7}$$

With $p_{L'',1'}$ known, the density $\rho_{1'}$ and velocity $u_{L'',1'}$ behind the incident shock in material 1 can be calculated as

$$\rho_{1'} = \rho_1\left(\frac{\frac{\gamma-1}{\gamma+1} + \frac{p_{L'',1'}}{p_1}}{\frac{\gamma-1}{\gamma+1}\frac{p_{L'',1'}}{p_1} + 1}\right) \tag{2.8}$$

and

$$u_{L'',1'} = \frac{u_{L'}}{2} + \frac{1}{2}(p_{L'',1'} - p_1)\left[\frac{\frac{2}{(\gamma+1)\rho_1}}{p_{L'',1'} + \frac{\gamma-1}{\gamma+1}p_1}\right]^{\frac{1}{2}} - \frac{1}{2}(p_{L'',1'} - p_{L'})\left[\frac{\frac{2}{(\gamma+1)\rho_{L'}}}{p_{L'',1'} + \frac{\gamma-1}{\gamma+1}p_{L'}}\right]^{\frac{1}{2}}, \tag{2.9}$$

respectively. The pressure $p_{1'',R'}$ can then be determined by finding the root of the equation,

$$(p_{1'',R'} - p_{L'',1'}) \left[\frac{\frac{2}{(\gamma+1)\rho_{1'}}}{p_{1'',R'} + \frac{\gamma-1}{\gamma+1} p_{L'',1'}} \right]^{\frac{1}{2}} + (p_{1'',R'} - p_R) \left[\frac{\frac{2}{(\gamma+1)\rho_R}}{p_{1'',R'} + \frac{\gamma-1}{\gamma+1} p_R} \right]^{\frac{1}{2}} - u_{L'',1'} = 0. \tag{2.10}$$

The impedance of material 1 that maximizes the shock strengthening (i.e., that maximizes $p_{1'',R'}$) is determined by examining the behavior of $\frac{\partial p_{1'',R'}}{\partial I_1} = \frac{2I_1}{\gamma p_1} \frac{\partial p_{1'',R'}}{\partial \rho_1}$. Differentiating Equation 2.5 with respect to ρ_1 and solving for $\frac{\partial p_{L'',1'}}{\partial \rho_1}$ yields

$$\begin{aligned}
\frac{\partial p_{L'',1'}}{\partial \rho_1} = {} & \frac{(p_{L'',1'} - p_1)}{2} \left[\frac{\frac{2}{(\gamma+1)\rho_1}}{p_{L'',1'} + \frac{\gamma-1}{\gamma+1} p_1} \right]^{-\frac{1}{2}} \left[\frac{\left(p_{L'',1'} + \frac{\gamma-1}{\gamma+1} p_1\right) \left(\frac{2}{(\gamma+1)\rho_1^2}\right)}{\left(p_{L'',1'} + \frac{\gamma-1}{\gamma+1} p_1\right)^2} \right] \\
& \times \left\{ \frac{(p_{L'',1'} - p_{L'})}{2} \left[\frac{\frac{2}{(\gamma+1)\rho_{L'}}}{p_{L'',1'} + \frac{\gamma-1}{\gamma+1} p_{L'}} \right]^{-\frac{1}{2}} \left[\frac{\frac{-2}{(\gamma+1)\rho_{L'}}}{(p_{L'',1'} + \frac{\gamma-1}{\gamma+1} p_{L'})^2} \right] + \left[\frac{\frac{2}{(\gamma+1)\rho_1}}{p_{L'',1'} + \frac{\gamma-1}{\gamma+1} p_1} \right]^{\frac{1}{2}} \right. \\
& \left. + \frac{(p_{L'',1'} - p_1)}{2} \left[\frac{\frac{2}{(\gamma+1)\rho_1}}{p_{L'',1'} + \frac{\gamma-1}{\gamma+1} p_1} \right]^{-\frac{1}{2}} \left[\frac{\frac{-2}{(\gamma+1)\rho_1}}{(p_{L'',1'} + \frac{\gamma-1}{\gamma+1} p_1)^2} \right] + \left[\frac{\frac{2}{(\gamma+1)\rho_{L'}}}{p_{L'',1'} + \frac{\gamma-1}{\gamma+1} p_{L'}} \right]^{\frac{1}{2}} \right\}^{-1}.
\end{aligned} \tag{2.11}$$

Differentiating Equation 2.10 with respect to ρ_1 and solving for $\frac{\partial p_{1'',R'}}{\partial \rho_1}$ yields

$$\begin{aligned}
\frac{\partial p_{1'',R'}}{\partial \rho_1} = {} & \left\{ -\frac{\partial p_{L'',1'}}{\partial \rho_1} \left[\frac{\frac{2}{(\gamma+1)\rho_{1'}}}{p_{1'',R'} + \frac{\gamma-1}{\gamma+1} p_{L'',1'}} \right]^{\frac{1}{2}} - \frac{\partial u_{L'',1'}}{\partial \rho_1} + \frac{(p_{1'',R'} - p_{L'',1'})}{2} \left[\frac{\frac{2}{(\gamma+1)\rho_{1'}}}{p_{1'',R'} + \frac{\gamma-1}{\gamma+1} p_{L'',1'}} \right]^{-\frac{1}{2}} \right. \\
& \left. \times \left[\frac{\left(p_{1'',R'} + \frac{\gamma-1}{\gamma+1} p_{L'',1'}\right) \left(\frac{-2}{(\gamma+1)\rho_{1'}^2} \frac{\partial \rho_{1'}}{\partial \rho_1}\right) - \left(\frac{2}{(\gamma+1)\rho_{1'}}\right) \left(\frac{\gamma-1}{\gamma+1} \frac{\partial p_{L'',1'}}{\partial \rho_1}\right)}{\left(p_{1'',R'} + \frac{\gamma-1}{\gamma+1} p_{L'',1'}\right)^2} \right] \right\} \\
& \times \left\{ \frac{(p_{1'',R'} - p_{L'',1'})}{2} \left[\frac{\frac{2}{(\gamma+1)\rho_{1'}}}{p_{1'',R'} + \frac{\gamma-1}{\gamma+1} p_{L'',1'}} \right]^{-\frac{1}{2}} \left[\frac{\frac{2}{(\gamma+1)\rho_{1'}}}{\left(p_{1'',R'} + \frac{\gamma-1}{\gamma+1} p_{L'',1'}\right)^2} \right] - \left[\frac{\frac{2}{(\gamma+1)\rho_{1'}}}{p_{1'',R'} + \frac{\gamma-1}{\gamma+1} p_{L'',1'}} \right]^{\frac{1}{2}} \right. \\
& \left. - \left[\frac{\frac{2}{(\gamma+1)\rho_R}}{p_{1'',R'} + \frac{\gamma-1}{\gamma+1} p_R} \right]^{\frac{1}{2}} - \frac{(p_{1'',R'} - p_R)}{2} \left[\frac{\frac{2}{(\gamma+1)\rho_R}}{p_{1'',R'} + \frac{\gamma-1}{\gamma+1} p_R} \right]^{-\frac{1}{2}} \left[\frac{\frac{-2}{(\gamma+1)\rho_R}}{\left(p_{1'',R'} + \frac{\gamma-1}{\gamma+1} p_R\right)^2} \right] \right\}^{-1},
\end{aligned} \tag{2.12}$$

where $\frac{\partial \rho_{1'}}{\partial \rho_1}$ can be determined by differentiating Equation 2.8,

$$\frac{\partial \rho_{1'}}{\partial \rho_1} = \rho_1 \left[\frac{\left(\frac{\gamma-1}{\gamma+1}\frac{p_{L'',1'}}{p_1}+1\right)\frac{1}{p_1}\frac{\partial p_{L'',1'}}{\partial \rho_1} - \left(\frac{\gamma-1}{\gamma+1}+\frac{p_{L'',1'}}{p_1}\right)\frac{\gamma-1}{\gamma+1}\frac{1}{p_1}\frac{\partial p_{L'',1'}}{\partial \rho_1}}{\left(\frac{\gamma-1}{\gamma+1}\frac{p_{L'',1'}}{p_1}+1\right)^2} \right] + \left(\frac{\frac{\gamma-1}{\gamma+1}+\frac{p_{L'',1'}}{p_1}}{\frac{\gamma-1}{\gamma+1}\frac{p_{L'',1'}}{p_1}+1} \right), \quad (2.13)$$

and $\frac{\partial u_{L'',1'}}{\partial \rho_1}$ can be determined by differentiating Equation 2.9,

$$\begin{aligned}\frac{\partial u_{L'',1'}}{\partial \rho_1} = \frac{(p_{L'',1'}-p_1)}{4} & \left[\frac{\left(p_{L'',1'}+\frac{\gamma-1}{\gamma+1}p_1\right)\left(\frac{-2}{(\gamma+1)\rho_1^2}\right) - \frac{2}{(\gamma+1)\rho_1}\frac{\partial p_{L'',1'}}{\partial \rho_1}}{\left(p_{L'',1'}+\frac{\gamma-1}{\gamma+1}p_1\right)^2} \right] \left[\frac{\frac{2}{(\gamma+1)\rho_1}}{p_{L'',1'}+\frac{\gamma-1}{\gamma+1}p_1} \right]^{-\frac{1}{2}} \\ & + \frac{1}{2}\frac{\partial p_{L'',1'}}{\partial \rho_1} \left[\frac{\frac{2}{(\gamma+1)\rho_1}}{p_{L'',1'}+\frac{\gamma-1}{\gamma+1}p_1} \right]^{\frac{1}{2}} - \frac{(p_{L'',1'}-p_{L'})}{4} \left[\frac{\frac{2}{(\gamma+1)\rho_{L'}}}{p_{L'',1'}+\frac{\gamma-1}{\gamma+1}p_{L'}} \right]^{-\frac{1}{2}} \left[\frac{\frac{-2}{(\gamma+1)\rho_{L'}}\frac{\partial p_{L'',1'}}{\partial \rho_1}}{\left(p_{L'',1'}+\frac{\gamma-1}{\gamma+1}p_{L'}\right)^2} \right] \\ & - \frac{1}{2}\frac{\partial p_{L'',1'}}{\partial \rho_1} \left[\frac{\frac{2}{(\gamma+1)\rho_{L'}}}{p_{L'',1'}+\frac{\gamma-1}{\gamma+1}p_{L'}} \right]^{\frac{1}{2}}. \quad (2.14)\end{aligned}$$

Substitution of Equations 2.11, 2.13, and 2.14 into Equation 2.12 yields an equation for $\frac{\partial p_{1'',R'}}{\partial \rho_1}$ exclusively in terms of known quantities from which it is determined simply from substitution of a given intermediate material density that

$$\frac{\partial p_{1'',R'}}{\partial \rho_1} \begin{cases} < 0 & \text{when } \rho_L < \rho_1 < \sqrt{\rho_L \rho_R} \\ = 0 & \text{when } \rho_1 = \sqrt{\rho_L \rho_R} \\ > 0 & \text{when } \rho_1 > \sqrt{\rho_L \rho_R} < \rho_R \end{cases}.$$

Substituting for $\rho_i = \frac{I_i^2}{\gamma p_i}$ for $i = (L, 1, R)$,

$$\frac{\partial p_{1'',R'}}{\partial I_1} \begin{cases} < 0 & \text{when } I_L < I_1 < \sqrt{I_L I_R} \\ = 0 & \text{when } I_1 = \sqrt{I_L I_R} \\ > 0 & \text{when } I_1 > \sqrt{I_L I_R} < I_R \end{cases},$$

from which it is concluded that the impedance that maximizes the shock strengthening for a single intermediate material for a shock propagating into substances of increasing impedance ($I_L < I_1 < I_R$) is $I_1 = \sqrt{I_L I_R}$ for shocks approaching the weak and strong shock limit ($\rho_{L'}/\rho_L \to 1$

and $\rho_{L'}/\rho_L \rightarrow 4$, respectively, for $\gamma = 5/3$). Furthermore, Figure 2.8 demonstrates that shock strengthening cannot be achieved for intermediate material impedances outside of the range defined by the impedances of the left and right materials. Equation 2.12 can also be used to interrogate the slight downward shift (as much as 1.2% for the range of parameters in the present work) in the intermediate material impedance that maximizes the shock strengthening for incident shocks of moderate strength.

For the case of a shock propagating into materials of decreasing impedance ($I_L > I_1 > I_R$), the pressure behind the shock transmitted into the intermediate material $p_{L'',1'}$ is determined by finding the root of the equation,

$$\frac{2}{\gamma-1}\left(\frac{\gamma p_{L'}}{\rho_{L'}}\right)^{\frac{1}{2}}\left[\left(\frac{p_{L'',1'}}{p_{L'}}\right)^{\frac{\gamma-1}{2\gamma}}-1\right]+(p_{L'',1'}-p_1)\left[\frac{\frac{2}{(\gamma+1)\rho_1}}{p_{L'',1'}+\frac{\gamma-1}{\gamma+1}p_1}\right]^{\frac{1}{2}}-u_{L'}=0, \tag{2.15}$$

where $p_{L'}$ and $u_{L'}$ are still given by Equations 2.6 and 2.7, respectively. The pressure behind the shock transmitted into the right material is then determined by finding the root of the equation,

$$\frac{2}{\gamma-1}\left(\frac{\gamma p_{L'',1'}}{\rho_{1'}}\right)^{\frac{1}{2}}\left[\left(\frac{p_{1'',R'}}{p_{L'',1'}}\right)^{\frac{\gamma-1}{2\gamma}}-1\right]+(p_{1'',R'}-p_R)\left[\frac{\frac{2}{(\gamma+1)\rho_R}}{p_{1'',R'}+\frac{\gamma-1}{\gamma+1}p_R}\right]^{\frac{1}{2}}-u_{L'',1'}=0, \tag{2.16}$$

where $\rho_{1'}$ is still given by Equation 2.8, but $u_{L'',1'}$ is now given by

$$u_{L'',1'}=\frac{u_{L'}}{2}+\frac{1}{2}(p_{L'',1'}-p_1)\left[\frac{\frac{2}{(\gamma+1)\rho_1}}{p_{L'',1'}+\frac{\gamma-1}{\gamma+1}p_1}\right]^{\frac{1}{2}}-\frac{1}{\gamma-1}\left(\frac{\gamma p_{L'}}{\rho_{L'}}\right)^{\frac{1}{2}}\left[\left(\frac{p_{L'',1'}}{p_{L'}}\right)^{\frac{\gamma-1}{2\gamma}}-1\right]. \tag{2.17}$$

The analysis then proceeds as for the increasing-impedance case, where Equations 2.15 and 2.16 are differentiated with respect to the density of the intermediate material, and substitutions are made to express $\frac{\partial p_{1'',R'}}{\partial \rho_1}$ explicitly in terms of known quantities. The same logic is then utilized to conclude that the intermediate material impedance that maximizes the shock strengthening is $I_1 = \sqrt{I_L I_R}$ for shocks approaching either the weak or strong shock limit.

CHAPTER 3

Shock Compression of Helium to 3.5 Mbar

This chapter is adapted from M. J. Wadas et al., Shock compression of helium to 3.5 Mbar, *In preparation for Physical Review Letters* [278].

3.1 Abstract

Hugoniot data are obtained for helium in excess of 3.5 Mbar. Helium is precompressed to 2.8-3.4 times its ambient-pressure cryogenic liquid density in a diamond anvil cell prior to laser-driven shock compression delivering 3.9-5.5 kJ of energy at the OMEGA laser facility. The data show significant reflectivity and an increase in compressibility, well predicted by first-principles modeling, likely caused by the onset of continuous ionization. The novel data serve as important benchmarks for density functional theory and models for Jovian interiors and white dwarf atmospheres.

3.2 Introduction

Helium is the second most abundant element in the universe, and characterizing its behavior in high-pressure environments is essential for our understanding of Jovian interiors and white dwarfs [38, 123, 159, 171, 172, 236]. In particular, the metallization of fluid helium and its miscibility with hydrogen at megabar-level pressures may have dramatic consequences on the dynamics of the convective barrier thought to exist in the interior of Jupiter separating helium-depleted and helium-rich layers [29, 172, 250, 255, 305]. Competing models predict considerably different band-gap closures occurring at ~$2\,\mathrm{g\,cm^{-3}}$ [36] and ~$10\,\mathrm{g\,cm^{-3}}$ [249], with the latter suggesting that only insulating helium exists within Jupiter, motivating the need for additional experimental data. In addition, the helium-rich atmospheres of white dwarfs, while comprising only a small fraction of the overall mass, are the primary source of observational data constraining models of interior structure and thermal evolution, which are highly sensitive to ionization behavior [15, 101, 124, 214]. Finally, helium bubbles are expected to form on the highly irradiated walls of fusion reactors [57, 205], and its ionization behavior is important in hohlraum-laser interactions during inertial confinement fusion experiments [2, 17], motivating the need to understand the response of helium to high pressures in both magnetically and inertially confined fusion.

Early experimental studies utilized diamond anvil cell (DAC) devices to statically compress helium up to 240 kbar and examined the pressure dependence of the refractive index and melting line [143, 268, 276], while experiments using gas-gun facilities to dynamically compress helium with shock waves documented the pressure-density shock equation of state up to 560 kbar [196]. The maximum projectile velocity in such experiments [179], however, limits the pressures that can be achieved. Furthermore, achievable thermodynamic states are constrained to the material shock Hugoniot anchored to ambient conditions and therefore lack independent control of pressure and temperature. These challenges are ameliorated through the combination of static and dynamic techniques, where a DAC is used for tailored precompression followed by laser-driven shock compression [105], enabling access to conditions relevant to planetary interiors and white dwarf atmospheres [30, 36, 75].

In addition to the aforementioned physics applications, the simplicity of helium makes it an important benchmark for quantum mechanical modelling techniques such as density functional theory (DFT), molecular dynamics (MD), and path integral Monte-Carlo (PIMC) calculations, especially at the megabar-level pressures of the notoriously challenging warm dense matter regime [72]. In particular, its monoatomic nature makes helium, as opposed to hydrogen, the simplest element for which pressure- or temperature-induced ionization physics can be isolated from the effects of molecular dissociation [13, 88, 119, 138, 167, 168, 169, 181, 213, 226, 293]. While past studies have shown evidence for the ionization of helium, it remains unclear whether the ionization is abrupt (i.e., first-order) or continuous and, if continuous, the range over which ionization occurs [80, 215, 271]. Further obfuscating our understanding are discrepancies in the pressure response predicted from existing models [145, 170, 188, 197, 235] beyond approximately 1 Mbar for shocked helium initially precompressed near 10 kbar, a regime where experimental data is limited to only four past experiments [36, 75]. Even after reanalysis of these experiments with improved quartz standard models [30] discrepancies with existing models [145, 188, 197], including the First-Principles Equation of State (FPEOS) [170], remain, motivating the need for experimental data to elucidate the behavior of helium and discriminate between existing models.

This work presents data from four experiments at the OMEGA laser facility compressing helium in a DAC from initial static pressures of 7.6-12.0 kbar (~3 times its cryogenic liquid density at ambient pressures) to 2.7-3.6 Mbar, extending the range of experimental data to a novel regime where predictions from existing equation of state (EOS) models diverge [145, 170, 188, 197, 235]. The record pressures were achieved by designing the DAC such that the desired precompressed state could be reached with the thinnest front diamond window possible (200 µm), efficiently coupling the pressure from the 1 ns-optimized laser drive to the sample [279]. The data show increases in reflectivity consistent with continuous ionization, which is also reflected in the increased compressibility. The pressure and temperature response is well captured by FPEOS, resolving past discrepancies [30, 36, 75] and enabling critical insight for the behavior of warm dense helium in Jovian interiors, white dwarf atmospheres, and fusion energy.

3.3 Target Preparation

In each experiment, supercritical fluid helium is compressed in a DAC with a back sapphire window to densities between 0.350-0.422 g cm^{-3} at room temperature using a gas loading system and a ruby for pressure characterization [30, 105]. In order of increasing precompression, the experiments are referred to as S74727, S70906, S74722, and S72497 throughout this work. The DAC setup is similar to those employed by [29, 105, 176] and is shown schematically in Figure 3.1a. A quartz impedance standard sits at the base of the diamond, and a thin layer of gold shields the DAC from radiation from the laser-driven side of the target, preventing preheat. Additional details about target preparation and the characterization of the initial state are provided in Section 3.6. Ten or twelve lasers are used to generate a 1 ns, 351 nm-wavelength square pulse delivering between 3.9 and 5.5 kJ of energy to the plastic ablator, driving a shock wave into the DAC which subsequently passes into the helium sample through the quartz standard, as shown schematically in Figure 3.1b.

3.4 Results

The reflective, self-emitting shock front is visualized using the line-imaging velocity interferometer for any reflector (VISAR) system at the OMEGA Laser Facility [35, 37], generating the raw data shown in Figure 3.1c, where shifts in the fringes are proportional to changes in shock velocity, U_s. As the shock wave passes from the quartz to the helium, it sets the interface into motion at velocity U_p, and the difference in shock impedance causes the shock wave to instantaneously change velocity, resulting in a discontinuous shift in the VISAR fringes. The velocity ambiguity introduced by this discontinuous shift is resolved through the use of two VISAR channels with different fringe sensitivities controlled by different etalon thicknesses (16.0829 km s^{-1} per fringe for the 3.096 mm etalon and 6.9065 km s^{-1} per fringe for the 7.2095 mm etalon). Any remaining ambiguity is resolved by matching the time-integrated shock velocity through the quartz layer to its known thickness. The effects of precompression on the quartz [85] and helium [63] indices of refraction are considered for an accurate velocity measurement.

Because the particle velocity and pressure on either side of the shocked interface between the quartz and helium are equal, the known response of the quartz standard to the high pressure loading

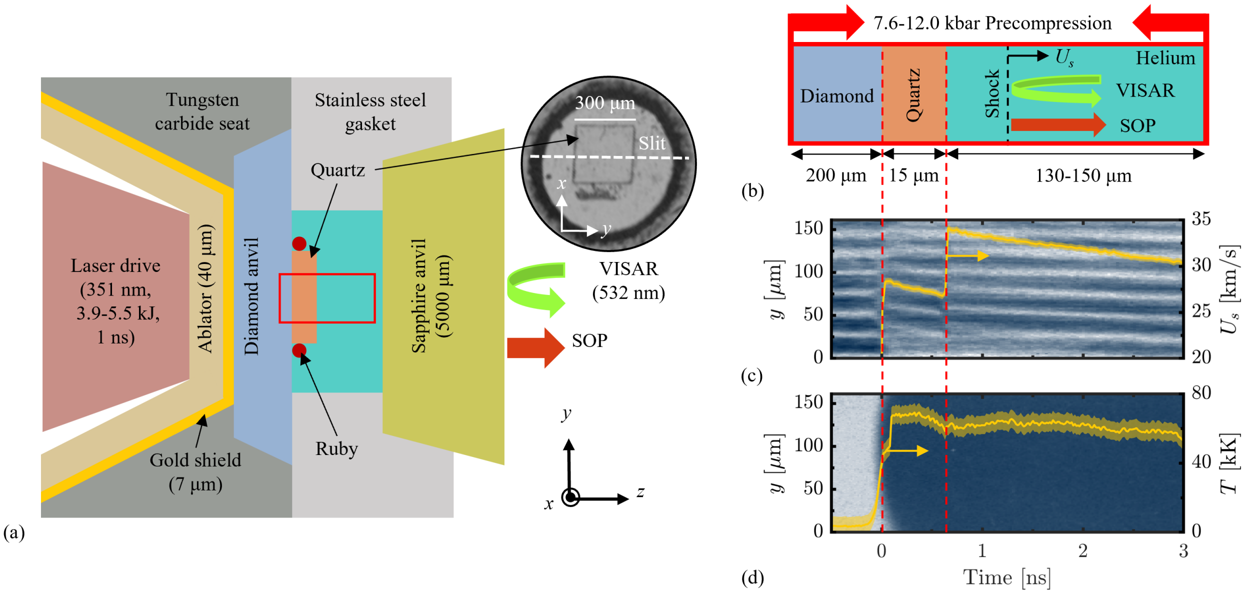

Figure 3.1: (a) A schematic showing the geometry of the DAC used in the present work, including a micrograph (right) of the pressure chamber showing the quartz reference plate and the projection of the VISAR streak camera entrance slit onto the target (white-dashed line) for S74722. (b) A close-up of the schematic in (a) detailing the sample geometry, precompression, and shock transit. (c) The VISAR trace with overlaid shock velocity (yellow line) from S74722. The transition of the shock between materials is clearly seen as a discontinuous jump in the shock velocity. (d) The SOP data with overlaid temperature (yellow line) from S74722. The slight increase in the signal intensity immediately following the breakout of the shock into the helium is likely caused by space-time distortions and nonlinearity in the diagnostic sweep rate [78, 173]. In (c,d) the shaded yellow region indicates measurement error (see Section 3.6).

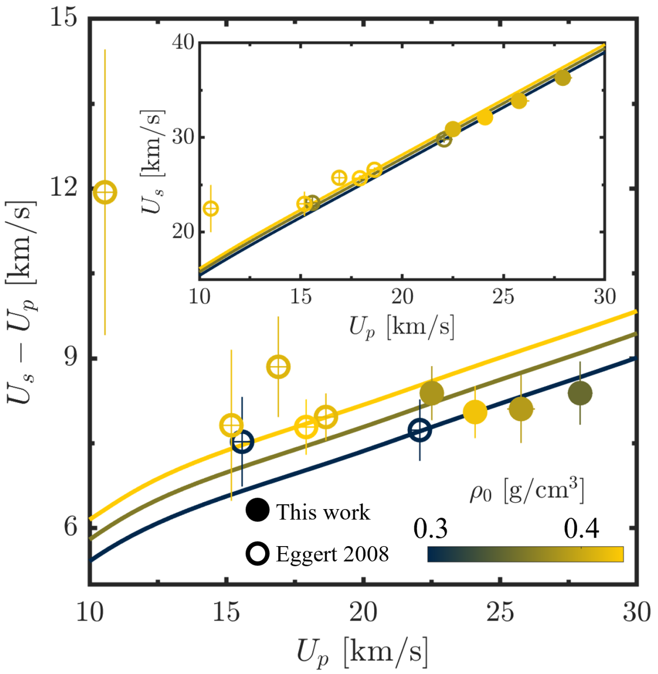

Figure 3.2: The shock versus particle velocity in helium for the present work (closed symbols) and past work (open symbols) [30, 36, 75]. Color indicates the precompressed density. Several FPEOS Hugoniot curves [170] spanning the range of initial densities in the experimental data are shown.

can be used to determine the state in the shocked helium using standard impedance matching techniques, detailed in Section 3.6. The key measurement enabling the state calculation is the velocity of the shock in quartz and helium immediately before and after, respectively, the shock breaks out into the helium. The agreement between the two VISAR measurements before and following the break out is used to determine the measurement error, as described in the Section 3.6. Figure 3.2 shows the shock velocity in helium versus the particle velocity for the new data and existing data from [30, 36, 75] exploring shocked helium precompressed between 0.51 and 1.25 GPa, overlapping the range explored in the present work, compared to predictions from FPEOS, an EOS database that combines results from PIMC and DFT-MD simulations [170]. The overall agreement is good, with experimental errors smaller than past data [30, 36, 75].

The calculated velocities in quartz and helium are used to determine the pressure and density behind the shock in the helium [30, 121], as shown in Figure 3.3, again alongside past data and predictions from FPEOS. The data indicate pressures near and in excess of 3.5 Mbar and again show good agreement with FPEOS, as seen in the upper-right panel. The three highest-pressure experiments suggest a slightly greater compressibility than the prediction of FPEOS, but still fall within, or very nearly within, the experimental error bars. The lower-right panel of Figure 3.3 shows the predicted Hugoniot curve for S74722 from additional equation of state models including

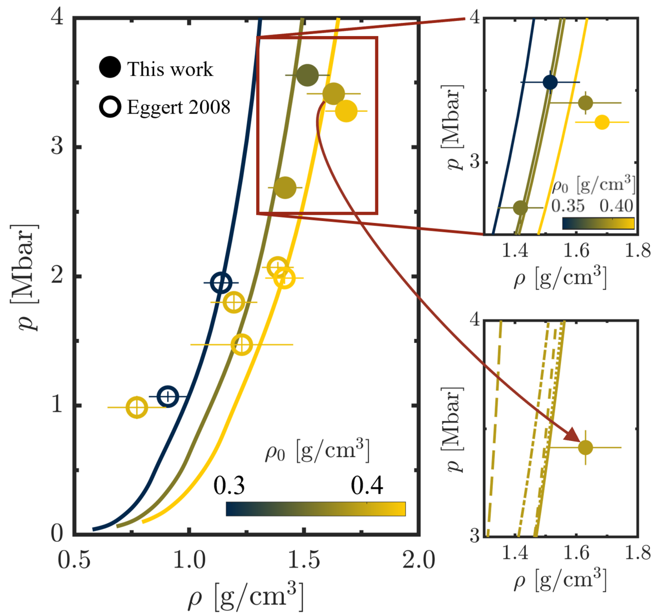

Figure 3.3: Left: The pressure versus density in helium for the present work (closed symbols) and past work (open symbols) [30, 36, 75]. Color indicates the precompressed density. Three FPEOS Hugoniot curves [170] spanning the range of initial densities in the experimental data are shown. Upper right: close-up view of the new data with an expanded color scale. Bottom right: S74722 (ρ_0 = 0.390 g/cm^3) with Hugoniot curves from LEOS20 (long-dashed) [188], SESAME3764 (dash-dotted), SESAME3761 (short-dashed) [145], REOS (dotted) [197], and FPEOS (solid) [170].

LEOS20 and SESAME, EOS tables from Lawrence Livermore and Los Alamos National Laboratories, respectively, that use a modified Thomas-Fermi model constrained to experimental data [145, 188], and REOS, an MD-based EOS that incorporates chemical modeling from Universität Rostock [197]. The prediction of these EOS models for S74727, S70906, and S72497 show similar trends. Of these models, FPEOS is the most compressible and therefore provides the most accurate prediction [235]. The greater compressibility may be related to an increase in the internal molecular degrees of freedom due to the onset of ionization [167, 168, 169, 170], which is further elucidated by reflectivity measurements discussed next.

While the phase of the VISAR signal enables a velocity measurement, the amplitude encodes information that can be used to determine the shock reflectivity in helium, where the signal in quartz again acts as a measurement standard [97]. Accounting for changes in the index of refraction resulting from precompression [30, 175], we calculate shock reflectivity in helium in excess of 30% (data for each experiment and a description of the error analysis are provided in Section 3.6), as indicated by the size of the data points in Figure 3.4. The measured reflectivity exceeds that of past experiments [36, 75] by up to 75%, consistent with the enhanced compressibility observed in Figure 3.3 and the onset of ionization.

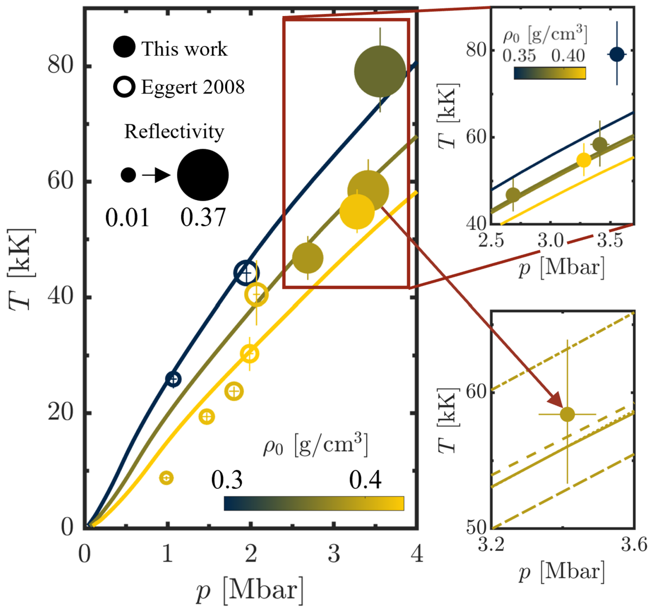

Figure 3.4: Left: The temperature versus pressure in helium for the present work (closed symbols) and past work (open symbols) [30, 36, 75]. Color indicates the precompressed density, while the symbol size indicates reflectivity. Three FPEOS Hugoniot curves [170] spanning the range of initial densities in the experimental data are shown. Upper right: close-up view of the new data with an expanded color scale. Bottom right: S74722 (ρ_0 = 0.390 g/cm^3) with Hugoniot curves from LEOS20 (long-dashed) [188], SESAME3764 (dash-dotted), SESAME3761 (short-dashed) [145], REOS (dotted) [197], and FPEOS (solid) [170].

Figure 3.4 also shows the temperature behind the shock in helium inferred from streaked optical pyrometry (SOP) data, an example of which is shown in Figure 3.1d. The self-emission of the shock front [173] enables a measurement of the spectral radiance, which we observe to be similar in the quartz and helium. Combined with the measured reflectivity, the spectral radiance can be used to infer temperature using the grey-body radiation approximation, with details provided in Section 3.6. In the present experiments, the shock speed in quartz exceeds the range over which we have qualified quartz as a shock temperature standard for precompressed targets. However, because the precompression of the targets for the present experiments is relatively low, we utilize a temperature model for quartz that is experimentally validated for uncompressed targets at the shock velocities obtained [97, 175]. Ongoing work aims to extend the capabilities of precompressed quartz as a temperature standard to shock velocities in excess of 30 km s^{-1} [58], but presently, we estimate the effect of precompression with a correction derived from differences in our existing models that either consider or neglect precompression at the greatest experimentally validated shock velocities (see Section 3.6).

The agreement between the prediction of FPEOS and the data is generally good, as seen in the upper right panel of Figure 3.4. Our temperature measurement for S74727 may be artificially high due to a possible overprediction of the reflectivity from our experimental fit to the present and preexisting data [30, 36, 75] (see Section 3.6). As in Figure 3.3, the lower-right panel also shows predictions from LEOS20, SESAME3764, SESAME3761, and REOS for S74722. The temperature measurements further enable a prediction of conductivity according to the Drude-like model of [249], giving 264, 90, 143, and 123 kS m^{-1} for S74727, S70906, S74722, and S72497, respectively, exceeding previous measurements by up to a factor of 2 and providing further evidence of the increasing ionization in the present pressure regime.

3.5 Conclusion

Four experiments achieved a novel state in warm, dense fluid helium that shows evidence of continuous ionization [168, 169, 214, 215], with measured reflectivity in excess of 30% over pressures ranging from 2.7 to 3.6 Mbar. The increase in compressibility likely caused by increasing internal energy from the onset of ionization [167] is well captured by FPEOS, affirming the ability of first-principles techniques like PIMC and DFT-MD to predict the EOS of warm dense helium in a regime where ionization becomes important. These data provide an important benchmark for models of the thermal evolution and interior structure of Jupiter, atmospheric profiles of white dwarfs, and the behavior of fusion products. Additional experiments utilizing greater precompression are ongoing to further probe the insulator-to-metal transition.

This work is supported by the Lawrence Livermore National Laboratory under Subcontract No.

B632749 and the U. S. Department of Energy (DOE) as part of the Stewardship Science Graduate Fellowship Program under Grant No. De-NA0003960. Part of this work was performed under the auspices of the US DOE by Lawrence Livermore National Laboratory (LLNL) under contract DE-AC52-07NA27344 and supported by LLNL LDRD Program No. 19-ERD-031. VISAR and SOP data in this work were analyzed with LLNL AnalyzeVISAR code.

3.6 Supplemental Material

This supplemental material provides additional detail regarding target preparation and measurement analysis.

3.6.1 Preparation of High-Pressure Anvil Cells

Each of the experiments examined shocked helium loaded in a diamond-sapphire anvil cell, see Figure 3.1a in the main text. The portion of the cell compressed to 0.76-1.20 kbar consists of layers of diamond (200 µm), quartz (15-17 µm), helium (100-180 µm), and sapphire (500 µm). Adjacent to the quartz standard are ruby spheres 5-10 µm in diameter used for pressure characterization [41]. The laser-irradiated side of the target (i.e., the diamond side) is electroplated with 3-7 µm of gold to shield the sample from x-ray preheat. Immediately upstream of the shield is the 40 µm plastic ablator. The diamond is fixed in place by a tungsten-carbide seat, while a stainless steel gasket surrounds the remainder of the compressed portion of the target. The sapphire and quartz utilize an anti-reflective coating to minimize spurious signals from being recorded on the VISAR streak camera.

The conditions in the compressed anvil cell are summarized in Table 3.1. The pressure in the anvil cells was determined using the luminescence spectra of the ruby pressure gauges to within 0.3 kbar [41]. The temperature was determined with negligible error compared to that of the pressure. The density and corresponding uncertainty of the quartz standard were determined using coefficients from [33] and the Murnaghan equation of state, and the refractive index and corresponding uncertainty were characterized according to [85] for the VISAR probe wavelength of 532 nm [30]. The density and corresponding uncertainty of the helium were determined according to the equation of state from [268], and the refractive index and corresponding uncertainty were characterized according to [63].

3.6.2 Impedance Matching and Velocity Measurement

The pressure and density downstream of the shock immediately after it passes into the helium can be determined with standard impedance matching. We use a model for the shock Hugoniot in the

Table 3.1: The precompressed conditions for each of the experiments performed in this work. The error on the last reported digit is given in parenthesis, e.g., 2.701(3) is the same as 2.701 ± 0.003.

Shot ID	p_0 [kbar]	T_0 [K]	$\rho_{0,q}$ [g cm^{-3}]	$n_{0,q}$ $[ND]$	$\rho_{0,He}$ [g cm^{-3}]	$n_{0,He}$ $[ND]$
74727	7.6 (3)	298	2.701 (3)	1.5544 (4)	0.351 (6)	1.070 (1)
70906	9.5 (3)	296	2.713 (3)	1.5562 (4)	0.385 (5)	1.077 (1)
74722	9.8 (3)	298	2.715 (3)	1.5565 (4)	0.390 (5)	1.078 (1)
72497	12.0 (3)	296	2.729 (3)	1.5586 (5)	0.422 (4)	1.084 (1)

precompressed quartz [30] and the measured shock velocity to determine the state in the quartz downstream of the shock immediately prior to breakout. The intersection of the quartz isentrope [62], representing the release wave emerging from the breakout interaction, passing through this state and the equation from the Rankine-Hugoniot equations representing momentum conservation for the shock in helium, which requires a measurement of the shock velocity in helium, gives the pressure and density in the helium.

With the initial states prior to shock interaction characterized, the key measurements enabling the impedance-matching technique are the shock velocities in the quartz standard and the helium immediately prior to and after the breakout event, respectively, which are obtained using the velocity interferometry system for any reflector (VISAR) on the OMEGA laser [35]. Shifts of the VISAR fringes (see Figure 3.1c in the main text) are proportional to changes in the vacuum velocity of the reflecting shock wave. For each experiment, two VISAR measurements are taken, each with a different fringe sensitivity to velocity shifts, which is determined by the thickness of the etalon. Two VISAR measurements, where the ratio of the fringe sensitivities is a rational number, are required to resolve the ambiguity introduced by the instantaneous change in the shock velocity as it passes from the quartz standard to the helium sample, which causes a discontinuous jump in the fringes of the VISAR measurement. For the present experiments, the etalon thickensses are 7.2095 mm and 3.096 mm, corresponding to sensitivities of 6.9065 km s^{-1} and 16.0829 km s^{-1} per fringe, respectively. Resolving the fringe discontinuity yields solutions for the shock velocity, modulo the fringe sensitivity ratio (3:7 in the present work). This ambiguity is then resolved by verifying that the integrated shock velocity through the quartz is consistent with its known thickness. The shock velocity in the quartz and the helium are then determined by fitting lines to both velocity histories leading up to and following shock breakout, respectively, and extrapolating to the breakout time. The final velocity is then determined as the average between the velocity for each history weighted by the inverse of the fringe sensitivity and is shown for each experiment in Table 3.2.

The error in the velocity measurements is taken to be the L2 norm between the velocity histories from each VISAR measurement in both the quartz and helium according to

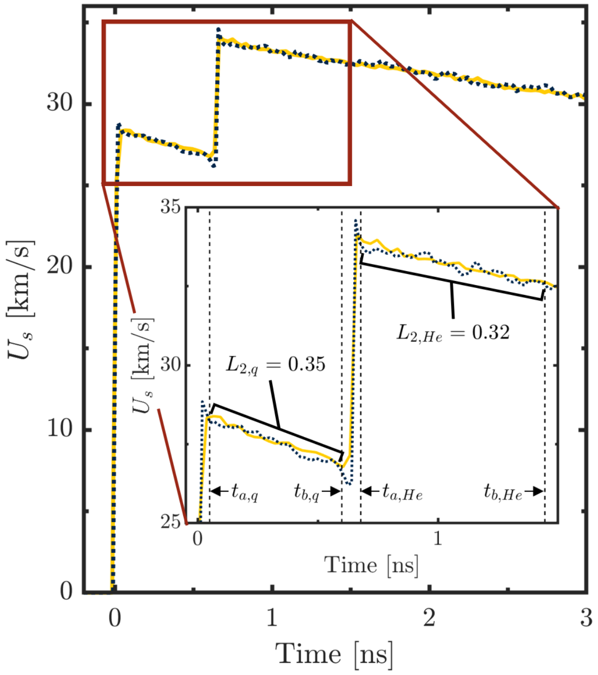

Figure 3.5: The velocity histories for the 7.2095 mm etalon (solid yellow) and 3.096 mm etalon (dotted blue) for shot 74722. Vertical dashed lines in the inset indicate the bounds for the integral in Equation 3.1 used to calculate the error shown.

$$L_{2,m} = \left[\frac{1}{t_{b,m} - t_{a,m}} \int_{t_{a,m}}^{t_{b,m}} \left(U_{s,et_1} - U_{s,et_2} \right)^2 dt \right]^{1/2}. \tag{3.1}$$

Equation 3.1 is therefore a measure of the average amount by which the velocity histories from both VISAR measurements with different etalons U_{s,et_1} and U_{s,et_2} differ over the time interval $t_{a,m}$ to $t_{b,m}$, where the subscript m refers to the material, quartz (q) or helium (He). Figure 3.5 shows the vacuum velocity histories from S74722 along with the L2 norm in both the quartz and helium calculated according to Equation 3.1. Error from the refractive index (see Table 3.1) is propagated into the velocity measurement by multiplication with the calculated breakout velocity. The final error in the velocity measurement is the sum of the L2 norm and the error from the refractive index and is given in Table 3.2.

3.6.3 Error Propagation and Pressure and Density Measurements

Error from measurements of the precompressed state in helium (density and pressure) and the shock velocities in both the quartz standard and the helium are propagated into the impedance matching calculation used to determine the density and pressure behind the shock as it breaks out

Table 3.2: The energy delivered to the target and the calculated shock velicities for the present work.

Shot ID	E [J]	$U_{s,q}$ [km s^{-1}]	$U_{s,He}$ [km s^{-1}]
74727	5460	28.04 ± 0.31	36.31 ± 0.36
70906	3923	23.94 ± 0.26	30.89 ± 0.37
74722	4986	26.62 ± 0.38	33.87 ± 0.35
72497	4649	25.49 ± 0.26	32.14 ± 0.35

Table 3.3: The energy delivered to the target and the calculated density and pressure in helium.

Shot ID	E [J]	ρ [g cm^{-3}]	p [Mbar]
74727	5460	1.515 ± 0.097	3.556 ± 0.082
70906	3923	1.418 ± 0.075	2.686 ± 0.059
74722	4986	1.630 ± 0.118	3.413 ± 0.081
72497	4649	1.684 ± 0.092	3.279 ± 0.053

into the helium. The Monte-Carlo methodology detailed in Ref. [120] is utilized with the model for the precompressed shock Hugoniot curve in quartz [30], the model for the quartz release [62], and the condition from the Rankine-Hugoniot equations representing momentum conservation to determine the error in density and pressure for the present work. The results of the impedance matching analysis and error calculation for the four experiments are presented in Table 3.3.

3.6.4 Reflectivity and Temperature Analysis

The reflectivity in helium R_{He} is determined by comparing the intensity of the VISAR signal in the quartz I_q and helium I_{He}, where the reflectivity of the shock in the precompressed quartz standard is a known function of its velocity $R_q(U_{s,q})$ [30]. Specifically, the reflectivity in helium is given by $R_{He} = R_q(U_{s,q})I_{He}/I_q$. As in the quartz standard, the reflectivity in helium is a function of the shock velocity $U_{s,He}$ as shown in Figure 3.6. A four-parameter Hill equation, with the constraint that the reflectivity must be between 0 and 100%, is then fit to the combined data, which includes the re-analyzed past data detailed in Chapter 3 [30], from which the reflectivity is extracted. The error reported in Table 3.4 is the sum of the error propagated from the velocity measurement and the standard deviation of the data from each experiment from the combined fit.

The temperature in helium is determined by a comparison of the thermal emission of the shock front in quartz and helium measured by the streaked optical pyrometry (SOP) system. With the reflectivity now known, the temperature T is related to the spectral radiance I using a grey-body

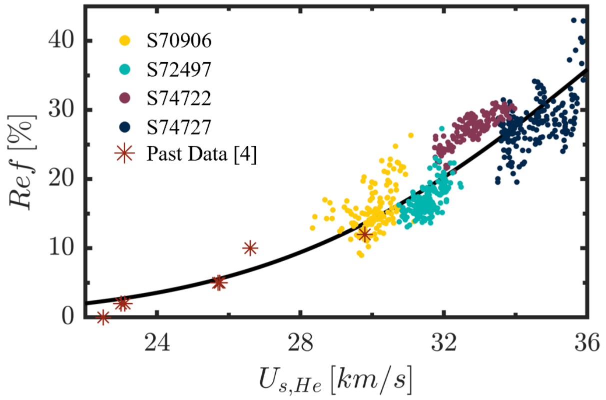

Figure 3.6: Reflectivity versus shock velocity in helium for S70906 (yellow), S72497 (teal), S74722 (purple), S74727 (blue), and past data (red stars) [30] with a combined Hill fit (black line).

approximation as

$$T = T_0\{\ln\left[(1 - R)A/I + 1\right]\}^{-1}, \tag{3.2}$$

where the calibration parameter T_0 is a function of the system peak sensitivity ($T_0 = 1.9$ eV for the present work) and A is a system calibration constant. Because the temperature in the helium is determined relative to the temperature in the quartz standard, the calibration parameter A drops out giving

$$T_{He} = T_0\left\{\ln\left[(e^{T_0/T_q(U_{s,q})} - 1)I_q^*/I_{He}^* + 1\right]\right\}^{-1}, \tag{3.3}$$

where $I^* = I_{ADU}/(1 - R)$ and I_{ADU} represents the analog-to-digital counts of the measured SOP signal. The temperature in the quartz standard as a function of the shock velocity $T_q(U_{s,q})$ is therefore required to determine the temperature in the helium.

While efforts are currently underway to extend the characterization of quartz as a thermal standard [58], the shock velocities in the present work exceed the velocities of available data for which corrections for the effects of precompression have been determined [30]. Given that the precompression for the present work does not exceed 1.2 GPa, we utilize a model for the quartz temperature that neglects precompression but is otherwise valid for the present range of shock velocities [175]. Following [30], we estimate a correction for the effect of precompression from the ratio of quartz temperatures given by models that either neglect or consider precompression,

$$\frac{T_{q,cor}}{T_{q,uncor}} = 1 - \frac{-14786 + 1555U_{s,q}}{1860 + 3.56U_{s,q}^{3.036}}\left(\rho_{0,q} - 2.65\right), \tag{3.4}$$

where $U_{s,q} = 20\,\mathrm{km\,s^{-1}}$ is the maximum velocity for which both models are experimentally validated

Table 3.4: The energy delivered to the target and the calculated reflectivity and temperature in helium.

Shot ID	E [J]	R_{He} [%]	T [kK]
74727	5460	37.24 +5.18, -5.17	79.0 +7.6, -7.1
70906	3923	16.72 +5.06, -5.02	46.9 +3.8, -3.8
74722	4986	27.11 +5.69, -5.66	58.5 +5.5, -5.1
72497	4649	20.75 +3.66, -3.62	54.8 +3.9, -3.7

and densities are expressed in g cm^{-3}. Then, from Equation 3.3, the corrected temperature in helium is given by

$$\frac{T_{He,cor}}{T_{He,uncor}} = \frac{\ln\left[(e^{T_0/T_{q,uncor}} - 1)I_q^*/I_{He}^* + 1\right]}{\ln\left[(e^{T_0/T_{q,cor}} - 1)I_q^*/I_{He}^* + 1\right]}. \tag{3.5}$$

The corrected temperature is reported in Table 3.4, and the error is the sum of the standard deviation of the temperature from a moving average of the data with a window of 0.4 ns and the error propagated from the reflectivity measurement.

3.6.5 Correction for Ghost-Fringe Reflections

Despite the use of anti-reflective coatings, the VISAR signal is polluted with reflection from the stationary diamond-sapphire interface as the shock breaks out of the quartz-helium interface, causing "ghost fringes." To remove the influence of the stationary interface reflection, a fast-Fourier transform is performed in a temporal region of the VISAR signal after the unsupported shock front has weakened to the point of vanishing reflectivity, i.e., a region consisting exclusively of ghost fringes. The amplitude of the ghost fringes, assumed to be constant throughout the experiment, is then determined and subtracted from the signal, effectively removing the influence of the stationary reflection from the impedance matching analysis.

CHAPTER 4

Interactions of Two Bubbles Along a Gaseous Interface Undergoing the Richtmyer-Meshkov Instability in Two Dimensions

This chapter is adapted from M. J. Wadas and E. Johnsen, Interactions of two bubbles along a gaseous interface undergoing the Richtmyer-Meshkov instability in two dimensions, *Physica D: Nonlinear Phenomena*, 409:132489, 2020 [280].

4.1 Abstract

The vorticity-driven interactions involving bubbles and spikes along a shock-accelerated interface significantly affect the dynamics of the flow and likely contribute to an eventual turbulent transition. In this study, the interaction of two adjacent bubbles of different sizes undergoing the Richtmyer-Meshkov process is investigated numerically in two dimensions. In particular, we compare two-bubble configurations with different initial amplitude ratios and wavelength ratios. Simulations are performed using an in-house, high-order accurate discontinuous Galerkin code solving the Euler equations for a shock-accelerated interface initially perturbed with a periodic array of alternating sinusoids of different sizes. Two types of departures from existing bubble-merging models are observed, caused by a vorticity imbalance on the sides of the bubbles leading to spikes that either diverge or converge beneath the larger bubble, thus resulting in the generation of vortex dipoles escaping the confines of the mixing region or in the reacceleration of the larger bubbles. A vorticity-based criterion for predicting the generation of vortex dipoles and the reacceleration of larger bubbles from the initial conditions is developed.

4.2 Introduction

The Richtmyer-Meshkov instability (RMI) occurs when a perturbed interface separating fluids of different densities is accelerated by a shock wave [162, 220]. After the shock wave traverses the interface, the fluids begin to interpenetrate, forming an alternating configuration of bubbles of relatively light fluid rising into the heavy fluid and spikes of relatively heavy fluid falling into the light fluid. Bubbles and spikes interact with each other such that the mixing region may eventually transition to a state of turbulence. The mixing induced by this process has important consequences in astrophysics and fusion research. In particular, this interpenetration of heavy and light fluids is partially responsible for the ejection of heavy elements from the centers of stars into the surrounding galaxy during core-collapse supernovae [89, 110] and for decreasing the compression required for a sustained nuclear fusion reaction in inertial confinement fusion experiments [17, 28].

Significant effort has been devoted to understanding the growth of the RMI. Richtmyer first performed the linear analysis suggesting, and later validated by the experiments of Meshkov, that the amplitude of a shock-accelerated perturbation initially increases linearly in time [162, 220]. Models for the nonlinear growth phase have been developed based on potential flow theory and simple force balance arguments [95, 133, 165, 166, 253]. Concurrent with the development of these models was experimental work leveraging a wide variety of platforms including shock tubes, laser facilities, and linear electric motors [66, 68, 275].

While the single-mode RMI is relatively well understood, prediction of the evolution of arbitrary interfacial perturbations, i.e., perturbations consisting of the superposition of many modes, is more challenging. As in the single-mode case, theoretical [5, 95, 253] and experimental [127, 128, 154, 228] studies considered the linear and nonlinear behavior of multimode interfaces. Beyond the nonlinear growth phase, experimental [218, 275, 284] and theoretical [5, 76, 207, 253] studies are additionally aimed at quantifying the asymptotic behavior of the mixing region. In addition, large-scale numerical simulations have generated an enormous amount of data that can be used to investigate the physics of late-time RMI-induced mixing [203, 204, 263, 265, 296]. The modal interactions that are the focus of such studies can cause the reacceleration of bubbles, and vortex dipoles have been observed to escape the mixing region [66, 204, 218, 263, 265, 284, 296]. These phenomena are prevalent in the context of but not unique to the RMI; studies of the Rayleigh-Taylor instability also show evidence of similar escaping dipoles and reaccelerating bubbles [66, 67, 217, 294, 296]. These features can lead to enhanced mixing and are likely related to the transition to a turbulent state, which remains an active area of research [263, 265, 307, 308].

A number of investigations of multimode instability growth focus on interfaces initially composed of superimposed sine waves (i.e., Fourier modes) [127, 128, 154, 204, 265]. However, another class of studies considers interfaces composed of adjacent bubbles initialized as neighbor-

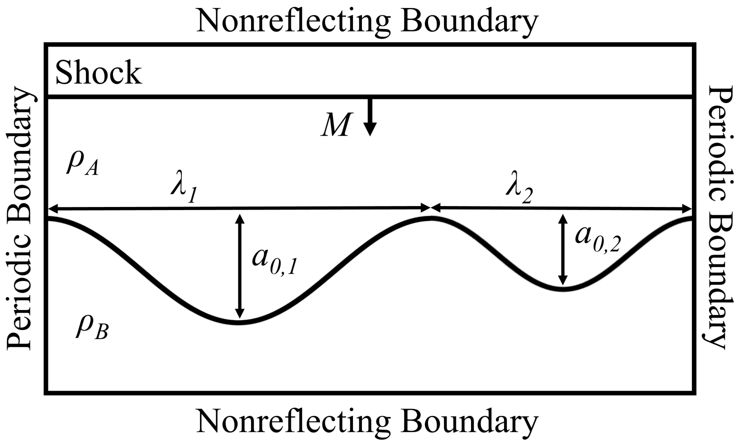

Figure 4.1: The computational setup for the simulations performed.

ing sinusoids of different period and amplitude and investigates competition between these bubbles [5, 95, 228]. In the present study we focus on the latter to enable an accurate comparison to the experiments of Ref. [228].

Our objective is to numerically investigate the generation of vortex dipoles that escape the confines of the mixing region, as well as the reacceleration of bubbles, for interfaces subject to the RMI. Our hypothesis is that the escape of a vortex dipole from the interface and the reacceleration of large bubbles can be predicted from the initial vorticity associated with the bubbles. To investigate these dynamics, we solve the two-dimensional multispecies Euler equations.

The chapter is organized as follows. Section 4.3 describes the numerical method and computational setup. Section 4.4 presents the results of the numerical simulations, alongside predictions from existing bubble merging models [5, 95], and elaborates on a criterion for differentiating between the two types of interface growth observed. Results are summarized and conclusions drawn in Section 4.5.

4.3 Methods and Problem Setup

Numerical simulations are performed using our in-house discontinuous Galerkin interface- and shock-capturing code to solve the two-dimensional multispecies Euler equations [59, 60]. The base spatial scheme is fifth-order accurate ($p = 2$) with a Roe solver and hierarchical limiting applied at discontinuities (shocks and interfaces) only. Fourth-order explicit Runge-Kutta is used for time marching.

As illustrated in Figure 4.1, the computational domain is a rectangle of width $\lambda = 1$, where λ is a base wavelength, and length sufficiently long to ensure that the perturbation does not grow beyond the end of the domain. The interface position, $h(x,t)$, is initialized as a piecewise sinusoidal function such that

$$h(x,0) = \begin{cases} -a_{1,0}\cos(2\pi k_1 x) & \text{for } x \leq \frac{1}{k_1} \\ -a_{2,0}\cos[2\pi k_2(x - \frac{1}{k_1})] - (a_{1,0} - a_{2,0}) & \text{for } x > \frac{1}{k_1} \end{cases} \tag{4.1}$$

where k_1 and $a_{1,0}$ are the wavenumber and initial amplitude of the left sinusoid, and $k_2 = 1/(\lambda - 1/k_1)$ and $a_{2,0}$ are the wavenumber and initial amplitude of the sinusoid to the right in Figure 4.1. The wavelengths of the initial perturbations are $\lambda_i = 2\pi/k_i$ where $i = 1, 2$ and $\lambda = \lambda_1 + \lambda_2$. The position of each bubble is taken to be the vertical position, y, where the mass fraction between the two interpenetrating fluids is 0.5 at the horizontal positions of $x = \frac{\lambda_1}{2}$ for the larger bubble and $x = \lambda_1 + \frac{\lambda_2}{2}$ for the smaller bubble. A shock wave with Mach number M is initialized at $y = 2(a_{1,0} + a_{1,2})$. The pre-shock Atwood number is given by $A = (\rho_A - \rho_B)/(\rho_A + \rho_B)$, where ρ_A is the density of the fluid in which the shock is initiated and ρ_B is the density of the fluid into which the shock passes. The variables are non-dimensionalized by λ, ρ_A, and the speed of sound in the light fluid, $c_A = \sqrt{\frac{\gamma p_0}{\rho_A}}$ where γ is the ratio of specific heats, assumed constant for both fluids, and the pressure $p_0 = 100\,\text{kPa}$ [59, 60]. Periodic boundary conditions are implemented at the edges of the domain and nonreflecting on the top and bottom.

A uniform mesh is used with 256 cells across the domain width, and the interface is initialized with a thermodynamically consistent exponential diffusion function [131], which in practice gives rise to an interface thickness of approximately 20 cells. The interface thickness is chosen to be consistent with past studies utilizing this code in which validation studies were conducted against single-mode RMI experiments [59, 60]. The simulations are run to a time well into the nonlinear growth regime. Although pointwise convergence cannot be achieved with the Euler equations, integral quantities such as the mixing width thickness are sufficiently converged at the resolutions and times explored.

Simulations are performed with parameters enabling a comparison with the shock tube experiments of Ref. [228], in which the Mach number is $M = 1.3$, the Atwood number $A = -0.67$, and the initial bubble wavelength ratios $\lambda_1/\lambda_2 \in (1.59, 2.50)$. To further investigate the bubble merging behavior, additional simulations are performed for five different initial bubble amplitude ratios $a_{0,1}/a_{0,2}$ for a Mach number of $M = 1.85$, Atwood number $A = 0.49$, and initial bubble wavelength ratios $\lambda_1/\lambda_2 \in (1.50, 2.00, 3.00)$. The initial bubble amplitude ratios are evenly spaced between $a_{0,1}/a_{0,2} = 1$ (each bubble having the same initial amplitude) and $a_{1,0}/a_{2,0} = \lambda_1/\lambda_2$ (each bubble having the same initial amplitude to wavelength ratio). These latter shock Mach number and Atwood number are chosen to match the conditions explored in Ref. [265]. The initial bubble amplitudes are such that the refraction of the shock passing through the interface is regular at all times ($a_i/\lambda_i < 0.1$ where $i = 1, 2$) [231]. Although the applications of interest are inherently three dimensional, particularly at late times, the two-dimensional case is explored as a first step toward a deeper understanding of the physics at times when the flow may still preserve two-dimensional structures from two-dimensional initial conditions.

4.4 Results

We begin by analyzing the simulation results designed to match the experimental set up of Ref. [228]. After highlighting agreements and discrepancies between the bubble merging model and the simulation results, we examine the mechanism responsible for the disparity in a set of simulations matching the numerical studies of [265]. From observations of these two sets of simulation studies, we develop a criterion based on initial conditions for predicting the escape of a vortex dipole from the confines of the interface and the reacceleration of bubbles.

4.4.1 Comparison to Experiments and Models

We first qualitatively consider the evolution of a perturbation of alternating large, $\lambda_1 = 27$ mm and $a_{0,1} = 2.00$ mm, and small, $\lambda_2 = 17$ mm and $a_{0,2} = 1.26$ mm, bubbles initially separating air and SF_6 ($A = -0.67$) in a shock tube. An $M = 1.3$ shock wave passes from air into SF_6 and initiates the RMI process. This setup matches that of Ref. [228]. Figure 4.2 shows the time evolution of the perturbation for both the experiments of Ref. [228] and our numerical simulation. Both the large and small bubbles grow and begin to compete for space before the larger bubble starts to overtake the smaller bubble. Beyond this point, the larger bubble dominates and the size of the smaller bubble decreases as the larger bubble expands to fill the space originally occupied by both bubbles [228]. Until approximately 1.4 ms, the potential model of Refs. [5, 95] agrees well with the experiments. According to the model, the mixing region begins to behave as a single array of bubbles with a wavelength equal to the width originally occupied by both bubbles as the larger bubble overtakes the smaller bubble [5, 95, 228].

The simulation results show good agreement with the experiments. The density contours show that the spikes begin to diverge beneath the smaller bubbles and converge beneath the larger bubbles. Careful inspection of the images from the experiment (Figure 4.2a) show the same behavior, where the spikes appear as dark shadows converging beneath the larger bubbles.

To quantify the evolution of the bubbles, Figure 4.3 shows the bubble position for $a_{0,1}/a_{0,2} = \lambda_1/\lambda_2$ (bubbles initiated with the same amplitude to wavelength ratio) and $a_{0,1}/a_{0,2} = 1$ (bubbles initiated with the same amplitude). The position of the tips of the large and small bubbles from simulation are compared to the prediction from the bubble merger model [5, 95] relative to the position of an unperturbed interface. For bubbles starting with the same amplitude to wavelength

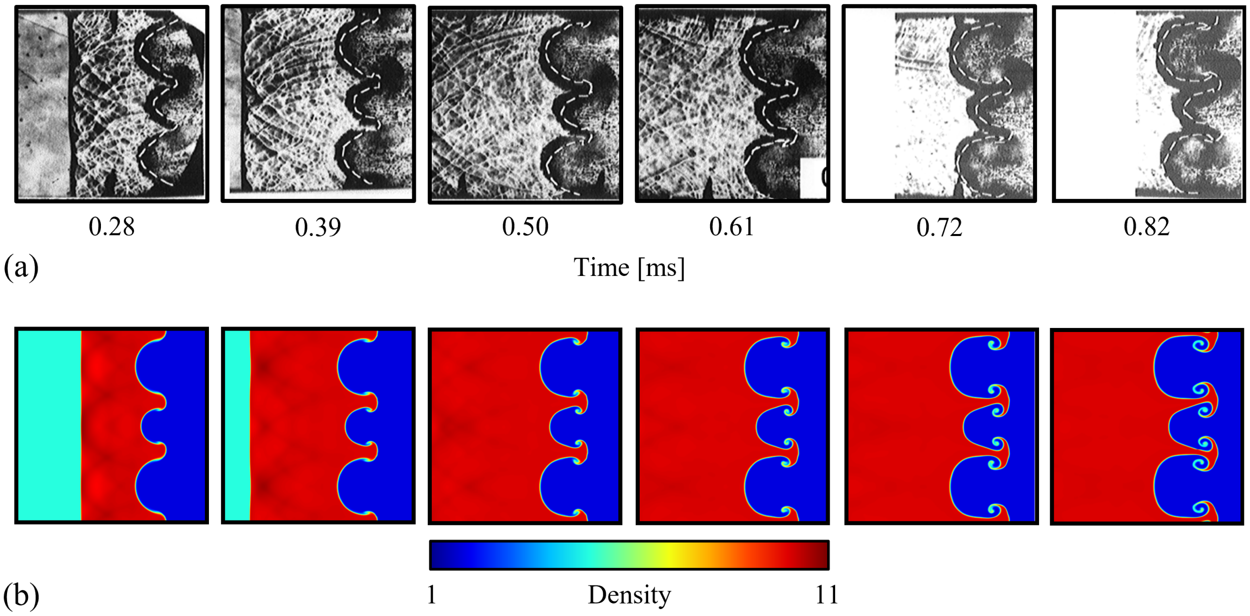

Figure 4.2: (a) Schlieren images showing the bubble competition process observed in the experiments of Ref. [228] (white dashed lines are simulations performed in Ref. [228]), reproduced with permission, and (b) density plots of a simulation performed for this work matching the experimental conditions of Ref. [228] where $M = 1.3$, $A = -0.67$, $\lambda_1/\lambda_2 = 1.59$, and $a_{0,1}/a_{0,2} = \lambda_1/\lambda_2$.

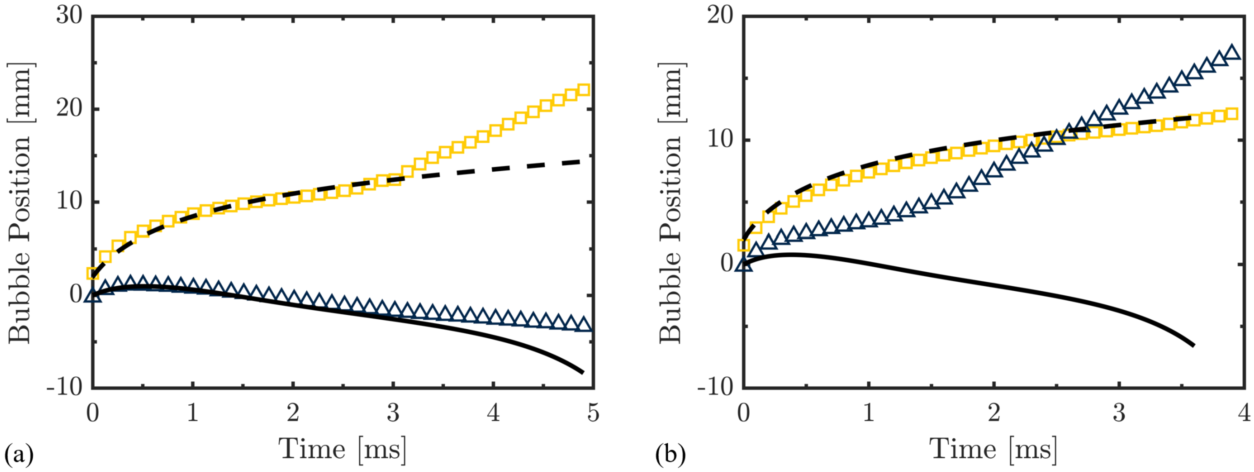

Figure 4.3: The larger (yellow squares/dashed line) and smaller (blue triangles/solid line) bubble tip positions from simulation/the model of Refs. [5, 95] for $M = 1.3$, $A = -0.67$, $\lambda_1/\lambda_2 = 1.59$ and (a) $a_{0,1}/a_{0,2} = \lambda_1/\lambda_2$ and (b) $a_{0,1}/a_{0,2} = 1$.

ratio, both bubbles begin to increase in amplitude immediately after the passage of the shock wave. After approximately 0.5 ms, however, the smaller bubble begins to decrease in size while the larger bubble continues to grow. The model agrees with the simulations until approximately 2.7 ms, shortly after the end of the experiment. At this point, the position of the smaller bubble begins to level off while the larger bubble begins to increase in size more rapidly than predicted by the model. The mechanism governing this behavior is the focus of the next section.

In the case of bubbles starting with the same initial amplitude, both bubbles begin to grow after the passage of the shock wave. The growth of the smaller bubble, however, immediately diverges from the model. Unlike the case with $a_{0,1}/a_{0,2} = \lambda_1/\lambda_2$, the smaller bubble is always moving in positive y. In fact, by approximately 1 ms, the smaller bubble is moving faster than the larger bubble, and at approximately 2.5 ms, the tip of the smaller bubble overtakes that of the larger bubble. After this, the smaller bubble continues to distance itself from the larger bubble at a relatively constant velocity. Throughout the simulation, the motion of the larger bubble is well predicted by the bubble merger model.

The simulations therefore show a clear deviation from the bubble merging model; in the case with $a_{0,1}/a_{0,2} = \lambda_1/\lambda_2$, the reacceleration of the bubble occurs sooner than predicted by the model and in the case with $a_{0,1}/a_{0,2} = 1$, the model cannot predict the escape of the vortex dipole. Because the model is derived from the interaction of adjacent bubble tips, it does not account for the behavior of the spikes. The next section, however, highlights the important role of the spikes in affecting the interface dynamics and explaining the deviation from the bubble merging model.

4.4.2 Vortex Escape and Bubble Reacceleration

To illustrate the mechanics that govern the bubble interactions, Figure 4.4 shows density, numerical Schlieren, and vorticity contours for two cases: $a_{0,1}/a_{0,2} = 1$ and $\lambda_1/\lambda_2 = 3$ (bubbles initiated with the same amplitude), and $a_{0,1}/a_{0,2} = 3$ and $\lambda_1/\lambda_2 = 3$ (bubbles initiated with the same amplitude to wavelength ratio). In each of these cases, an $M = 1.85$ shock wave passes from the heavier fluid into the lighter fluid ($A = 0.49$). These conditions are chosen to match the setup of Ref. [265]. Because the Atwood number is positive, the initial perturbation experiences a phase inversion before the onset of significant perturbation growth. In the case with $a_{0,1}/a_{0,2} = 1$, the vorticity deposited onto the interface during the passage of the shock wave causes the smaller bubble to develop into a vortex dipole. The dipole accelerates upward as it ejects fluid downward and is able to surpass the larger bubble. At later times, the escaped dipole continues to flee the mixing region while the larger bubble expands to fill the space formerly occupied by both bubbles. After the escape of the vortex dipole, the interface largely behaves as though it were initialized as a single-mode perturbation with a wavelength given by the sum of the wavelengths of the original two perturbations. Such dipoles

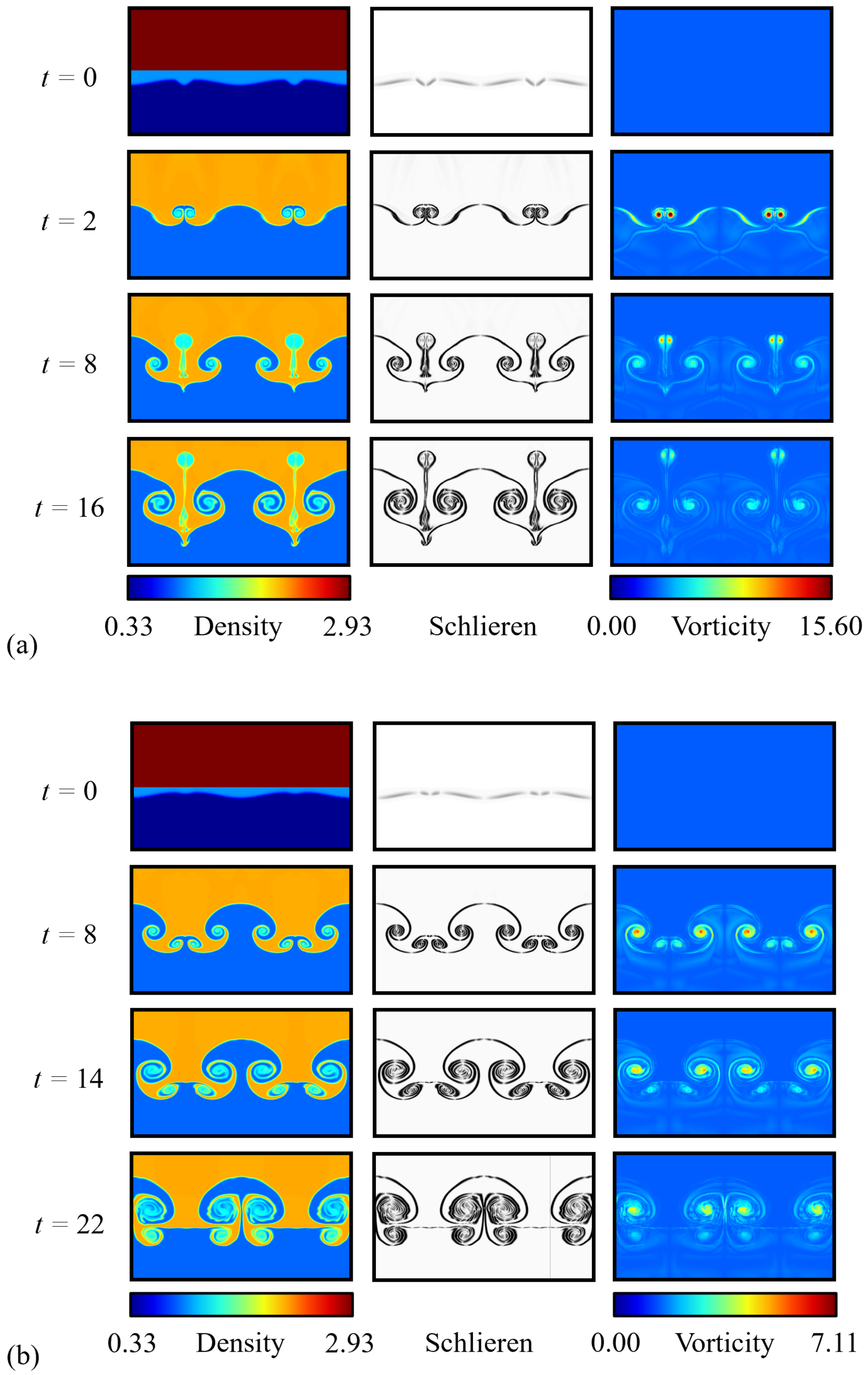

Figure 4.4: Density (left), numerical Schlieren (center), and vorticity magnitude (right) at the times shown for the simulations corresponding to $M = 1.85$, $A = 0.49$, and $\lambda_1/\lambda_2 = 3$ for (a) $a_{0,1}/a_{0,2} = 1$ and (b) $a_{0,1}/a_{0,2} = \lambda_1/\lambda_2$.

have been observed in both numerical and experimental studies of shock-accelerated perturbed interfaces [66, 204, 218, 263, 265, 284, 296].

In the case where $a_{0,1}/a_{0,2} = \lambda_1/\lambda_2$, the vorticity imbalance on the sides of the adjacent bubbles generated by the passage of the shock wave through the interface causes the developing spikes to rotate towards one another underneath the larger bubble. The smaller bubble spreads and flattens as the spikes diverge beneath it. The larger bubble, however, is reaccelerated after the spikes collide due to fluid from the spikes being forced upward. Upon the spike collision, fluid is also forced downward, ultimately resulting in a vertical alignment of the bubble and spike. The expansion of the larger bubble to fill the space originally occupied by both bubbles is hindered by the reacceleration caused by the spike collision. This mechanism is responsible for the larger bubble reacceleration seen in Figure 4.3a.

It is possible for the width of the larger bubble, W, to decrease, as seen in Figure 4.5, which shows the width of the larger bubble as a function of time for each simulation performed. There is a clear separation between the widths of the larger bubbles in situations where the large and small bubbles start out with the same amplitude, which lead to the generation of a vortex dipole, and where the large and small bubbles start out with the same amplitude to wavelength ratio, in which the larger bubble experiences reacceleration. In the simulations that generate an escaping vortex dipole, the width of the larger bubble increases over time until it reaches a size on the order of the overall wavelength. In cases where the larger bubble reaccelerates, the width of the larger bubble decreases immediately following the spike collision beneath it. This process can be understood as a consequence of incompressibility after the passage of the shock wave: a fluid squeezed in one direction elongates in the perpendicular direction. This narrowing of the bubble is in opposition to the drag-minimization process that causes an inverse cascade of bubble sizes as an unstable, pressure-wave-accelerated interface evolves [253].

All of the simulations for the given parameters can be grouped into two categories. In the first, the smaller bubble forms a vortex dipole that escapes the mixing region as in Figure 4.4a. In the second, the smaller bubble does not escape the mixing region and a spike collision beneath the larger bubble causes the reacceleration of the larger bubble as in Figure 4.4b. The next section develops a criterion that predicts which case emerges based on initial conditions.

4.4.3 Vorticity-Based Criterion

The escape of a vortex dipole and the collision of spikes beneath the larger bubble can be understood by examining the vorticity dynamics. In our simulations of two-dimensional compressible inviscid flow, the shock wave passing through the perturbed interface deposits baroclinic vorticity, which evolves according to

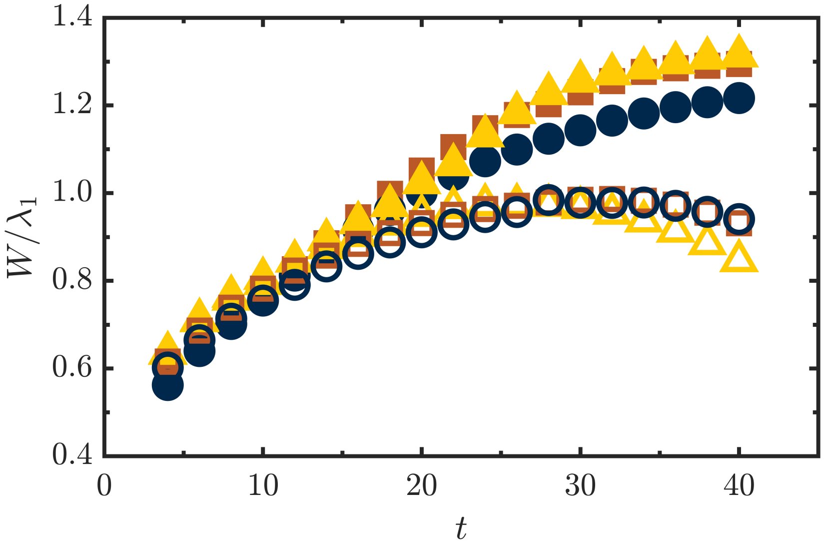

Figure 4.5: Larger bubble width normalized by wavelength as a function of time for simulations where $a_{0,1}/a_{0,2} = 1$ (filled symbols) and $a_{1,0}/a_{2,0} = \lambda_1/\lambda_2$ (open symbols), and $\lambda_1/\lambda_2 = 1.50$ (blue circles), $\lambda_1/\lambda_2 = 2.00$ (orange squares), and $\lambda_1/\lambda_2 = 3.00$ (yellow triangles).

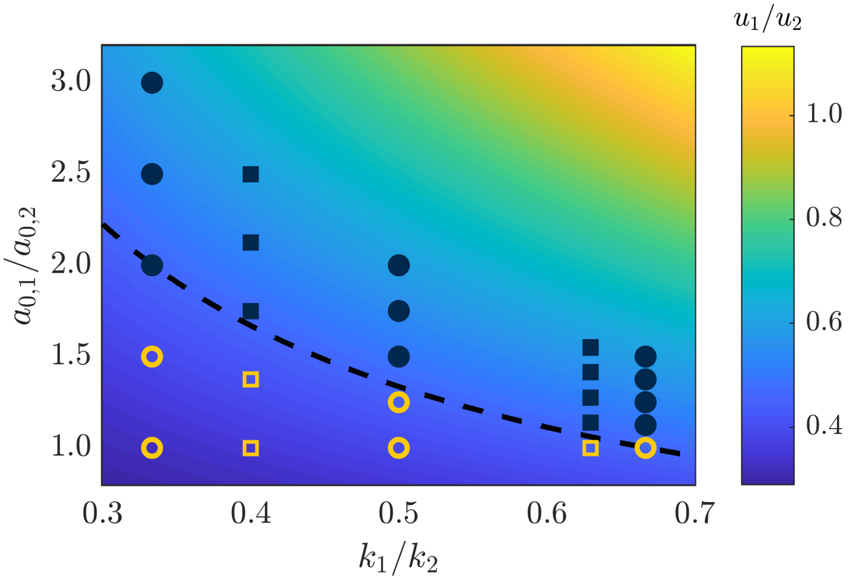

Figure 4.6: The large-to-small bubble velocity ratio as a function of initial bubble amplitude ratio and wavenumber ratio. Data points correspond to conditions from Ref. [228] (squares) and Ref. [265] (circles). The black dashed line is where $\frac{u_1}{u_2} = 0.65$. Simulations producing an escaping vortex dipole are in yellow (open symbols) while simulations that did not are in blue (closed symbols).

$$\frac{D(\omega/\rho)}{Dt} = \frac{\nabla\rho \times \nabla p}{\rho^3}, \tag{4.2}$$

where ω is vorticity. During the shock-interface interaction, the baroclinic vorticity is deposited due to the misalignment of the pressure gradient (across the shock) and the density gradient (across the interface). The RMI process therefore naturally induces vorticity dipoles [265]. It is reasonable to expect from a dimensionality argument that the velocity of the resulting dipole should scale as

$$u_{dipole} \sim \frac{\Gamma}{\lambda}, \tag{4.3}$$

where Γ is the circulation along one half of the bubble interface, which can be determined analytically for a weak shock wave passing through a sinusoidal interface with a small perturbation amplitude [231]. The small bubble should be able to escape the interface as a vortex dipole if its velocity is sufficiently large compared to that of the dipole corresponding to the larger bubble. This criterion for vortex dipole escape can thus be reformulated as

$$\frac{u_1}{u_2} < c, \tag{4.4}$$

where u_1 and u_2 are the velocities of the dipoles corresponding to the large and small bubbles, respectively, and c is a constant. Because both bubbles exist along the same interface, they are subject to the same Mach and Atwood number. Therefore, to first order, the ratio of dipole velocities, and therefore c, is not expected to depend on the Mach or Atwood number, though other quantities, such as the rate at which the instability develops, may [231]. However, c will depend on the geometry of the interface, which here is described by the ratio of the initial amplitudes and wavenumbers of each bubble.

Figure 4.6 shows the ratio of the vortex dipole velocities as a function of initial amplitude ratio and wavenumber ratio and labels which sets of parameters lead to dipole escape or not. This velocity ratio increases with increasing initial amplitude ratio and increasing wavenumber ratio. These trends can be understood with Equations 4.2-4.4. Both a greater initial amplitude and wavenumber ratio correspond to the sinusoidal interface forming a greater angle with the horizontal at the position of the larger bubble. As a result, the angle between the density gradient and the pressure gradient increases, which enhances the baroclinic vorticity deposition according to Equation 4.2. An increase in vorticity corresponds to greater circulation along the larger bubble, resulting in a greater velocity of the larger bubble (Equation 4.3), and a greater bubble velocity ratio (Equation 4.4). Figure 4.6 indicates that there is a threshold below which the vortex dipoles escape the mixing region. This threshold closely follows a line of constant velocity ratio, $c = 0.65$, obtained by fitting to the data. More precise identification of the threshold for vortex dipole escape may require additional simulations in the transition region of the phase space presented in Figure 4.6, though the proposed vorticity-based criterion appears to be satisfactory. It should also be noted that, although the derivation of the criterion is valid only for Mach numbers not too much greater than unity, the criterion is able to identify cases involving an escaping vortex dipole even for the simulations matching the setup of Ref. [265], where the Mach number is 1.85.

4.5 Conclusions

Numerical simulations are performed to investigate the interaction between two bubbles on an interface undergoing the RMI process. Depending on the initial conditions, two distinct evolution patterns emerge. For adjacent bubbles with relatively small wavenumber and initial amplitude ratios, the smaller bubble forms a vortex dipole that surpasses the larger bubble and escapes the mixing region while the larger bubble expands to fill the space originally occupied by both bubbles; the mixing region continues to evolve as though it were a single-mode perturbation with a period given by the sum of the wavelengths of the original two bubbles. For adjacent bubbles with relatively large wavenumber and initial amplitude ratios, the smaller bubble does not escape the mixing region as a spike collision occurs beneath the larger bubble, leading to a reacceleration of the larger bubble, a delay in or possible prevention of the expansion of the larger bubble to fill the space originally occupied by both bubbles, and an aligned configuration of bubbles and spikes. A scaling argument based on vorticity dynamics is proposed to develop a criterion for determining which pattern emerges. The data suggest that the smaller bubble escapes the mixing region if the ratio of the initial velocity of the larger bubble to the smaller bubble is less than a critical value.

The bubble competition process obtained from simulation is compared to experiments and existing bubble merger models. It is found that the models correctly predict the behavior of the bubbles in the case where the smaller bubble does not escape the interface up until the point where the rapid reacceleration of the larger bubble occurs. While the models accurately predict the behavior of the larger bubble in the case where the smaller bubble forms an isolated vortex dipole, they cannot describe the escape of the smaller bubble from the interface.

This work examines the vorticity dynamics in the mixing region of shock-accelerated flows that may contribute to an eventual turbulent transition, the modeling of which is an important feature of many hydrocodes [12]. Future work will explore these physics in three dimensions where the effects of vortex stretching introduce a significant challenge not present in two dimensions. These studies may also incorporate additional physics, like diffusion, that enhance the ability of the code to describe turbulent behavior, enabling the study of the RMI later in time [109]. Additionally, future studies may address the effect of different advection schemes on the escape of a vortex dipole. While the large-scale motion of the competing bubbles may not be significantly altered, the choice of advection scheme may significantly affect borderline cases when the vortex dipole velocity ratio is near the critical value [61, 108]. Finally, future efforts may aim to leverage reduced-order modeling techniques to explore the evolution of more complex initial interfaces and identify key physical parameters governing escaping dipoles and reaccelerated bubbles.

This work is supported by the Lawrence Livermore National Laboratory under subcontract B632749, the U. S. Department of Energy under grant DE-NA0003864, and the Extreme Science and Engineering Discovery Environment (XSEDE) Comet system under grant TG-CTS130005 [269]. The authors would also like to thank Sam Pellone for fruitful discussions.

CHAPTER 5

Saturation of Vortex Rings Ejected From Shock-Accelerated Interfaces

This chapter is adapted from M. J. Wadas, L. H. Khieu, G. S. Cearley, H. J. LeFevre, C. C. Kuranz, and E. Johnsen, Saturation of vortex rings ejected from shock-accelerated interfaces, *Physical Review Letters*, 130:194001, 2023 [281].

5.1 Abstract

Structures evoking vortex rings can be discerned in shock-accelerated flows ranging from astrophysics to inertial confinement fusion. By constructing an analogy between vortex rings produced in conventional propulsion systems and rings generated by a shock impinging upon a high-aspect-ratio protrusion along a material interface, we extend classical, constant-density vortex-ring theory to compressible multifluid flows. We further demonstrate saturation of such vortex rings as the protrusion aspect ratio is increased, thus explaining morphological differences observed in practice.

5.2 Introduction

The mixing induced by the interaction of shocks with interfaces separating different fluids has implications for problems ranging from inertial confinement fusion (ICF) to astrophysics. In ICF, laser-generated shocks pass through layers of a capsule containing fusion fuel, compressing and heating it to extreme conditions at which self-sustained nuclear fusion may occur [2, 17, 311, 312]. The mixing of the capsule material with fuel in the hotspot due to imperfections on the capsule surface and from the gas fill tube is a primary source of decreased performance [14, 91, 102, 219, 240, 286, 310]. In core-collapse supernovae, shocks generated from rapid energy release propagate outward through the layers of the collapsing stars, causing heavy core elements to jet into outer layers [1, 110, 127, 128, 299]. An understanding of these turbulent, shock-driven mixing

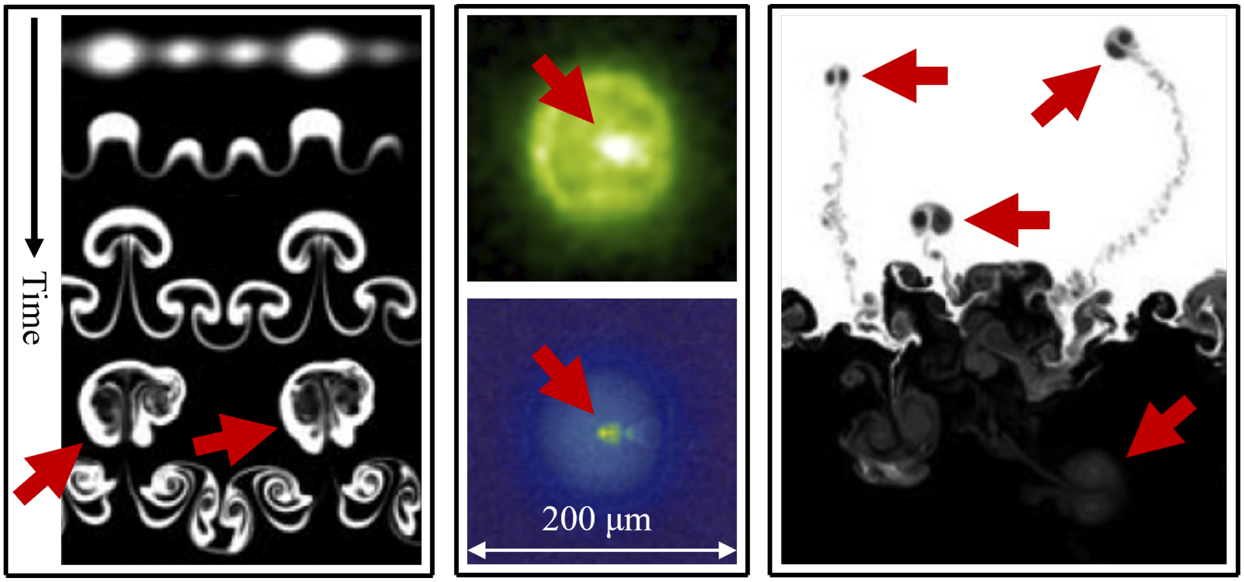

Figure 5.1: Left: evolution of a multimode shocked fluid layer experiment [11]. Middle: experimental (top) and simulated (bottom) x-ray self-emission during an ICF capsule implosion [10]. Right: volume fraction from RMI simulations [265]. Red arrows indicate likely vortex rings/dipoles. All images are reproduced with permission.

phenomena is crucial for the success of ICF and may help elucidate the mechanisms by which heavy and light elements mix in the universe. While efforts are underway to develop models describing these turbulent phenomena [12, 69], their initialization is problematic given the lack of understanding of the transition to turbulence in these shock-accelerated flows.

As it traverses a perturbed material interface, a shock deposits baroclinic vorticity due to the misalignment of the density and pressure gradients, driving interfacial perturbation growth via the Richtmyer-Meshkov instability (RMI) [162, 220]. Perturbations initially grow linearly in time before saturating and rolling up into a mushroom-like shape as nonlinear effects dominate [48, 228]. Theoretical studies have long described early-time RMI dynamics in terms of point vortices or vortex sheets [103, 140, 211, 222]. In complex situations (e.g., multimode, re-shock, late times, etc.), the multi-material mixing region may evolve to turbulence [47, 122, 131, 204, 241], which spreads as eddies entrain adjacent fluid parcels of different densities [192, 266]. Although linear and, to some extent, early nonlinear theory describing perturbation growth is well established [98, 133, 228, 273], turbulence transition and late-time mixing are poorly understood due to the inhomogeneity and intermittency of the flow. There is no doubt, however, that vorticity dynamics play a role in transition and mixing [211, 307, 308].

Advances in diagnostics, in particular, micron-scale x-ray imaging with Fresnel zone plates and lithium fluoride detectors [71, 77, 148, 221], and numerical methods have enabled high-resolution visualizations of shock-induced mixing regions. In recent studies [10, 11, 91, 93, 204, 264, 265, 280, 309], flow structures intermittently ejected from the mixing region can be discerned, in some cases to distances many times their characteristic length, as illustrated in Figure 5.1. Though explicitly connected to vortex rings [122, 264, 301, 302], these structures cannot be described by (nonlinear) RMI theory or existing models [5, 95, 133, 165, 273, 280]. A criterion for vortex dipole ejection based on the initial interface geometry was developed [280], though this study fell short of quantitatively describing the ejection mechanism. Predicting this shock-induced ejection of vortex rings is critical to determine the growth of the mixing region because these structures transport kinetic energy and circulation from the mixing region and therefore affect its size and intensity. Furthermore, such rings may perturb other flow structures away from the mixing region (e.g., other nearby interfaces). While vortex rings generated by drawing a piston in an open-ended cylinder have received significant attention in a completely different context [84, 182], the mechanism explaining the formation and ejection of vortex rings and dipoles from shock-induced mixing regions has yet to be established.

In this letter, we outline a theory quantitatively describing the formation, ejection, and evolution of vortex rings from shock-accelerated interfaces. Drawing from classical studies [84], we develop a setup enabling us to systematically investigate the formation and ejection of vortex rings from mixing regions generated by the interaction of a shock with an interface. Our analysis, verified by direct simulations of the Euler equations, fully describes the vortex ring dynamics, thereby extending classical theory for piston-cylinder systems to more general geometries and vorticity sources, including compressible multifluid flows. This theory allows us to calculate the kinetic energy and circulation leaving the confines of the mixing region, which are key quantities in turbulence modeling, and identify situations when vortex ring saturation occurs. Furthermore, our theory may elucidate flows dominated by shock-induced jets at interfaces, such as those observed in ICF due to the fill tube and capsule defects [10, 91, 93], astrophysics [20, 94, 112, 299], and possibly ejecta physics [32, 238].

5.3 Theory

We first revisit the basic attributes of classical vortex rings in propulsion systems, in which an impulsively started jet is generated by forcing a piston through a hollow cylinder. The vortex sheet produced along the inner edge of the orifice separates and rolls up to form a ring [150, 199, 242]. As long as the ring is attached to the jet, it accumulates circulation as it convects downstream. However, beyond a critical stroke-to-diameter ratio, the ring detaches from the jet, and no additional circulation can be imparted to it. Over a wide range of experiments and simulations [55, 56, 183, 210, 224, 225, 234], this saturation occurs at a stroke-to-diameter ratio of approximately 4, deemed the *formation number*, which equivalently represents the timescale over which vortex rings form by expressing the stroke length as the time-integrated piston velocity [84, 182].

Given morphological similarities between classical vortex rings and rings ejected from shock-accelerated interfaces (see Section 5.6), we postulate that the vorticity deposited by a shock interacting with a high-aspect-ratio protrusion along a material interface serves the same purpose as that produced along the cylinder wall. If this hypothesis is correct, vortex rings ejected from shock-accelerated interfaces would exhibit behavior similar to classical rings, e.g., in terms of their circulation and formation number (including saturation), as well as their energy and impulse. We therefore expect that an initial interfacial geometry analogous to the cylinder may lead to similar vorticity dynamics. As illustrated in Figure 5.2, we set up our problem with heavy fluid of density ρ_H adjacent to light fluid of density ρ_L, with a heavy-fluid protrusion of diameter D and depth L in the light fluid. The shock propagates from right to left. The compression ratio across the shock $\rho_{H'}/\rho_H$ characterizes the shock strength (equivalently, a Mach number, M, could be defined), where $\rho_{H'}$ is the density of the shocked heavy fluid. The shock is transmitted through the interface, compressing the light fluid to density ρ_{L^*}, and a rarefaction is reflected from the interface, decompressing the shocked heavy fluid to density ρ_{H^*}. These densities are obtained by solving the Riemann problem initialized between the unshocked light fluid and the shocked heavy fluid. The protrusion, modelled as decompressed shocked heavy fluid of depth $L' = (\rho_H/\rho_{H^*})L$, starts inverting due to the sign of the vorticity. During inversion, the fluid in the protrusion is ejected into the heavy fluid at speed U_i relative to the interface, analogous to the piston speed in the classical system, entraining the light fluid and forming a vortex ring of density ρ_R. As in past studies [182], we model the ring as belonging to the Norbury [200] family, but must account for compressibility and multiple fluids. For an unsaturated ring, the circulation, impulse, and energy of the fluid slug ejected from the protrusion equal those corresponding to the ring. Extending the analysis to the present multi-material system yields:

$$\Gamma_{slug} = \frac{1}{2}L'U_i = \frac{1}{2}\frac{\rho_H}{\rho_{H*}}LU_i = (\Omega\alpha l)\, l\Gamma_N = \Gamma_{VR}, \tag{5.1a}$$

$$I_{slug} = \frac{1}{4}\rho_H \pi D^2 L U_i = \rho_R\,(\Omega\alpha l)\, l^3 I_N = I_{VR}, \tag{5.1b}$$

$$E_{slug} = \frac{1}{8}\rho_H \pi D^2 L U_i^2 = \rho_R\,(\Omega\alpha l)^2\, l^3 E_N = E_{VR}, \tag{5.1c}$$

where Ω is the vorticity density (i.e., vorticity divided by distance from the ring centerline [200]), α is the nondimensional mean vortex core radius, l is the ring radius, and the subscript N denotes nondimensional quantities that are functions only of α. Equations 5.1 can be re-arranged to yield the formation number

$$\frac{L}{D} = \sigma\sqrt{\frac{\pi}{2}\frac{I_N^{1/2}\Gamma_N^{3/2}}{E_N}} = \sigma\sqrt{\frac{\pi}{2}\frac{\Gamma_N^{3/2}}{U_N I_N^{1/2}}}, \tag{5.2}$$

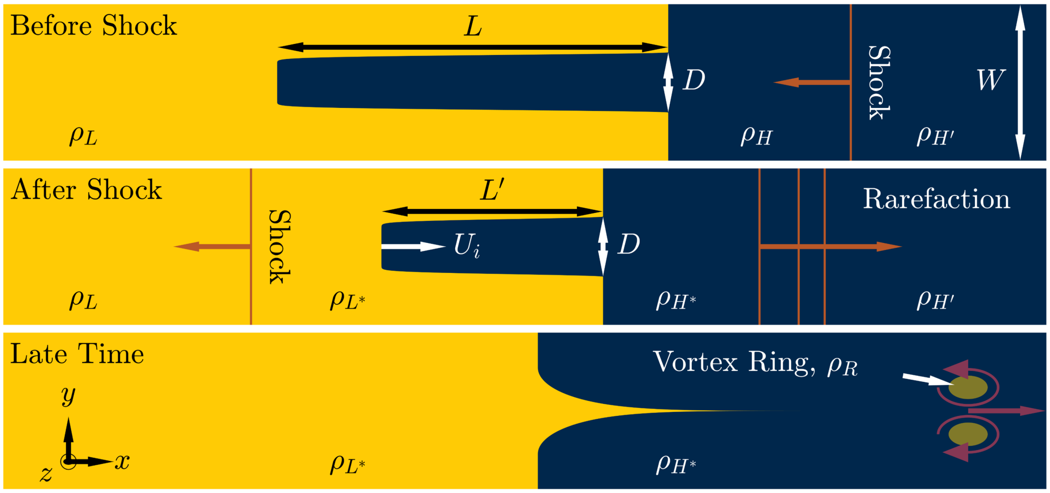

Figure 5.2: Schematic showing the problem setup. Top: a shock approaches an interface separating heavy and light fluids with a heavy-fluid protrusion. Middle: the shock is transmitted through the interface, compressing the protrusion and setting the interface into motion, while a rarefaction is reflected. Bottom: the protrusion inverts and ejects a vortex ring into the heavy fluid.

where $L' = \frac{\rho_H}{\rho_{H^*}} L$, $U_i = 2(\Omega\alpha l)U_N$ [182], and

$$\sigma = \sqrt{\frac{\rho_{H^*}}{\rho_R}\frac{\rho_{H^*}}{\rho_H}}. \tag{5.3}$$

As with classical vortex rings, the formation number depends on the circulation, impulse, and energy, but now also depends on the shock strength and interface density ratio. Equation 5.2 states that maximal circulation, impulse, and energy generated by the inverting protrusion is contained within the resulting ring. The parameter σ is a formation number multiplier generalizing the classical formation number (compare Equation 5.2 in the present work to Equations 12 and 13 in Ref. [182]) to rings generated from shocked interfaces, i.e.,

$$(L/D)_{sat,\,shock} = \sigma (L/D)_{sat,\,classical}. \tag{5.4}$$

The formation number multiplier accounts for both the interface density ratio and shock strength. The *multifluid factor* $\sqrt{\rho_{H^*}/\rho_R}$ is the square root of the relative density of the protrusion with respect to the ring after shock interaction. We approximate the ring density as the average of the post-shock fluid densities, $\rho_R \approx (\rho_{H^*} + \rho_{L^*})/2$, which is consistent with both simulations and the entrainment properties of saturated Norbury rings [200], though other mixing models could be used. As the density ratio is increased, the relative density of the vortex ring decreases. The resulting decrease in the ring's impulse and energy allows it to support additional impulse and energy from the inverting protrusion, which can be increased by increasing the protrusion depth (Equations 5.1b and 5.1c), thereby producing a larger formation number. The *compression factor* ρ_{H^*}/ρ_H describes shock compression of the protrusion. Because the circulation supplied by the inverting protrusion is proportional to protrusion depth and thus inversely proportional to shock strength (Equation 5.1a), the unshocked depth, and therefore formation number, must increase as the shock strength is increased to supply the same amount of circulation. If a vortex ring is produced with no compression ($\rho_{H'} \to \rho_H$) and no density difference ($\rho_H \to \rho_L$), the classical limit $\sigma = 1$ is recovered. The classical formation number is generally accepted to be $3.0 \leq (L/D)_{sat} \leq 4.6$ [182], and therefore it is expected that in the present shock-accelerated case the formation number falls within the range

$$3.0\sigma \leq (L/D)_{sat,shock} \leq 4.6\sigma. \tag{5.5}$$

5.4 Results

To verify these theoretical results, we use an in-house code [59, 60, 109] (see Section 5.6) solving the three-dimensional Euler equations for the setup in Figure 5.2. Sets of simulations, detailed in Table 5.1, are performed for different density ratios and shock strengths similar to those in [47, 48, 204, 241, 280]. In cases 1-4, L is varied from 1 to 8 while keeping D constant. Cases 5 and 6 explore stronger shocks and larger interface density ratios. The simulations evolve in time long enough for pinch-off to occur, leading to a steady, self-propagating vortex ring identified by the $\lambda_2 = 0$ criterion, a standard method for identifying vortices based on eigenvalues, $\lambda_1 < \lambda_2 < \lambda_3$, related to the velocity gradient tensor [106]. To illustrate the dynamics, Figure 5.3 shows out-of-plane vorticity ω and density contours along the centerplane, as well as the three-dimensional surface of $\lambda_2 = 0$, for a shock of strength $\rho_{H'}/\rho_H = 1.34$ with interface density ratio $\rho_H/\rho_L = 2$ and protrusions of aspect ratios $L/D = 1$ and 5. For the $L/D = 1$ case, the protrusion inversion ejects a vortex ring that quickly pinches off and steadily separates from the original interface. Although some vorticity is confined to the interface, most of the vorticity is concentrated within the ring; there are no vortices between the ring and the interface. For the $L/D = 5$ case, which is near the formation number predicted by our theory, a pinched-off ring still steadily propagates away from the interface, but a trailing jet with vortices is evident. A known signature of exceeding the formation number, this jet forms because the saturated ring cannot support additional circulation from the vortex ring generator, which accumulates in the trailing jet [84].

These results suggest that the ring circulation saturates at sufficiently large protrusion aspect ratios, consistent with the classical case. To confirm that the formation number has been reached, Figure 5.4 shows the circulation of the pinched-off rings for different protrusion aspect ratios L/D. At low aspect ratios, the circulation of the ejected rings increases as the protrusion aspect ratio

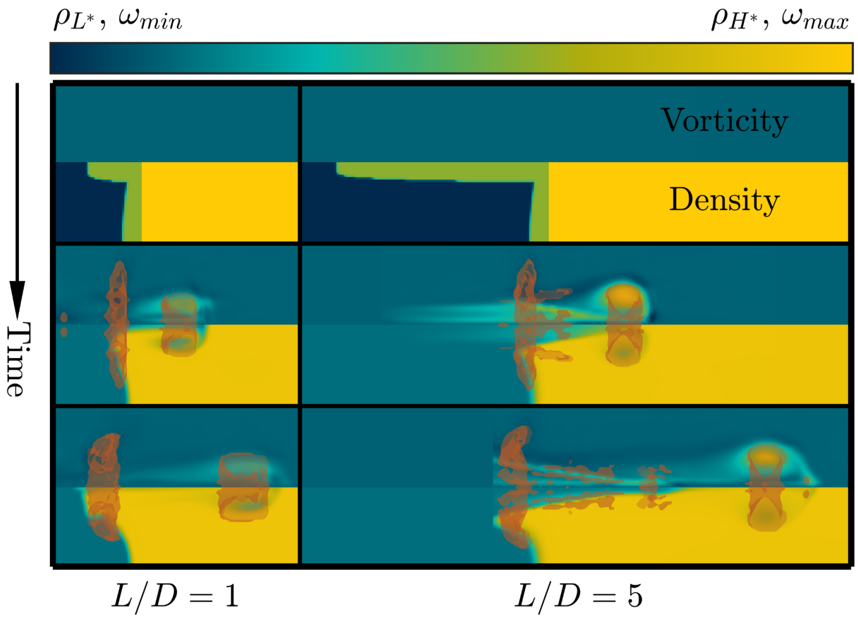

Figure 5.3: Evolution of the vorticity (top) and density (bottom) following the interaction of a shock of strength $\rho_{H'}/\rho_H = 1.34$ with heavy-fluid protrusions with aspect ratios $L/D = 1$ (left) and $L/D = 5$ (right) along an interface with $\rho_H/\rho_L = 2$. Orange surfaces enclose vortex rings, as identified by the $\lambda_2 = 0$ criterion [106].

is increased. As L/D is further increased, however, the circulation saturates; at this point, no further circulation can be imparted to the ring. We take the formation number to be the value of L/D at the intersection of a line fit to points with $L/D \le 3$, where the ring circulation appears to be growing linearly, and the average circulation of points with $L/D \ge 7$, where the circulation plateaus. The formation number for each set of simulations and the expected range based on our theory, summarized in Table 5.1 and the upper-left inset of Figure 5.4, differs from classical theory, but falls near the center of the range predicted by our extended theory.

As an example application, we estimate the formation number for the fill-tube jet for experiment N210808 at the National Ignition Facility [2, 125] as

$$(L/D)_{sat,shock} = 3.8\sigma = 3.8\sqrt{\frac{2\rho_{e^*}}{\rho_{a^*} + \rho_{e^*}}\frac{\rho_{e^*}}{\rho_e}} \approx 7, \tag{5.6}$$

where ρ_{e^*} and ρ_{a^*} are the densities of the epoxy and ablator, respectively, after a strong shock releases off the ablator-ice interface and ρ_e is the unshocked epoxy density. Although a 2 µm fill tube was utilized, the diameter of the epoxy-filled bore hole was $D = 8.4$ µm [125], making epoxy the appropriate material to model the protrusion. In this experiment, the ablator thickness was $L = 79$ µm, and therefore $L/D = 9.4$. Because $L/D > (L/D)_{sat,shock}$, a saturated vortex ring and a trailing jet are expected, consistent with Figure 5.1. The circulation, impulse, and energy injected

Table 5.1: Simulation parameters and expected formation numbers and ranges predicted by our theory.

Case	$\rho_{H'}/\rho_H$	M	ρ_H/ρ_L	3.0σ	4.6σ	$(L/D)_{sat,\,shock}$
1	1.17	1.1	2	3.94	6.05	5.16
2	1.17	1.1	5	4.27	6.54	5.52
3	1.34	1.2	2	4.42	6.78	5.47
4	1.34	1.2	5	4.65	7.13	6.03
5	1.86	1.5	8	5.54	8.50	6.79
6	2.67	2.0	11	6.33	9.70	7.59

into the hotspot by the ring can then be calculated from Equation 5.1 with $L/D = (L/D)_{sat,shock}$. Furthermore, by replacing L with an integrated protrusion, or jet, velocity, our theory provides the timescale on which the ring forms. Although the calculated formation number appears to agree with observations of fill-tube jetting, the authors advise caution for direct applications to ICF, which involves fill-tube configurations that differ from our canonical setup, intense radiation, and convergent geometries. These and other effects would likely need to be considered for a precise determination of the fill-tube formation number.

The lack of a trailing jet for rings generated from smaller defects, and in the late nonlinear phase of the RMI, suggest that these rings are unsaturated. Both saturated and unsaturated rings transport kinetic energy, thus giving rise to a reduction in the kinetic energy of the mixing region the ring originates from. Ejected rings could also interact with other flow structures away from the mixing region. While the effects of viscosity and magnetic fields are not presently considered based on Reynolds number and plasma beta, Re and β, respectively, in ICF, where $Re \sim 10^4$ [285] and $\beta \sim 10^5$ [254], and for many supernovae, where $Re \sim 10^{10}$ and $\beta \sim 10^4$ [227], the conservation arguments central to our theory support a path to explore diffusive effects and magnetic fields. Because such mechanisms would tend to inhibit the conversion of circulation, impulse, and energy from the inverting protrusion to the vortex ring, a greater protrusion aspect ratio would likely be required to form a saturated ring. These and other effects, including molecular diffusion and radiation, may be quantifiable with appropriate source terms in Equation 5.1.

5.5 Conclusion

In this chapter, we demonstrate that vortex rings generated following the interaction of a shock with a cylindrical protrusion originate due to the baroclinic torque deposited along the interface, which ejects the fluid initially in the protrusion as it inverts. The resulting dynamics are consistent

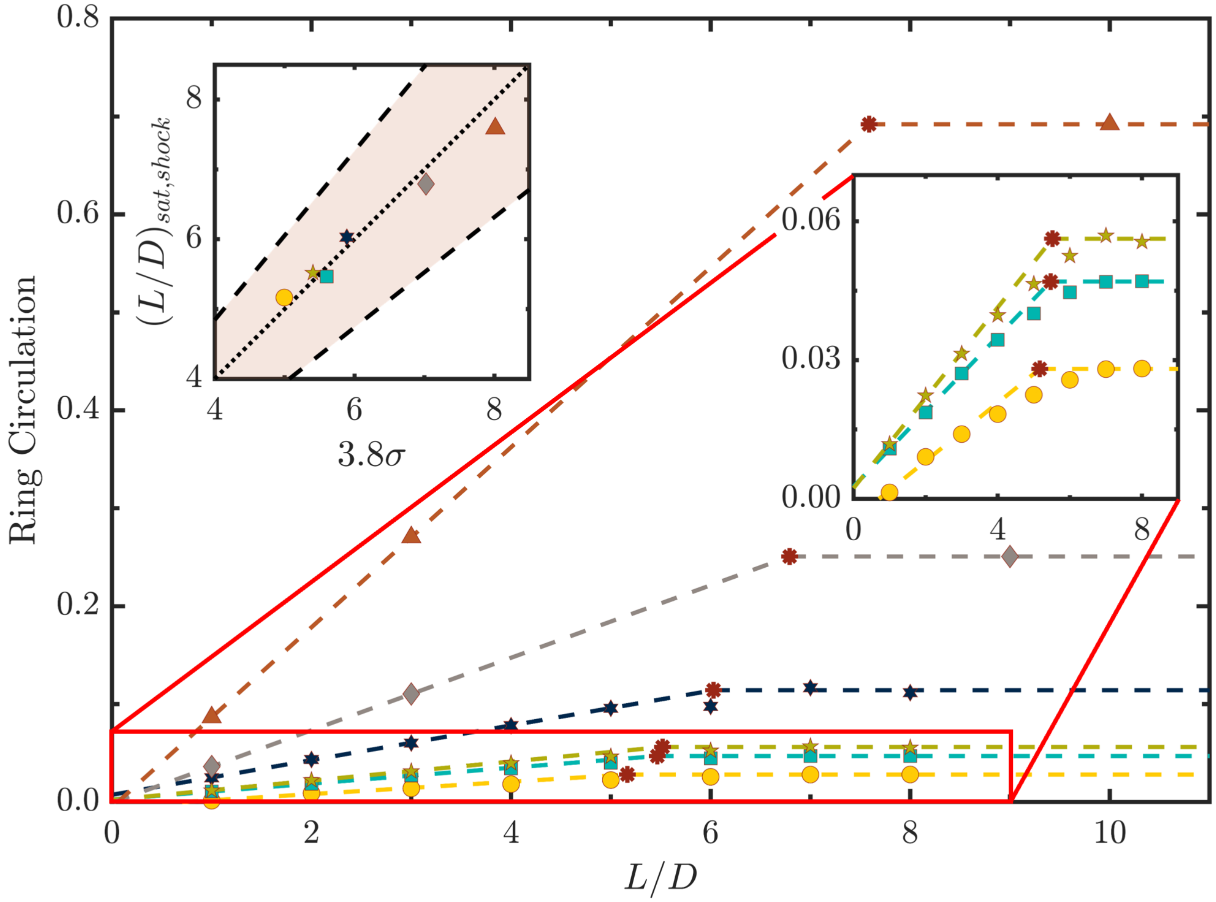

Figure 5.4: Ring circulation vs. protrusion aspect ratio for cases 1-6 (yellow circles, green pentagrams, teal squares, dark blue hexagrams, grey diamonds, and orange triangles, respectively) in Table 5.1. The right inset is a close-up of cases 1-3. The horizontal location of each red star identifies the formation number. The upper-left inset shows the formation number from simulations vs. our theory. The dotted line indicates where $(L/D)_{sat,shock} = 3.8\sigma$, and the dashed lines bound the shaded region where $3.0\sigma \leq (L/D)_{sat,shock} \leq 4.6\sigma$.

with classical piston-cylinder systems, exhibiting ring saturation coincident with the emergence of a trailing jet. However, the formation number is augmented by a factor accounting for the different fluid densities and shock compression. Our analysis thus generalizes the classical theory to compressible multifluid flows and explains morphological differences observed in practice. While the computations presented support the theory, simulations exploring a wider range of parameters may help elucidate certain details, including late-time shock-induced turbulent mixing, as ejected vortex rings may affect mixing layer development and turbulent transition.

The present findings may have implications in ICF and astrophysics. In ICF, the fill tube may generate a vortex ring that impinges on the hotspot. Our theory also describes a mechanism that may affect mixing following supernovae and explain the presence of stellar core elements in the outer layers of expanding remnants. Furthermore, the results of our analysis could be used to deduce quantities of interest for shock-induced ejecta or jets.

This work is supported by the Lawrence Livermore National Laboratory under Subcontract No. B632749 and the U. S. Department of Energy (DOE) as part of the Stewardship Science Graduate Fellowship Program under Grant No. De-NA0003960. Computational resources were provided by the Extreme Science and Engineering Discovery Environment Comet GPU system, USA under grant TG-CTS130005 and the Oak Ridge Leadership Computing Facility, a DOE Office of Science User Facility supported under Contract DE-AC05-00OR22725.

5.6 Supplemental Material

This supplemental material provides additional detail regarding the applicability of the piston-cylinder model to the inverting protrusion along with a description of the numerical methods utilized.

5.6.1 Protrusion Inversion Process

Figure 5.5 shows the x- and y-components of the velocity during the inversion of a protrusion of aspect ratio $L/D = 8$ initially along an interface separating two fluids with a density ratio $\rho_H/\rho_L = 2$ following the passage of a shock wave of strength $\rho_{H'}/\rho_H = 1.34$. The velocity into and out of the plane is negligible. In our setup, the resulting vorticity deposited causes the highly collimated inversion of the protrusion similar to the flow exiting a piston-cylinder device. Figure 5.5 also shows the horizontal velocity profile at the location of the residual interface, analogous to the orifice of the piston-cylinder setup, at three times during the protrusion inversion, along with a parabolic profile for comparison. While the shear layer that causes the deviation from a uniform profile does appear to be thicker than that of the piston-cylinder setup [84, 225] immediately after

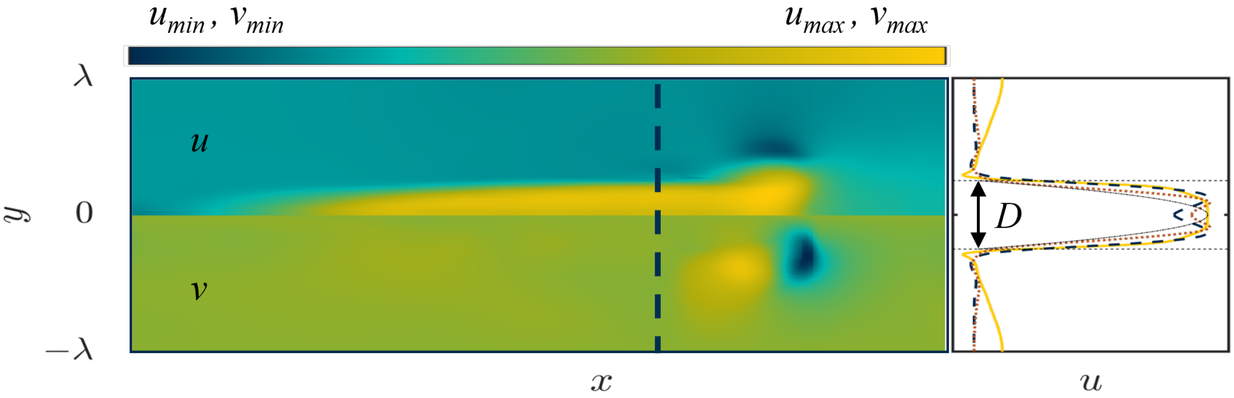

Figure 5.5: The x- (top) and y- (bottom) components of velocity as a protrusion of aspect ratio $L/D = 8$ initially along an interface separating two fluids with a density ratio $\rho_H/\rho_L = 2$ inverts following the passage of a shock wave of strength $\rho_{H'}/\rho_H = 1.34$ (left), and the horizontal velocity profile of the inverting protrusion at the horizontal location of the residual interface (i.e., the portion of the interface that does not include the protrusion) immediately after shock passage (yellow solid line), as the protrusion is inverting (blue dashed line), and near the end of the protrusion inversion process (orange dotted line). The vertical blue dashed line over the velocity contours indicates the horizontal location of the residual interface at the time shown, which also corresponds to the blue dashed velocity profile. The horizontal thin dashed black lines indicate the original protrusion diameter D and the thin dashed-dotted line shows a parabolic profile for reference.

the shock passes through the interface, it is significantly flatter than parabolic. The curvature in the profile at this time beyond the radius of the protrusion is a result of the slight curvature of the initial interface outside of the protrusion and is observed to flatten out in time. As the inversion process continues, the convexity near the center of the profile changes as a result of the positive horizontal velocity from the forming vortex ring as the centers of the cores are approached from the center of the ring (i.e., as $y = \pm D/2$ is approached from $y = 0$). While this represents a further departure from a parabolic profile, outside of this region near $y = 0$, the profile appears to be to approaching a parabolic shape, but does not converge to a parabola before the protrusion inversion process is complete. The transition from a relatively flat to near-parabolic profile observed in our simulations is consistent with the piston-cylinder systems on which we base our theory [84, 225]. The width of the profile D remains relatively constant throughout the inversion process.

5.6.2 Numerical Methods

Our in-house discontinuous-Galerkin (DG) code [60] is used for the computations presented in this chapter solving the Euler equations governing inviscid fluid flow. The base spatial scheme is fifth-order accurate for cases 1-4 outlined in Table 5.1 of the manuscript and third-order accurate for cases 5 and 6, while fourth-order explicit Runge-Kutta is used for time advancement. Fluxes are calculated with a Roe solver and hierarchical limiting is applied selectively at discontinuities based on a sensor to enable interface and shock capturing [60, 109]. The code is parallelized with MPI and CUDA so that it can run on CPU- and GPU-based clusters. The code has been validated against experiments for Richtmyer-Meshkov problems [59, 60, 280].

An ideal gas equation of state with an adiabatic index of $\gamma = 1.4$ is utilized throughout the chapter. The interface surrounding the heavy-fluid protrusion consists of a low-amplitude perturbation to facilitate the pinch-off of the vortex ring. The shape of the protrusion is a steepened sinusoid, creating a nearly cylindrical protrusion with both steep edges and smooth corners that facilitate the computation. Specifically, as a function of the radius $r = \sqrt{(x - x_0)^2 + (z - z_0)^2}$, where (x_0, z_0) defines centerline of the protrusion, and $\theta = \tan^{-1}\left(\frac{z-z_0}{x-x_0}\right) \in (-\pi, \pi)$, the depth of the interface is given by

$$l(r,\theta) = \begin{cases} L\left[1 - \cos\left(\pi\frac{r}{D}\right)\right]^5 - L & \text{for } r \leq \frac{D}{2} \\ 0.06\Big\{1 - \cos\left[\frac{\pi}{2} * \left(\Lambda(\theta) - r + \frac{D}{2}\right)/\Lambda(\theta)\right]\Big\} - 0.06 & \text{for } r > \frac{D}{2} \end{cases} \tag{5.7}$$

where

$$\Lambda(\theta) = \begin{cases} \frac{W/2}{|\sin\theta|} - \frac{D}{2} & \text{for } \frac{\pi}{4} < |\theta| < \frac{3\pi}{4} \\ \frac{W/2}{|\cos\theta|} - \frac{D}{2} & \text{otherwise} \end{cases} \tag{5.8}$$

is the distance between the edge of the circular protrusion and the edge of the computational domain with a square cross section.

For cases 1-4 outlined in Table 5.1, the simulations are performed on a regular Cartesian mesh of $32 \times 160 \times 32$ cells each supporting a quadratic tensor product polynomial basis. Cases 5 and 6 utilize a linear tensor product polynomial basis to enable accurate and robust representation of the stronger shocks. Given the problem symmetry, a quarter of the domain is simulated. The width of the protrusion is $D = W/4$, where W is twice the width of the computational domain (see Figure 5.2 in Chapter 5). All quantities are non-dimensionalized by the width of the domain and the sound speed in the unshocked heavy fluid. Non-reflecting boundaries are prescribed in the direction of shock propagation, with reflecting boundaries along the remaining sides. While this set-up physically corresponds to a semi-infinite array of protrusions, the effects of neighboring rings on the formation number is negligible. We verify by a set of simulations with $D = W/3$ performed with the same protrusion resolution that the formation number differs by approximately 1% from the simulations with $D = W/4$. The assertion that neighboring rings do not affect the formation number is further supported by recent work [56] examining confined vortex rings concluding that the effects of boundaries are negligible when they exist at or beyond four times the radius of a

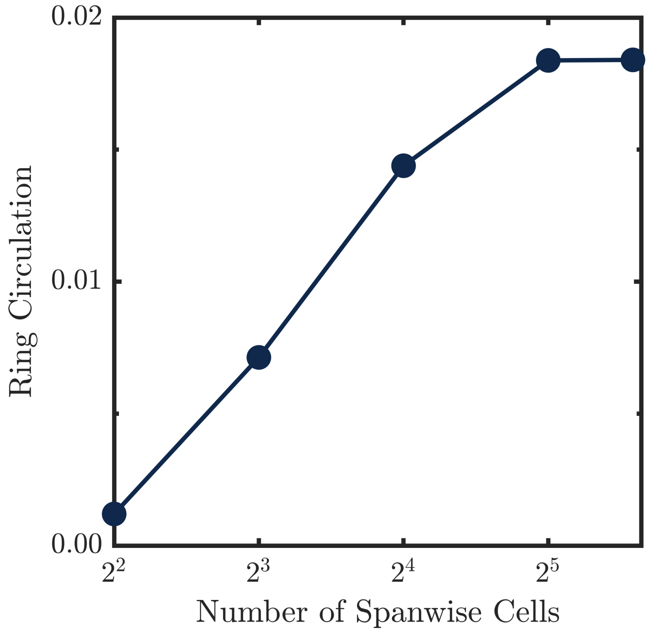

Figure 5.6: Vortex ring circulation vs. number of spanwise cells after a shock of strength $\rho_{H'}/\rho_H = 1.34$ accelerates a $\rho_H/\rho_L = 2$ (see case 3 in Table 5.1 in main text) interface with an $L/D = 0.5$ heavy-fluid protrusion. While computational constraints limit us from examining simulations at twice the resolution performed in this work, the simulation with 48 cells indicates convergence of the circulation with 32 cells, the resolution for all simulations performed.

ring-generating cylinder, a condition that is satisfied in the present work. Integral quantities like the circulation are well converged at the selected resolution for each case explored, as exemplified in Figure 5.6.

CHAPTER 6

On the Stability of a Pair of Vortex Rings

This chapter is adapted from M. J. Wadas, S. Balakrishna, H. J. LeFevre, C. C. Kuranz, A. Towne, and E. Johnsen, On the stability of a pair of vortex rings, *Under Review in Journal of Fluid Mechanics* [277].

6.1 Abstract

The growth of perturbations subject to the Crow instability along two vortex rings of equal and opposite circulation undergoing a head-on collision is examined. Unlike the planar case for semi-infinite line vortices, the zero-order geometry of the flow (i.e., the ring radius, core thickness, and separation distance) and by extension the growth rates of perturbations vary in time. The governing equations are therefore temporally integrated to characterize the perturbation spectrum. The analysis, which considers the effects of ring curvature and the distribution of vorticity within the vortex cores, explains several key flow features observed in experiments. First, the zero-order motion of the rings is accurately reproduced. Next, the predicted emergent wavenumber, which sets the number of secondary vortex structures emerging after the cores come into contact, agrees with experiments, including the observed increase in the number of secondary structures with increasing Reynolds number. Finally, the analysis predicts an abrupt transition at a critical Reynolds number to a regime dominated by a higher-frequency, faster-growing instability mode that may be consistent with the experimentally observed rapid generation of a turbulent puff following the collision of rings at high Reynolds numbers. While the present chapter considers the stability of vortex cores in the absence of both shocks and interfaces, it builds the necessary theory to describe a previously unexplained astrophysical phenomenon, the focus of the next and final technical chapter.

6.2 Introduction

Vortical flows comprise a vast range of fluid mechanics including propeller and turbine wakes [126, 274, 287], mixing from the interaction of a shock wave with a material interface [280, 300, 307, 308], and turbulent transition [74, 295, 306]. Understanding the dynamics of isolated or a small number of vortices is essential for successful operation of engineering applications in propulsion and energy generation [230] and elucidates naturally occurring flows involving, for example, jellyfish mobility [54, 195] or cardiac hemodynamics [83, 180]. The interactions between such vortices are governed in part by the growth of unstable perturbations causing the vortices to stretch and bend, rapidly increasing the complexity of the flow [135]. Two instability mechanisms are primarily responsible for this growth: the Crow instability (CI) [53] and the elliptic instability [116, 136, 163, 187, 270]. The present work concerns the former, which often develops in isolation before stimulating the later [135].

The CI was originally considered in the context of wingtip vortices shed into the wakes of large aircraft [53]. These highly coherent and violent fluid structures pose a safety hazard for small crafts as well as ground structures near runways; expediting the dissipation of wing-tip vortices remains an active area of research [24, 52, 92, 189]. Perturbations along such pairs of line vortices grow under the influence of their mutual and self induction until they come into contact, triggering a complex vortex reconnection process that can ultimately result in the formation of a series of vortex rings [79, 100, 117, 272, 295]. The original stability analysis, based on planar, irrotational vortex cores, generally yields three distinct wavenumbers with locally maximal growth rates. Two of these wavenumbers are associated with a symmetric mode, where perturbations on one core appear as a reflection of those along the other core, and the third is associated with an anti-symmetric mode of in-phase perturbations. While the classical analysis predicts faster-growing anti-symmetric and high-frequency symmetric modes, these high-frequency modes were shown to be spurious for elliptically loaded wings [135, 137, 292], and the low-frequency symmetric mode therefore emerges in practice. Following the original analysis, advancements were made including extensions to general core vorticity distributions and axial flow [186, 291], stratified surrounding fluids [229, 233], and alternate geometries including vortex arrays and co-rotating cores [107, 223].

The CI and the formation of secondary vortex rings were observed in experiments of colliding co-axial vortex rings of equal strength [141], spurring subsequent studies of the phenomenon examining the evolution of enstrophy during different stages of the ring collision [46], compressibility [177], and numerical requirements for accurate simulation [147]. More recently, this canonical flow was used to study vortex interactions and the generation of scales leading up to the transition to turbulence, in particular the emergence of a turbulent puff beyond a critical Reynolds number [25, 144, 157, 158, 178, 198]. While the importance of the CI is well recognized in vortex ring collisions, existing stability analyses ignore the effects of ring curvature and zero-order motion of the flow, instead applying the existing planar analysis once the perturbation amplitudes are visible in experiments and the rings have expanded to large radii [53, 141]. By this point in the flow evolution, however, the linear growth of the perturbations is nearly saturated, and such treatment therefore is unable to capture the details of the prior instability growth through orders of magnitude originating from the initial perturbation. Furthermore, because the ring collision results in small core separation distances, an accurate description of the vorticity distribution within the cores is essential [135]. In addition, studying the turbulent transition behaviour of colliding rings requires viscous analysis. Although the effects of general vorticity distributions and viscosity on vortex cores have been considered, theoretical stability studies have not specifically examined coaxial vortex ring collisions [229, 230, 290, 291] or are otherwise numerical in nature with a more general focus on flow morphology [39, 40, 118, 147].

While complex fluid mechanisms are expected to affect the collision of two co-axial vortex rings (e.g., vortex reconnection, other instabilities, and turbulent transitions), especially at late times, the CI serves as the backbone on which the flow initially develops. Our objective is therefore to analyze the linear stability of the cylindrical CI for colliding, co-axial vortex rings while considering the effects of ring curvature, zero-order motion, core vorticity distributions, and viscosity. The present focus is on rings of equal and opposite strengths, but the analysis can be readily extended to asymmetric vortex ring interactions. Similar to the classical stability analysis, our model enables an analytical solution for the eigenvalues that directly yields the growth rates for all wavenumbers. Unlike the classical planar case, the growth rate of the most unstable mode varies due to the zero-order motion of the flow. Despite this difficulty, our analysis correctly predicts the emergent wavenumber in experiments, corresponding to the number of observed secondary vortex rings, and furthermore provides an additional explanation for the emergence of the low-frequency symmetric mode even for flows where the higher-frequency symmetric and anti-symmetric modes may not be spurious. Finally, our analysis demonstrates a mechanism by which viscosity affects the number of secondary rings that emerge and the onset of a turbulent cloud beyond a critical Reynolds number. The chapter is organized as follows: Section 6.3 outlines our model flow and the corresponding linear stability analysis, Section 6.4 reports on the results of the analysis alongside validation with existing experimental data, Section 6.5 discusses important implications of the present work, results are summarized and conclusions drawn in Section 6.6, and supplemental material is provided in Section 6.7.

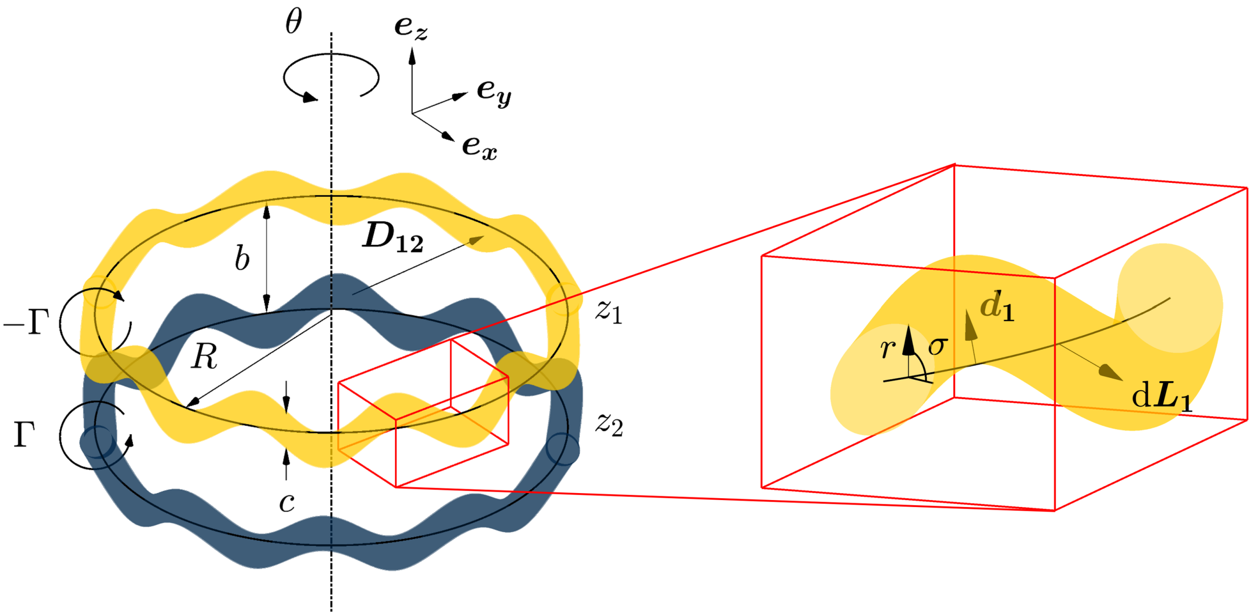

Figure 6.1: The setup for the stability analysis showing two perturbed circular vortex cores radius R, core thickness c, and separation distance b of equal and opposite circulation Γ.

6.3 Linear Stability Analysis

We consider the stability of perturbations $\boldsymbol{d_n}$ along two co-axial counter-rotating vortex rings of radius R and thickness c separated by a distance b of equal circulation magnitude Γ, as depicted in Figure 6.1. We begin by extending the classical analysis of Ref. [53], where the rings are modeled as irrotational vortices in an incompressible, inviscid fluid. The velocity at any point along either ring is then given by the Biot-Savart law,

$$\boldsymbol{U_n} = \sum_{m=1}^{2} \frac{\Gamma_m}{4\pi} \int \frac{\boldsymbol{D_{mn}} \times d\boldsymbol{L_m}}{|\boldsymbol{D_{mn}}|^3} = \boldsymbol{e_x} u_n + \boldsymbol{e_y} v_n + \boldsymbol{e_z} w_n, \tag{6.1}$$

where $\boldsymbol{D_{mn}}$ is the displacement vector to a point on ring m from a point on ring n, $d\boldsymbol{L_n}$ is the differential tangent vector, and $\boldsymbol{e_x}$, $\boldsymbol{e_y}$, and $\boldsymbol{e_z}$ are Cartesian unit vectors in the x-, y-, z-directions, respectively. Mathematically,

$$\begin{aligned}
\boldsymbol{d_n} &= \boldsymbol{e_x} h_n(\theta_n, t) \cos\theta_n + \boldsymbol{e_y} h_n(\theta_n, t) \sin\theta_n + \boldsymbol{e_z} s_n(\theta_n, t), \\
\boldsymbol{D_{mn}} &= \boldsymbol{e_x} R \left(\cos\theta_{m'} - \cos\theta_n\right) + \boldsymbol{e_y} R \left(\sin\theta_{m'} - \sin\theta_n\right) + \boldsymbol{e_z} \left(z_m - z_n\right) + \left(\boldsymbol{d_{m'}} - \boldsymbol{d_n}\right), \\
d\boldsymbol{L_n} &= \left(-\boldsymbol{e_x} R \sin\theta_n + \boldsymbol{e_y} R \cos\theta_n + \frac{\partial \boldsymbol{d_n}}{\partial \theta_n}\right) d\theta_n,
\end{aligned} \tag{6.2}$$

where $\theta_n = \tan^{-1}\frac{y_n}{x_n}$, $h_n(\theta_n, t)$ is the perturbation amplitude in the $x - y$ plane, and $s_n(\theta_n, t)$ is the perturbation amplitude in the the z-direction. The m' subscript applies when $m = n$ (i.e., when evaluating the influence of one ring at a point on the same ring). Perturbations evolve under the constraint that they move at the local fluid velocity,

$$\frac{\partial \boldsymbol{d_n}}{\partial t} + u_n \frac{\partial \boldsymbol{d_n}}{\partial x_n} + v_n \frac{\partial \boldsymbol{d_n}}{\partial y_n} + w_n \frac{\partial \boldsymbol{d_n}}{\partial z_n} = \boldsymbol{e_x} u_n + \boldsymbol{e_y} v_n + \boldsymbol{e_z} w_n. \tag{6.3}$$

Up to this point, the analysis accurately describes the system as long as the ratio between the core separation distance and the core thickness b/c remains large. However, as the rings approach, this condition is violated. We therefore model the cross section of each ring as a Lamb-Oseen vortex core with azimuthal vorticity

$$\omega(r,t) = \frac{\Gamma}{4\pi\nu(t - t_0)\,(c/c_0)^2} \exp\left[-\frac{r^2}{4\nu(t - t_0)\,(c/c_0)^2}\right], \tag{6.4}$$

where r is the distance from the vortex core center, t is time, t_0 is the initial time, ν is the fluid viscosity, and c_0 is the initial core thickness. The c/c_0 factor is a consequence of mass conservation and accounts for the concentration of vorticity due to changes in the vortex core thickness. The Lamb-Oseen core given in Equation 6.4 is incorporated into the analysis by means of an effective core separation distance for the velocity in both the vertical and radial directions $b_{ef,z}$ and $b_{ef,rad}$, respectively, similar to Ref. [291]. Physically, the effective core separation distance is the separation distance of an irrotational vortex core that induces the same velocity at the center of the other core as given by a Lamb-Oseen vortex core at the separation distance. For example, the vertical velocity at the top core imparted by a bottom irrotational core separated by $b_{ef,z}$ is the same as that for a Lamb-Oseen vortex core separated by b. The effective separation distances are computed by equating the components of the following vector equation expressing the aforementioned velocity equivalence,

$$\frac{\Gamma_2}{4\pi} \int \frac{\boldsymbol{D_{IR}} \times d\boldsymbol{L_{IR}}}{|\boldsymbol{D_{IR}}|^3} = \frac{1}{4\pi} \int_0^{R_{0.99\Gamma}} \int_0^{2\pi} \int_0^{2\pi} \omega(r,t) \frac{\boldsymbol{D_{LO}} \times d\boldsymbol{L_{LO}}}{|\boldsymbol{D_{LO}}|^3} r\, d\sigma\, dr, \tag{6.5}$$

where

$$\begin{aligned}
\boldsymbol{D_{IR}} &= \boldsymbol{e_x} R\left(\cos\theta_2 - \cos\theta_1\right) + \boldsymbol{e_y} R\left(\sin\theta_2 - \sin\theta_1\right) + \boldsymbol{e_z}\left(-b_{ef}\right), \\
d\boldsymbol{L_{IR}} &= \left(-\boldsymbol{e_x} R \sin\theta_2 + \boldsymbol{e_y} R \cos\theta_2\right) d\theta_2, \\
\boldsymbol{D_{LO}} &= \boldsymbol{e_x}\left[R\left(\cos\theta_2 - \cos\theta_1\right) + r\cos\sigma\cos\theta_2\right] + \boldsymbol{e_y}\left[R\left(\sin\theta_2 - \sin\theta_1\right) + r\cos\sigma\cos\theta_2\right] \\
&\quad + \boldsymbol{e_z}\left(-b + r\sin\sigma\right), \\
d\boldsymbol{L_{LO}} &= \left[-\boldsymbol{e_x}\left(R + r\cos\sigma\right)\sin\theta_2 + \boldsymbol{e_y}\left(R + r\cos\sigma\right)\cos\theta_2\right] d\theta_2,
\end{aligned} \tag{6.6}$$

σ is the angle within the core, $R_{0.99\Gamma} = \sqrt{-4\nu t(c/c_0)^2 \ln(1-0.99)}$ is the radius that encloses 99% of the Lamb-Oseen vortex circulation, which is sufficient for the convergence of the integral in Equation 6.5, and θ_1 can be any angle. We choose $\theta_1 = 0$, and b_{ef} is understood to be $b_{ef,z}$ or $b_{ef,rad}$ for the vector component equations in the vertical, $\boldsymbol{e_z}$, or radial, $\boldsymbol{e_x}$, directions, respectively.

With the effective separation distances calculated, the analysis proceeds by equating Equation 6.1 and Equation 6.3 with substitutions from Equation 6.2. The resulting equations are then linearized in the reference frame of the zero-order motion of the flow under the assumption that the zero-order motion is quasi-steady compared to the first-order motion, which is verified later. A normal modes ansatz is assumed for the perturbations $\boldsymbol{d_n} = \widetilde{\boldsymbol{d_n}} e^{at+ik\theta_n}$, where $a = \alpha + i\mu$, α is the growth rate, μ is the temporal frequency, and k is the integer wavenumber of the perturbation, resulting in an eigenvalue system of the form

$$a \begin{bmatrix} \widetilde{h}_1 \\ \widetilde{s}_1 \\ \widetilde{h}_2 \\ \widetilde{s}_2 \end{bmatrix} = \begin{bmatrix} M_{1,1} & M_{1,2} & M_{1,3} & M_{1,4} \\ M_{2,1} & M_{2,2} & M_{2,3} & M_{2,4} \\ M_{3,1} & M_{3,2} & M_{3,3} & M_{3,4} \\ M_{4,1} & M_{4,2} & M_{4,3} & M_{4,4} \end{bmatrix} \begin{bmatrix} \widetilde{h}_1 \\ \widetilde{s}_1 \\ \widetilde{h}_2 \\ \widetilde{s}_2 \end{bmatrix}, \tag{6.7}$$

where the matrix coefficients are provided in Section 6.7. General eigenvalues can be computed directly from Equation 6.7, including for interactions that are asymmetric (e.g., rings with different radii, core thicknesses, strengths, and lines of axisymmetry). However, due to the symmetry of the colliding rings in the present case, $M_{3,1} = M_{1,3}$, $M_{3,2} = -M_{1,4}$, $M_{3,3} = M_{1,1}$, $M_{3,4} = -M_{1,2}$, $M_{4,1} = -M_{2,3}$, $M_{4,2} = M_{2,4}$, $M_{4,3} = -M_{2,1}$, and $M_{4,4} = M_{2,2}$. These coefficients may include integrals from Equation 6.1, which are evaluated along the length of the vortex cores. For the planar case examined by [53], where the vortex cores are infinite lines extending in the x-direction, the integrals are evaluated from $x \in (-\infty, \infty)$. In the cylindrical case examined here, the integrals are evaluated from $\theta_n \in (0, 2\pi)$ when $m \neq n$. The cutoff model is used to represent the finite core thickness by evaluating the integral from $\theta_n \in (d/R, 2\pi - d/R)$ when $m = n$, circumventing the singularity in Equation 6.1 when $D_{mn} \to 0$ as in Ref. [53]. In the classical analysis, the cutoff distance, d, is found by matching the translational velocity of a thin-core vortex ring to that predicted by the cutoff method [53, 113]. However, because the cores of rings that emerge from piston-cylinder devices relevant to experiments are not necessarily thin, we use a cutoff parameter that is a function of the core thickness calibrated to the translational velocity of the Norbury family of vortex rings [200], as shown in Figure 6.2.

As in the planar case [53], the eigenvalues associated with Equation 6.4 can be combined into symmetric and anti-symmetric modes,

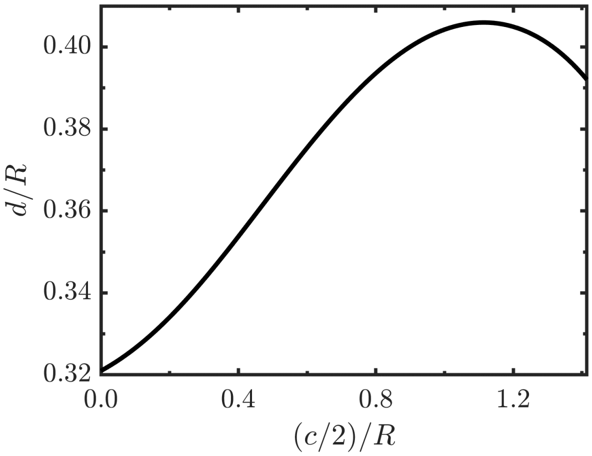

Figure 6.2: The cutoff parameter as a function of the core thickness.

$$\begin{aligned}
&\widetilde{s}_S = \widetilde{s}_2 - \widetilde{s}_1, \widetilde{h}_S = \widetilde{h}_2 + \widetilde{h}_1,\\
&\widetilde{s}_A = \widetilde{s}_2 + \widetilde{s}_1, \widetilde{h}_A = \widetilde{h}_2 - \widetilde{h}_1,
\end{aligned} \tag{6.8}$$

respectively, yielding four roots,

$$\begin{aligned}
a_{S^\pm} = \; & \tfrac{1}{2}\Big\{M_{1,1} + M_{1,3} + M_{2,2} - M_{2,4} \pm \big\{(M_{1,1} + M_{1,3} + M_{2,2} - M_{2,4})^2 \\
& -4\left[(M_{1,1} + M_{1,3})(M_{2,2} - M_{2,4}) - (M_{1,2} - M_{1,4})(M_{2,1} + M_{2,3})\right]\big\}^{\frac{1}{2}}\Big\},\\
a_{A^\pm} = \; & \tfrac{1}{2}\Big\{M_{1,1} - M_{1,3} + M_{2,2} + M_{2,4} \pm \big\{(M_{1,1} - M_{1,3} + M_{2,2} + M_{2,4})^2 \\
& -4\left[(M_{1,1} - M_{1,3})(M_{2,2} + M_{2,4}) - (M_{1,2} + M_{1,4})(M_{2,1} - M_{2,3})\right]\big\}^{\frac{1}{2}}\Big\}.
\end{aligned} \tag{6.9}$$

The coefficients $M_{1,1}, M_{1,3}, M_{2,2}, M_{2,4} \to 0$ with increasing ring radius, and the planar case is indeed recovered as $R \to \infty$.

In addition to the generalized roots in Equation 6.9, a key difference distinguishing the cylindrical case from the classical planar case is the zero-order motion of the flow. In the planar case, the constant downward velocity of the vortex cores affects neither the core separation distance nor the core thickness and therefore does not alter the stability. In the present work, however, the motion of circular vortex cores causes their separation distance, radius, and thickness to vary in time, resulting in time-dependent growth rates. The governing equations must therefore be integrated in time to determine the growth of perturbations along the vortex cores. The zero-order velocity can be determined using Equation 6.1, substitutions from Equation 6.2 with $h_n, s_n = 0$ (i.e., no perturbations) and the effective separation distance, and the cutoff method [53] with the Norbury-calibrated cutoff parameter. The integration is handled with a simple forward-Euler scheme that updates the ring radius and separation distance from the calculated radial and vertical velocities, respectively, at each time step. Since the flow is assumed incompressible, the core size is then updated to conserve the volume of the ring. The growth rates from Equation 6.9 are then used to update the amplitudes of the perturbations of both the symmetric and anti-symmetric modes, which are initialized as a uniform spectrum of amplitude $\sqrt{\widetilde{s}_S^2 + \widetilde{h}_S^2} = \sqrt{\widetilde{s}_A^2 + \widetilde{h}_A^2} = q_0$. The number of vortex rings emerging as a result of the CI is taken to correspond to the wavenumber of the mode that first reaches an amplitude on the order of the ring separation distance. Spurious high-frequency unstable modes (i.e., unstable modes occurring at larger wavenumbers than those of the high-frequency symmetric and anti-symmetric modes) are ignored as in [53].

6.4 Results

After verifying the zero-order motion of the flow, the growth of perturbations is examined for a collision involving two vortex rings of relatively low strength (i.e., circulation). Later, a collision of stronger vortex rings is examined in the context of a mechanism that may contribute to the transition of the flow to a turbulent puff.

6.4.1 Zero-Order Motion

We examine a set of initial conditions approximately matching the experiments of Ref. [157] where the initial geometry is given by $R_0 = 17.5\,\text{mm}$, $c_0 = 7.0\,\text{mm}$, and $b_0 = 70.0\,\text{mm}$. The rings in this experiment are generated from a piston-cylinder device submerged in a water tank with a stroke-to-diameter ratio $SR = 2.5$, and the Reynolds number based on the diameter of the cylinder, the piston velocity, and the viscosity of water is $Re = 4000$. The model of Refs. [64, 65] can be used to estimate the ring circulation as

$$\Gamma = \left(1.14 + \frac{0.32}{SR}\right) Re\, \nu, \tag{6.10}$$

where $\nu = 1.0\,\text{mm}^2\,\text{s}^{-1}$ and t_0 is chosen such that the vorticity profile within the cores matches experiments at $t = 0$, see Equation 6.4. Figure 6.3a shows the zero-order motion of the flow. Initially, when the separation distance is large, the vortex rings propagate at a nearly constant velocity with minimal change in their radii or core thicknesses, consistent with the motion of two isolated, steady vortex rings. As they approach, however, their translational speed decreases and their radii begin to increase due to the influence of each ring on the other, as shown in Figure 6.3b. After a period of rapidly increasing radial velocity, the ring radii increase at a nearly constant rate as their separation distance approaches a nearly constant value. After $t \approx 1.0\,\text{s}$, the agreement between the model and the experimental data diverges slightly. This time, however, corresponding to a ring radius of approximately 80 mm, is consistent with the visible onset of the instability [157], as evidenced by the sudden shift in the vertical location of the ring cores, Figure 6.3c, and the increase in the scatter in the experimental core thickness data, Figure 6.3d. Finally, Figure 6.3e shows the values of $b_{ef,z}$ and $b_{ef,rad}$. Early in time, when the rings are far apart, the effective separation distance is near the value of the separation distance. Physically, this behaviour is a result of the velocity field from one ring at the location of the other for both an irrotational vortex and a Lamb-Oseen vortex being similar. As the rings approach, however, the velocity field from the Lamb-Oseen core diverges from that of an irrotational core because of the weighted influence of the vorticity in the core nearer to the other ring. This discrepancy causes the effective radial separation distance to decrease while the effective vertical separation distance increases. As the rings continue their approach, both effective separation distances decrease to a constant value. The agreement between the model and experiments in Figure 6.3b-d demonstrates that the zero-order motion of the present system adequately represents physical experiments.

Figure 6.3b also shows the ring radius as a function of time assuming $b_{ef} = b$, i.e., the cores are assumed irrotational, as in the classical analysis. While this model works well for adequately separated cores, it breaks down as the rings approach, resulting in erroneously large ring radii. Because the vorticity within an irrotational vortex is confined to a line, there is no mechanism preventing the separation distance between the cores from approaching zero, at which point the rate at which the ring radii expand unphysically approaches infinity. The consideration of a finite-vorticity distribution within the cores is therefore essential to accurately describe the zero-order motion of this flow. Moreover, because the zero-order parameters of the flow affect the evolution of perturbations, see Equation 6.9, their accurate description is required for the linear analysis, which is discussed next.

6.4.2 First-Order Motion

The evolution of linear perturbations (i.e., the first-order motion of the flow) is given as a function of wavenumber and time in Figure 6.4. The analysis considers perturbation growth only from the CI and neglects instabilities associated with isolated vortex cores [292]. Perturbations are initialized as a uniform spectrum with an amplitude on the order of the mean free path of the flow, $q_0 = 0.13\,\text{nm}$, which is also enforced as the minimum perturbation amplitude. Physical quantities are nondimensionalized by the vortex ring circulation and initial radius. We examine the growth rates and perturbation amplitudes for both the symmetric and anti-symmetric modes to illustrate the evolution of perturbations at three different nondimensional times corresponding to the initial, intermediate, and final stages of perturbation growth, $t^{init}_{Re=4000}$, $t^{inter}_{Re=4000}$, $t^{fin}_{Re=4000}$, respectively, as

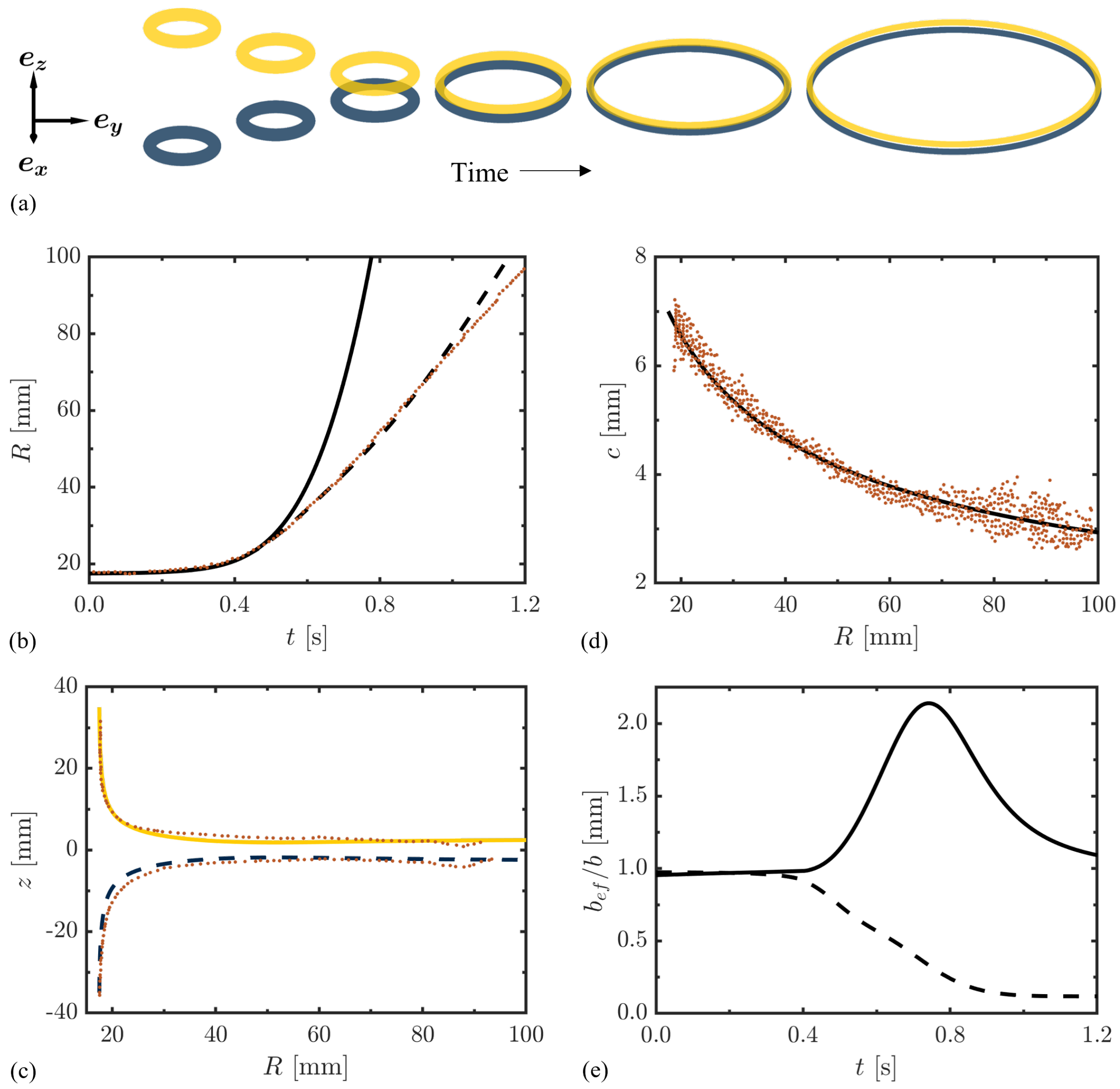

Figure 6.3: The zero-order motion for colliding rings (a), ring radius versus time for irrotational (solid line) and Lamb-Oseen (dashed line) vortices (b), vertical position of the upper (yellow solid line) and lower (blue dashed line) rings versus ring radius for Lamb-Oseen vortices (c), core thickness versus ring radius (d), and the vertical (dashed line) and radial (solid line) effective separation distances (e) for rings with $R_0 = 17.5\,\text{mm}$, $b_0 = 70.0\,\text{mm}$, $c_0 = 7.0\,\text{mm}$, and $Re = 4000$. Experimental data (orange dots) [157] is provided for comparison (b-d). In (a), each subsequent image from left to right is 200 ms later in time than the previous.

shown in Figure 6.4c,f.

After the flow initially becomes unstable, three separate bands of spatial frequencies experience perturbation growth, as shown in Figure 6.4 at time $t^{init}_{Re=4000} = 9.1$, indicated by the dotted line. The symmetric mode is excited within a band extending from $k = 1$ to some $k > 1$, which we refer to as the low-frequency symmetric band, and a separate band between two higher frequencies, which we refer to as the high-frequency symmetric band. The anti-symmetric mode is excited within a single range of frequencies, namely the anti-symmetric band, in the vicinity of the high-frequency symmetric band. At any given time, the wavenumber with the fastest growth rate exists within the anti-symmetric band. The amplitudes of these excited modes increases, with the largest growth experienced by the wavenumber associated with the fastest growing mode within the anti-symmetric band.

At time $t^{inter}_{Re=4000} = 13.3$, indicated by the dashed lines in Figure 6.4, growth rates increase primarily because of the decreasing separation distance. Furthermore, as the cores expand, they can support the growth of increasingly large wavenumbers. The high- and low-frequency bands of the symmetric mode merge, though there are still two local growth rate maxima. The fastest growth rate is still experienced by a wavenumber within the anti-symmetric band; however, at this time, the wavenumber with the greatest amplitude exists within the symmetric band. By this time, the zero-order motion of the flow, while slow compared to the growth of perturbations, causes the anti-symmetric band to migrate to an entirely different range of wavenumbers than at time $t^{init}_{Re=4000}$. The low-frequency symmetric band, however, excites a wider range of wavenumbers that includes those excited at time $t^{init}_{Re=4000}$. As a result, although these wavenumbers are never growing as fast as the maximally excited wavenumber within the anti-symmetric band, they grow for a longer period of time and therefore reach greater amplitudes.

The final time examined, $t^{fin}_{Re=4000} = 16.7$, indicated by the solid lines in Figure 6.4, corresponds to the time when the perturbation amplitude reaches the separation distance. The growth rates decrease from time $t^{inter}_{Re=4000}$ because the separation distance increases slightly as a result of the viscous relaxation of the Lamb-Oseen vortex core and a tendency of the colliding rings to rebound. The high- and low-frequency bands of the symmetric mode separate, and the increasing radii of the expanding cores enable all three bands to support growth at larger wavenumbers. As before, the anti-symmetric band migrates to a different range of frequencies, along with the high-frequency band of the symmetric mode, while the low-frequency band of the symmetric mode is still causing perturbation growth at the lower frequencies excited at earlier times. As a result, the slower-growing symmetric mode dominates the linear evolution once the perturbations are large enough to be examined experimentally. The wavenumber with an amplitude that first reaches the separation distance, which we herein refer to as the emergent wavenumber, is associated with the symmetric mode and equal to $k^{emerg} = 18$, which is consistent with the number of secondary rings observed

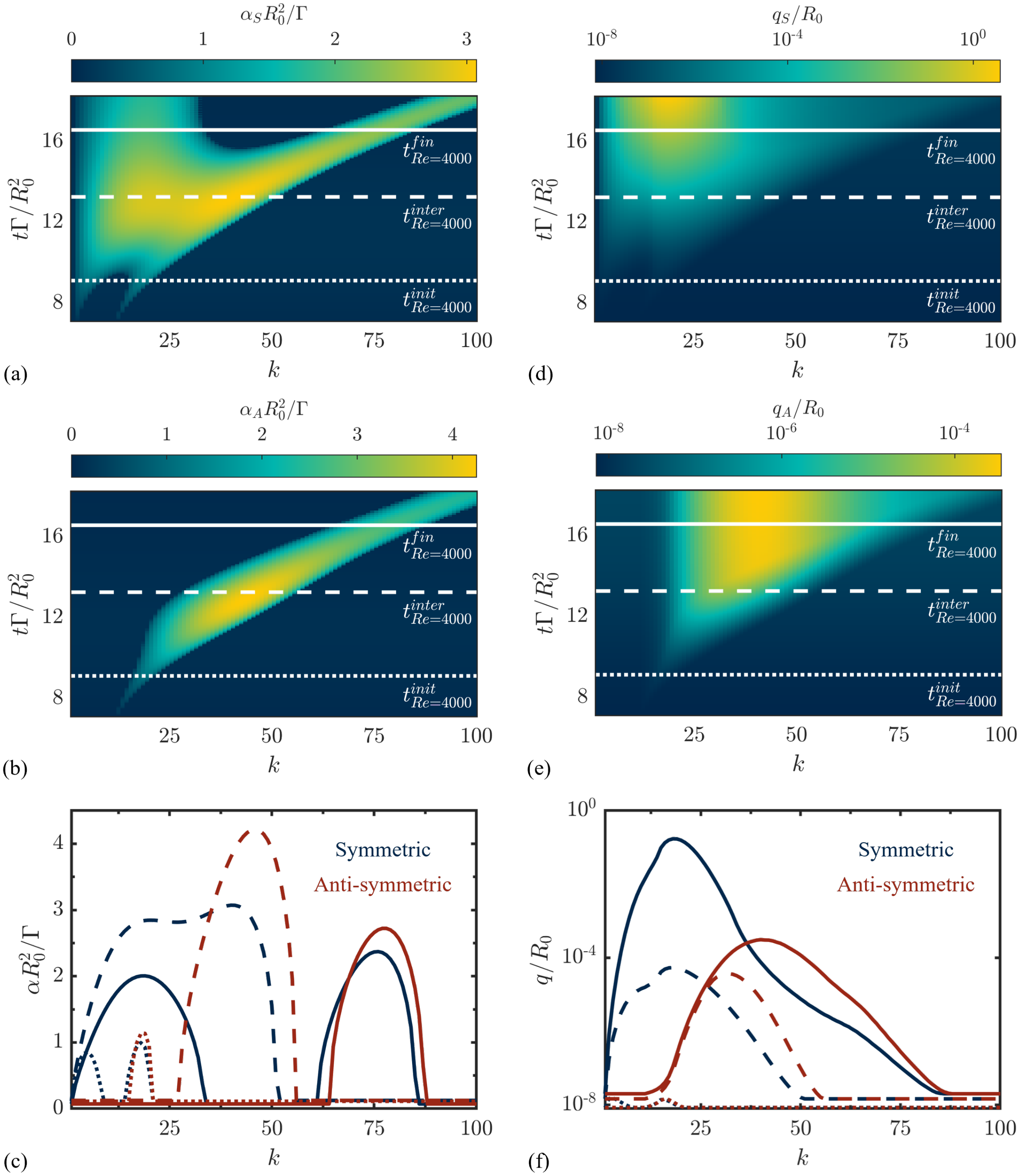

Figure 6.4: The growth rates (a-c) and perturbation amplitudes (d-f) of the symmetric (a,d) and anti-symmetric (b,e) modes for colliding rings with $b_0/R_0 = 4$, $c_0/R_0 = 0.4$, and $Re = 4000$. Lineouts in (c,f) correspond to $t^{init}_{Re=4000} = 9.1$ (dotted), $t^{inter}_{Re=4000} = 13.3$ (dashed), and $t^{fin}_{Re=4000} = 16.7$ (solid).

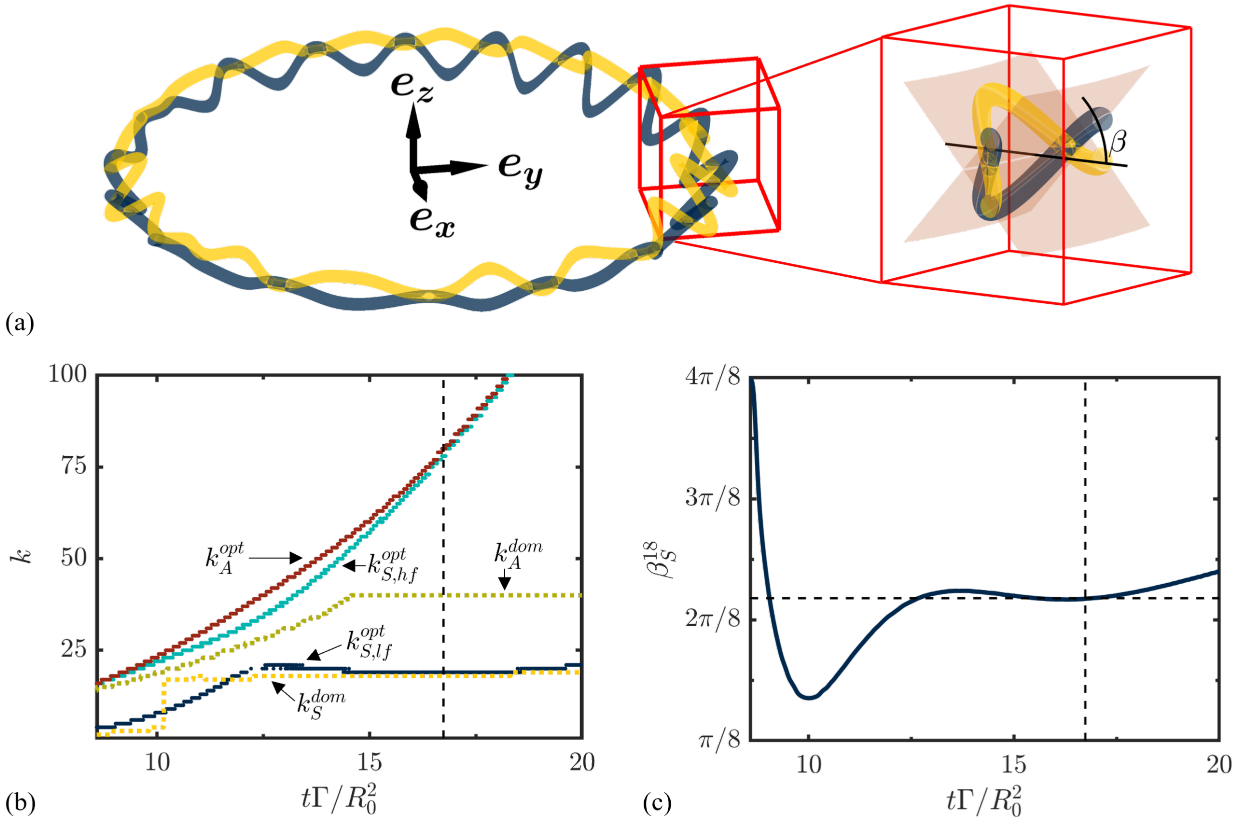

Figure 6.5: The vortex cores at a time when the amplitude of the emergent wavenumber is on the order of the core separation distance (a), the wavenumbers experiencing maximal growth in the low- (blue solid line) and high-frequency (teal solid line) symmetric band and the anti-symmetric (red solid line) band and the largest amplitude symmetric (yellow dotted line) and anti-symmetric (green dotted line) wavenumbers (b), and the growth angle of the emergent wavenumber versus time (c). The thin black vertical dashed lines indicate the time represented in (a) and the thin horizontal black dashed line in (c) indicates $\beta = 0.86\,\mathrm{rad}$.

in the experiments of Ref. [157]. The dimensional time at which this happens, $t \approx 1\,\mathrm{s}$, is also consistent with the visible onset of the instability.

Figure 6.5a shows the perturbed vortex cores at time $t_{Re=4000}^{fin}$, where perturbations associated with each wavenumber are added together with a random phase angle. While the cores here are shown intersecting one another, in reality, a complex vortex reconnection process occurs when the cores come in contact that results in the original cores breaking up into a series of smaller, or secondary, vortex structures [100, 117, 272, 295]. The number of these smaller structures can be reasonably approximated by the emergent wavenumber. However, because other wavenumbers also experience significant growth, the number of secondary structures, and their sizes, may vary, as seen in experiments [141, 157].

The means by which perturbations grow from their initial amplitudes to those represented in

Figure 6.5a is a complex process during which the wavenumber that grows the fastest, the maximal wavenumber k^{max}, and the wavenumber with the greatest amplitude, the dominant wavenumber k^{dom}, vary in time for both the symmetric and anti-symmetric modes, as shown in Figure 6.5b. The discretized appearance of the data results from the restriction of all wavenumbers to integer values. Initially, the dominant wavenumber of the symmetric mode k_S^{dom} exists in the low-frequency symmetric band, lagging behind the maximal wavenumber within that band $k_{S,lf}^{max}$ due to the expansion of the ring radius constantly pushing the maximal wavenumber to greater values. The dominant wavenumber of the symmetric mode abruptly shifts to greater wavenumbers after approximately $t\Gamma/R_0^2 = 10.1$, when growth from the high-frequency symmetric band becomes dominant. For a period of time, the dominant wavenumber of the symmetric mode experiences perturbation growth from a combination of the low- and high-frequency bands of the symmetric mode, which merge to excite an unbroken range of wavenumbers. The gap in the maximal wavenumber of the low-frequency symmetric band from $t\Gamma/R_0^2 = 12.2$ to $t\Gamma/R_0^2 = 12.5$ results from the single maximum in the combined symmetric band associated with the high-frequency symmetric band. Throughout the duration of the merged symmetric band, the influence of the high-frequency maximal wavenumber $k_{S,hf}^{max}$ wanes while that of the low-frequency maximal wavenumber waxes, until the growth experienced by the dominant wavenumber of the symmetric mode is once again controlled by the low-frequency symmetric band after the symmetric bands split at $t\Gamma/R_0^2 = 15.8$. At this point, the growing ring radius tends to increase the maximal wavenumber of the low-frequency symmetric band, and a slight increase in separation distance, caused by the viscous relaxation of the vortex cores and the tendency of the cores to rebound slightly after reaching a minimum separation distance, tends to decrease the maximal wavenumber of the low-frequency symmetric band. These competing influences cause the maximal wavenumber of the low-frequency symmetric band to decrease slightly starting around $t\Gamma/R_0^2 = 13.3$ before increasing again after $t\Gamma/R_0^2 = 18.2$. At the time when the amplitude of the dominant mode reaches the separation distance $t_{Re=4000}^{fin}$, the dominant wavenumber and the maximal wavenumber of the low-frequency symmetric band are nearly the same, a coincidence elaborated on in Section 6.5.

The evolution of the anti-symmetric mode is more straightforward. Caused primarily by the expansion of the ring, both the dominant and maximal wavenumbers of the anti-symmetric band k_A^{dom} and k_A^{max}, respectively, migrate to larger values as time progresses. However, at around $t\Gamma/R_0^2 = 14.6$, the growth rate of the maximal wavenumber is small enough compared to the rate at which the maximal wavenumber migrates to greater wavenumbers such that the dominant wavenumber ceases to increase beyond a value of $k_A^{dom} = 40$.

As in the planar case, perturbed modes grow at an angle given by $\beta = \tan^{-1}\frac{s}{h}$, shown in Figure 6.5c for the emergent wavenumber, β_S^{18} (the subscript "S" indicates the symmetric mode while the superscript "18" is the emergent wavenumber). In the planar case, the low-frequency symmetric

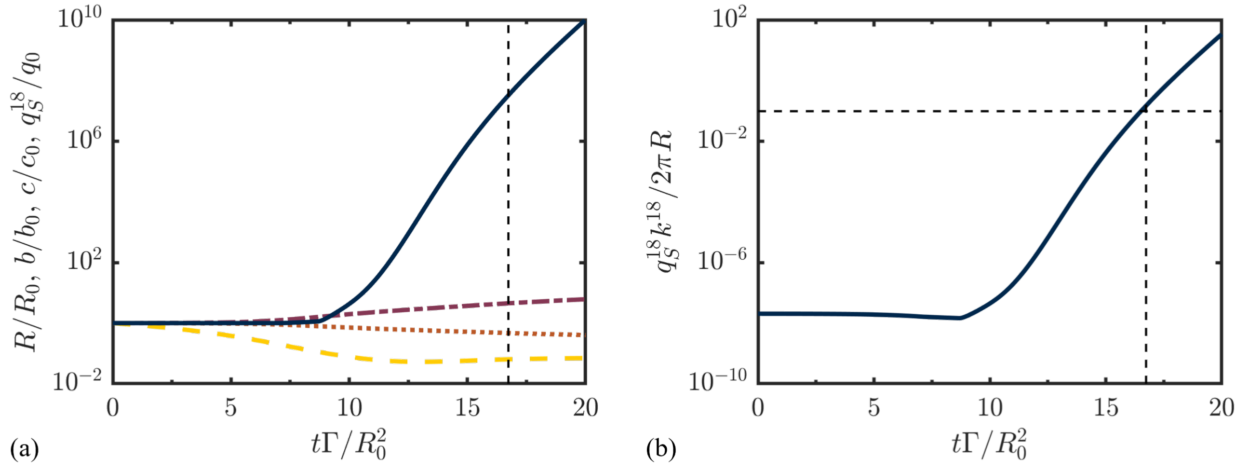

Figure 6.6: The radius (purple dot-dashed line), separation distance (yellow dashed line), core thickness (orange dotted line), and emergent perturbation amplitude (blue solid line) (a) and the product of the emergent perturbation amplitude and wavenumber (b) versus time. The thin vertical black dashed line indicates the time when the amplitude of the emergent wavenumber is on the order of the separation distance, $t^{fin}_{Re=4000}$, and the thin horizontal black dashed line indicates an amplitude-wavenumber product of 0.1.

mode grows at an angle of $\beta = 0.86$ rad. The emergent wavenumber similarly grows at $\beta = 0.86$ rad when it is maximally excited, which occurs at $t\Gamma/R_0^2 = 9.0$, 12.7, 15.5, and 16.9, but in general, the growth angle varies in time.

The analysis assumes that the zero-order motion is slow compared to the growth of perturbations, which we now verify. Figure 6.6a shows the radius, separation distance, core thickness, and amplitude of the emergent wavenumber as a function of time. Between the time when perturbations first become unstable, $t\Gamma/R_0^2 = 7.1$, and time $t^{fin}_{Re=4000}$, indicated by the thin, vertical black dashed line, the radius increases by a factor of 3.57, the separation distance decreases by a factor of 3.00, the core thickness decreases by a factor of 1.89, and the amplitude of the emergent wavenumber increases by a factor of 3.33×10^7. On average, the relevant perturbations therefore evolve 10^6 times faster, relative to their initial value, than the zero-order motion of the flow, verifying the assumption of quasi-steadiness.

We further verify that perturbations remain in the linear regime throughout the growth process. Figure 6.6b shows the amplitude-wavenumber product $q_S^{18}k^{18}$ of the emergent wavenumber as a function of time. We considered perturbations to be linear so long as this product remains less than 0.1 (i.e., linear terms are an order of magnitude larger than leading nonlinear terms), indicated by the horizontal dashed line. The amplitude-wavenumber product of the emergent wavenumber is equal to 0.1 at time $t\Gamma/R_0^2 = 16.5$. This indicates that the linear analysis begins to break down just prior to time $t^{fin}_{Re=4000} = 16.7$. However, it is unlikely that the dominant wavenumber changes significantly between these two times. The linear assumption is therefore verified for nearly the entire duration of the flow leading up to the emergence of secondary vortex structures, the number of which is expected to be set by the emergent wavenumber.

6.4.3 Collisions of Strong Vortex Rings

We now examine the collision of two vortex rings with the same initial geometry as the previous case but with a higher Reynolds number of $Re = 24000$, at which a turbulent puff, as opposed to an array of secondary vortex structures, is expected experimentally [141, 157, 158]. The initial core vorticity profile, see Equation 6.4, is set by assuming that the vortex ring reaches the initial separation distance in an initial time that is inversely proportional to the vortex ring velocity (i.e., t_0 is inversely proportional to Re). As before, the evolution of the first-order motion is given as growth rates and perturbation amplitudes for both the symmetric and anti-symmetric modes as functions of time and wavenumber in Figure 6.7, and we similarly examine three distinct nondimensional times, $t^{init}_{Re=24000}$, $t^{inter}_{Re=24000}$, $t^{fin}_{Re=24000}$, after the onset of perturbation growth. Similar to the lower-Reynolds number case, three separate spatial frequency bands (low-frequency symmetric, high-frequency symmetric, and anti-symmetric) initially experience perturbation growth at time $t^{init}_{Re=24000}$, indicated by the dotted line in Figure 6.7, when the fastest-growing and greatest-amplitude wavenumbers are those associated with the anti-symmetric mode. Shortly after, the high- and low-frequency bands of the symmetric mode merge. Moreover, by time $t^{inter}_{Re=24000}$, indicated by the dashed line in Figure 6.7, the symmetric mode has a single maximum. At this point, the wavenumber with the greatest amplitude is associated with the symmetric mode for the same reasons as described in the lower-Reynolds number case.

Beyond time $t^{inter}_{Re=24000}$, however, the nature of the solution changes compared to the lower-Reynolds number case. While the increasing radius of the ring still tends to shift the anti-symmetric band to higher wavenumbers, the decreased influence of the viscous relaxation of the vorticity within the Lamb-Oseen vortex cores yields relatively thinner cores, resulting in a tendency to excite lower wavenumbers. At the same time, because the cores are thinner, they can come into closer contact with one another, decreasing the separation distance, which causes greater growth rates overall and pushes the bands to higher wavenumbers. The overall effect of this competition results in the anti-symmetric band still migrating toward higher wavenumbers, but exciting a wider range of wavenumbers and lingering on lower wavenumbers long enough to cause significantly more growth than the lower-Reynolds number case. By the time the perturbation grows to be on the order of the separation distance at time $t^{fin}_{Re=24000}$, indicated by the solid line in Figure 6.7, the amplitude of the anti-symmetric mode exceeds that of the symmetric mode and the emergent wavenumber is therefore associated with the higher-frequency, faster-growing anti-symmetric mode.

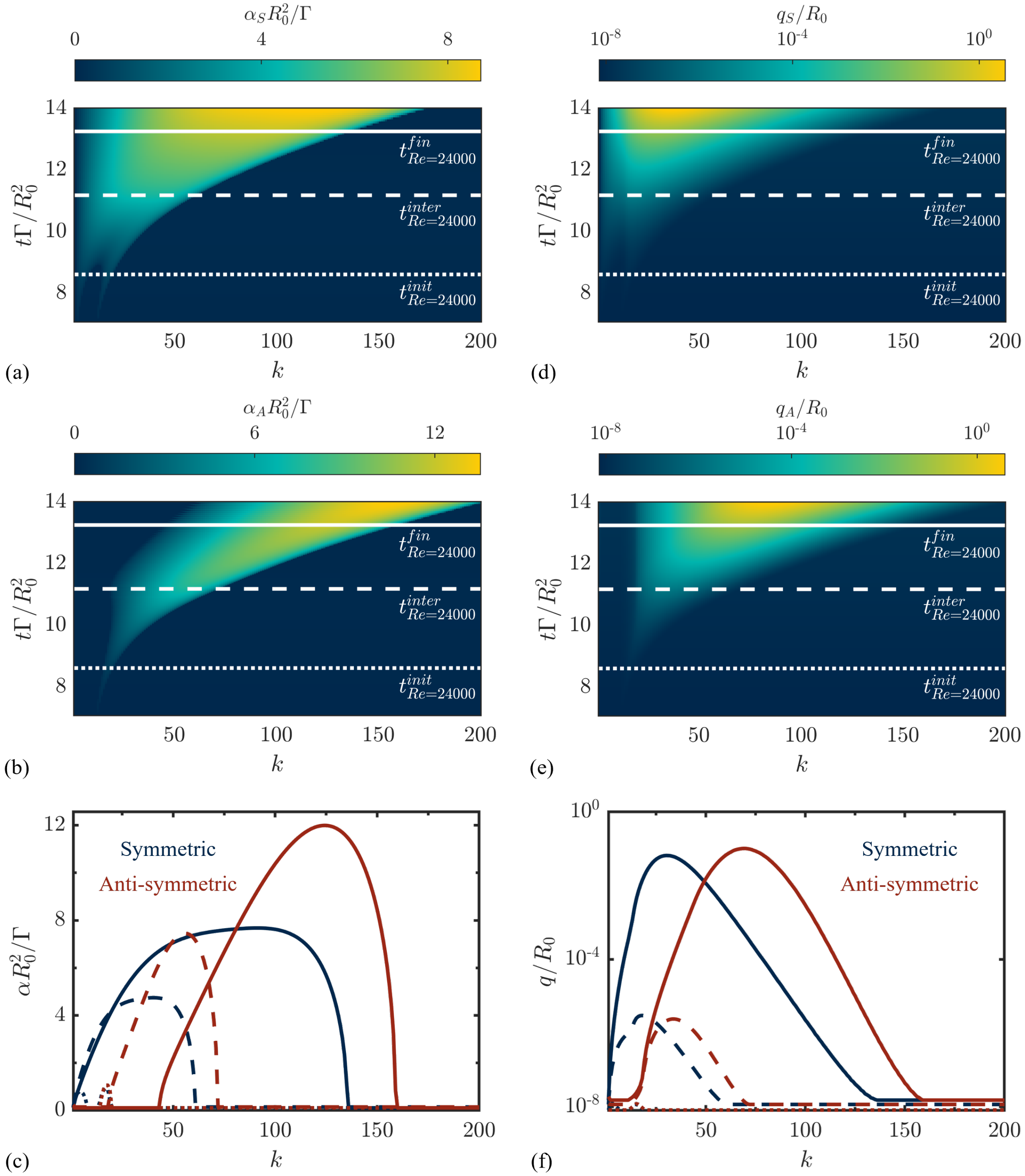

Figure 6.7: The growth rates (a-c) and perturbation amplitudes (d-f) of the symmetric (a,d) and anti-symmetric (b,e) modes for two colliding rings with $b_0/R_0 = 4$, $c_0/R_0 = 0.4$, and $Re = 24000$. Lineouts in (c,f) correspond to $t^{init}_{Re=24000} = 8.6$ (dotted), $t^{inter}_{Re=24000} = 11.2$ (dashed), and $t^{fin}_{Re=24000} = 13.3$ (solid).

The variation of the emergent wavenumber with the Reynolds number, shown in Figure 6.8, has implications relevant to experimental observations. Our analysis correctly predicts the increase in the emergent wavenumber with increasing Reynolds number observed in experiments [141, 157]. Physically, the reason for this behavior is that the tendency of the expanding ring to excite larger wavenumbers becomes relatively more important than the tendency of the viscous relaxation of the vorticity in the cores to excite lower wavenumbers as the Reynolds number increases. Because the emergent wavenumber at these Reynolds numbers is associated with the symmetric mode, vortex reconnection causes the separation of a number of secondary vortex structures roughly equal to the emergent wavenumber, though some variation will exist due to other wavenumbers also experiencing significant growth. Specifically, the variation in the number and size of secondary vortex structures will likely scale with the width of the perturbation amplitude spectrum.

Our analysis also predicts a sharp transition to emergent wavenumbers associated with the anti-symmetric mode that is consistent with the experimentally observed transition to a turbulent puff [141, 157]. In the absence of the vortex reconnection that terminates the growth of the symmetric mode, the growth and stretching of this higher-wavenumber, faster-growing anti-symmetric mode would rapidly continue into a nonlinear phase, possibly stimulating the turbulent puff. We furthermore note that while the maximum amplitude of perturbations experiencing anti-symmetric growth q_A^{dom} (red dotted line in Figure 6.8) are up to five orders of magnitude smaller than their symmetric counterparts for the lower-Reynolds number cases, the maximum amplitude of the perturbations experiencing symmetric growth q_S^{dom} (red dashed line in Figure 6.8) are only up to one order of magnitude smaller than their dominating anti-symmetric counterparts for the higher-Reynolds number cases. As a result, near and beyond the Reynolds number where the flow becomes dominated by the anti-symmetric mode, there is significant perturbation growth throughout a broader range of wavenumbers excited by both modes, further promoting the transition to a turbulent puff.

Experimentally, the transition to a turbulent puff is observed to occur near $Re = 8000$ [157], indicated by the thin black dashed vertical line in Figure 6.8, while our analysis predicts the transition to an anti-symmetric dominated regime near $Re = 22000$. This discrepancy may be attributed to several causes. First, the present analysis is restricted to circular vortex cores; however, experiments clearly show deformation to elliptic or possibly even semi-circular cores [46, 157]. The failure of irrotational vortices to describe the zero-order motion in the present analysis, see Figure 6.3b, is evidence that the distribution of vorticity within the cores is critical, and extending this work to allow core shape deformation would likely increase the accuracy of the results. Second, the current analysis neglects the elliptic instability [292]. A combined stability analysis that simultaneously considers the Crow and elliptic instabilities may be needed for a more complete description of the transition to a turbulent puff [135, 157, 158]. Third, the present analysis cannot accurately capture wavenumbers beyond a critical wavenumber-core-thickness product [53, 113, 292], as discussed

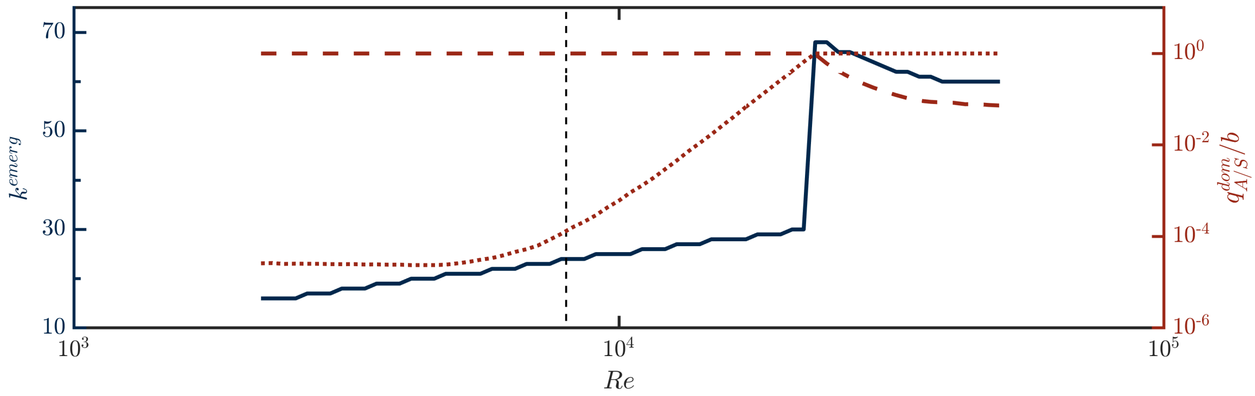

Figure 6.8: The emergent wavenumber (blue solid line) and the amplitude of the symmetric (red dashed line) and anti-symmetric (red dotted line) modes when $q = b$. The black dashed line indicates $Re = 8000$.

in Section 6.5. Despite these limitations, the present analysis provides an accurate quantitative description of the lower-Reynolds number case, correctly predicting the number of secondary vortex structures and the time scales on which they emerge, and may provide key insights into the transition of the flow to a turbulent puff.

6.5 Discussion of Higher-Frequency Modes and Experimental Implications

We further discuss the effect of the anti-symmetric and the high-frequency symmetric modes on the evolution of the perturbation spectrum of the CI. The original analysis of Ref. [53] notes that the fastest-growing wavenumber is that associated with the anti-symmetric mode, though the emergent wavenumber in airplane wakes is consistent with the low-frequency symmetric mode. At the time, this was attributed to the structure of atmospheric turbulence imposing an initial perturbation spectrum that favors low-frequency modes [53]. Later, Ref. [292] pointed out that the unstable high-frequency anti-symmetric mode is spurious due to Crow's use of the low-frequency approximation of the dispersion relation describing the propagation of waves around a columnar vortex to calibrate the cutoff model for the self-induction integral [53, 113]. Figure 6.9 shows the rotation rate for a disturbance τ traveling around a constant-vorticity columnar vortex with rotation rate Ω calculated from the exact dispersion relation and from the low-wavenumber approximation [186]. The dominant anti-symmetric mode in Crow's analysis for an elliptically loaded wing [252] is predicted to grow with a wavenumber-core-thickness product of $kc = 3.34$, where in the planar case k is the dimensional wavenumber [53]. As Figure 6.9a shows, the rotation rate of the disturbance predicted by the low-wavenumber approximation is zero when the product of the

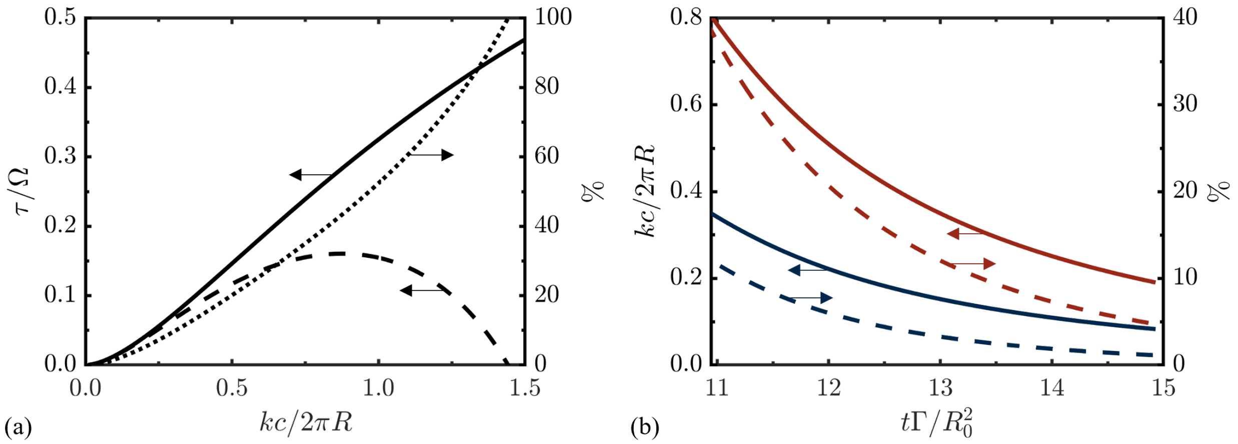

Figure 6.9: The exact rotation rate of a disturbance propagating about a constant-vorticity column (black solid line), the rotation rate from the long-wavelength limit (black dashed line), and the percent difference between the two (black dotted line) versus the product of the wavenumber and core thickness (a) and the product of the wavenumber and core thickness (solid lines) and the percent difference between the exact and long-wavelength-limit rotation rates (dashed lines) for a wavenumber of $k = 69$ (red lines) and $k = 30$ (blue lines) versus time for the $Re = 24000$ case (b). Arrows indicate corresponding axes.

wavenumber and core thickness is 1.44. Beyond this value, the low-wavenumber approximation is in complete disagreement with the exact rotation rate, confirming the assertion that the high-frequency anti-symmetric mode in Crow's analysis is indeed spurious [292].

In the present work, however, the product of the wavenumber and core thickness for the emergent wavenumber of the anti-symmetric mode for the $Re = 24000$ case, $k^{emerg} = 69$, never exceeds 0.8. As Figure 6.9b shows, the error in the disturbance rotation rate from the low-wavenumber approximation decreases from 39% to 5% while the emergent wavenumber is experiencing perturbation growth. For comparison, the error for the dominant wavenumber of the symmetric mode, $k_S^{dom} = 30$, decreases from 12% to 1%, also shown in Figure 6.9b. The low wavelength-core-thickness product for the present cylindrical case, compared to the planar case, is largely caused by the tendency of the core thickness to decrease as the cores expand. The anti-symmetric mode is therefore not necessarily spurious for colliding vortex rings and may play a role in the experimentally observed sharp transition to a turbulent puff as described earlier. It is possible that a stability analysis for colliding vortex rings utilizing the exact dispersion relation may indeed show that the anti-symmetric mode never dominates the low-frequency symmetric mode, but as Figure 6.9 indicates, the anti-symmetric mode may still cause a potentially significant amount of growth in the perturbation spectrum that may contribute to the transition to a turbulent puff.

Furthermore, the effect of the zero-order motion of two colliding vortex rings on the stability provides additional insight for both the planar case and more general flows. While the vertical translation of two planar cores does not explicitly affect the stability, other factors may in the applications. For example, wingtip vortices may encounter background flows causing their separation distance to change, which would suppress the emergence of instability modes exciting narrow, higher-frequency wavenumber bands (if they are not already spurious). The viscous relaxation of a vortex core may have the same effect, as it does in the present work. An accurate characterization of the perturbation spectrum for any number of interacting vortex cores would generally require such considerations.

The first experiments demonstrating the CI along colliding vortex rings [141] utilized the radius, core separation distance, and core thickness, once perturbations were visible, in a planar analysis [53] and found reasonable agreement between the fastest growing wavenumber of the low-frequency symmetric mode and the number of secondary vortex structures. The present analysis, however, indicates that this agreement is partially coincidental, i.e., the dominant and maximal wavenumbers for the low-frequency symmetric mode happen to be similar at the time when the perturbations are visible in experiments, as shown in Figure 6.5. The present analysis provides a complete description of the time-dependent growth of the emergent wavenumber, and all other wavenumbers, from the beginning stages of perturbation growth. Such information is required to fully characterize the modal content of the perturbation spectrum with important implications for the transition of the flow to a possibly turbulent state. It furthermore enables a prediction of the fluid dynamics, rather than post-experimental analysis only.

Finally, while the present work concerns the direct collision of two vortex rings approaching from an initially large separation distance, the analysis for an expanding vortex dipole formed from an annular starting jet is identical, with an appropriate definition of the vortex cores in the dipole. Given the difficulties associated with precisely aligning two vortex ring generators for a direct collision, the latter may be a more convenient, and possibly more controllable, experimental setup for examining the vortex core interactions that are the subject of many recent studies [25, 157, 158, 178, 198, 216]. Moreover, the growth of the CI along an annular starting jet may be relevant to certain astrophysical systems. In particular, the CI may affect mass accumulation along circumstellar tori emitted from stars like Sanduleak -69 202 [152], WeBo 1 [22], Wolf-Rayet 140 [132], and many others.

6.6 Conclusion

The linear stability of two colliding coaxial vortex rings of equal strength is examined. The analysis considers the effects of curvature, the zero-order motion, the distribution of vorticity in the cores, and viscosity within a framework that enables direct calculation of the eigenvalues of the system. Unlike the planar case for line vortices, the zero-order motion of the flow causes the growth rates of the symmetric and anti-symmetric modes to vary. The equations are therefore integrated in time to elucidate the evolution of the perturbation spectrum.

The analysis is validated by comparison to existing experimental data showing good agreement with both the zero- and first-order motion of the flow, enabling a prediction of the number of secondary vortex structures that emerge following the collision of two vortex rings at low-to-moderate Reynolds numbers, which is found to be approximately equal to the calculated emergent wavenumber. The analysis additionally captures the evolution of all other wavenumbers and shows how the zero-order motion causes narrow unstable wavenumber bands, not necessarily spurious, to migrate. As a result, these bands stimulate some growth but, for low Reynolds numbers, never enough to be visible in experiments.

Moreover, the analysis provides key insights into the variation of the emergent wavenumber with the Reynolds number. In particular, the analysis correctly predicts the increase in the emergent wavenumber, and therefore the number of secondary vortex structures that emerge in experiments, with increasing Reynolds number. This behaviour is a physical consequence of the rings expanding to larger radii, and therefore being able to support perturbation growth at larger wavenumbers, faster than the timescales on which their cores relax under the influence of viscosity. Furthermore, the decreased separation distances at higher Reynolds numbers also cause the wavenumber bands excited by both the high-frequency symmetric and anti-symmetric modes to widen, enabling them to excite faster growth for a long enough period of time such that the perturbation amplitudes are on the order of or exceed those of the low-frequency symmetric mode. This enhanced modal content may contribute to the experimentally observed transition of the flow to a turbulent puff.

This work is funded by the U. S. Department of Energy (DOE) as part of the Stewardship Science Graduate Fellowship Program under Grant No. DE-NA0003960 and the U.S. Department of Energy NNSA Center of Excellence under cooperative agreement number DE-NA0003869.

6.7 Supplemental Material

This supplemental material details the stability analysis and provides the coefficients for the matrix-eigenvalue problem in Equation 6.7. Linearizing Equation 6.3 in the reference frame of the zero-order motion of the flow (i.e., subtracting out zero-order terms) yields

$$\frac{\partial \boldsymbol{d_n}}{\partial t} = \boldsymbol{e_x}\frac{\partial h_n}{\partial t}\cos\theta_n + \boldsymbol{e_y}\frac{\partial h_n}{\partial t}\sin\theta_n + \boldsymbol{e_z}\frac{\partial s_n}{\partial t} = \boldsymbol{e_x}u_n + \boldsymbol{e_y}v_n + \boldsymbol{e_z}w_n. \tag{6.11}$$

Equating the velocity components of Equation 6.11 with Equation 6.1 after substitution of Equation 6.2 and linearization, again in the reference frame of the zero-order motion, yields

$$
\begin{aligned}
&\frac{\partial h_n}{\partial t}\cos\theta_n = \\
&\sum_{m=1}^{2}\frac{\Gamma_m}{4\pi}\int\Bigg\{\Bigg\{R\sin\theta_{m'}\frac{\partial s_{m'}}{\partial\theta_{m'}} - R\sin\theta_n\frac{\partial s_{m'}}{\partial\theta_{m'}} - R(s_{m'}-s_n)\cos\theta_{m'} - \\
&\qquad (z_m-z_n)\frac{\partial h_{m'}}{\partial\theta_{m'}}\sin\theta_{m'} - (z_m-z_n)h_{m'}\cos\theta_{m'}\Bigg\}\Big/ \\
&\qquad \Bigg\{\Big[(R\cos\theta_{m'}-R\cos\theta_n)^2 + (R\sin\theta_{m'}-R\sin\theta_n)^2 + (z_m-z_n)^2\Big]^{\frac{3}{2}}\Bigg\} \\
&\qquad + \Bigg\{3R(z_m-z_n)\cos\theta_{m'}\big[Rh_{m'}\cos^2\theta_{m'} - R(h_n+h_{m'})\cos\theta_{m'}\cos\theta_n \\
&\qquad + Rh_n\cos^2\theta_n + Rh_{m'}\sin^2\theta_{m'} - R(h_n-h_{m'})\sin\theta_{m'}\sin\theta_n \\
&\qquad + Rh_n\sin^2\theta_n + (s_{m'}-s_n)(z_m-z_n)\big]\Bigg\}\Big/ \\
&\qquad \Bigg\{\Big[(R\cos\theta_{m'}-R\cos\theta_n)^2 + (R\sin\theta_{m'}-R\sin\theta_n)^2 + (z_m-z_n)^2\Big]^{\frac{5}{2}}\Bigg\}\Bigg\}d\theta_{m'},
\end{aligned}
\tag{6.12}
$$

$$
\begin{aligned}
&\frac{\partial s_n}{\partial t} = \\
&\sum_{m=1}^{2}\frac{\Gamma_m}{4\pi}\int\Bigg\{\Bigg\{R\cos\theta_{m'}\frac{\partial h_{m'}}{\partial\theta_{m'}}\sin\theta_{m'} + 2Rh_{m'}\cos^2\theta_{m'} - R\cos\theta_n\frac{\partial h_{m'}}{\partial\theta_{m'}}\sin\theta_{m'} \\
&\qquad - Rh_{m'}\cos\theta_n\cos\theta_{m'} - Rh_n\cos\theta_n\cos\theta_{m'} - R\sin\theta_{m'}\frac{\partial h_{m'}}{\partial\theta_{m'}}\cos\theta_{m'} \\
&\qquad + 2Rh_{m'}\sin^2\theta_{m'} + R\sin\theta_n\frac{\partial h_{m'}}{\partial\theta_{m'}}\cos\theta_{m'} - Rh_{m'}\sin\theta_n\sin\theta_{m'} \\
&\qquad - Rh_n\sin\theta_n\sin\theta_{m'}\Bigg\}\Big/ \\
&\qquad \Bigg\{\Big[(R\cos\theta_{m'}-R\cos\theta_n)^2 + (R\sin\theta_{m'}-R\sin\theta_n)^2 + (z_m-z_n)^2\Big]^{\frac{3}{2}}\Bigg\} \\
&\qquad - \Bigg\{3R^2(1-\cos\theta_n\cos\theta_{m'}-\sin\theta_n\sin\theta_{m'})\big[Rh_{m'}\cos^2\theta_{m'} \\
&\qquad - R(h_n+h_{m'})\cos\theta_{m'}\cos\theta_n + Rh_n\cos^2\theta_n + Rh_{m'}\sin^2\theta_{m'} \\
&\qquad - R(h_n-h_{m'})\sin\theta_{m'}\sin\theta_n + Rh_n\sin^2\theta_n + (s_{m'}-s_n)(z_m-z_n)\big]\Bigg\}\Big/ \\
&\qquad \Bigg\{\Big[(R\cos\theta_{m'}-R\cos\theta_n)^2 + (R\sin\theta_{m'}-R\sin\theta_n)^2 + (z_m-z_n)^2\Big]^{\frac{5}{2}}\Bigg\}\Bigg\}d\theta_{m'},
\end{aligned}
\tag{6.13}
$$

noting that due to the problem symmetry, the equation for the velocity in the y-direction is redundant and therefore omitted. Applying normal modes of the form $\boldsymbol{d_n} = \widetilde{\boldsymbol{d}}_{\boldsymbol{n}} e^{at+ik\theta_n}$ yields

$$
\begin{aligned}
&a\widetilde{h}_1 \cos\theta_1 = \\
&\frac{\Gamma_1}{4\pi}\int_{\theta_1+\frac{d}{R}}^{\theta_1+2\pi-\frac{d}{R}} \Big\{\{R\sin\theta_{1'}[-\widetilde{s}_{1'}k\sin(k\theta_{1'})] - R\sin\theta_1[-\widetilde{s}_{1'}k\sin(k\theta_{1'})] \\
&\qquad\qquad - R[\widetilde{s}_{1'}\cos(k\theta_{1'}) - \widetilde{s}_1\cos(k\theta_1)]\cos(\theta_{1'})\}/ \\
&\qquad\qquad \Big\{\big[(R\cos\theta_{1'} - R\cos\theta_1)^2 + (R\sin\theta_{1'} - R\sin\theta_1)^2\big]^{\frac{3}{2}}\Big\}\Big\}d\theta_{1'} \\
&\quad + \frac{\Gamma_2}{4\pi}\int_0^{2\pi}\Big\{\{R\sin\theta_{2'}[-\widetilde{s}_{2'}k\sin(k\theta_{2'})] - R\sin\theta_1[-\widetilde{s}_{2'}k\sin(k\theta_{2'})] \\
&\qquad\qquad - R[\widetilde{s}_{2'}\cos(k\theta_{2'}) - \widetilde{s}_1\cos(k\theta_1)]\cos(\theta_{2'}) + b[-\widetilde{h}_{2'}k\sin(k\theta_{2'})]\sin\theta_{2'} \\
&\qquad\qquad + b\widetilde{h}_{2'}\cos(k\theta_{2'})\cos\theta_{2'}\}/ \\
&\qquad\qquad \Big\{[(R\cos\theta_{1'} - R\cos\theta_1)^2 + (R\sin\theta_{1'} - R\sin\theta_1)^2 + b^2]^{\frac{3}{2}}\Big\} \\
&\qquad\qquad - \Big\{3Rb\cos\theta_{2'}[R\widetilde{h}_{2'}\cos(k\theta_{2'})\cos^2\theta_{2'} \\
&\qquad\qquad - R(\widetilde{h}_1\cos(k\theta_1) + \widetilde{h}_{2'}\cos(k\theta_{2'}))\cos(\theta_{2'})\cos(\theta_1) + R\widetilde{h}_1\cos(k\theta_1)\cos^2(\theta_1) \\
&\qquad\qquad + R\widetilde{h}_{2'}\cos(k\theta_{2'})\sin^2\theta_{2'} - R(\widetilde{h}_1\cos(k\theta_1) - \widetilde{h}_{2'}\cos(k\theta_{2'}))\sin(\theta_{2'})\sin(\theta_1) \\
&\qquad\qquad + R\widetilde{h}_1\cos(k\theta_1)\sin^2\theta_1 - b(\widetilde{s}_{2'}\cos(k\theta_{2'}) - \widetilde{s}_1\cos(k\theta_1))]\Big\}/ \\
&\qquad\qquad \Big\{\big[(R\cos\theta_{1'} - R\cos\theta_1)^2 + (R\sin\theta_{1'} - R\sin\theta_1)^2 + b^2\big]^{\frac{5}{2}}\Big\}\Big\}d\theta_{2'},
\end{aligned}
\tag{6.14}
$$

$$
\begin{aligned}
&a\widetilde{s}_1 = \\
&\frac{\Gamma_1}{4\pi}\int_{\theta_1+\frac{d}{R}}^{\theta_1+2\pi-\frac{d}{R}} \Bigg\{\{-R\cos\theta_{1'}\widetilde{h}_{1'}k\sin(k\theta_{1'})\sin\theta_{1'} + 2R\widetilde{h}_{1'}\cos(k\theta_{1'})\cos^2\theta_{1'} \\
&\qquad + R\cos\theta_1\widetilde{h}_{1'}k\sin(k\theta_{1'})\sin\theta_{1'} - R\cos\theta_1\widetilde{h}_{1'}\cos(k\theta_{1'})\cos\theta_{1'} \\
&\qquad - \widetilde{h}_1\cos(k\theta_1)\cos\theta_1 R\cos\theta_{1'} + R\sin\theta_{1'}\widetilde{h}_{1'}k\sin(k\theta_{1'})\cos\theta_{1'} \\
&\qquad + 2R\widetilde{h}_{1'}\cos(k\theta_{1'})\sin^2\theta_{1'} - R\sin\theta_1\widetilde{h}_{1'}k\sin(k\theta_{1'})\cos\theta_{1'} \\
&\qquad - R\sin\theta_1\widetilde{h}_1\cos(k\theta_{1'})\sin\theta_{1'} - R\sin\theta_1\widetilde{h}_{1'}\cos(k\theta_{1'})\sin\theta_{1'}\}/ \\
&\qquad \Big\{[(R\cos\theta_{1'} - R\cos\theta_1)^2 + (R\sin\theta_{1'} - R\sin\theta_1)^2 + b^2]^{\frac{3}{2}}\Big\} \\
&\qquad - \Big\{3R^2(1-\cos\theta_1\cos\theta_{1'} - \sin\theta_1\sin\theta_{1'})[R\widetilde{h}_{1'}\cos(k\theta_{1'})\cos^2\theta_{1'} \\
&\qquad - R(\widetilde{h}_1\cos(k\theta_1) + \widetilde{h}_{1'}\cos(k\theta_{1'}))\cos(\theta_{1'})\cos(\theta_1) + R\widetilde{h}_1\cos(k\theta_1)\cos^2(\theta_1) \\
&\qquad + R\widetilde{h}_{1'}\cos(k\theta_{1'})\sin^2\theta_{1'} - R(\widetilde{h}_1\cos(k\theta_1) - \widetilde{h}_{1'}\cos(k\theta_{1'}))\sin(\theta_{1'})\sin(\theta_1) \\
&\qquad + R\widetilde{h}_1\cos(k\theta_1)\sin^2\theta_1]\Big\}/ \\
&\qquad \Big\{[(R\cos\theta_{1'} - R\cos\theta_1)^2 + (R\sin\theta_{1'} - R\sin\theta_1)^2 + b^2]^{\frac{5}{2}}\Big\}\Bigg\}d\theta_{1'} \\
&\quad + \frac{\Gamma_2}{4\pi}\int_0^{2\pi} \Bigg\{\{-R\cos\theta_{2'}\widetilde{h}_{2'}k\sin(k\theta_{2'})\sin\theta_{2'} + 2R\widetilde{h}_{2'}\cos(k\theta_{2'})\cos^2\theta_{2'} \\
&\qquad + R\cos\theta_1\widetilde{h}_{2'}k\sin(k\theta_{2'})\sin\theta_{2'} - R\cos\theta_1\widetilde{h}_{2'}\cos(k\theta_{2'})\cos\theta_{2'} \\
&\qquad - \widetilde{h}_1\cos(k\theta_1)\cos\theta_1 R\cos\theta_{2'} + R\sin\theta_{2'}\widetilde{h}_{2'}k\sin(k\theta_{2'})\cos\theta_{2'} \\
&\qquad + 2R\widetilde{h}_{2'}\cos(k\theta_{2'})\sin^2\theta_{2'} - R\sin\theta_1\widetilde{h}_{2'}k\sin(k\theta_{2'})\cos\theta_{2'} \\
&\qquad - R\sin\theta_1\widetilde{h}_1\cos(k\theta_{2'})\sin\theta_{2'} - R\sin\theta_1\widetilde{h}_{2'}\cos(k\theta_{2'})\sin\theta_{2'}\}/ \\
&\qquad \Big\{[(R\cos\theta_{2'} - R\cos\theta_1)^2 + (R\sin\theta_{2'} - R\sin\theta_1)^2 + b^2]^{\frac{3}{2}}\Big\} \\
&\qquad - \Big\{3R^2(1-\cos\theta_1\cos\theta_{2'} - \sin\theta_1\sin\theta_{2'})[R\widetilde{h}_{2'}\cos(k\theta_{2'})\cos^2\theta_{2'} \\
&\qquad - R(\widetilde{h}_1\cos(k\theta_1) + \widetilde{h}_{2'}\cos(k\theta_{2'}))\cos(\theta_{2'})\cos(\theta_1) + R\widetilde{h}_1\cos(k\theta_1)\cos^2(\theta_1) \\
&\qquad + R\widetilde{h}_{2'}\cos(k\theta_{2'})\sin^2\theta_{2'} - R(\widetilde{h}_1\cos(k\theta_1) - \widetilde{h}_{2'}\cos(k\theta_{2'}))\sin(\theta_{2'})\sin(\theta_1) \\
&\qquad + R\widetilde{h}_1\cos(k\theta_1)\sin^2\theta_1 - b(\widetilde{s}_{2'}\cos(k\theta_{2'}) - \widetilde{s}_1\cos(k\theta_1))]\Big\}/ \\
&\qquad \Big\{[(R\cos\theta_{2'} - R\cos\theta_1)^2 + (R\sin\theta_{2'} - R\sin\theta_1)^2 + b^2]^{\frac{5}{2}}\Big\}\Bigg\}d\theta_{2'}.
\end{aligned}
\tag{6.15}
$$

Complementary equations for $\widetilde{h}_2$ and $\widetilde{s}_2$ are obtained from Equation 6.14 and Equation 6.15, respectively, by interchanging the subscripts 1 and 2 and by substituting $-b$ for b. The matrix entries for the eigenvalue problem Equation 6.7 are then formed by collecting terms in Equations 6.14-6.15 in the perturbation quantities, giving

$$\begin{aligned}
M_{1,1} = \frac{\Gamma_2}{4\pi\cos\theta_1}\int_0^{2\pi} d\theta_{2'}\Bigg\{\Big\{&3R\cos(k\theta_1)\cos\theta_{2'}\cos\theta_1 - 3R\cos(k\theta_1)\cos^2\theta_1 \\
&+ 3R\cos(k\theta_1)\sin_{\theta_{2'}}\sin\theta_1 - 3R\cos(k\theta_1)\sin^2\theta_1\Big\} bR\cos\theta'_2 / \\
&\big\{[R\cos(\theta_{2'}) - R\cos(\theta_1)]^2 + [R\sin(\theta_{2'}) - R\sin(\theta_1)]^2 + b^2\big\}^{\frac{5}{2}}\Bigg\},
\end{aligned}$$

$$\begin{aligned}
M_{1,2} = \frac{\Gamma_1}{4\pi\cos\theta_1}\int_{\theta_1+\frac{d}{R}}^{\theta_1+2\pi-\frac{d}{R}} d\theta_{1'}\Bigg\{\Big\{&-R\sin(\theta_{1'})k\sin(k\theta_{1'}) + R\sin(\theta_1)k\sin(k\theta_{1'}) \\
&- R\cos(k\theta_{1'})\cos(\theta_{1'}) + R\cos(k\theta_1)\cos(\theta_{1'})\Big\} / \\
&\big\{[R\cos(\theta_{1'}) - R\cos(\theta_1)]^2 + [R\sin(\theta_{1'}) - R\sin(\theta_1)]^2\big\}^{\frac{3}{2}}\Bigg\} \\
+\frac{\Gamma_2}{4\pi\cos\theta_1}\int_0^{2\pi} d\theta_{2'}\Bigg\{\Big\{&R\cos(k\theta_1)\cos(\theta_{2'})\Big\} / \\
&\big\{[R\cos(\theta_{2'}) - R\cos(\theta_1)]^2 + [R\sin(\theta_{2'}) - R\sin(\theta_1)]^2 + b^2\big\}^{\frac{3}{2}}\Bigg\} \\
+\frac{\Gamma_2}{4\pi\cos\theta_1}\int_0^{2\pi} d\theta_{2'}\Bigg\{\Big\{&-3b\cos(k\theta_1)\cos(\theta_{2'})\Big\} bR\cos(\theta_{2'}) / \\
&\big\{[R\cos(\theta_{2'}) - R\cos(\theta_1)]^2 + [R\sin(\theta_{2'}) - R\sin(\theta_1)]^2 + b^2\big\}^{\frac{5}{2}}\Bigg\},
\end{aligned}$$

$$
\begin{aligned}
M_{1,3} = \frac{\Gamma_2}{4\pi\cos\theta_1}\int_0^{2\pi} & d\theta_{2'}\Bigg\{\Big\{-bk\sin(k\theta_{2'})\sin(\theta_{2'}) + b\cos(k\theta_{2'})\cos\theta_{2'}\Big\}/ \\
& \Big\{[R\cos(\theta_{2'}) - R\cos(\theta_1)]^2 + [R\sin(\theta_{2'}) - R\sin(\theta_1)]^2 + b^2\Big\}^{\frac{3}{2}}\Bigg\} \\
+\frac{\Gamma_2}{4\pi\cos\theta_1}\int_0^{2\pi} & d\theta_{2'}\Bigg\{\Big\{-3R\cos(k\theta_{2'})\cos^2(\theta_{2'}) + 3R\cos(k\theta_{2'})\cos(\theta_{2'})\cos(\theta_1) \\
& - 3R\cos(k\theta_{2'})\sin^2(\theta_{2'}) - 3R\cos(k\theta_{2'})\sin(\theta_{2'})\sin(\theta_1)\Big\}bR\cos(\theta_{2'})/ \\
& \Big\{[R\cos(\theta_{2'}) - R\cos(\theta_1)]^2 + [R\sin(\theta_{2'}) - R\sin(\theta_1)]^2 + b^2\Big\}^{\frac{5}{2}}\Bigg\},
\end{aligned}
$$

$$
\begin{aligned}
M_{1,4} = \frac{\Gamma_2}{4\pi\cos\theta_1}\int_0^{2\pi} & d\theta_{2'}\Bigg\{\Big\{-R\sin(\theta_{2'})k\sin(k\theta_{2'}) + R\sin(\theta_1)k\sin(k\theta_{2'}) \\
& - R\cos(k\theta_{2'})\cos(\theta_{2'})\Big\}/ \\
& \Big\{[R\cos(\theta_{2'}) - R\cos(\theta_1)]^2 + [R\sin(\theta_{2'}) - R\sin(\theta_1)]^2 + b^2\Big\}^{\frac{3}{2}}\Bigg\} \\
+\frac{\Gamma_2}{4\pi\cos\theta_1}\int_0^{2\pi} & d\theta_{2'}\Bigg\{\Big\{3b\cos(k\theta_{2'})\Big\}bR\cos(\theta_{2'})/ \\
& \Big\{[R\cos(\theta_{2'}) - R\cos(\theta_1)]^2 + [R\sin(\theta_{2'}) - R\sin(\theta_1)]^2 + b^2\Big\}^{\frac{5}{2}}\Bigg\},
\end{aligned}
$$

$$
\begin{aligned}
M_{2,1} = \frac{\Gamma_1}{4\pi}\int_{\theta_1+\frac{d}{R}}^{\theta_1+2\pi-\frac{d}{R}} d\theta_{1'} \Bigg\{ \Big\{ & -R\cos(\theta_1) k \sin(k\theta_{1'})\sin(\theta_{1'}) + R\cos(k\theta_{1'})\cos^2(\theta_{1'}) \\
& + R\cos(k\theta_{1'})\cos^2(\theta_{1'}) + R\cos(\theta_1) k \sin(k\theta_{1'})\sin(\theta_{1'}) \\
& - R\cos(\theta_1)\cos(k\theta_{1'})\cos(\theta_{1'}) - R\cos(k\theta_1)\cos(\theta_1)\cos(\theta_{1'}) \\
& + R\sin(\theta_{1'}) k \sin(k\theta_{1'})\cos(\theta_{1'}) + R\cos(k\theta_{1'})\sin^2(\theta_{1'}) \\
& + R\cos(k\theta_{1'})\sin^2(\theta_{1'}) - R\sin(\theta_1) k \sin(k\theta_{1'})\cos(\theta_{1'}) \\
& - R\sin(\theta_1)\cos(k\theta_{1'})\sin(\theta_{1'}) - R\cos(k\theta_1)\sin(\theta_1)\sin(\theta_{1'}) \Big\} / \\
& \left\{ [R\cos(\theta_{1'}) - R\cos(\theta_1)]^2 + [R\sin(\theta_{1'}) - R\sin(\theta_1)]^2 \right\}^{\frac{3}{2}} \Bigg\} \\
+ \frac{\Gamma_1}{4\pi}\int_{\theta_1+\frac{d}{R}}^{\theta_1+2\pi-\frac{d}{R}} d\theta_{1'} \Bigg\{ \Big\{ & -3R\cos(k\theta_{1'})\cos^2(\theta_{1'}) + 3R\cos(k\theta_1)\cos(\theta_{1'})\cos(\theta_1) \\
& + 3R\cos(k\theta_{1'})\cos(\theta_{1'})\cos(\theta_1) - 3R\cos(k\theta_1)\cos^2(\theta_1) \\
& - 3R\cos(k\theta_{1'})\sin^2(\theta_{1'}) + 3R\cos(k\theta_1)\sin(\theta_{1'})\sin(\theta_1) \\
& - 3R\cos(k\theta_{1'})\sin(\theta_{1'})\sin(\theta_1) - 3R\cos(k\theta_1)\sin^2(\theta_1) \Big\} \\
& \times R^2\, [1 - \cos(\theta_1)\cos(\theta_{1'}) - \sin(\theta_1)\sin(\theta_{1'})]\, / \\
& \left\{ [R\cos(\theta_{1'}) - R\cos(\theta_1)]^2 + [R\sin(\theta_{1'}) - R\sin(\theta_1)]^2 \right\}^{\frac{5}{2}} \Bigg\} \\
+ \frac{\Gamma_2}{4\pi}\int_0^{2\pi} d\theta_{2'} \Bigg\{ \Big\{ & -R\cos(k\theta_1)\cos(\theta_1)\cos(\theta_{2'}) - R\cos(k\theta_1)\sin(\theta_1)\sin(\theta_{2'}) \Big\} / \\
& \left\{ [R\cos(\theta_{2'}) - R\cos(\theta_1)]^2 + [R\sin(\theta_{2'}) - R\sin(\theta_1)]^2 + b^2 \right\}^{\frac{3}{2}} \Bigg\} \\
+ \frac{\Gamma_2}{4\pi}\int_0^{2\pi} d\theta_{2'} \Bigg\{ \Big\{ & 3R\cos(k\theta_1)\cos(\theta_{2'})\cos(\theta_1) - 3R\cos(k\theta_1)\cos^2(\theta_1) \\
& + 3R\cos(k\theta_1)\sin(\theta_{2'})\sin(\theta_1) - 3R\cos(k\theta_1)\sin^2(\theta_1) \Big\} \\
& \times R^2\, [1 - \cos(\theta_1)\cos(\theta_{1'}) - \sin(\theta_1)\sin(\theta_{1'})]\, / \\
& \left\{ [R\cos(\theta_{2'}) - R\cos(\theta_1)]^2 + [R\sin(\theta_{2'}) - R\sin(\theta_1)]^2 + b^2 \right\}^{\frac{5}{2}} \Bigg\},
\end{aligned}
$$

$$
\begin{aligned}
M_{2,2} = \frac{\Gamma_2}{4\pi}\int_0^{2\pi} d\theta_{2'} \Bigg\{ & \Big\{ -3b\cos(k\theta_1) \Big\} R^2\, [1 - \cos(\theta_1)\cos(\theta_{1'}) - \sin(\theta_1)\sin(\theta_{1'})]\, / \\
& \left\{ [R\cos(\theta_{2'}) - R\cos(\theta_1)]^2 + [R\sin(\theta_{2'}) - R\sin(\theta_1)]^2 + b^2 \right\}^{\frac{5}{2}} \Bigg\},
\end{aligned}
$$

$$
\begin{aligned}
M_{2,3} = \frac{\Gamma_2}{4\pi} \int_0^{2\pi} d\theta_{2'} \Bigg\{ \Big\{ & -R\cos(\theta_{2'}) k \sin(k\theta_{2'}) \sin(\theta_{2'}) + R\cos(k\theta_{2'}) \cos^2(\theta_{2'}) \\
& + R\cos(k\theta_{2'}) \cos^2(\theta_{2'}) + R\cos(\theta_1) k \sin(k\theta_{2'}) \\
& - R\cos(\theta_1) \cos(k\theta_{2'}) \cos(\theta_{2'}) + R\sin(\theta_{2'}) k \sin(k\theta_{2'}) \cos(\theta_{2'}) \\
& + R\cos(k\theta_{2'}) \sin^2(\theta_{2'}) + R\cos(k\theta_{2'}) \sin^2(\theta_{2'}) \\
& - R\sin(\theta_1) k \sin(k\theta_{2'}) \cos(\theta_{2'}) - R\sin(\theta_1) \cos(k\theta_{2'}) \sin(\theta_{2'}) \Big\} / \\
& \left\{ [R\cos(\theta_{2'}) - R\cos(\theta_1)]^2 + [R\sin(\theta_{2'}) - R\sin(\theta_1)]^2 + b^2 \right\}^{\frac{3}{2}} \Bigg\} \\
+ \frac{\Gamma_2}{4\pi} \int_0^{2\pi} d\theta_{2'} \Bigg\{ \Big\{ & -3R\cos(k\theta_{2'}) \cos^2(\theta_{2'}) + 3R\cos(k\theta_{2'}) \cos(\theta_{2'}) \cos(\theta_1) \\
& - 3R\cos(k\theta_{2'}) \sin^2(\theta_{2'}) - 3R\cos(k\theta_{2'}) \sin(\theta_{2'}) \sin(\theta_1) \Big\} \\
& \times R^2 \left[1 - \cos(\theta_1)\cos(\theta_{1'}) - \sin(\theta_1)\sin(\theta_{1'}) \right] / \\
& \left\{ [R\cos(\theta_{2'}) - R\cos(\theta_1)]^2 + [R\sin(\theta_{2'}) - R\sin(\theta_1)]^2 + b^2 \right\}^{\frac{5}{2}} \Bigg\},
\end{aligned}
$$

$$
\begin{aligned}
M_{2,4} = \frac{\Gamma_2}{4\pi} \int_0^{2\pi} d\theta_{2'} \Bigg\{ & \Big\{ 3b\cos(k\theta_{2'}) \Big\} R^2 \left[1 - \cos(\theta_1)\cos(\theta_{1'}) - \sin(\theta_1)\sin(\theta_{1'}) \right] / \\
& \left\{ [R\cos(\theta_{2'}) - R\cos(\theta_1)]^2 + [R\sin(\theta_{2'}) - R\sin(\theta_1)]^2 + b^2 \right\}^{\frac{5}{2}} \Bigg\}.
\end{aligned}
$$

CHAPTER 7

A Hydrodynamic Mechanism for Clumping Along the Equatorial Rings of SN1987A and Other Stars

This chapter is adapted from M. J. Wadas, W. White, H. J. LeFevre, C. C. Kuranz, A. Towne, and E. Johnsen, A hydrodynamic mechanism initiating clumping along the equatorial rings of SN1987A and other stars, *In Preparation for Physical Review Letters* [282].

7.1 Abstract

A prominent feature of SN1987A is the equatorial ring surrounding the location of the progenitor star, along which there are 28 mass clumps – or “hot spots.” Our hydrodynamic analysis of the expanding ring prior to the supernova demonstrates that it is subject to the Crow instability between vortex cores. We find that the dominant unstable wavenumber is consistent with the number of observed clumps, suggesting that the Crow instability initiates clumping in SN1987A and other star systems with equatorial rings.

7.2 Introduction

The recency and proximity of Supernova 1987A (SN1987A) to Earth make it an unparalleled source of astrophysical data shaping our understanding of stellar evolution [8, 151, 152]. Light from the supernova initially illuminated a complex three-ring structure surrounding the progenitor consisting of an equatorial ring (ER), with the progenitor at its center, and two outer rings roughly coplanar and axisymmetric with the ER, but with larger radii and offset in the polar directions. Telescopic observation indicates that the ER consists of 28 clumps of mass nearly evenly spaced along the ring [81]. Approximately 5600 days after the collapse of the progenitor, the blast wave from the supernova reached the ER, heating and illuminating the clumps, which are commonly referred to as “hot spots,” shown in Figure 7.1a [81, 130, 164, 208, 257].

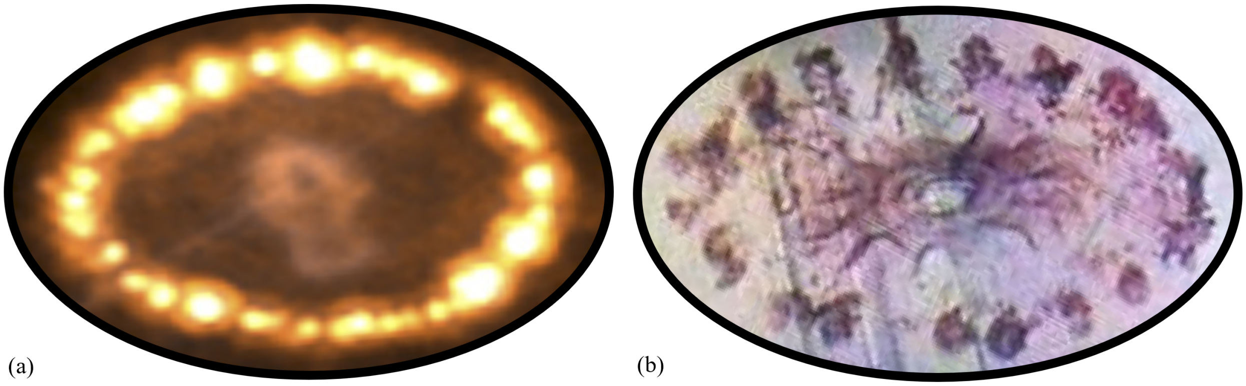

(a) (b)

Figure 7.1: Hot spots along the equatorial ring of SN1987A [130] (a) and pinch-off of isolated vortex structures from a radially expanding vortex dipole fluid flow [141] (b). Images are reproduced with permission.

Several theories attempt to describe the origin of the ER. The current expansion velocity, $V_{ER} = 10.3\,\mathrm{km\,s^{-1}}$ [51], and present-day radius, 0.6 ly [31], of the ER suggest it was formed from mass ejected by the progenitor 20,000 years prior to the supernova [152]. Leading theories explain the mass ejection as the result of a binary star merger [190, 191, 248] and/or the interaction of stellar winds from different stages of the progenitor evolution [19, 45, 283], while additional theories evoke magnetic fields [261], polar jets [4], or a pre-existing protostellar disk [153].

Despite the extensive effort to understand the rings, little is known about the origin of the clumps comprising the ER [104]. Past studies assert that the clumping is the result of hydrodynamic forces [206, 256], but do not identify the specific mechanism or provide an explanation for the observed number of clumps. Other work suggests that the clumps are spikes due to the Rayleigh-Taylor fluid instability [307, 308] but requires unevidenced mechanisms departing from more plausible theories and is still unable to predict the number of clumps [4, 111, 303].

We propose that the formation of the clumps in the ER is indeed driven by hydrodynamics but results from the Crow instability (CI) between vortex cores. Our analysis considers the stability of perturbations along an annular torus ejected from the progenitor, a common feature of every theory describing the three-ring nebula, and yields a dominant unstable wavenumber consistent with the number of observed clumps. In this chapter, we first describe the CI and how it relates to the expanding ER. Next, we present the stability analysis. We conclude with a discussion of the relevance of our stability analysis to other star systems exhibiting ERs.

7.3 Setup, Governing Equations, and Stability Analysis

The CI describes the growth of perturbations along interacting vortex cores [53, 135, 137]. Originally studied in planar geometries relevant to aircraft wingtip vortices [251], the CI was later observed along radially expanding vortex dipoles [46, 141, 157, 158, 216]. Perturbations along the interacting cores grow until they touch, triggering a complex reconnection process resulting in the pinch-off of isolated vortex structures, as shown in Figure 7.1b [9, 39, 117, 141, 295]. The expanding ER in SN1987A likely acquired vorticity, either from its interaction with mass ejected during a binary merger [190, 191] or stellar winds [19, 45, 283]. Regardless of its source, the vorticity, which would be equal and opposite in magnitude on opposing sides of the equatorial plane given the symmetry of the ER, would cause the ER to develop into an expanding vortex dipole [19, 149] potentially unstable to the CI. The subsequent growth of perturbations would then result in pinch-off into the observed isolated clumps.

Our analysis therefore considers the stability of two circular vortex cores of opposite circulation forming a radially expanding vortex dipole. Figure 7.2 shows a schematic of the setup involving two vortex cores with circular cross sections of thickness c, separation distance b, radius R, and circulation magnitude Γ, with core-displacement perturbations in the azimuthal direction θ, of integer azimuthal wavenumber k. While the expanding torus leading to the formation of the vortex cores is a common feature among theories describing the ER of SN1987A, we evoke the binary-merger theory of Refs. [190, 191] to initialize our stability problem. According to this theory, as the radius of the binary orbit decreased leading up to the merger, mass transfer between the two stars formed a common mass envelope which, due to its angular momentum, was elongated in the equatorial plane forming a torus of radius $R_T = 3 \times 10^{12}$ m and thickness $D_T = 2 \times 10^{12}$ m. When the stars merged, the release of orbital energy caused an ejected portion of the envelope to flow past the torus at approximately $V_{EJ} = 25\,\mathrm{km\,s^{-1}}$, setting the torus into motion through the pre-existing stellar wind. We therefore estimate the circulation available for the formation of the vortex cores to be $\Gamma = V_{EJ} D_T$ [84, 182]. Following Ref. [258], we assume an ambient red supergiant wind environment formed from a constant stellar mass ejection rate of $\dot{m}_{RSG} = 6.3 \times 10^{17}\,\mathrm{kg\,s^{-1}}$ at constant radial velocity $V_{RSG} = 10\,\mathrm{km\,s^{-1}}$ and constant pressure $p_{RSG} = 1 \times 10^{-8}$ Pa.

Following potential theory, the velocity along the center of each core is governed by the Biot-Savart law,

$$\boldsymbol{U_n} = \sum_{m=1}^{2} \frac{\Gamma_m}{4\pi} \int \frac{\boldsymbol{L_{mn}} \times d\boldsymbol{S_m}}{|\boldsymbol{L_{mn}}|^3}, \tag{7.1}$$

where $n = 1$ or 2 denotes the top or bottom core, respectively, $\boldsymbol{L_{mn}}$ is the displacement vector to a point on core m from a point on core n, and $d\boldsymbol{S_n}$ is the differential tangent vector. Equation 7.1

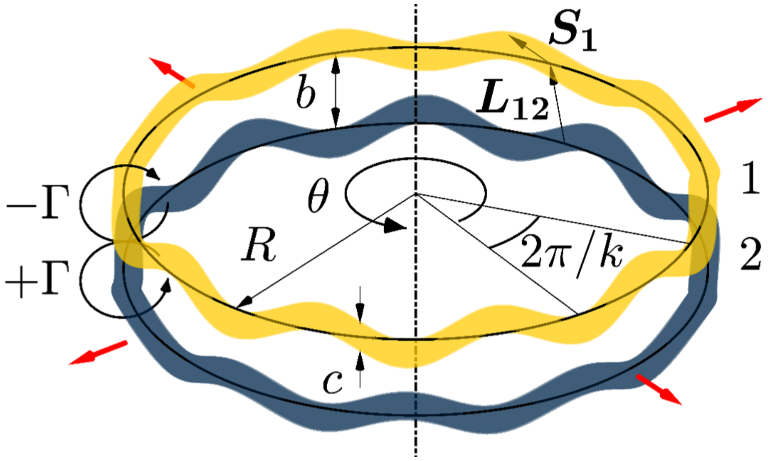

Figure 7.2: Schematic of the stability analysis parameters. Red arrows indicate the direction of the dipole expansion.

holds provided that the flow is incompressible, inviscid, and continuous, which is supported by the Mach, Reynolds, and Knudsen numbers, respectively, relevant to the expanding ring. For an ideal gas, the Mach number is

$$M = \frac{V_{ER} - V_{RSG}}{a} = (V_{ER} - V_{RSG})\sqrt{\frac{\rho}{\gamma p}}, \tag{7.2}$$

where a is the sound speed, $\rho = \dot{m}_{RSG}/4\pi R^2 V_{RSG}$ is the density, and $\gamma = 5/3$ is the adiabatic index. The Reynolds number is

$$Re = \frac{\Gamma}{\nu} = \frac{\Gamma}{2.3 \times 10^{-12}\sqrt{A}T^{5/2}/\Lambda Z^4 \rho}, \tag{7.3}$$

where ν is the kinematic viscosity [23, 227], A is the atomic mass of the gas (assumed to be hydrogen) in atomic mass units, $\Lambda = 10$ is the Coulomb logarithm, Z is the atomic number of the gas, and T is the temperature in Kelvin (calculated assuming an ideal gas equation of state), with the density and circulation expressed in SI units. Finally, the Knudsen number is related to the Mach and Reynolds numbers,

$$Kn = \frac{\lambda}{D_T} = \frac{M}{Re}\sqrt{\frac{\gamma\pi}{2}}, \tag{7.4}$$

where λ is the mean free path.

Figure 7.3 shows the radial dependence of the Mach, Reynolds, and Knudsen numbers according to Equations 7.2-7.4. Shortly (~40 years) after the binary merger, the flow enters a regime where $M \lesssim 0.3$, $Re \lesssim 10^3$, and $Kn \lesssim 10^{-3}$, which endures for approximately 3000 years, as indicated by the shaded region in Fig 7.3. During this time, the incompressible, inviscid, and continuous

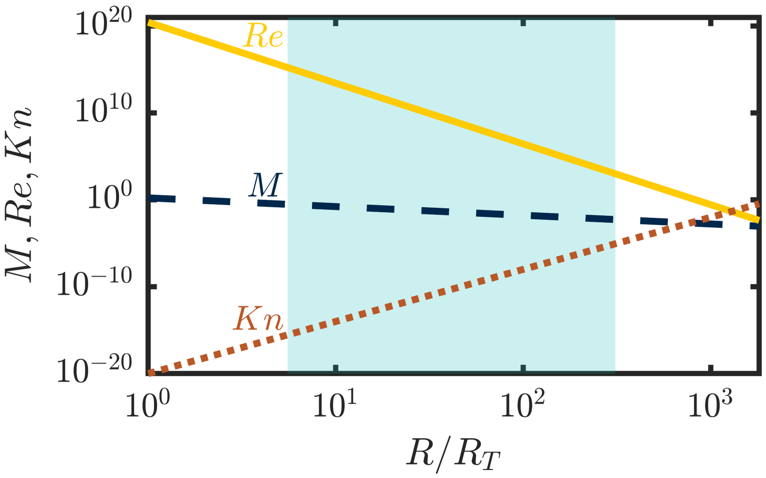

Figure 7.3: Mach (blue dashed), Reynolds (yellow solid), and Knudsen (orange dotted) numbers versus radius. The teal shaded region satisfies $M < 0.3$, $Re > 10^3$, and $Kn < 10^{-3}$.

assumptions are well supported, such that the expanding torus would be subject to the formation of vortex cores unstable to the CI.

Recent work [277] (see Chapter 6) examines the cylindrical CI governed by the Biot-Savart law for the setup in Figure 7.2, which we apply presently. Equation 7.1 is linearized, a normal-modes ansatz is assumed for perturbations, and first-order coefficients are organized into a matrix-eigenvalue problem. The solution yields growth rates, α_k, where the subscript denotes the wavenumber, for a symmetric and antisymmetric mode, where perturbations on one core grow as a mirror image of or in phase with the perturbations on the other core, respectively. Because the zero-order motion (i.e., the core radius, core separation distance, and core thickness) is not constant, the growth rate is a function of time and therefore integrated to determine the perturbation spectrum. The effect of viscosity on the zero-order motion is considered in Ref. [277] but presently neglected due to the initially large Reynolds number. Instead, the radial vorticity distribution within each core is assumed Gaussian such that the boundary of the core is located at two standard deviations from the maximum vorticity at the vortex core center, consistent with experimental measurements of vortex core boundaries and vorticity distributions [106, 157, 158, 200, 212]. We refer readers to Chapter 6 for additional detail.

7.4 Results

We initialize the stability analysis 40 years after the binary merger event, when the flow is approximately incompressible, inviscid, and continuous. By this time, the torus would have expanded to a radius $R_0 = R_T + V_{ER} \times 40$ years. Based on past studies examining vortex dipole formation from

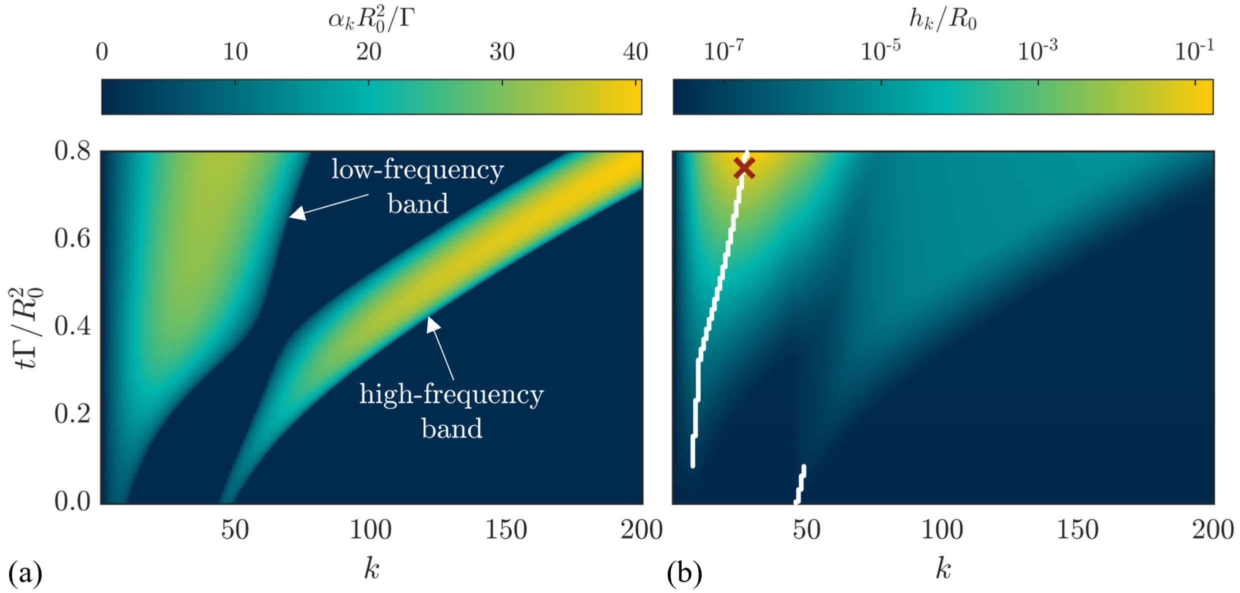

Figure 7.4: The growth rate (a) and perturbation amplitude (b) of the symmetric mode versus wavenumber and time. The white line indicates the wavenumber of maximum perturbation amplitude, and the red X denotes the time and wavenumber when the maximum perturbation amplitude is equal to the core separation distance.

laterally accelerated cylinders [90, 202, 212], we estimate the torus would form a vortex dipole with initial core separation distance and thickness $b_0 = D_T/2$ and $c_0 = b_0/2$, respectively. Perturbations amplitudes h_k, where the subscript denotes the wavenumber, are initialized as a uniform spectrum equal to the mean free path, i.e., $h_k(t = 0) = \lambda$.

Figure 7.4 presents the results of the stability analysis applied to SN1987A in terms of the growth rate and the perturbation amplitude of the symmetric mode as a function of wavenumber and time, with all dimensional quantities nondimensionalized by the initial radius and circulation magnitude. At any given time, symmetric perturbation growth is experienced within two distinct wavenumber ranges, which we refer to as the low- and high-frequency bands. The greatest growth rate always exists in the high-frequency band, which initially causes wavenumbers within that band to dominate their low-frequency counterparts, as indicated by the white line in Figure 7.4b, which tracks the integer wavenumber associated with the highest-amplitude perturbation. However, the expansion of the dipole radius causes the high-frequency band to migrate to higher wavenumbers, while the low-frequency band always includes a range of wavenumbers starting at $k = 2$. As a result, while perturbations in the low-frequency band may not grow as fast as those in the high-frequency band, they grow continuously and soon overtake those in the high-frequency band. The low-frequency band similarly dominates a band of wavenumbers experiencing antisymmetric perturbation growth (omitted for brevity) nearly coincident with the high-frequency band.

Symmetric perturbations grow until their amplitude is on the order of the core separation distance, which first occurs for a wavenumber of $k = 27$ at the time indicated by the red X in Figure 7.4, corresponding to a dimensional time of 70 years, or 110 years following the binary merger. The dominant wavenumber of the CI, which corresponds to the number of pinched-off secondary vortex structures, see Figure 7.1, is remarkably close to the reported number of observed hot spots, 28, in SN1987A. In addition, other wavenumbers experiencing significant perturbation growth would introduce variability in the pinch-off locations, yielding secondary vortex structures with different sizes, which accounts for the range of observed hot spot sizes in the ER of SN1987A. Furthermore, the time dynamics associated with perturbation growth occur well within the time frame during which the governing equations, derived from the Biot-Savart law, are valid. Finally, although we evoke the binary merger hypothesis [190, 191] to generate initial conditions for the stability analysis, the radially expanding torus and source of vorticity conducive to dipole formation are nearly ubiquitous features among theories explaining the rings of SN1987A.

To illustrate the dynamics predicted by our stability analysis, Figure 7.5 shows a simulation performed using our in-house, finite-volume hydrodynamics code solving the two-fluid Euler equations [134, 304]. The ER is initialized as a torus geometrically scaled to the ER at the start of the stability analysis, 40 years following the binary merger, with a radial velocity of $M = 0.3$ with respect to the ambient fluid. The torus cross section has constant radial axis thickness τ and perturbed vertical axis thickness, $\tau[1 + 0.08 \sin(2\pi\theta \times 28)]$. Because computational constraints limit the resolvable amplitudes, the perturbation can only be simulated through a small portion of its growth from an initial amplitude, on the order of the mean free path, to the core separation distance. Still, the simulation demonstrates the key physics. The torus rolls up into an expanding vortex dipole, identified by an isosurface of the Q-criterion [99], which indicates the intensity of rotational relative to straining motions. An isosurface of the mass fraction, where $\xi = 1$ denotes the fluid comprising the initial torus, is also shown. The formation of the dipole leaves behind a thin skirt of the original torus fluid in the wake of the vortex cores, which is seen in experiments of dipole formation [90, 141, 202]. After the perturbed vortex cores become unstable to the CI at approximately $t\Gamma/R_0^2 = 0.2$, the perturbation amplitude rapidly increases to the point where nonlinear effects begin to initiate the vortex reconnection process, leading to the pinch-off of 28 isolated secondary vortex structures, i.e., clumps. Although the final time shown is long after the linear stability analysis is valid, the number of enduring clumps is set by the dominant wavenumber. The complete pinch-off of isolated secondary vortex structures is not necessarily required for the formation of clumps in astrophysical systems. Once the CI sets the number of locations where the ER starts to thin, corresponding to the dominant wavenumber, other physics, including gravitational and radiative effects, may become relevant and complete the clump formation [16].

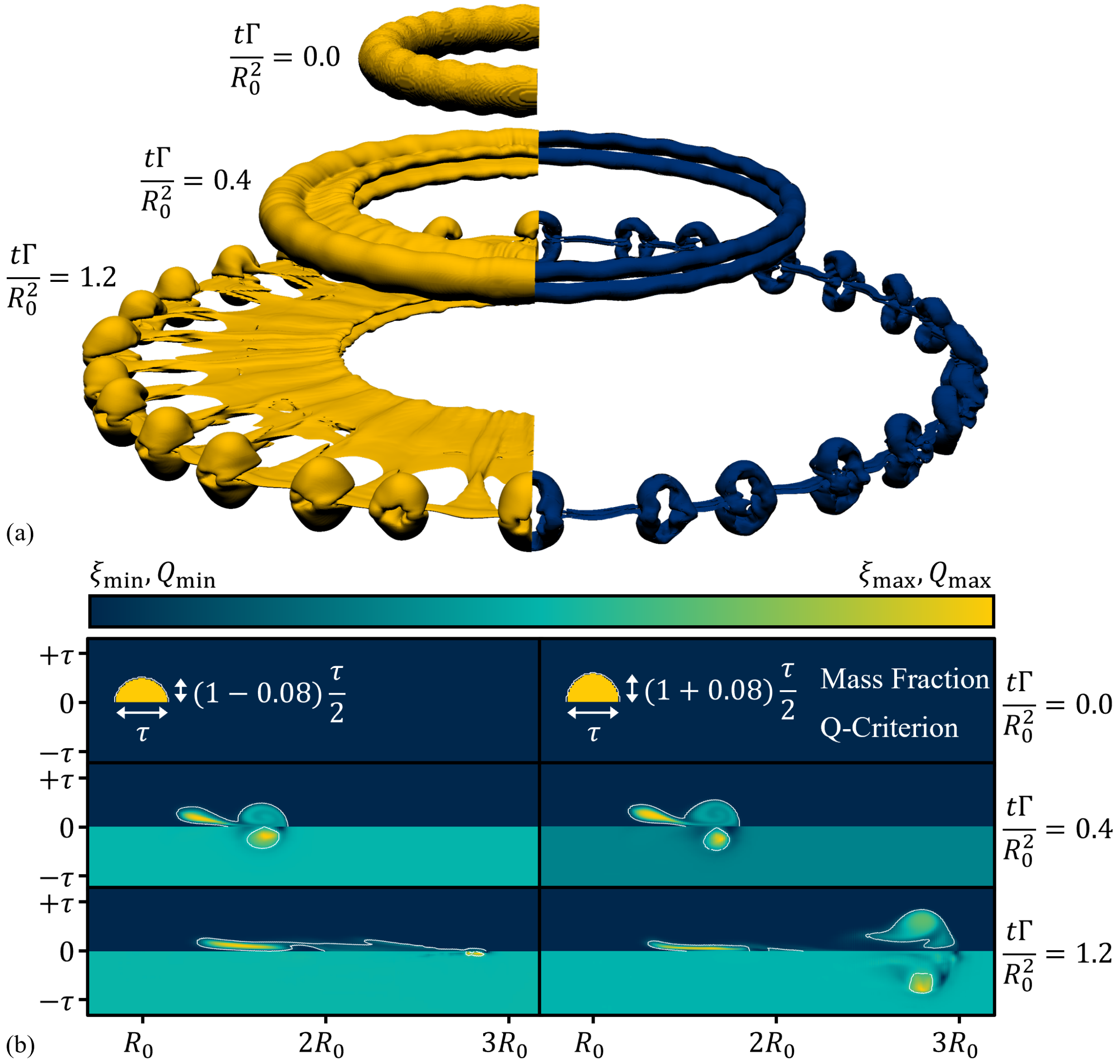

Figure 7.5: Isosurfaces (a) of mass fraction $\xi = 0.10$ (left) and $Q = 0.15$ (right) at the indicated times and two-dimensional slices in the radial-vertical plane (b) at the indicated times of mass fraction (top, at each time) and Q-criterion (bottom, at each time) for a narrow (left), where pinch-off occurs, and thick (right) portion of the perturbation. White lines indicate the intersection of the respective surface with the two-dimensional slice. The colorbar is rescaled in each time step such that $\xi_{\min} = (0.00, 0.00, 0.00)$, $\xi_{\max} = (1.00, 0.93, 0.85)$, $Q_{\min} = (0.00, -4.34, -0.50)$, and $Q_{\max} = (0.00, 4.25, 0.48)$ at times $t\Gamma/R_0^2 = (0.0, 0.4, 1.2)$, respectively, for the narrow portion of the perturbation (left), and $\xi_{\min} = (0.00, 0.00, 0.00)$, $\xi_{\max} = (1.00, 0.98, 0.57)$, $Q_{\min} = (0.00, -2.85, -0.68)$, and $Q_{\max} = (0.00, 6.04, 0.70)$, respectively, for the thick portion of the perturbation (right).

7.5 Conclusion

While the focus of the present work is the ER of SN1987A, we conclude with a brief discussion of other star systems exhibiting ERs with similar clumping behavior, including Fomalhaut [21], WeBo 1 [22], SBW1 [244], HR 4796A [114], HD 98800 [115], and many others, including those documented as part of the Disk Substructures at High Angular Resolution Project [7]. While these systems do not all exhibit the three-ring structure of SN1987A, similar hypotheses (e.g. binary merger, transition from a red to a blue supergiant, etc.) explain the formation of the observed ERs, which would similarly be subject to clump formation via the CI. Moreover, many of these ERs are thought to be protoplanetary disks, suggesting the clumping mechanism described in the present work may be a precursor to the formation of orbital bodies in these and other systems, possibly including our own solar system.

In this chapter, we propose that clumping in the ER of SN1987A and other star systems may be caused by hydrodynamic instabilities of circular line vorticies, i.e., the CI. Our stability analysis shows the dominant unstable wavenumber is consistent with the number of observed hot spots, suggesting that the CI initiates and sets the number of clumps. In other systems that do not undergo a supernova event, this clumping may ultimately lead to the formation of orbital bodies, possibly including planets.

This work is supported by the U. S. Department of Energy (DOE) as part of the Stewardship Science Graduate Fellowship Program under Grant No. De-NA0003960. Computational resources were provided by the Extreme Science and Engineering Discovery Environment Stampede 2 system, USA under grant TG-CTS130005.

CHAPTER 8

Conclusion

The goal of the present thesis is to document advancements in comprehending hydrodynamic phenomena arising from the interaction of shock waves with interfaces for applications in dynamic compression experiments, inertial confinement fusion (ICF) research, and astrophysics. The final chapter of this thesis summarizes and discusses key findings and suggests several avenues for future work, some of which are already in progress.

8.1 Summary of Key Findings

Each of the previous six technical chapters presents novel research contributions summarized as follows:

1. A technique for strengthening shock waves in dynamic compression experiments is developed, which relies on using intermediate materials to bridge impedance gaps when a shock passes through different layers of a diamond anvil cell (DAC), or similar, apparatus. Each intermediate material temporarily allows a stronger shock wave to break out into the subsequent material, as demonstrated analytically with one-dimensional gas-dynamics theory, with an exponential discretization of impedance yielding the most efficient shock strengthening. In practice, the number of intermediate materials is limited by the choice of real materials and the amount of time that the stronger shock can be supported, which diminishes with an increasing number of intermediate materials. In certain cases, the technique enables 25% greater pressures, pushing experimental access for equation-of-state characterization to new boundaries.

2. Helium is dynamically compressed in a DAC to record pressures exceeding 3.5 Mbar. The density and temperature along the primary shock Hugoniot are determined, and the electrical conductivity is calculated. The data indicate increased compressibility caused by the onset of a continuous ionization process and are well described by first-principles density functional theory, molecular dynamics, and path-integral Monte Carlo techniques.

3. A criterion for the ejection of vortex dipoles from two-dimensional shock-induced mixing regions is developed based on the dipole velocities of two interacting Richtmyer-Meshkov bubbles. Such ejections are not predicted by existing models and effect the development of the residual mixing region through the transport of energy and circulation. The ejected dipoles also have the potential to stimulate other regions of the flow, including nearby interfaces.

4. The formation and scaling of vortex rings ejected from shocked interfaces are determined. Such vortex rings form when interfacial protrusions invert after the passage of a shock wave. The theory generalizes past research on single-fluid, incompressible flows to interfacial flows with shock waves. The circulation of the vortex ring increases as the length of the protrusion increases up to a critical length beyond which the vortex ring saturates and a trailing jet emerges behind it. Such vortex rings may form during ICF implosions, where they can disrupt the symmetry of the central burning plasma, and supernovae, where they may be directly responsible for stimulating the transport of stellar core elements.

5. The linear stability analysis for the cylindrical Crow instability (CI) along interacting vortex cores is determined. The analysis suggests that both a symmetric and anti-symmetric mode experience perturbation growth, and unlike the planar case, the anti-symmetric mode may not be spurious. An additional departure from the planar case is that the growth experienced by a given wavenumber is a function of time and the governing equations must therefore be integrated to determine the perturbation spectrum. While the anti-symmetric mode experiences faster growth, the wavenumber range that it excites migrates in time, potentially resulting in less integrated perturbation growth than the slower symmetric mode, which consistently excites lower wavenumber ranges. However, it is determined that anti-symmetric perturbation amplitudes become comparable to their symmetric counterparts under conditions at which a sharp turbulent transition is experimentally observed to occur, suggesting that the anti-symmetric mode may play a role in the transition.

6. The mechanics that stimulates clumping along stellar debris rings like that of Supernova 1987A (SN1987A) is uncovered. The ejection of such rings and their subsequent interaction with stellar winds may cause the formation of an expanding vortex dipole unstable to the CI. The dominant wavenumber predicted by the analysis is remarkably consistent with the observed number of clumps in SN1987A, suggesting that the CI stimulates the formation of the clumps.

8.2 Discussion

A major advantage of the technique for strengthening shock waves presented in Chapter 2 is its compatibility with existing shock compression platforms. Targets for compression experiments are typically constructed by layering together different portions of the DAC. While the small size of the targets, typically on the order of 1 mm, makes them challenging to fabricate, techniques involving material films, electroplated foils, and even high-precision additive manufacturing can routinely generate layers on the order of 10 µm or less [96]. Such techniques can readily be used to incorporate the intermediate materials that enable shock strengthening with a minimal increase in fabrication costs. Furthermore, the technique does not require any modifications to existing laser facilities. As a result, it can immediately be applied to achieve record states on high-energy facilities like the NIF and Omega laser systems. Furthermore, with the increasing attention paid to high-repetition rate lasers to accelerate advancements in fusion-energy science [146], shock strengthening with intermediate materials can prevent new facilities, with increased firing frequency coming at the cost of laser energy, from sacrificing shock pressure.

Beyond the direct consequences the novel states achieved in helium presented in Chapter 3 have on our understanding of gas giant interiors and white dwarf atmospheres, the data serve as an important benchmark for computational tools describing a wide range of materials [170]. The validation of such tools with experimental data increases the confidence with which predictions are made in wide range of research areas. In particular, improved EOS characterization that includes complex ionization physics in warm dense matter has the potential to advance research on nuclear fusion and planetary and stellar interiors [72].

Despite decades of research, the late-time dynamics of the RMI remain a challenge [307, 308]. Of particular importance is how, or whether, the flow will transition to turbulence. Such physics are difficult to probe experimentally given the finite amount of time that a shocked mixing region has to develop before the arrival of additional reflected waves at the interface [241]. In the absence of guidance from late-time experiments that definitively achieve turbulence, simulations of the RMI, which can be allowed to evolve to arbitrarily late times with adequate computational resources, must rely on other means for incorporating turbulence. Currently, hydrocodes supporting the design of ICF experiments and analysis of supernova remnants rely on RMI models, like those discussed in Chapter 4, to determine when to activate turbulence models [69]. Such descriptions of the RMI, however, struggle to correctly capture the evolution of the flow when high-vorticity ejecta escape the confines of the mixing region. The criterion for vortex dipole ejection developed in Chapter 4, based only on the initial conditions, can therefore identify flows a priori for which RMI models are expected to fail and, conversely, succeed. The incorporation of such a criterion into existing hydrocodes could therefore lead to better predictions of ICF implosions and understanding of supernovae.

Chapter 5 builds on the idea presented in Chapter 4 that ejecta from shocked interfaces can be treated as vortex dipoles to uncover the formation dynamics of vortex rings, the azimuthally symmetric analog to vortex dipoles, emerging from shocked interfacial flows. The generalized scaling can be used to quantify time scales on which such vortex rings form along with the circulation, impulse, and energy that they transport out of the mixing region, key quantities for turbulence modeling and transitions in the RMI. Furthermore, the inverting interfacial protrusion in the computational setup is closely related to similar jets stemming from high-aspect-ratio pits, voids, and the fill tube in ICF capsules. The theory can therefore be similarly applied to understand the mechanisms that affect the formation and scaling of these jets, hopefully informing techniques to mitigate their deleterious effect on fusion performance.

Shifting from the formation to the stability of vortex cores, the linear theory presented in Chapter 6 has critical implications for both classical and high-energy-density flows. While the importance of the CI has long been recognized in airplane wakes and more recently in vortex ring collisions, the novel analysis details the time dependence of its evolution in cylindrical geometries. Unlike the planar case, perturbation growth must be integrated in time due to the varying core separation distance, radius, and thickness. This time variance also uncovers a new mechanism that may further inhibit the high-frequency anti-symmetric mode. Specifically, any changes to the zero-order motion, which may include the core thickness under the action of viscous mechanisms or a change in core separation distance caused by a background flow in the planar case, causes the migration of narrow high-frequency bands to different wavenumbers. As a result, the integrated growth of such modes is diminished compared to their symmetric counter parts, which consistently excite a lower-wavenumber range. However, the zero-order motion may also enhance the growth of the anti-symmetric mode, long considered spurious based on arguments in the planar case that apply differently to the cylindrical case, as the Reynolds number increases. While in reality the symmetric mode may still dominate the flow, perturbation growth stimulated by the anti-symmetric mode is not necessarily prohibited in the cylindrical case and may contribute to the transition of vortex collisions to turbulent puffs.

Finally, the CI may be responsible for stimulating clumping in SN1987A, as discussed in Chapter 7. SN1987A is the first supernova visible to the naked eye since Kepler's Supernova in 1604, the only one since the advent of modern telescopes. As a result, SN1987A is a critical source of data related to stellar evolution and one of the most intensely studied astrophysical systems to date [151, 152]. Despite decades of intense research, the mechanism responsible for the formation of the clumps along the equatorial ring illuminated by the blast is unknown. The mechanism proposed in Chapter 7, based on the CI, predicts a dominant wavenumber remarkably consistent with the observed number of clumps and reproduces key features of the astrophysical system, essentially solving this nearly four-decades-old problem of great scientific interest. Beyond SN1987A, the same clumping mechanism may be responsible for stimulating the formation of orbital bodies along other stellar equatorial rings, many of which are predicted to be protoplanetary disks [7]. If the same mechanism is at work in these systems, the CI may be responsible for stimulating the formation of planets, a breakthrough in our understanding of planetary formation.

8.3 Future Work

Many of the findings summarized in the previous section open up new areas of research that are herein recommended as future work. They include additional dynamic compression experiments to constrain the ionization behavior of helium, experiments validating the theory for vortex rings ejected from shocked interfaces, and a generalization of the CI to star systems with equatorial rings including protoplanetary disks.

8.3.1 Experiments Probing Helium Ionization Physics

While the present work expands the available data on shock compressed helium, more experiments are needed to characterize the ionization behavior at conditions relevant to planetary interiors and white dwarf atmospheres. In particular, whether the ionization of helium is primarily driven by density or temperature remains unclear. Figure 8.1 shows conductivity, a quantity dependent on ionization, as function of temperature and density according to two competing Drude-like ionization models [36, 249]. At or below densities of $\sim 1.5\,\mathrm{g\,cm^{-3}}$, conditions at which experimental data exist, the models yield similar predictions, despite their vastly different predictions at higher densities. The model from Ref. [249] predicts primarily temperature-driven, continuous ionization with band-gap closure near $10\,\mathrm{g\,cm^{-3}}$ compared to the density-driven, sharp ionization with band-gap closure near $2\,\mathrm{g\,cm^{-3}}$ predicted by Ref. [36].

Additional experimental data examining shocked helium from a higher-pressure precompressed state than that explored in the present thesis would enable differentiation between the existing models. Achieving more extreme precompressed states in a DAC, however, requires a thicker front diamond window, which takes longer for the laser-induced shock to traverse. The shock therefore becomes more attenuated from the release wave launched when the laser pulse terminates, resulting in a weaker shock that may struggle to achieve the desired pressures. This challenge may be partially ameliorated through the use of the shock strengthening technique introduced in Chapter 2. In addition, the experiments could be carried out at a facility with more laser energy, such as the NIF.

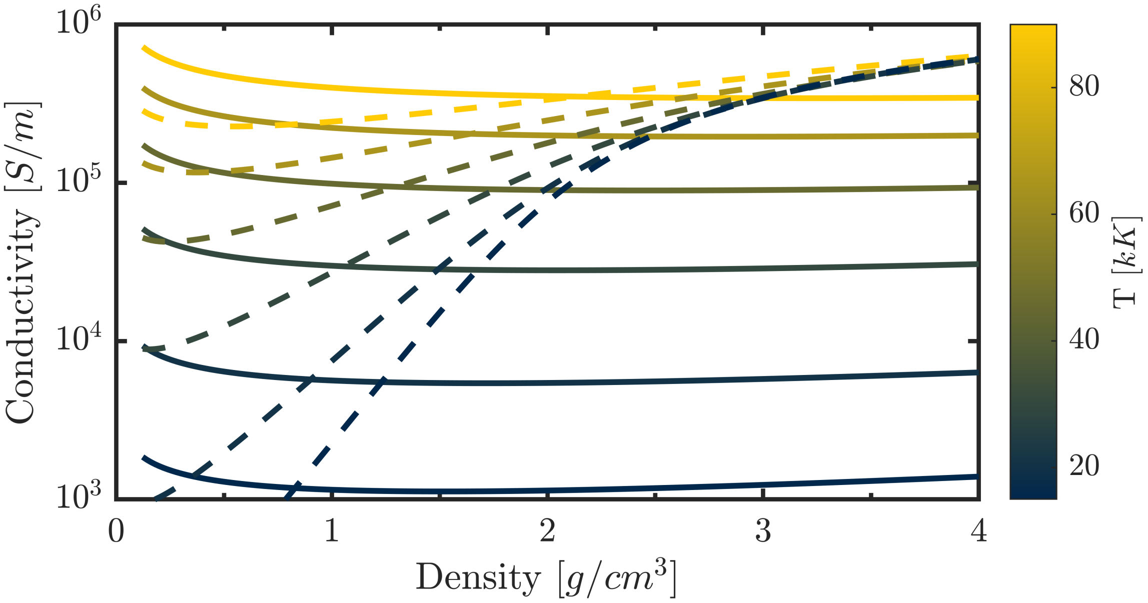

Figure 8.1: The Drude-like helium conductivity models of Ref. [249] (solid) and Ref. [36] (dashed) for selected isotherms.

8.3.2 Experiments Exploring High-Energy-Density Vortex Rings

While vortex-ring-like structures have long been observed in both experiments and simulations emerging from shocked interfacial mixing regions (see Figure 5.1), an experimental study has yet to isolate their formation physics. The next step is to explore the vortex ring formation dynamics described in Chapter 5 experimentally, with four shot days awarded at the OMEGA EP laser facility through the LaserNetUS and National Laser User Facility programs. Targets for these experiments will consist of a set of low- and high-aspect ratio doped protrusions visualized with radiography at different stages of the vortex-ring formation process. It is expected that the low-aspect ratio protrusions form an isolated vortex ring, while the high-aspect ratio protrusions form a vortex ring and a trailing jet, indicating that the formation number has been exceeded. These experiments will therefore demonstrate conceptual proof that vortex rings formed at the leading edge of jets resulting from the interaction of a shock with an interface exhibit scaling behavior analogous to their classical counterparts and establish a platform to experimentally explore the formation dynamics. The objectives are therefore to:

1. Demonstrate the ability to constrain the formation number to within ±2,
2. Validate theoretical predictions for the affect of the interface density ratio,
3. Examine the influence of different driving waves (e.g., supported shock versus blast), and

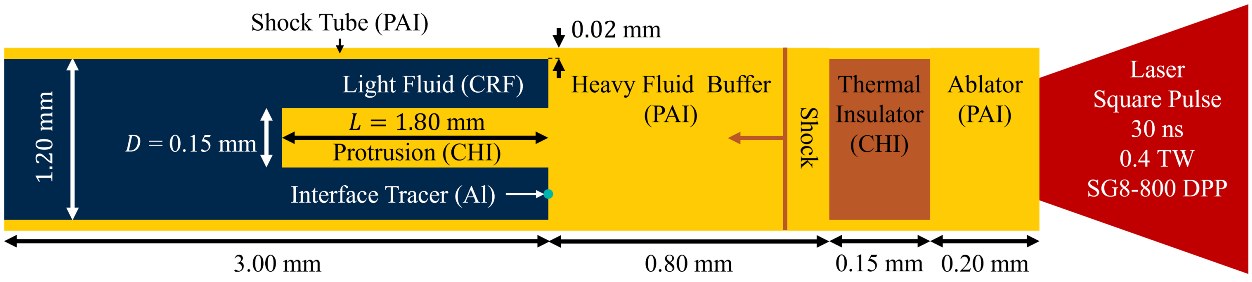

Figure 8.2: A schematic showing a sample target for the awarded experiments. Dimensions are not to scale.

4. Explore the dynamics of different protrusion geometries leading into future experiments.

The awarded experiments will examine the formation of a vortex ring from an interface between polyamide-imide plastic (PAI) and carbonized resorcinol formaldehyde foam (CRF) along which there is a cylindrical iodine-doped plastic (CHI) protrusion into the foam with a density that matches that of the PAI, shown schematically in Figure 8.2. The laser pulse will irradiate the back end of the ablator, driving a shock wave through the interface, which will stimulate the inversion of the protrusion and the formation of a vortex ring. This ring, formed from the doped protrusion, will be visualized with x-ray radiography, and the presence of the trailing jet will be used as a metric to determine if the formation number has been exceeded.

The diameter of the protrusion will be constant between experiments, and it is expected that the trailing jet will emerge beyond a critical protrusion length, as shown in preliminary FLASH [82] simulation results in Figure 8.3. Therefore, the formation number can be determined by fielding targets with incremented protrusion lengths (objective 1), constrained by the longest protrusion that does not generate a trailing jet (lower bound) and the shortest protrusion that does (upper bound). This technique for constraining the formation number can then be utilized to explore the effect of varying the density ratio (objective 2), achieved by using a foam with a different density, and different driving wave profiles (objective 3), enabled by laser pulse shaping. The influence of the protrusion geometry (objective 4) will be similarly explored by examining a protrusion comprised of a single period of a sinusoid. These experiments will directly lead into future work exploring competition between a series of forming vortex rings.

It is expected that the proposed experiments would enable the further development and validation of a generalized theory for vortex ring formation, including those generated following the interaction of a shock with an interface. The theory would enable the calculation of the time scale on which such vortex rings form along with the ring circulation, impulse, and energy. These key quantities are necessary for designing strategies to mitigate the effects of fill-tube and surface-pit jets in ICF implosions, understanding the ejection of stellar core material in supernova explosions, and

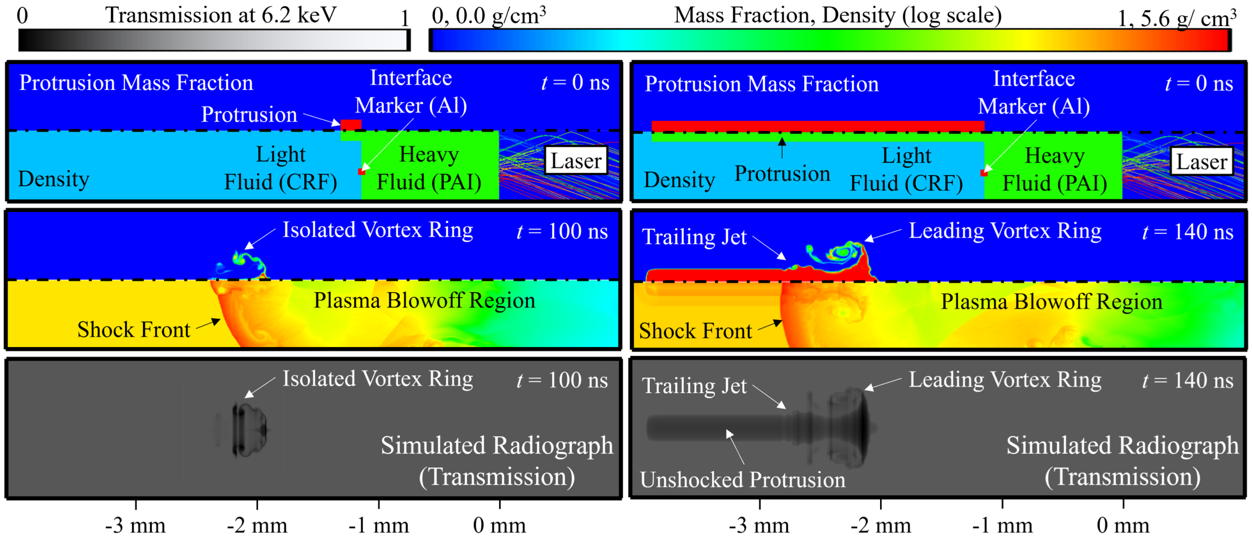

Figure 8.3: Mass fraction (above line of axisymmetry) and density (below line of axisymmetry) fields at two times from FLASH simulations showing the formation of a vortex ring from a low- (left) and high- (right) aspect ratio shocked protrusion. The density scale is linear at time $t = 0\,\text{ns}$ and logarithmic otherwise. The bottom row shows corresponding simulated radiographs.

calculating energy transport that may affect turbulent transition in the RMI.

The OMEGA EP laser is uniquely suited to explore the physics of vortex ring formation from shocked interfaces. An isolated protrusion along a fluid interface cannot be reliably generated with classical techniques, necessitating the use of solid, machinable materials to generate the initial conditions. Furthermore, the long-pulse capabilities of OMEGA EP are essential for supporting the shock on the time scales on which the hydrodynamics develop, and the pulse-shaping capabilities will enable the study of the effects of the driving wave profile (objective 3). Finally, a kilo-Joule class system is ideal for its ability to generate conditions consistent with the applications.

8.3.3 The Crow Instability and Orbital Body Formation

While the research presented in Chapter 7 focuses on Supernova 1987A (SN1987A), many other star systems exhibit equatorial rings with clumping that may be similarly governed by the Crow instability (CI) [7]. In particular, the CI may be the mechanism that stimulates the formation of orbital bodies in protoplanetary disks. Stars are believed to form from the gravity-driven coalescence of mass in rotating protostellar disks, while the left-over mass, now a protoplanetary disk, then accumulates in orbital bodies [156]. Gravity causes heavier elements to occupy smaller radii of the protoplanetary disk, leading to the formation of rocky planets, while the lighter gases at larger radii accumulate into gas giants. Once clumps start to form, gravitational and radiative mechanisms drive the condensation of this relatively low density gas and dust into planets [16].

As Chapter 7 demonstrates, the CI offers a precise mechanism for stimulating clumps that is highly consistent with observational data [7]. The source of vorticity driving the CI could be wind from the newly formed star at the center of the protoplanetary disk [19]. As Chapter 5 demonstrates, there is a limit to the amount of material that can roll up into a vortex ring or dipole. As a result, multiple expanding vortex dipoles may be formed as the solar wind passes over the disk, with denser dipoles nearer the star and less dense dipoles at larger radii, thus establishing the initial orbital radius of clumps stimulated by the CI. Like the planets in our solar system, the clumps would be expected to vary in size due to CI-driven perturbation growth over a range of wavenumbers. The resulting differences in angular momentum would establish the newly formed orbital bodies at different radii from the star. Subsequent collisions between the bodies and gravitational interactions would continue to adjust their orbits. Elucidating the details of this theory will involve simulations representing the interaction of density-varying protoplanetary disk with solar wind and corresponding experiments.

BIBLIOGRAPHY

[1] S. I. Abarzhi, A. K. Bhowmick, A. Naveh, A. Pandian, N. C. Swisher, R. F. Stellingwerf, and W. D. Arnett. Supernova, nuclear synthesis, fluid instabilities, and interfacial mixing. *Proc. Natl. Acad. Sci.*, 116(37):18184–18192, 2019.

[2] H. Abu-Shawareb, R. Acree, P. Adams, J. Adams, B. Addis, R. Aden, et al. Lawson criterion for ignition exceeded in an inertial fusion experiment. *Phys. Rev. Lett.*, 129(7):075001, 2022.

[3] D. Adhikari and T. T. Lim. Evolution and breakdown of elliptic vortex ring. *Gallery of Fluid Motion*, 2015.

[4] M. Akashi, E. Sabach, O. Yogev, and N. Soker. Forming equatorial rings around dying stars. *Mon. Notices Royal Astron. Soc.*, 453(2):2115–2125, 2015.

[5] U. Alon, J. Hecht, D. Mukamel, and D. Shvarts. Scale invariant mixing rates of hydrodynamically unstable interfaces. *Phys. Rev. Lett.*, 72(18):2867, 1994.

[6] J. D. Anderson. *Modern Compressible Flow: With Historical Perspective*, volume 12. McGraw-Hill New York, 1990.

[7] S. M. Andrews, J. Huang, L.M. Pérez, A. Isella, C. P. Dullemond, N. Kurtovic, et al. The disk substructures at high angular resolution project (DSHARP). i. motivation, sample, calibration, and overview. *Astrophys. J. Letters*, 869(2):L41, 2018.

[8] W. D. Arnett, J. N. Bahcall, R. P. Kirshner, and S. E. Woosley. Supernova 1987A. *Annu. Rev. Astron. Astrophys.*, 27(1):629–700, 1989.

[9] W. T. Ashurst and D. I. Meiron. Numerical study of vortex reconnection. *Phys. Rev. Lett.*, 58(16):1632, 1987.

[10] K. L. Baker, C. A. Thomas, T. R. Dittrich, O. Landen, G. Kyrala, D. T. Casey, et al. Fill tube dynamics in inertial confinement fusion implosions with high density carbon ablators. *Phys. Plasmas*, 27(11):112706, 2020.

[11] S. Balasubramanian, G. C. Orlicz, and K. P. Prestridge. Experimental study of initial condition dependence on turbulent mixing in shock-accelerated Richtmyer–Meshkov fluid layers. *J. Turbul.*, 14(3):170–196, 2013.

[12] A. Banerjee, R. A. Gore, and M. J. Andrews. Development and validation of a turbulent-mix model for variable-density and compressible flows. *Phys. Rev. E*, 82(4):046309, 2010.

[13] A. Becker, W. Lorenzen, J. J. Fortney, N. Nettelmann, M. Schöttler, and R. Redmer. Ab initio equations of state for hydrogen (H-REOS. 3) and helium (He-REOS. 3) and their implications for the interior of brown dwarfs. *Astrophys. J. Suppl. Ser.*, 215(2):21, 2014.

[14] G. R. Bennett, M. C. Herrmann, M. J. Edwards, B. K. Spears, C. A. Back, E. W. Breden, et al. Fill-tube-induced mass perturbations on x-ray-driven, ignition-scale, inertial-confinement-fusion capsule shells and the implications for ignition experiments. *Phys. Rev. Lett.*, 99(20):205003, 2007.

[15] P. Bergeron, D. Saumon, and F. Wesemael. New model atmospheres for very cool white dwarfs with mixed H/He and pure He compositions. *Astrophys. J.*, 443:764–779, 1995.

[16] F. Bertoldi. The photoevaporation of interstellar clouds. I-radiation-driven implosion. *Astrophys. J.*, 346:735–755, 1989.

[17] R. Betti and O. A. Hurricane. Inertial-confinement fusion with lasers. *Nat. Phys.*, 12(5):435–448, 2016.

[18] G. A. Bird. The motion of a shock-wave through a region of non-uniform density. *J. Fluid Mech.*, 11(2):180–186, 1961.

[19] J. M. Blondin and P. Lundqvist. Formation of the circumstellar shell around SN 1987A. *Astrophys. J.*, 405:337–352, 1993.

[20] B. E. Blue, H. F. Robey, S. G. Glendinning, M. J. Bono, S. C. Burkhart, J. R. Celeste, et al. Three-dimensional hydrodynamic experiments on the National Ignition Facility. *Phys. Plasmas*, 12(5):056313, 2005.

[21] A. C. Boley, M. J. Payne, S. Corder, W. R. F. Dent, E. B. Ford, and M. Shabram. Constraining the planetary system of Fomalhaut using high-resolution ALMA observations. *Astrophys. J. Lett.*, 750(1):L21, 2012.

[22] H. E. Bond, D. L. Pollacco, and R. F. Webbink. WeBo 1: A young barium star surrounded by a ringlike planetary nebula. *Astron. J.*, 125(1):260, 2003.

[23] S. I. Braginskii. Transport processes in a plasma. *Rev. Plasma Phys.*, 1:205, 1965.

[24] C. Breitsamter. Wake vortex characteristics of transport aircraft. *Prog. Aerosp. Sci.*, 47(2):89–134, 2011.

[25] M. P. Brenner, S. Hormoz, and A. Pumir. Potential singularity mechanism for the Euler equations. *Phys. Rev. Fluids*, 1(8):084503, 2016.

[26] R. Briggs, F. Coppari, M. G. Gorman, R. F. Smith, S. J. Tracy, A. L. Coleman, A. Fernandez-Pañella, M. Millot, J. H. Eggert, and D. E. Fratanduono. Measurement of body-centered cubic gold and melting under shock compression. *Phys. Rev. Lett.*, 123(4):045701, 2019.

[27] D. Broege, S. Fochs, G. Brent, J. Bromage, C. Dorrer, R. F. Earley, et al. The dynamic compression sector laser: A 100-j UV laser for dynamic compression research. *Rev. Sci. Instrum.*, 90(5):053001, 2019.

[28] M. Brouillette. The Richtmyer-Meshkov instability. *Annu. Rev. Fluid Mech.*, 34(1):445–468, 2002.

[29] S. Brygoo, P. Loubeyre, M. Millot, J. R. Rygg, P. M. Celliers, J. H. Eggert, R. Jeanloz, and G. W. Collins. Evidence of hydrogen- helium immiscibility at Jupiter-interior conditions. *Nature*, 593(7860):517–521, 2021.

[30] S. Brygoo, M. Millot, P. Loubeyre, A. E. Lazicki, S. Hamel, T. Qi, et al. Analysis of laser shock experiments on precompressed samples using a quartz reference and application to warm dense hydrogen and helium. *J. Appl. Phys.*, 118(19):195901, 2015.

[31] C. J. Burrows, J. Krist, J. J. Hester, R. Sahai, J. T. Trauger, K. R. Stapelfeldt, et al. Hubble space telescope observations of the SN 1987A triple ring nebula. *Astrophys. J.*, 452(2):680–684, 1995.

[32] W. T. Buttler, D. M. Oró, D. L. Preston, K. O. Mikaelian, F. J. Cherne, R. S. Hixson, et al. Unstable Richtmyer–Meshkov growth of solid and liquid metals in vacuum. *J. Fluid Mech.*, 703:60–84, 2012.

[33] E. Calderon, M. Gauthier, F. Decremps, G. Hamel, G. Syfosse, and A. Polian. Complete determination of the elastic moduli of α-quartz under hydrostatic pressure up to 1 GPa: an ultrasonic study. *J. Phys. Condens. Matter*, 19(43):436228, 2007.

[34] C. J. Catherasoo and B. Sturtevant. Shock dynamics in non-uniform media. *J. Fluid Mech.*, 127:539–561, 1983.

[35] P. M. Celliers, D. K. Bradley, G. W. Collins, D. G. Hicks, T. R. Boehly, and W. J. Armstrong. Line-imaging velocimeter for shock diagnostics at the OMEGA laser facility. *Rev. Sci. Instrum.*, 75(11):4916–4929, 2004.

[36] P. M. Celliers, P. Loubeyre, J. H. Eggert, S. Brygoo, R. S. McWilliams, D. G. Hicks, T. R. Boehly, R. Jeanloz, and G. W. Collins. Insulator-to-conducting transition in dense fluid helium. *Phys. Rev. Lett.*, 104(18):184503, 2010.

[37] P. M. Celliers and M. Millot. Imaging velocity interferometer system for any reflector (VISAR) diagnostics for high energy density sciences. *Rev. Sci. Instrum.*, 94(1), 2023.

[38] G. Chabrier, S. Mazevet, and F. Soubiran. A new equation of state for dense hydrogen–helium mixtures. *Astrophys. J.*, 872(1):51, 2019.

[39] P. Chatelain, D. Kivotides, and A. Leonard. Reconnection of colliding vortex rings. *Phys. Rev. Lett.*, 90(5):054501, 2003.

[40] M. Cheng, J. Lou, and T. T. Lim. Collision and reconnection of viscous elliptic vortex rings. *Phys. Fluids*, 31(6):067107, 2019.

[41] J. C. Chervin, B. Canny, and M. Mancinelli. Ruby-spheres as pressure gauge for optically transparent high pressure cells. *High Press. Res.*, 21(6):305–314, 2001.

[42] W. Chester. The quasi-cylindrical shock tube. *Lond. Edinb. Dublin Philos. Mag. J. Sci.*, 45(371):1293–1301, 1954.

[43] R. F. Chisnell. The normal motion of a shock wave through a non-uniform one-dimensional medium. *Proc. Math. Phys. Eng. Sci.*, 232(1190):350–370, 1955.

[44] R. F. Chisnell and M. Yousaf. The effect of the overtaking disturbance on a shock wave moving in a non-uniform medium. *J. Fluid Mech.*, 120:523–533, 1982.

[45] S. M. Chiţă, N. Langer, A. J. Van Marle, G. García-Segura, and A. Heger. Multiple ring nebulae around blue supergiants. *Astron. Astrophys.*, 488(2):L37–L41, 2008.

[46] C. C. Chu, C. T. Wang, C. C. Chang, R. Y. Chang, and W. T. Chang. Head-on collision of two coaxial vortex rings: experiment and computation. *J. Fluid Mech.*, 296:39–71, 1995.

[47] R. H. Cohen, W. P. Dannevik, A. M. Dimits, D. E. Eliason, A. A. Mirin, Y. Zhou, D. H. Porter, and P. R. Woodward. Three-dimensional simulation of a Richtmyer–Meshkov instability with a two-scale initial perturbation. *Phys. Fluids*, 14(10):3692–3709, 2002.

[48] B. D. Collins and J. W. Jacobs. PLIF flow visualization and measurements of the Richtmyer–Meshkov instability of an air/SF_6 interface. *J. Fluid Mech.*, 464:113–136, 2002.

[49] F. Coppari, R. F. Smith, J. H. Eggert, J. Wang, R. R. Rygg, A. Lazicki, J. A. Hawreliak, G. W. Collins, and T. S. Duffy. Experimental evidence for a phase transition in magnesium oxide at exoplanet pressures. *Nat. Geosci.*, 6(11):926–929, 2013.

[50] R. Courant and K. O. Friedrichs. *Supersonic Flow and Shock Waves*, volume 21. Springer Science & Business Media, 1999.

[51] A. P. S. Crotts and S. R. Heathcote. Velocity structure of the ring nebula around supernova 1987A. *Nature*, 350(6320):683–685, 1991.

[52] J. Crouch. Airplane trailing vortices and their control. *C. R. Phys.*, 6(4-5):487–499, 2005.

[53] S. C. Crow. Stability theory for a pair of trailing vortices. *AIAA J.*, 8(12):2172–2179, 1970.

[54] J. O. Dabiri. Optimal vortex formation as a unifying principle in biological propulsion. *Annu. Rev. Fluid Mech.*, 41:17–33, 2009.

[55] J. O. Dabiri and M. Gharib. Fluid entrainment by isolated vortex rings. *J. Fluid Mech.*, 511:311–331, 2004.

[56] I. Danaila, F. Luddens, F. Kaplanski, A. Papoutsakis, and S. S. Sazhin. Formation number of confined vortex rings. *Phys. Rev. Fluids*, 3(9):094701, 2018.

[57] S. Das. Recent advances in characterising irradiation damage in tungsten for fusion power. *SN Appl. Sci.*, 1(12):1614, 2019.

[58] E. J. Davies, P. M. Celliers, T. R. Boehly, R. Boni, G. W. Collins, A. Ernesti, et al. Pushing the α-quartz shock temperature pyrometry standard to 4 TPa. *In preparation for Phys. Rev. Lett.*, 2022.

[59] M. T. Henry de Frahan, P. Movahed, and E. Johnsen. Numerical simulations of a shock interacting with successive interfaces using the discontinuous Galerkin method: the multilayered Richtmyer–Meshkov and Rayleigh–Taylor instabilities. *Shock Waves*, 25:329–345, 2015.

[60] M. T. Henry de Frahan, S. Varadan, and E. Johnsen. A new limiting procedure for discontinuous galerkin methods applied to compressible multiphase flows with shocks and interfaces. *J. Comput. Phys.*, 280:489–509, 2015.

[61] F. Denner, C.-N. Xiao, and B. G. M. van Wachem. Pressure-based algorithm for compressible interfacial flows with acoustically-conservative interface discretisation. *J. Comput. Phys.*, 367:192–234, 2018.

[62] M. P. Desjarlais, M. D. Knudson, and K. R. Cochrane. Extension of the Hugoniot and analytical release model of α-quartz to 0.2–3 TPa. *J. Appl. Phys.*, 122(3):035903, 2017.

[63] A. Dewaele, J. H. Eggert, P. Loubeyre, and R. Le Toullec. Measurement of refractive index and equation of state in dense He, H_2, H_2O, and Ne under high pressure in a diamond anvil cell. *Phys. Rev. B*, 67(9):094112, 2003.

[64] N. Didden. On the formation of vortex rings: rolling-up and production of circulation. *Z. Agnew. Math. Phys.*, 30(1):101–116, 1979.

[65] N. Didden. On vortex formation and interaction with solid boundaries. In *Vortex Motion*, pages 1–17. Springer, 1982.

[66] G. Dimonte. Nonlinear evolution of the Rayleigh–Taylor and Richtmyer–Meshkov instabilities. *Phys. Plasmas*, 6(5):2009–2015, 1999.

[67] G. Dimonte and M. Schneider. Turbulent Rayleigh-Taylor instability experiments with variable acceleration. *Phys. Rev. E*, 54(4):3740, 1996.

[68] G. Dimonte and M. Schneider. Turbulent Richtmyer–Meshkov instability experiments with strong radiatively driven shocks. *Phys. Plasmas*, 4(12):4347–4357, 1997.

[69] G. Dimonte and R. Tipton. K-l turbulence model for the self-similar growth of the Rayleigh-Taylor and Richtmyer-Meshkov instabilities. *Phys. Fluids*, 18(8):085101, 2006.

[70] P. E. Dimotakis. The mixing transition in turbulent flows. *J. Fluid Mech.*, 409:69–98, 2000.

[71] A. Do, A. M. Angulo, G. N. Hall, S. R. Nagel, N. Izumi, B. J. Kozioziemski, T. McCarville, J. M. Ayers, and D. K. Bradley. X-ray imaging of Rayleigh–Taylor instabilities using Fresnel zone plate at the National Ignition Facility. *Rev. Sci. Instrum.*, 92(5):053511, 2021.

[72] T. Dornheim, Z. A. Moldabekov, K. Ramakrishna, P. Tolias, A. D. Baczewski, D. Kraus, et al. Electronic density response of warm dense matter. *Phys. Plasmas*, 30(3):032705, 2023.

[73] R. P. Drake. High-energy-density physics. *Phys. Today*, 63(6):28, 2010.

[74] V. D. Duong, V. D. Nguyen, and V. L. Nguyen. Turbulence cascade model for viscous vortex ring-tube reconnection. *Phys. Fluids*, 33(3):035145, 2021.

[75] J. Eggert, S. Brygoo, P. Loubeyre, R. S. McWilliams, P. M. Celliers, D. G. Hicks, T. R. Boehly, R. Jeanloz, and G. W. Collins. Hugoniot data for helium in the ionization regime. *Phys. Rev. Lett.*, 100:124503, Mar 2008.

[76] Y. Elbaz and D. Shvarts. Modal model mean field self-similar solutions to the asymptotic evolution of Rayleigh-Taylor and Richtmyer-Meshkov instabilities and its dependence on the initial conditions. *Phys. Plasmas*, 25(6):062126, 2018.

[77] A. Y. Faenov, T. A. Pikuz, P. Mabey, B. Albertazzi, T. H. Michel, G. Rigon, et al. Advanced high resolution x-ray diagnostic for HEDP experiments. *Sci. Rep.*, 8(1):16407, 2018.

[78] M. Fiedler. Modeling streak camera sweep speeds.

[79] T. Fohl and J. S. Turner. Colliding vortex rings. *Phys. Fluids*, 18(4):433–436, 1975.

[80] A. Förster, T. Kahlbaum, and W. Ebeling. Equation of state and the phase diagram of dense fluid helium in the region of partial ionization. *Laser Part. Beams*, 10(2):253–262, 1992.

[81] C. Fransson, J. Larsson, K. Migotto, D. Pesce, P. Challis, R. A. Chevalier, et al. The destruction of the circumstellar ring of SN 1987A. *Astrophys. J. Lett.*, 806(1):L19, 2015.

[82] B. Fryxell, K. Olson, P. Ricker, F. X. Timmes, M. Zingale, D. Q. Lamb, P. MacNeice, R. Rosner, J. W. Truran, and H. Tufo. FLASH: An adaptive mesh hydrodynamics code for modeling astrophysical thermonuclear flashes. *Astrophys. J.*, 131(1):273, 2000.

[83] M. Gharib, E. Rambod, A. Kheradvar, D. J. Sahn, and J. O. Dabiri. Optimal vortex formation as an index of cardiac health. *Proc. Natl. Acad. Sci.*, 103(16):6305–6308, 2006.

[84] M. Gharib, E. Rambod, and K. Shariff. A universal time scale for vortex ring formation. *J. Fluid Mech.*, 360:121–140, 1998.

[85] G. Ghosh. Dispersion-equation coefficients for the refractive index and birefringence of calcite and quartz crystals. *Opt. Commun.*, 163(1-3):95–102, 1999.

[86] G. Gilmore. The short spectacular life of a superstar. *Science*, 304(5679):1915–1916, 2004.

[87] R. Grover and J. W. Hardy. The propagation of shocks in exponentially decreasing atmospheres. *Astrophys. J.*, 143:48, 1966.

[88] V. K. Gryaznov, I. L. Iosilevskiy, and V. E. Fortov. Thermodynamics of hydrogen and helium plasmas in megabar and multi-megabar pressure range under strong shock and isentropic compression. *plasma Phys. Control. Fusion*, 58(1):014012, 2015.

[89] J. Guzman and T. Plewa. Non-spherical core-collapse supernovae: evolution towards homologous expansion. *Nonlinearity*, 22(11):2775, 2009.

[90] J.-F. Haas and B. Sturtevant. Interaction of weak shock waves with cylindrical and spherical gas inhomogeneities. *J. Fluid Mech.*, 181:41–76, 1987.

[91] B. M. Haines, R. E. Olson, W. Sweet, S. A. Yi, A. B. Zylstra, P. A. Bradley, et al. Robustness to hydrodynamic instabilities in indirectly driven layered capsule implosions. *Phys. Plasmas*, 26(1):012707, 2019.

[92] J. N. Hallock and F. Holzäpfel. A review of recent wake vortex research for increasing airport capacity. *Prog. Aerosp. Sci.*, 98:27–36, 2018.

[93] B. A. Hammel, H. A. Scott, S. P. Regan, C. Cerjan, D. S. Clark, M. J. Edwards, et al. Diagnosing and controlling mix in National Ignition Facility implosion experiments. *Phys. Plasmas*, 18(5):056310, 2011.

[94] P. Hartigan, J. M. Foster, B. H. Wilde, R. F. Coker, P. A. Rosen, J. F. Hansen, B. E. Blue, R. J. R. Williams, R. Carver, and A. Frank. Laboratory experiments, numerical simulations, and astronomical observations of deflected supersonic jets: Application to HH 110. *Astrophys. J.*, 705(1):1073, 2009.

[95] J. Hecht, U. Alon, and D. Shvarts. Potential flow models of Rayleigh–Taylor and Richtmyer–Meshkov bubble fronts. *Phys. Fluids*, 6(12):4019–4030, 1994.

[96] M. J. Herman, D. Peterson, K. Henderson, T. Cardenas, C. E. Hamilton, J. Oertel, and B. M. Patterson. Lithographic printing via two-photon polymerization of engineered foams. *Fusion Sci. Technol.*, 73(2):166–172, 2018.

[97] D. G. Hicks, T. R. Boehly, J. H. Eggert, J. E. Miller, P. M. Celliers, and G. W. Collins. Dissociation of liquid silica at high pressures and temperatures. *Phys. Rev. Lett.*, 97(2):025502, 2006.

[98] R. L. Holmes, G. Dimonte, B. Fryxell, M. L. Gittings, J. W. Grove, M. Schneider, D. H. Sharp, A. L. Velikovich, R. P. Weaver, and Q. Zhang. Richtmyer–Meshkov instability growth: experiment, simulation and theory. *J. Fluid Mech.*, 389:55–79, 1999.

[99] J. C. R. Hunt, A. A. Wray, and P. Moin. Eddies, streams, and convergence zones in turbulent flows. *Studying turbulence using numerical simulation databases, 2. Proceedings of the 1988 summer program*, 1988.

[100] F. Hussain and K. Duraisamy. Mechanics of viscous vortex reconnection. *Phys. Fluids*, 23(2):021701, 2011.

[101] C. A. Iglesias, F. J. Rogers, and D. Saumon. Density effects on the opacity of cool helium white dwarf atmospheres. *Astrophys. J.*, 569(2):L111, 2002.

[102] I. V. Igumenshchev, V. N. Goncharov, W. T. Shmayda, D. R. Harding, T. C. Sangster, and D. D. Meyerhofer. Effects of local defect growth in direct-drive cryogenic implosions on OMEGA. *Phys. Plasmas*, 20(8):082703, 2013.

[103] J. W. Jacobs and J. M. Sheeley. Experimental study of incompressible Richtmyer–Meshkov instability. *Phys. Fluids*, 8(2):405–415, 1996.

[104] P. Jakobsen, R. Albrecht, C. Barbieri, J. C. Blades, A. Boksenberg, P. Crane, et al. First results from the Faint Object Camera-SN 1987A. *Astrophys. J.*, 369:L63–L66, 1991.

[105] R. Jeanloz, P. M. Celliers, G. W. Collins, J. H. Eggert, K. M. Lee, R. S. McWilliams, S. Brygoo, and P. Loubeyre. Achieving high-density states through shock-wave loading of precompressed samples. *Proc. Natl. Acad. Sci.*, 104(22):9172–9177, 2007.

[106] J. Jeong and F. Hussain. On the identification of a vortex. *J. Fluid Mech.*, 285:69–94, 1995.

[107] J. Jimenez. Stability of a pair of co-rotating vortices. *Phys. Fluids*, 18(11):1580–1581, 1975.

[108] E. Johnsen and T. Colonius. Implementation of WENO schemes in compressible multicomponent flow problems. *J. Comput. Phys.*, 219(2):715–732, 2006.

[109] P. E. Johnson and E. Johnsen. The compact gradient recovery discontinuous Galerkin method for diffusion problems. *J. Comput. Phys.*, 398:108872, 2019.

[110] J. Kane, R. P. Drake, and B. A. Remington. An evaluation of the Richtmyer-Meshkov instability in supernova remnant formation. *Astrophys. J.*, 511(1):335, 1999.

[111] Y.-G. Kang, H. Nishimura, H. Takabe, K. Nishihara, A. Sunahara, T. Norimatsu, K. Nagai, H. Kim, M. Nakatsuka, and H.-J. Kong. Laboratory simulation of the collision of supernova 1987A with its circumstellar ring nebula. *Plasma Phys. Rep.*, 27(10), 2001.

[112] P. A. Keiter, J. B. Elliott, B. E. Blue, J. H. Cooley, J. Edwards, G. A. Kyrala, H. F. Robey, B. Spears, and D. C. Wilson. Measurement and simulation of jet mass caused by a high-aspect ratio hole perturbation. *Phys. Plasmas*, 17(6):062704, 2010.

[113] Kelvin. Vibrations of a columnar vortex. *Proc. R. Soc. Edinb.*, 10:155–168, 1880.

[114] G. M. Kennedy, S. Marino, L. Matra, O. Panić, D. Wilner, M. C. Wyatt, and B. Yelverton. ALMA observations of the narrow hr 4796A debris ring. *Mon. Notices Royal Astron. Soc.*, 475(4):4924–4938, 2018.

[115] G. M. Kennedy, L. Matrà, S. Facchini, J. Milli, O. Panić, D. Price, D. J. Wilner, M. C. Wyatt, and B. M. Yelverton. A circumbinary protoplanetary disk in a polar configuration. *Nat. Astron.*, 3(3):230–235, 2019.

[116] R. R. Kerswell. Elliptical instability. *Annu. Rev. Fluid Mech.*, 34:83, 2002.

[117] S. Kida and M. Takaoka. Vortex reconnection. *Annu. Rev. Fluid Mech.*, 26(1):169–177, 1994.

[118] S. Kida, M. Takaoka, and F. Hussain. Collision of two vortex rings. *J. Fluid Mech.*, 230:583–646, 1991.

[119] A. Kietzmann, B. Holst, R. Redmer, M. P. Desjarlais, and T. R. Mattsson. Quantum molecular dynamics simulations for the nonmetal-to-metal transition in fluid helium. *Phys. Rev. Lett.*, 98(19):190602, 2007.

[120] Y.-J. Kim, B. Militzer, B. Boates, S. Bonev, P. M. Celliers, G. W. Collins, et al. Evidence for dissociation and ionization in shock compressed nitrogen to 800 GPa. *Phys. Rev. Lett.*, 2022.

[121] M. D. Knudson and M. P. Desjarlais. Shock compression of quartz to 1.6 TPa: Redefining a pressure standard. *Phys. Rev. Lett.*, 103(22):225501, 2009.

[122] I. W. Kokkinakis, D. Drikakis, and D. L. Youngs. Vortex morphology in Richtmyer–Meshkov-induced turbulent mixing. *Phys. D: Nonlinear Phenom.*, 407:132459, 2020.

[123] P. J. Kortbeek and J. A. Schouten. Equation of state of fluid helium to very high pressure. *Chem. Phys.*, 95(6):4519–4524, 1991.

[124] P. M. Kowalski, S. Mazevet, D. Saumon, and M. Challacombe. Equation of state and optical properties of warm dense helium. *Phys. Rev. B*, 76(7):075112, 2007.

[125] J. Kuczek and B. Haines. The impact of fill tube geometry on recent high yield implosions on the National Ignition Facility. *Talk presented at the 17th International Workshop on the Physics of Compressible Turbulent Mixing*, 2022.

[126] P. Kumar and K. Mahesh. Large eddy simulation of propeller wake instabilities. *J. Fluid Mech.*, 814:361–396, 2017.

[127] C. C. Kuranz, R. P. Drake, M. J. Grosskopf, A. Budde, C. Krauland, D. C. Marion, et al. Three-dimensional blast-wave-driven Rayleigh–Taylor instability and the effects of long-wavelength modes. *Phys. Plasmas*, 16(5):056310, 2009.

[128] C. C. Kuranz, R. P. Drake, E. C. Harding, M. J. Grosskopf, H. F. Robey, B. A. Remington, et al. Two-dimensional blast-wave-driven Rayleigh–Taylor instability: experiment and simulation. *Astrophys. J.*, 696(1):749, 2009.

[129] J. T. Larsen and S. M. Lane. HYADES—a plasma hydrodynamics code for dense plasma studies. *J. Quant. Spectrosc. Radiat. Transf.*, 51(1-2):179–186, 1994.

[130] J. Larsson, C. Fransson, G. Östlin, P. Gröningsson, A. Jerkstrand, C. Kozma, et al. X-ray illumination of the ejecta of supernova 1987A. *Nature*, 474(7352):484–486, 2011.

[131] M. Latini, O. Schilling, and W. S. Don. Effects of WENO flux reconstruction order and spatial resolution on reshocked two-dimensional Richtmyer–Meshkov instability. *J. Comput. Phys.*, 221(2):805–836, 2007.

[132] R. M. Lau, M. J. Hankins, Y. Han, I. Argyriou, M. F. Corcoran, J. J. Eldridge, et al. Nested dust shells around the Wolf–Rayet binary WR 140 observed with JWST. *Nat. Astron.*, 6(11):1308–1316, 2022.

[133] D. Layzer. On the instability of superposed fluids in a gravitational field. *Astrophys. J.*, 122:1, 1955.

[134] B. Van Leer. Towards the ultimate conservative difference scheme. V. a second-order sequel to Godunov's method. *J. Comput. Phys.*, 32(1):101–136, 1979.

[135] T. Leweke, S. Le Dizes, and C. H. K. Williamson. Dynamics and instabilities of vortex pairs. *Annu. Rev. Fluid Mech.*, 48:507–541, 2016.

[136] T. Leweke and C. H. K. Williamson. Cooperative elliptic instability of a vortex pair. *J. Fluid Mech.*, 360:85–119, 1998.

[137] T. Leweke and C. H. K. Williamson. Experiments on long-wavelength instability and reconnection of a vortex pair. *Phys. Fluids*, 23(2):024101, 2011.

[138] Z.-G. Li, Y. Cheng, Q.-F. Chen, and X.-R. Chen. Equation of state and transport properties of warm dense helium via quantum molecular dynamics simulations. *Phys. Plasmas*, 23(5):052701, 2016.

[139] E. H. Lieb and H.-T. Yau. A rigorous examination of the Chandrasekhar theory of stellar collapse. *Astrophys. J.*, 323:140–144, 1987.

[140] O. A. Likhachev and J. W. Jacobs. A vortex model for Richtmyer–Meshkov instability accounting for finite Atwood number. *Phys. Fluids*, 17(3):031704, 2005.

[141] T. T. Lim and T. B. Nickels. Instability and reconnection in the head-on collision of two vortex rings. *Nature*, 357(6375):225–227, 1992.

[142] K. T. Lorenz, M. J. Edwards, A. F. Jankowski, S. M. Pollaine, R. F. Smith, and B. A. Remington. High pressure, quasi-isentropic compression experiments on the Omega laser. *High Energy Density Phys.*, 2(3-4):113–125, 2006.

[143] P. Loubeyre, J. M. Besson, J. P. Pinceaux, and J. P. Hansen. High-pressure melting curve of ^{4}He. *Phys. Rev. Lett.*, 49:1172–1175, Oct 1982.

[144] L. Lu and C. R. Doering. Limits on enstrophy growth for solutions of the three-dimensional Navier-Stokes equations. *Indiana Univ. Math. J.*, pages 2693–2727, 2008.

[145] S. P. Lyon. Sesame: the Los Alamos National Laboratory equation of state database. *Los Alamos National Laboratory report LA-UR-92-3407*, 1992.

[146] T. Ma, D. Mariscal, R. Anirudh, T. Bremer, B. Z. Djordjevic, T. Galvin, et al. Accelerating the rate of discovery: Toward high-repetition-rate hed science. *Plasma Phys. Control. Fusion*, 63(10):104003, 2021.

[147] J. R. Mansfield, O. M. Knio, and C. Meneveau. Dynamic LES of colliding vortex rings using a 3D vortex method. *J. Comput. Phys.*, 152(1):305–345, 1999.

[148] F. J. Marshall, S. T. Ivancic, C. Mileham, P. M. Nilson, J. J. Ruby, C. Stoeckl, B. S. Scheiner, and M. J. Schmitt. High-resolution x-ray radiography with Fresnel zone plates on the University of Rochester's OMEGA Laser Systems. *Rev. Sci. Instrum.*, 92(3):033701, 2021.

[149] C. L. Martin and D. Arnett. The origin of the rings around SN 1987A: an evaluation of the interacting-winds model. *Astrophys. J.*, 447:378, 1995.

[150] T. Maxworthy. Some experimental studies of vortex rings. *J. Fluid Mech.*, 81(3):465–495, 1977.

[151] R. McCray. Supernova 1987A revisited. *Annu. Rev. Astron. Astrophys.*, 31(1):175–216, 1993.

[152] R. McCray and C. Fransson. The remnant of supernova 1987A. *Annu. Rev. Astron. Astrophys.*, 54:19–52, 2016.

[153] R. McCray and D. N. C. Lin. Is the ring around SN1987A a protostellar disk? *Nature*, 369(6479):378–380, 1994.

[154] J. A. McFarland, D. Reilly, W. Black, J. A. Greenough, and D. Ranjan. Modal interactions between a large-wavelength inclined interface and small-wavelength multimode perturbations in a Richtmyer-Meshkov instability. *Phys. Rev. E*, 92(1):013023, 2015.

[155] D. McGonegle, P. G. Heighway, M. Sliwa, C. A. Bolme, A. J. Comley, L. E. Dresselhaus-Marais, et al. Investigating off-Hugoniot states using multi-layer ring-up targets. *Sci. Rep.*, 10(1):13172, 2020.

[156] C. F. McKee and E. C. Ostriker. Theory of star formation. *Annu. Rev. Astron. Astrophys.*, 45:565–687, 2007.

[157] R. McKeown, R. Ostilla-Mónico, A. Pumir, M. P. Brenner, and S. M. Rubinstein. Cascade leading to the emergence of small structures in vortex ring collisions. *Phys. Rev. Fluids*, 3(12):124702, 2018.

[158] R. McKeown, R. Ostilla-Mónico, A. Pumir, M. P. Brenner, and S. M. Rubinstein. Turbulence generation through an iterative cascade of the elliptical instability. *Sci. Adv.*, 6(9):eaaz2717, 2020.

[159] J. M. McMahon, M. A. Morales, C. Pierleoni, and D. M. Ceperley. The properties of hydrogen and helium under extreme conditions. *Rev. Mod. Phys.*, 84(4):1607, 2012.

[160] R. Menikoff and B. J. Plohr. The Riemann problem for fluid flow of real materials. *Rev. Mod. Phys.*, 61(1):75, 1989.

[161] E. C. Merritt, J. P. Sauppe, E. N. Loomis, T. Cardenas, D. S. Montgomery, W. S. Daughton, et al. Experimental study of energy transfer in double shell implosions. *Phys. Plasmas*, 26(5):052702, 2019.

[162] E. E. Meshkov. Instability of the interface of two gases accelerated by a shock wave. *Fluid Dyn.*, 4(5):101–104, 1969.

[163] P. Meunier and T. Leweke. Elliptic instability of a co-rotating vortex pair. *J. Fluid Mech.*, 533:125–159, 2005.

[164] E. Michael, R. McCray, C. S. J. Pun, P. Garnavich, P. Challis, R. P. Kirshner, et al. Hubble Space Telescope spectroscopy of spot 1 on the circumstellar ring of SN 1987A. *Astrophys. J.*, 542(1):L53, 2000.

[165] K. O. Mikaelian. Analytic approach to nonlinear Rayleigh-Taylor and Richtmyer-Meshkov instabilities. *Phys. Rev. Lett.*, 80(3):508, 1998.

[166] K. O. Mikaelian. Reshocks, rarefactions, and the generalized layzer model for hydrodynamic instabilities. *Phys. Fluids*, 21(2):024103, 2009.

[167] B. Militzer. First principles calculations of shock compressed fluid helium. *Phys. Rev. Lett.*, 97(17):175501, 2006.

[168] B. Militzer. Correlations in hot dense helium. *J. Phys. A: Math. Theor.*, 42(21):214001, 2009.

[169] B. Militzer. Path integral Monte Carlo and density functional molecular dynamics simulations of hot, dense helium. *Phys. Rev. B*, 79(15):155105, 2009.

[170] B. Militzer, F. González-Cataldo, S. Zhang, K. P. Driver, and F. Soubiran. First-principles equation of state database for warm dense matter computation. *Phys. Rev. E*, 103(1):013203, 2021.

[171] B. Militzer, W. B. Hubbard, S. Wahl, J. I. Lunine, E. Galanti, Y. Kaspi, et al. Juno spacecraft measurements of Jupiter's gravity imply a dilute core. *Planet. Sci.*, 3(8):185, 2022.

[172] B. Militzer, F. Soubiran, S. M. Wahl, and W. Hubbard. Understanding Jupiter's interior. *J. Geophys. Res. Planets*, 121(9):1552–1572, 2016.

[173] J. E. Miller, T. R. Boehly, A. Melchior, D. D. Meyerhofer, P. M. Celliers, J. H. Eggert, D. G. Hicks, C. M. Sorce, J. A. Oertel, and P. M. Emmel. Streaked optical pyrometer system for laser-driven shock-wave experiments on OMEGA. *Rev. Sci. Instrum.*, 78(3):034903, 2007.

[174] M. Millot, F. Coppari, J. R. Rygg, A. Correa Barrios, S. Hamel, D. C. Swift, and J. H. Eggert. Nanosecond x-ray diffraction of shock-compressed superionic water ice. *Nature*, 569(7755):251–255, 2019.

[175] M. Millot, N. Dubrovinskaia, A. Černok, S. Blaha, L. Dubrovinsky, D. G. Braun, P. M. Celliers, G. W. Collins, J. H. Eggert, and R. Jeanloz. Shock compression of stishovite and melting of silica at planetary interior conditions. *Science*, 347(6220):418–420, 2015.

[176] M. Millot, S. Hamel, J. R. Rygg, P. M. Celliers, G. W. Collins, F. Coppari, D. E. Fratanduono, R. Jeanloz, D. C. Swift, and J. H. Eggert. Experimental evidence for superionic water ice using shock compression. *Nat. Phys.*, 14(3):297–302, 2018.

[177] T. Minota, M. Nishida, and M. G. Lee. Head-on collision of two compressible vortex rings. *Fluid Dyn. Res.*, 22(1):43, 1998.

[178] A. Mishra, A. Pumir, and R. Ostilla-Mónico. Instability and disintegration of vortex rings during head-on collisions and wall interactions. *Phys. Rev. Fluids*, 6:104702, Oct 2021.

[179] A. C. Mitchell and W. J. Nellis. Diagnostic system of the Lawrence Livermore National Laboratory two-stage light-gas gun. *Rev. Sci. Instrum.*, 52(3):347–359, 1981.

[180] R. Mittal, J. H. Seo, V. Vedula, Y. J. Choi, H. Liu, H. H. Huang, S. Jain, L. Younes, T. Abraham, and R. T. George. Computational modeling of cardiac hemodynamics: current status and future outlook. *J. Comput. Phys.*, 305:1065–1082, 2016.

[181] M. A. Mochalov, R. I. Il'kaev, V. E. Fortov, A. L. Mikhailov, V. A. Arinin, A. O. Blikov, S. E. Elfimov, V. A. Komrakov, V. A. Ogorodnikov, and A. V. Ryzhkov. Thermodynamic parameters of helium under shock-wave and quasi-isentropic compressions at pressures up to 4800 GPa and compression ratios up to 900. *J. Exp. Theor. Phys.*, 125(5):948–963, 2017.

[182] K. Mohseni and M. Gharib. A model for universal time scale of vortex ring formation. *Phys. Fluids*, 10(10):2436–2438, 1998.

[183] K. Mohseni, H. Ran, and T. Colonius. Numerical experiments on vortex ring formation. *J. Fluid Mech.*, 430:267–282, 2001.

[184] K. Molvig, M. J. Schmitt, R. Betti, E. M. Campbell, and P. McKenty. Stable and confined burn in a revolver ignition capsule. *Phys. Plasmas*, 25(8):082708, 2018.

[185] D. S. Montgomery, W. S. Daughton, B. J. Albright, A. N. Simakov, D. C. Wilson, E. S. Dodd, et al. Design considerations for indirectly driven double shell capsules. *Phys. Plasmas*, 25(9):092706, 2018.

[186] D. W. Moore and P. G. Saffman. The motion of a vortex filament with axial flow. *Philos. Trans. R. Soc. A*, 272(1226):403–429, 1972.

[187] D. W. Moore and P. G. Saffman. The instability of a straight vortex filament in a strain field. *Proc. R. Soc. Lond.*, 346(1646):413–425, 1975.

[188] R. M. More, K. H. Warren, D. A. Young, and G. B. Zimmerman. A new quotidian equation of state (QEOS) for hot dense matter. *Phys. Fluids*, 31(10):3059–3078, 1988.

[189] S. E. Morris and C. H. K. Williamson. Impingement of a counter-rotating vortex pair on a wavy wall. *J. Fluid Mech.*, 895, 2020.

[190] T. Morris and P. Podsiadlowski. The triple-ring nebula around SN 1987A: fingerprint of a binary merger. *Science*, 315(5815):1103–1106, 2007.

[191] T. Morris and P. Podsiadlowski. A binary merger model for the formation of the supernova 1987A triple-ring nebula. *Mon. Notices Royal Astron. Soc.*, 399(2):515–538, 2009.

[192] P. Movahed and E. Johnsen. A solution-adaptive method for efficient compressible multifluid simulations, with application to the Richtmyer–Meshkov instability. *J. Comput. Phys.*, 239:166–186, 2013.

[193] B. Musci, S. Petter, G. Pathikonda, B. Ochs, and D. Ranjan. Supernova hydrodynamics: A lab-scale study of the blast-driven instability using high-speed diagnostics. *Astrophys. J.*, 896(2):92, 2020.

[194] B. Nagler, B. Arnold, G. Bouchard, R. F. Boyce, R. M. Boyce, A. Callen, et al. The matter in extreme conditions instrument at the Linac coherent light source. *J. Synchrotron Radit.*, 22(3):520–525, 2015.

[195] J. C. Nawroth, H. Lee, A. W. Feinberg, C. M. Ripplinger, M. L. McCain, A. Grosberg, J. O. Dabiri, and K. K. Parker. A tissue-engineered jellyfish with biomimetic propulsion. *Nat. Biotechnol.*, 30(8):792–797, 2012.

[196] W. J. Nellis, N. C. Holmes, A. C. Mitchell, R. J. Trainor, G. K. Governo, M. Ross, and D. A. Young. Shock compression of liquid helium to 56 GPa (560 kbar). *Phys. Rev. Lett.*, 53(13):1248, 1984.

[197] N. Nettelmann, B. Holst, A. Kietzmann, M. French, R. Redmer, and D. Blaschke. Ab initio equation of state data for hydrogen, helium, and water and the internal structure of Jupiter. *Astrophys. J.*, 683(2):1217, 2008.

[198] V. L. Nguyen, T. D. Phan, V. D. Duong, and N. T. P. Le. Turbulent energy cascade associated with viscous reconnection of two vortex rings. *Phys. Fluids*, 33(8):085117, 2021.

[199] M. Nitsche and R. Krasny. A numerical study of vortex ring formation at the edge of a circular tube. *J. Fluid Mech.*, 276:139–161, 1994.

[200] J. Norbury. A family of steady vortex rings. *J. Fluid Mech.*, 57(3):417–431, 1973.

[201] J. W. Nunziato and E. K. Walsh. Propagation and growth of shock waves in inhomogeneous fluids. *Phys. Fluids*, 15(8):1397–1402, 1972.

[202] D. Olmstead, P. Wayne, J.-H. Yoo, S. Kumar, C. R. Truman, and P. Vorobieff. Experimental study of shock-accelerated inclined heavy gas cylinder. *Exp. Fluids*, 58:1–20, 2017.

[203] B. J. Olson and J. Greenough. Large eddy simulation requirements for the Richtmyer-Meshkov instability. *Phys. Fluids*, 26(4):044103, 2014.

[204] B. J. Olson and J. A. Greenough. Comparison of two-and three-dimensional simulations of miscible Richtmyer-Meshkov instability with multimode initial conditions. *Phys. Fluids*, 26(10):101702, 2014.

[205] J. Ongena, R. Koch, R. Wolf, and H. Zohm. Magnetic-confinement fusion. *Nat. Phys.*, 12(5):398–410, 2016.

[206] S. Orlando, M. Miceli, M. L. Pumo, and F. Bocchino. Supernova 1987A: A template to link supernovae to their remnants. *Astrophys. J.*, 810(2):168, 2015.

[207] D. Oron, L. Arazi, D. Kartoon, A. Rikanati, U. Alon, and D. Shvarts. Dimensionality dependence of the Rayleigh–Taylor and Richtmyer–Meshkov instability late-time scaling laws. *Phys. Plasmas*, 8(6):2883–2889, 2001.

[208] N. Panagia, R. Gilmozzi, F. Macchetto, H.-M. Adorf, and R. P. Kirshner. Properties of the SN 1987A circumstellar ring and the distance to the Large Magellanic Cloud. *Astrophys. J.*, 380:L23–L26, 1991.

[209] S. Le Pape, L. F. Berzak Hopkins, L. Divol, A. Pak, E. L. Dewald, S. Bhandarkar, et al. Fusion energy output greater than the kinetic energy of an imploding shell at the National Ignition Facility. *Phys. Rev. Lett.*, 120(24):245003, 2018.

[210] G. Pawlak, C. Marugan Cruz, C. Martínez Bazán, and P. García Hrdy. Experimental characterization of starting jet dynamics. *Fluid Dyn. Res.*, 39(11-12):711, 2007.

[211] S. Pellone, C. A. Di Stefano, A. M. Rasmus, C. C. Kuranz, and E. Johnsen. Vortex-sheet modeling of hydrodynamic instabilities produced by an oblique shock interacting with a perturbed interface in the HED regime. *Phys. Plasmas*, 28(2):022303, 2021.

[212] R. T. Pierrehumbert. A family of steady, translating vortex pairs with distributed vorticity. *J. Fluid Mech.*, 99(1):129–144, 1980.

[213] M. Preising, W. Lorenzen, A. Becker, R. Redmer, M. D. Knudson, and M. P. Desjarlais. Equation of state and optical properties of warm dense helium. *Phys. Plasmas*, 25(1):012706, 2018.

[214] M. Preising and R. Redmer. Metallization of dense fluid helium from ab initio simulations. *Phys. Rev. B*, 102(22):224107, 2020.

[215] M. Preising and R. Redmer. Nonmetal-to-metal transition in dense fluid helium. *Contrib. to Plasma Phys.*, 61(10):e202100105, 2021.

[216] Y. Qi, S. Tan, N. Corbitt, C. Urbanik, A. K. R. Salibindla, and R. Ni. Fragmentation in turbulence by small eddies. *Nat. Commun.*, 13(1):1–8, 2022.

[217] P. Ramaprabhu, G. Dimonte, P. Woodward, C. Fryer, G. Rockefeller, K. Muthuraman, P.-H. Lin, and J. Jayaraj. The late-time dynamics of the single-mode Rayleigh-Taylor instability. *Phys. Fluids*, 24(7):074107, 2012.

[218] D. T. Reese, A. M. Ames, C. D. Noble, J. G. Oakley, D. A. Rothamer, and R. Bonazza. Simultaneous direct measurements of concentration and velocity in the Richtmyer–Meshkov instability. *J. Fluid Mech.*, 849:541–575, 2018.

[219] S. P. Regan, R. Epstein, B. A. Hammel, L. J. Suter, H. A. Scott, M. A. Barrios, et al. Hot-spot mix in ignition-scale inertial confinement fusion targets. *Phys. Rev. Lett.*, 111(4):045001, 2013.

[220] R. D. Richtmyer. Taylor instability in shock acceleration of compressible fluids. Technical report, Los Alamos Scientific Lab., N. Mex., 1954.

[221] G. Rigon, B. Albertazzi, T. Pikuz, P. Mabey, V. Bouffetier, N. Ozaki, et al. Micron-scale phenomena observed in a turbulent laser-produced plasma. *Nat. Commun.*, 12(1):2679, 2021.

[222] A. Rikanati, U. Alon, and D. Shvarts. Vortex model for the nonlinear evolution of the multimode Richtmyer-Meshkov instability at low Atwood numbers. *Phys. Rev. E*, 58(6):7410, 1998.

[223] A. C. Robinson and P. G. Saffman. Three-dimensional stability of vortex arrays. *J. Fluid Mech.*, 125:411–427, 1982.

[224] M. Rosenfeld, K. Katija, and J. O. Dabiri. Circulation generation and vortex ring formation by conic nozzles. *J. Fluids Eng.*, 131(9), 2009.

[225] M. Rosenfeld, E. Rambod, and M. Gharib. Circulation and formation number of laminar vortex rings. *J. Fluid Mech.*, 376:297–318, 1998.

[226] M. Ross and D. A. Young. Helium at high density. *Phys. Lett. A*, 118(9):463–466, 1986.

[227] D. Ryutov, R. P. Drake, J. Kane, E. Liang, B. A. Remington, and W. M. Wood-Vasey. Similarity criteria for the laboratory simulation of supernova hydrodynamics. *Astrophys. J.*, 518(2):821, 1999.

[228] O. Sadot, L. Erez, U. Alon, D. Oron, L. A. Levin, G. Erez, G. Ben-Dor, and D. Shvarts. Study of nonlinear evolution of single-mode and two-bubble interaction under Richtmyer-Meshkov instability. *Phys. Rev. Lett.*, 80(8):1654, 1998.

[229] P. G. Saffman. The motion of a vortex pair in a stratified atmosphere. *Stud. Appl. Math.*, 51(2):107–119, 1972.

[230] P. G. Saffman. *Vortex Dynamics*. Cambridge university press, 1995.

[231] R. Samtaney and N. J. Zabusky. Circulation deposition on shock-accelerated planar and curved density-stratified interfaces: models and scaling laws. *J. Fluid Mech.*, 269:45–78, 1994.

[232] M. A. Sandoval, W. R. Hix, O. E. B. Messer, E. J. Lentz, and J. A. Harris. Three-dimensional core-collapse supernova simulations with 160 isotopic species evolved to shock breakout. *Astrophys. J.*, 921(2):113, 2021.

[233] T. Sarpkaya. Trailing vortices in homogeneous and density-stratified media. *J. Fluid Mech.*, 136:85–109, 1983.

[234] R. Sau and K. Mahesh. Passive scalar mixing in vortex rings. *J. Fluid Mech.*, 582:449–461, 2007.

[235] D. Saumon. Evaluation of helium equation of state tables. Technical report, Los Alamos National Lab. (LANL), Los Alamos, NM (United States), 2020.

[236] D. Saumon, S. Blouin, and P.-E. Tremblay. Current challenges in the physics of white dwarf stars. *Phys. Rep.*, 988:1–63, 2022.

[237] D. Saumon and T. Guillot. Shock compression of deuterium and the interiors of Jupiter and Saturn. *Astrophys. J.*, 609(2):1170, 2004.

[238] A. M. Saunders, C. V. Stan, K. K. Mackay, B. Morgan, J. A. K. Horwitz, S. J. Ali, et al. Experimental observations of laser-driven tin ejecta microjet interactions. *Phys. Rev. Lett.*, 127(15):155002, 2021.

[239] B. Scheiner, M. J. Schmitt, S. C. Hsu, D. Schmidt, J. Mance, C. Wilde, et al. First experiments on revolver shell collisions at the OMEGA laser. *Phys. Plasmas*, 26(7):072707, 2019.

[240] M. J. Schmitt, P. A. Bradley, J. A. Cobble, J. R. Fincke, P. Hakel, S. C. Hsu, et al. Development of a polar direct-drive platform for studying inertial confinement fusion implosion mix on the National Ignition Facility. *Phys. Plasmas*, 20(5):056310, 2013.

[241] E. G. Sewell, K. J. Ferguson, V. V. Krivets, and J. W. Jacobs. Time-resolved particle image velocimetry measurements of the turbulent Richtmyer–Meshkov instability. *J. Fluid Mech.*, 917:A41, 2021.

[242] S. C. Shadden, K. Katija, M. Rosenfeld, J. E. Marsden, and J. O. Dabiri. Transport and stirring induced by vortex formation. *J. Fluid Mech.*, 593:315–331, 2007.

[243] A. H. Shapiro. The dynamics and thermodynamics of compressible fluid flow. *New York: Ronald Press*, 1953.

[244] N. Smith, W. D. Arnett, J. Bally, A. Ginsburg, and A. V. Filippenko. The ring nebula around the blue supergiant SBW1: pre-explosion snapshot of an SN 1987A twin. *Mon. Notices Royal Astron. Soc.*, 429(2):1324–1341, 2013.

[245] R. F. Smith, J. H. Eggert, R. Jeanloz, T. S. Duffy, D. G. Braun, J. R. Patterson, et al. Ramp compression of diamond to five terapascals. *Nature*, 511(7509):330–333, 2014.

[246] R. F. Smith, D. E. Fratanduono, D. G. Braun, T. S. Duffy, J. K. Wicks, P. M. Celliers, et al. Equation of state of iron under core conditions of large rocky exoplanets. *Nat. Astron.*, 2(6):452–458, 2018.

[247] R. F. Smith, K. T. Lorenz, D. Ho, B. A. Remington, A. Hamza, J. Rogers, S. Pollaine, S. Jeon, Y.-S. Nam, and J. Kilkenny. Graded-density reservoirs for accessing high stress low temperature material states. *Conference Paper*, 2007.

[248] N. Soker. Binary progenitor models for bipolar planetary nebulae. *Astrophys. J.*, 496(2):833, 1998.

[249] F. Soubiran, S. Mazevet, C. Winisdoerffer, and G. Chabrier. Helium gap in the warm dense matter regime and experimental reflectivity measurements. *Phys. Rev. B*, 86(11):115102, 2012.

[250] F. Soubiran, S. Mazevet, C. Winisdoerffer, and G. Chabrier. Optical signature of hydrogen-helium demixing at extreme density-temperature conditions. *Phys. Rev. B*, 87(16):165114, 2013.

[251] P. R. Spalart. Airplane trailing vortices. *Annu. Rev. Fluid Mech.*, 30(1):107–138, 1998.

[252] J. R. Spreiter and A. H. Sacks. The rolling up of the trailing vortex sheet and its effect on the downwash behind wings. *J. Aeronaut. Sci.*, 18(1):21–32, 1951.

[253] Y. Srebro, Y. Elbaz, O. Sadot, L. Arazi, and D. Shvarts. A general buoyancy–drag model for the evolution of the Rayleigh–Taylor and Richtmyer–Meshkov instabilities. *Laser Part. Beams*, 21(3):347–353, 2003.

[254] B. Srinivasan, G. Dimonte, and X.-Z. Tang. Magnetic field generation in Rayleigh-Taylor unstable inertial confinement fusion plasmas. *Phys. Rev. Lett.*, 108(16):165002, 2012.

[255] L. Stixrude and R. Jeanloz. Fluid helium at conditions of giant planetary interiors. *Proc. Natl. Acad. Sci.*, 105(32):11071–11075, 2008.

[256] B. E. K. Sugerman, A. P. S. Crotts, W. E. Kunkel, S. R. Heathcote, and S. S. Lawrence. The three-dimensional circumstellar environment of SN 1987A. *Astrophys. J. Suppl. Ser.*, 159(1):60, 2005.

[257] B. E. K. Sugerman, S. S. Lawrence, A. P. S. Crotts, P. Bouchet, and S. R. Heathcote. Evolution and geometry of hot spots in supernova remnant 1987A. *Astrophys. J.*, 572(1):209, 2002.

[258] T. Suzuki, T. Shigeyama, and K. Nomoto. X-ray emission from the collision of the ejecta with the ring nebula around supernova 1987A. *Astron. Astrophys.*, 274:883, 1993.

[259] D. C. Swift, T. E. Tierney IV, R. A. Kopp, and J. T. Gammel. Shock pressures induced in condensed matter by laser ablation. *Phys. Rev. E*, 69(3):036406, 2004.

[260] K. Takayama and T. Saito. Shock wave/geophysical and medical applications. *Annu. Rev. Fluid Mech.*, 36:347–379, 2004.

[261] T. Tanaka and H. Washimi. Formation of the three-ring structure around supernova 1987A. *Science*, 296(5566):321–322, 2002.

[262] W. Thomson. Xv. vortex statics. *Lond. Edinb. Dublin Philos. Mag. J. Sci.*, 10(60):97–109, 1880.

[263] B. Thornber, J. Griffond, O. Poujade, N. Attal, H. Varshochi, P. Bigdelou, et al. Late-time growth rate, mixing, and anisotropy in the multimode narrowband Richtmyer–Meshkov instability: The θ-group collaboration. *Phys. Fluids*, 29(10):105107, 2017.

[264] B. Thornber and Y. Zhou. Energy transfer in the Richtmyer-Meshkov instability. *Phys. Rev. E*, 86(5):056302, 2012.

[265] B. Thornber and Y. Zhou. Numerical simulations of the two-dimensional multimode Richtmyer-Meshkov instability. *Phys. Plasmas*, 22(3):032309, 2015.

[266] D. Tordella and M. Iovieno. Small-scale anisotropy in turbulent shearless mixing. *Phys. Rev. Lett.*, 107(19):194501, 2011.

[267] E. F. Toro. *Riemann Solvers and Numerical Methods for Fluid Dynamics: A Practical Introduction*. Springer Science & Business Media, 2013.

[268] R. Le Toullec, P. Loubeyre, and J.-P. Pinceaux. Refractive-index measurements of dense helium up to 16 GPa at T=298 K: Analysis of its thermodynamic and electronic properties. *Phys. Rev. B*, 40:2368–2378, Aug 1989.

[269] J. Towns, T. Cockerill, M. Dahan, I. Foster, K. Gaither, A. Grimshaw, et al. XSEDE: accelerating scientific discovery. *Comput. Sci. Eng.*, 16(5):62–74, 2014.

[270] C. Y. Tsai and S. E. Widnall. The stability of short waves on a straight vortex filament in a weak externally imposed strain field. *J. Fluid Mech.*, 73(4):721–733, 1976.

[271] V. D. Urlin. Equations of state and the phase diagram of dielectric and metallic helium-4. *J. Exp. Theor. Phys.*, 127(1):121–130, 2018.

[272] W. M. van Rees, F. Hussain, and P. Koumoutsakos. Vortex tube reconnection at Re=104. *Phys. Fluids*, 24(7):075105, 2012.

[273] A. L. Velikovich and G. Dimonte. Nonlinear perturbation theory of the incompressible Richtmyer-Meshkov instability. *Phys. Rev. Lett.*, 76(17):3112, 1996.

[274] L. J. Vermeer, J. N. Sørensen, and A. Crespo. Wind turbine wake aerodynamics. *Prog. Aerosp. Sci.*, 39(6-7):467–510, 2003.

[275] M. Vetter and B. Sturtevant. Experiments on the Richtmyer-Meshkov instability of an air/SF_6 interface. *Shock waves*, 4:247–252, 1995.

[276] W. L. Vos, M. G. E. van Hinsberg, and J. A. Schouten. High-pressure triple point in helium: The melting line of helium up to 240 kbar. *Phys. Rev. B*, 42:6106–6109, Oct 1990.

[277] M. J. Wadas, S. Balakrishna, H. J. LeFevre, C. C. Kurnaz, A. Towne, and E. Johnsen. On the stability of of a pair of vortex rings. *Under Review in J. Fluid Mech.*

[278] M. J. Wadas, S. Brygoo, P. Loubeyre, P. M. Celliers, G. W. Collins, J. H. Eggert, et al. Shock compression of helium to 3.5 Mbar. *In Preparation for Phys. Rev. Lett.*

[279] M. J. Wadas, G. S. Cearley, J. H. Eggert, E. Johnsen, and M. Millot. A theoretical approach for transient shock strengthening in high-energy-density laser compression experiments. *Phys. Plasmas*, 28(8):082708, 2021.

[280] M. J. Wadas and E. Johnsen. Interactions of two bubbles along a gaseous interface undergoing the Richtmyer–Meshkov instability in two dimensions. *Phys. D: Nonlinear Phenom.*, 409:132489, 2020.

[281] M. J. Wadas, L. H. Khieu, G. S. Cearley, H. J. LeFevre, C. C. Kuranz, and E. Johnsen. Saturation of vortex rings ejected from shock-accelerated interfaces. *Phys. Rev. Lett.*, 130(19):194001, 2023.

[282] M. J. Wadas, W. J. White, H. J. LeFevre, C. C. Kurnaz, A. Towne, and E. Johnsen. A hydrodynamic mechanism for clumping along the equatorial rings of SN1987A and other stars. *In Preparation for Phys. Rev. Lett.*

[283] L. Wang and P. A. Mazzali. Dynamical development of a ring-like structure in the supernova 1987A nebula. *Nature*, 355(6355):58–61, 1992.

[284] C. Weber, N. Haehn, J. Oakley, D. Rothamer, and R. Bonazza. Turbulent mixing measurements in the Richtmyer-Meshkov instability. *Phys. Fluids*, 24(7):074105, 2012.

[285] C. R. Weber, D. S. Clark, A. W. Cook, L. E. Busby, and H. F. Robey. Inhibition of turbulence in inertial-confinement-fusion hot spots by viscous dissipation. *Phys. Rev. E*, 89(5):053106, 2014.

[286] C. R. Weber, T. Döppner, D. T. Casey, T. L. Bunn, L. C. Carlson, R. J. Dylla-Spears, et al. First measurements of fuel-ablator interface instability growth in inertial confinement fusion implosions on the National Ignition Facility. *Phys. Rev. Lett.*, 117(7):075002, 2016.

[287] N. J. Wei, I. D. Brownstein, J. L. Cardona, M. F. Howland, and J. O. Dabiri. Near-wake structure of full-scale vertical-axis wind turbines. *J. Fluid Mech.*, 914, 2021.

[288] W. White, S. A. Beig, and E. Johnsen. Pressure fields produced by single-bubble collapse near a corner. *Phys. Rev. Fluids*, 8(2):023601, 2023.

[289] G. B. Whitham. On the propagation of shock waves through regions of non-uniform area or flow. *J. Fluid Mech.*, 4(4):337–360, 1958.

[290] S. E. Widnall. The structure and dynamics of vortex filaments. *Annu. Rev. Fluid Mech.*, 7(1):141–165, 1975.

[291] S. E. Widnall, D. Bliss, and A. Zalay. Theoretical and experimental study of the stability of a vortex pair. In *Aircraft Wake Turbulence and its Detection*, pages 305–338. Springer, 1971.

[292] S. E. Widnall, D. B. Bliss, and C.-Y. Tsai. The instability of short waves on a vortex ring. *J. Fluid Mech.*, 66(1):35–47, 1974.

[293] C. Winisdoerffer and G. Chabrier. Free-energy model for fluid helium at high density. *Phys. Rev. E*, 71(2):026402, 2005.

[294] J. Xin, R. Yan, Z.-H. Wan, D.-J. Sunand J. Zheng, H. Zhang, H. Aluie, and R. Betti. Two mode coupling of the ablative Rayleigh-Taylor instabilities. *Phys. Plasmas*, 26(3):032703, 2019.

[295] J. Yao and F. Hussain. Vortex reconnection and turbulence cascade. *Annu. Rev. Fluid Mech.*, 54:317–347, 2022.

[296] D. L. Youngs. Numerical simulation of mixing by Rayleigh–Taylor and Richtmyer–Meshkov instabilities. *Laser Part. Beams*, 12(4):725–750, 1994.

[297] M. Yousaf. The effect of overtaking disturbances on the motion of converging shock waves. *J. Fluid Mech.*, 66(3):577–591, 1974.

[298] M. Yousaf. Strong shocks in an exponential atmosphere. *Phys. Fluids*, 30(12):3669–3672, 1987.

[299] N. J. Zabusky. Are cosmic knots escaped vortex projectiles? In *APS April Meeting Abstracts*, pages K12–10, 1997.

[300] N. J. Zabusky. Vortex paradigm for accelerated inhomogeneous flows: Visiometrics for the Rayleigh-Taylor and Richtmyer-Meshkov environments. *Annu. Rev. Fluid Mech.*, 31:495, 1999.

[301] N. J. Zabusky and S. Zhang. Shock–planar curtain interactions in two dimensions: Emergence of vortex double layers, vortex projectiles, and decaying stratified turbulence. *Phys. Fluids*, 14(1):419–422, 2002.

[302] S. Zhang and N. J. Zabusky. Shock–planar curtain interactions: Strong secondary baroclinic deposition and emergence of vortex projectiles and late-time inhomogeneous turbulence. *Laser Part. Beams*, 21(3):463–470, 2003.

[303] S. Zhang, N. J. Zabusky, and K. Nishihara. Vortex structures and turbulence emerging in a supernova 1987A configuration: Interactions of “complex” blast waves and cylindrical/spherical bubbles. *Laser Part. Beams*, 21(3):471–477, 2003.

[304] W. Zhang, A. Almgren, V. Beckner, J. Bell, J. Blaschke, C. Chan, et al. AMReX: a framework for block-structured adaptive mesh refinement. *J. Open Source Softw.*, 4(37):1370–1370, 2019.

[305] J. Zheng, Q. F. Chen, Y. J. Gu, J. T. Li, Z. G. Li, C. J. Li, and Z. Y. Chen. Shock-adiabatic to quasi-isentropic compression of warm dense helium up to 150 GPa. *Phys. Rev. B*, 95(22):224104, 2017.

[306] J. Zhou, R. J. Adrian, S. Balachandar, and T. M. Kendall. Mechanisms for generating coherent packets of hairpin vortices in channel flow. *J. Fluid Mech.*, 387:353–396, 1999.

[307] Y. Zhou. Rayleigh–Taylor and Richtmyer–Meshkov instability induced flow, turbulence, and mixing. II. *Phys. Rep.*, 723:1–160, 2017.

[308] Y. Zhou. Rayleigh–Taylor and Richtmyer–Meshkov instability induced flow, turbulence, and mixing. I. *Phys. Rep.*, 720-722:1–136, 2017.

[309] Y. Zhou, M. Groom, and B. Thornber. Dependence of enstrophy transport and mixed mass on dimensionality and initial conditions in the Richtmyer–Meshkov instability induced flows. *J. Fluids Eng.*, 142(12), 2020.

[310] A. B. Zylstra, D. T. Casey, A. Kritcher, L. Pickworth, B. Bachmann, K. Baker, et al. Hot-spot mix in large-scale HDC implosions at NIF. *Phys. Plasmas*, 27(9):092709, 2020.

[311] A. B. Zylstra, O. A. Hurricane, D. A. Callahan, A. L. Kritcher, J. E. Ralph, H. F. Robey, et al. Burning plasma achieved in inertial fusion. *Nature*, 601(7894):542–548, 2022.

[312] A. B. Zylstra, A. L. Kritcher, O. A. Hurricane, D. A. Callahan, K. Baker, T. Braun, et al. Record energetics for an inertial fusion implosion at NIF. *Phys. Rev. Lett.*, 126(2):025001, 2021.